

Heavy Flavor Jet Quenching in Relativistic Heavy Ion Collisions at the LHC

Tingting Wang

Submitted in partial fulfillment of the
requirements for the degree of
Doctor of Philosophy
in the Graduate School of Arts and Sciences

COLUMBIA UNIVERSITY

2017

© 2017

Tingting Wang

All rights reserved

Abstract

Heavy Flavor Jet Quenching in Relativistic Heavy Ion Collisions at the LHC

Tingting Wang

This thesis describes the measurement of inclusive heavy flavor jet suppression in collisions between two lead nuclei with the center of mass energy per nucleon-nucleon pair of $\sqrt{s_{NN}} = 2.76$ TeV with the A Toroidal LHC ApparatuS (ATLAS) detector at the Large Hadron Collider (LHC).

The measurement of the heavy flavor jets and b -jet quenching at the LHC is important in the path towards the understanding of QGP. Parton showers initiated by heavy quarks are expected to be sensitive to the medium in a different way as the large quark mass suppresses the medium-induced radiation. This results in a different interplay between radiative and collisional energy loss. Therefore the analysis of the properties of jet associated with b hadrons (b -jet) is useful in understanding energy loss in the QGP.

The inclusive b -jet suppression R_{AA} has been measured using muons in jets, where a b -jet corresponds to a jet with at least one muon clustered with the anti- k_t algorithm with parameter $R = 0.2$. The b -jets of $p_T^{b\text{-jet}}$ between 30 GeV - 150 GeV and $|\eta| < 2.1$ are identified by the semileptonic decay of beauty hadrons. Muons originating from background sources, primarily Charm hadrons, pion and kaon decays, have been removed from the analysis using template fits to the distribution of a quantity (p_T^{rel}) capable of statistically distinguishing between signal and background. The measured nuclear modification factor R_{AA} has been presented in different centrality bins as a function of the b -jet transverse momentum p_T . The results of R_{AA} indicate that the yield of the most central event (0-10%) experiences more suppression compared to the most peripheral event (60-80%) by a factor of approximate 2.

Contents

List of Figures	v
List of Tables	xv
Acknowledgments	xv
1 Introduction	1
2 Heavy Ion Physics	4
2.1 Fundamentals of QCD	5
2.1.1 Asymptotic Freedom	6
2.2 Phase Structure of QCD Matter	8
2.2.1 Lattice QCD predictions	10
2.2.2 QCD Phase Diagram	12
2.3 QGP phenomenology at LHC	15
2.3.1 Pre-equilibrium	15
2.3.2 Collective Flow and Perfect Fluidity of QGP	23
2.3.3 Hadronization and Freeze out	27
3 Heavy Flavour Physics	29
3.1 Perturbative QCD and Hard Scattering	29

3.1.1	Parton Models	30
3.1.2	Deep Inelastic Scattering	31
3.1.3	Jets	32
3.2	Hard Processes in Nuclear Collisions	34
3.2.1	Glauber Model to Experimental Data Mapping	35
3.2.2	Nuclear effects	37
3.2.3	Jet Quenching	38
3.3	Jet Phenomenology Involving Heavy Flavor	46
3.3.1	Heavy Flavour Production	46
3.3.2	Semi-leptonic Decay	48
3.4	Heavy Flavor Quenching	49
4	Experimental Setup	53
4.1	The Large Hadron Collider	53
4.2	The ATLAS Experiment	55
4.2.1	Inner Detector	55
4.2.2	Calorimeters	58
4.2.3	Muon Spectrometer	62
4.2.4	Zero Degree Calorimeters	66
4.2.5	Minimum Bias Trigger Scintillators	67
4.2.6	Trigger System	67
5	Data Analysis	73
5.1	2011 Pb+Pb Data samples	73
5.2	Collision geometry and centrality definition	75
5.3	2013 <i>pp</i> data samples	76
5.4	Monte Carlo Simulation	83

5.5	Jet Reconstruction and Performance	84
5.5.1	Jet Reconstruction	84
5.5.2	Jet Performance	88
5.6	Muon Selection and Reconstruction Efficiency	94
5.6.1	Muon Reconstruction	94
5.6.2	Muon reconstruction efficiency	96
5.6.3	Muon performance	96
6	B-tagging Analysis	100
6.1	p_T^{rel} analysis	100
6.2	Jet Muon Pair Selection	100
6.3	Muon Tagged Jets	103
6.3.1	Combinatoric Background Subtraction	103
6.4	Template Fitting Procedure	117
6.4.1	Light Jet Template Construction	117
6.4.2	Extra Smearing on Light Jet	121
6.4.3	Template Fitting Result	126
6.5	Validation	133
6.5.1	Jet Energy Scale and Resolution	133
6.6	Unfolding	136
6.6.1	Acceptance Correction	138
6.7	Systematic Uncertainties	138
6.7.1	Jet Energy Scale	139
6.7.2	Jet Energy Resolution	140
6.7.3	Flavor Dependence of JES	142
6.7.4	JES between the Pb+Pb and the pp collisions	144
6.7.5	Uncertainties on b -jet Fraction	148

6.7.6	Uncertainties on efficiency	148
6.7.7	Uncertainties on $\langle T_{AA} \rangle$ and luminosity	148
7	Results	152
7.1	Heavy Flavor Fractions	152
7.2	b-jet Spectra	154
7.3	b-jet Suppression	156
8	Conclusions	159
	Bibliography	163

List of Figures

2.1	Summary of measurements of α_s as a function of the respective energy scale Q from [22]. The strong coupling strength clearly goes down as the momentum transfer increases.	8
2.2	Energy density divided by T^4 as a function of temperature in a lattice calculation using physical quark masses [27]	11
2.3	QCD Phase diagram represented in the direction of temperature and baryon chemical potential. Taken from NSAC Long Range Plan 2007 [30].	12
2.4	Event display of a heavy ion collision at LHC (ATLAS collaboration). Taken from [31].	14
2.5	Schematic representation of the various stages of a Heavy Ion Collisions as a function of time t and the longitudinal coordinate z (the collision axis). Taken from [33].	15
2.6	Schematic view of two colliding nuclei with left side presents transverse and right side presents longitudinal views. Taken from [34].	17
2.7	Left: Two nuclei A and B before collisions. Right: Nuclei A and B after collisions with energy deposited in region $z \sim 0$. Taken from [36].	19
2.8	Gluon distributions from HERA experiment as a function of x at three different Q^2 [37]	21
2.9	Gluon saturation in a hadron as x decreases [38]	22

2.10	Geometry of a non-central heavy ion collisions. Taken from [42].	24
2.11	Nuclear EOS of Hagedorn resonance gas model [41] (EOS H), an ideal gas model (EOS I) and a connection of the two (EOS Q). [43]	25
2.12	In an off-central collision between two heavy nuclei, the overlap region is almond-shaped with the length of the arrow indicates the expansion rate. The large pressure gradient in the horizontal direction (the collision plane) causes a faster expansion than in the vertical direction. Taken from [48]. . .	26
2.13	Contours of constant energy density in the transverse plan at different time after equilibrium [43]	26
2.14	Time evolution of spatial eccentricity and momentum anisotropy [43]	27
3.1	The single inclusive jet cross section ratio between data and theory at different energies [74, 75]	34
3.2	Schematic of the mapping of experimental observables (the number of charged particles N_{ch}) with Glauber quantities ($\vec{b}, \langle N_{part} \rangle$) [76]	36
3.3	Schematic of $R_i^A(x, Q^2)$ distribution as a function of x and the different nuclear effects in each x region [81]. In this figure, y_0 is the height at which shadowing levels out as $x \rightarrow 0$, x_a and y_a are the position and height, respectively, at which antishadowing is maximum, and x_e and y_e are the position and height at which the EMC-ect is minimum.	39
3.4	Diagrams for collisional (left) and radiative (right) energy loss of a quark with energy E passing through a QGP medium. Taken from [95].	40
3.5	Sketch of dijet production and pQCD factorisation in hadronic collisions: $f_{a/A}(x, Q^2)$ are the PDFs, $\mathcal{D}_{i \rightarrow h}(z, Q^2)$ are the FFs and ISF (FSR) represents initial (final) state radiation. Taken from [95].	45

3.6	Diagrams for examples of heavy-flavor production: Pair creation (a,b with leading order. c, with gluon emission), Flavour excitation (d), Gluon splitting (e), Events classified as gluon splitting but of flavor-excitation character. [113]	47
3.7	Left: Nuclear modification factor R_{AA} for electrons from heavy quark decays as function of p_T for the 10% most central Au + Au collisions at $\sqrt{s_{NN}} = 200$ GeV. The boxes show the point-to-point correlated systematic uncertainty. Right: Nuclear modification factors R_{AA} for open heavy-flavor electrons vs centrality, integrated above the $p_T^e > 4$ GeV range. Taken from [117]	50
3.8	Non-photonuclear electron nuclear modification factor R_{AA} (left) and elliptic flow v_2 (right) measured for 0–10% and 0–60% centrality intervals, respectively, in Au+Au collisions at $\sqrt{s_{NN}} = 200$ GeV. The vertical bars on data points indicate statistical uncertainties. The brackets and boxes around data points represent the systematic uncertainties from Au+Au and p+p collisions, respectively. Taken from [118].	51
3.9	The centrality integrated (0–100%) b -jet R_{AA} as a function of p_T . The normalization uncertainty from the integrated luminosity in pp collisions and from T_{AA} is represented by the green band around unity. The data are compared to pQCD-based calculations from Ref. [120]. Taken from [119]	52
4.1	A diagram of the ATLAS detector showing the major detector systems. Taken from [122].	56
4.2	A diagram of the ATLAS inner detector barrel region. Taken from [123].	57
4.3	A cut-out view of ATLAS calorimeter detectors. Taken from [124].	59
4.4	Schematic view of the muon spectrometer in the $x - y$ projections. Inner, Middle and Outer chamber stations are denoted BI, BM, BO in the barrel and EI, EM, EO in the end-cap. Taken from [125].	63

4.5	Schematic view of the muon spectrometer in the $z - y$ projections. Taken from [125].	64
4.6	Muon Spectrometer as both high and low momentum trigger. Taken from [40].	66
5.1	The MU4 trigger efficiency distributions in mid and forward pseudorapidity region are shown in different centrality intervals in 2011 Pb+Pb collisions. . .	75
5.2	Signal muon (a) and background muon (b) momentum balance distribution in different centrality intervals from 2011 Pb+Pb MC sample. Taken from [137].	77
5.3	Signal and background muon momentum balance distribution in pp collisions (red points) and Pb+Pb collisions (black points) in the 0-60% centrality interval. The signal and background distributions are separately normalized such that their integral is unity. The background distribution is binned more coarsely because of the limited statistics available in the background sample. Taken from [137].	78
5.4	$\frac{\Delta p}{p_{TD}}$ distribution for b -, c - and light-jets in different muon transverse momentum p_T intervals in the 2012 pp MC sample.	79
5.5	Fraction for b -, c - and light-jets that pass the $\frac{\Delta p}{p_{TD}}$ cut as a function of muon p_T in the 2012 pp MC sample.	80
5.6	The MU4_JET30 efficiency distributions at the L1 level in the mid and the forward pseudorapidity region are shown on the left and right, respectively, in 2013 pp collisions.	81
5.7	The MU4_JET30 trigger efficiency distributions at HLT in mid and forward pseudorapidity region are shown on the left and right, respectively, in 2013 pp collisions.	82
5.8	The MU4_JET30 trigger efficiency distributions in the mid and the forward pseudorapidity region are shown on the left and right, respectively, in 2013 pp collisions.	82

5.9	Left: Jet η and Right: Jet ϕ resolution distribution for the full jet p_T range.	89
5.10	Jet η resolution distribution with vertex correction for the full jet p_T range.	89
5.11	The relationship between jet $\Delta\eta$ and vx_z in different jet top : p_T and bottom: $ \eta $ bins in MC sample for the full centrality range.	90
5.12	The relationship between jet $\Delta\eta$ and vx_z as a function of jet top: p_T and bottom: $ \eta $ used for jet η correction in MC sample for the full centrality range.	91
5.13	The jet transverse momentum p_T and pseudorapidity η distributions from selected jet muon pairs are shown on the left and right, respectively, in 2011 Pb+Pb collisions for the full centrality range.	93
5.14	The jet transverse momentum p_T distributions from selected jet muon pairs in 2011 Pb+Pb muon triggered sample for the full centrality range on the left and jet p_T comparison between jet trigger and muon trigger sample on the right.	93
5.15	The jet transverse momentum p_T and pseudorapidity η distributions from selected jet muon pairs are shown on the left and right, respectively, in 2013 pp collisions.	94
5.16	Muon reconstruction efficiency in different centrality intervals in the Pb+Pb sample.	97
5.17	Muon reconstruction efficiency in the pp sample.	98
5.18	The muon transverse momentum p_T and pseudorapidity η distributions from selected jet muon pairs are shown on the left and right, respectively, in 2011 Pb+Pb collisions for the full centrality range.	99
5.19	The muon transverse momentum p_T and pseudorapidity η distributions from selected jet muon pairs are shown on the left and right, respectively, in 2013 pp collisions.	99

6.1	The jet transverse momentum p_T distributions from selected jet muon pairs in MC and data and their ratio in Pb+Pb and pp collisions are shown on the top and bottom, respectively.	102
6.2	p_T^{rel} distribution for b -, c - and light-jets (data driven) in different jet p_T intervals for the full centrality range in 2011 Pb+Pb MC and data sample respectively.	104
6.3	p_T^{rel} distribution for b -, c - and light-jets (data driven) in different jet p_T intervals in 2012 pp MC and data sample respectively.	105
6.4	The ΣE_T^{FCal} distributions in minimum bias (blue) and jet-triggered (red) events. The ratio, which defines the reweighting factors in the MC, is shown below and is fixed to unity above $\Sigma E_T^{\text{FCal}} > 3.5$ TeV. Taken from [133].	108
6.5	ΔR in different jet p_T bins for the full centrality range in 2011 Pb+Pb data, black is original distribution, red is from combinatoric background.	109
6.6	ΔR in different jet p_T bins after combinatoric subtraction for the full centrality range in 2011 Pb+Pb data.	110
6.7	p_T^{rel} in different jet p_T bins for the full centrality range in 2011 Pb+Pb data, black is original distribution, red is after combinatoric background subtraction.	111
6.8	ΔR in different centrality bins for the full jet p_T range in 2011 Pb+Pb data, black is original distribution, red is from combinatoric background.	112
6.9	ΔR in different centrality bins after combinatoric subtraction for the full jet p_T range in 2011 Pb+Pb data.	113
6.10	p_T^{rel} in different jet p_T bins for the full centrality range in 2011 Pb+Pb data, black is original distribution, red is after combinatoric background subtraction.	114
6.11	ΔR in different jet p_T bins in 2013 pp data.	115
6.12	p_T^{rel} in different jet p_T bins in 2013 pp data.	116

6.13	Weight distribution as a function of muon p_T in different jet p_T bin in 2011 Pb+Pb MC.	119
6.14	p_T^{rel} distribution between MC light-jet template and data driven template in different jet p_T bin	120
6.15	Top: p_T^{rel} distribution accounting for Jacobean between light-jet template and data, Bottom: p_T^{rel} width distribution for $30 < \text{jet } p_T < 50$ GeV in 2011 Pb+Pb data.	122
6.16	Top: p_T^{rel} distribution accounting for Jacobean between light-jet template after extra smearing and data, Bottom: p_T^{rel} width distribution for $30 < \text{jet } p_T < 50$ GeV in 2011 Pb+Pb data.	123
6.17	From top to bottom : b -jet, c -jet and light-jet's p_T^{rel} distribution in different centrality bins for the full jet p_T range in 2011 Pb+Pb MC.	124
6.18	p_T^{rel} mean distribution as a function of centrality for the full jet p_T range in 2011 Pb+Pb MC.	125
6.19	Template fitting result in different centrality intervals for $30 < \text{jet } p_T < 50$ GeV.	128
6.20	Template fitting result in different centrality intervals for $50 < \text{jet } p_T < 75$ GeV.	129
6.21	Template fitting result in different centrality intervals for $75 < \text{jet } p_T < 105$ GeV.	130
6.22	Template fitting result in different centrality intervals for $105 < \text{jet } p_T < 150$ GeV.	131
6.23	Template fitting result in different jet p_T intervals in pp sample.	132
6.24	The jet p_T and η distributions from selected jet muon pairs are shown on the left and right, respectively, in 2013 pp collisions.	134
6.25	b -jet energy scale closure for the full centrality range in Pb+Pb sample. . .	134
6.26	light-jet energy scale for the full centrality range in Pb+Pb sample.	135

6.27	Unfolding correction factor distribution in different centrality intervals after energy scale in 2011 Pb+Pb samples.	137
6.28	Unfolding correction factor distribution in 2012 pp samples.	138
6.29	Systematics uncertainties on R_{AA} from JES and JER as a function of jet transverse momentum p_T in different centrality intervals.	141
6.30	Left: Comparison of quark jet fraction of b -jet between the PYTHIA 6 and the HERWIG++ samples as a function of jet transverse momentum p_T . Right: Comparison of gluon jet fraction of b -jet between the PYTHIA 6 and the HERWIG++ samples as a function of jet transverse momentum p_T	143
6.31	Left: Response distribution of quark jets as a function of jet transverse momentum p_T in the PYTHIA 6 sample. Right: Response distribution of quark jets as a function of jet transverse momentum p_T in the PYTHIA 6 sample.	144
6.32	r_{trk} distributions between MC and data and their ratio as a function of jet p_T in centrality intervals in Pb+Pb sample.	145
6.33	r_{trk} distributions between MC and data and their ratio as a function of jet p_T in pp sample.	146
6.34	Systematics uncertainties on R_{AA} from JES between Pb+Pb and pp as a function of jet transverse momentum p_T are shown in different centrality intervals.	147
6.35	Systematics uncertainties on R_{AA} from b -jet fraction variations from template fitting procedure as a function of jet transverse momentum p_T in different centrality intervals.	149
6.36	Systematics on R_{AA} from muon trigger efficiency and muon reconstruction efficiency as a function of jet transverse momentum p_T in different centrality intervals.	150

7.1	<i>b</i> -jet fraction distribution in different centrality intervals in Pb+Pb and <i>pp</i> sample.	153
7.2	The <i>b</i> -jet yield as a function of jet transverse momentum p_T is shown for various centrality classes of Pb+Pb collisions as indicated in the legend. The yields are scaled by the equivalent number of minimum bias events sampled and by T_{AA} . The spectra are also scaled by powers of 10 for visibility. The <i>b</i> -jet cross section in <i>pp</i> collisions is also shown. The systematics uncertainties are shown as shaded boxes with transparent color filled. The statistical uncertainties are represented as error bars.	155
7.3	<i>b</i> -jet R_{AA} distribution as a function of jet transverse momentum p_T . Each panel indicates a different centrality interval. The fractional normalization uncertainties coming from the luminosity and the $\langle T_{AA} \rangle$ factors are indicated separately as shaded boxes centered at one with solid color filled. The systematics uncertainties due to the template fitting are shown as open boxes and they are uncorrelated in p_T . The remaining systematics uncertainties are fully correlated in p_T and are indicated by shaded boxes with transparent color filled. The statistical uncertainties are represented as error bars. . . .	157
7.4	<i>b</i> -jet R_{AA} distribution as a function of N_{part} . Each panel indicates a different range in jet transverse momentum p_T . The systematics uncertainties due to the template fitting are shown as open boxes and they are uncorrelated in N_{part} . The remaining systematics uncertainties are partially correlated in N_{part} and are shown as shaded boxes with transparent color filled, including the fractional normalization uncertainties coming from the luminosity and the $\langle T_{AA} \rangle$ factors. The statistical uncertainties are represented as error bars. . .	158

8.1	<i>b</i> -jet R_{AA} distribution as a function of jet transverse momentum p_T in Pb+Pb collisions between the ATLAS experiment and theory calculation [155]. The systematics uncertainties are shown as shaded boxes with transparent color filled. The statistical uncertainties are represented as error bars.	160
8.2	<i>b</i> -jet R_{AA} distribution as a function of jet transverse momentum p_T in Pb+Pb collisions between the ATLAS experiment and the CMS experiment [119]. The fractional normalization uncertainties coming from the luminosity and the $\langle T_{AA} \rangle$ factors are indicated separately as shaded boxes centered at one. The systematics uncertainties are shown as shaded boxes. The statistical uncertainties are represented as error bars.	161

List of Tables

2.1	g_{BE} and g_{FD} values at different temperature	9
5.1	The $\langle T_{AA} \rangle$ and $\langle N_{\text{part}} \rangle$ values and their uncertainties in each centrality bin	76
5.2	σ of the gaussian fit of $\frac{\Delta p}{p_{TD}}$ distribution from b, c - jets	79
5.3	MC samples used in Pb+Pb	83
5.4	MC samples used in pp	84
6.1	Number of jet muon pairs after jet and muon selection	101
6.2	JES systematics uncertainties on R_{AA} due to flavor effects in each p_T bin in %	143
7.1	Signal b-jet ratio in each centrality and p_T bin from Pb+Pb and pp sample	152

Acknowledgments

I would like to thank my parents for always being supportive throughout all these years, the fact that I know they are proud of me makes me move forward steadily when facing failures.

I want to thank my advisor Professor Brian Cole, his wisdom and kindness helped me a lot during my Ph.D. years. He taught me not how to do research well, but also how to do things right and how to cooperate with others.

I want to thank my entire group in Columbia University, Professor Bill Zajc, Aaron, Soumya, Sarah, Yujiao, Dennis, Laura, Felix and Xiao. They provided a friendly and independent atmosphere for me to do analysis, as well as enjoy graduate student life.

I want to express my special thank you to Ziyuan, who always stands by me and encourages me to be a better person. His consideration, optimism and unconditional supports give me strength under the pressure. The journey would be much more difficult if you were not there.

I would like to give many thanks to all my wonderful friends: Shuo, Jiechen, Luchang, Runzhi, Jue, Ying, Deke, Hanjie, Jingze, Jingkai, Te. Having someone to share your happiness is not a hard thing, but having someone to stay with you when you are down is precious. I'm lucky to have you all as my valuable friends all these years. I'm honorable to be part of Columbia University. The experience will inspire me to move forward in the future.

Chapter 1

Introduction

This thesis describes the measurement of inclusive heavy flavor jet suppression in collisions between two lead nuclei with the center of mass energy per nucleon-nucleon pair of $\sqrt{s_{NN}} = 2.76$ TeV with the ATLAS detector at the Large Hadron Collider (LHC).

The Pb+Pb collisions produce a hot and dense state of matter with the highest temperature accessible in the laboratory, called the quark-gluon plasma (QGP) [1]. The QGP is a fundamental physical system which can be described by quantum chromodynamics (QCD). This phase was once thought to consist of asymptotically free quarks and gluons, but we now know that it forms a strongly-coupled QGP which exhibits hydrodynamic behavior. Many measurements have been carried out in previous experimental searches for such a medium, at the Alternating Gradient Synchrotron (AGS), Super Proton Synchrotron (SPS), Relativistic Heavy Ion Collider (RHIC) and most recently in Pb+Pb collisions at the LHC.

In hard scattering processes, a parton shower is produced after highly virtual partons undergoing successive branchings. The ensemble of produced particles is highly collimated about the direction of the initial parton and contains a range of different momentum scales. The formation of “jets” from these produced particles and how they emerge from perturbative QCD (pQCD) calculations have been extensively studied in high-energy physics. A major

component of the current heavy-ion physics program is the study of the phenomenon of jet quenching, in which jet showers will lose energy or have partons hadronisation modified by interactions with the medium, even after the first generation of LHC measurements we only have a basic qualitative understanding of quenching mechanism.

There is disagreement in the theoretical literature regarding the interpretation of heavy quark suppression measurements in RHIC, particularly regarding the non-perturbative effects. The measurement of the heavy flavor jets and b -jet quenching at the LHC is thus important in the path towards the understanding of QGP. Parton showers initiated by heavy quarks are expected to be sensitive to the medium in a different way as the large quark mass suppresses the medium-induced radiation. This results in a different interplay between radiative and collisional energy loss. Also the angular pattern of medium-induced radiation can be altered through the “Dead cone” effect [2]. Therefore the analysis of the properties of jet associated with b hadrons (b -jet) is useful in understanding energy loss in the QGP.

The thesis is organized as follows:

1. Chapter 2 introduces the heavy-ion physics including the physical motivation, fundamentals of QCD and the phenomenology of QGP at the LHC.
2. Chapter 3 describes theoretical aspects of heavy flavor physics including hard processes in nuclear collisions and its probes of QGP, pQCD and hard scattering in heavy flavor physics, jet phenomenology and heavy flavor jet quenching.
3. Chapter 4 gives an introduction to the experimental apparatuses, the LHC and the ATLAS detector, used to provide data for the measurements in this thesis.
4. Chapter 5 provides the definition of centrality, also including the description of jet and muon reconstruction in this analysis.
5. Chapter 6 gives a detailed description of the methods used in the heavy flavor suppression measurement.

6. Chapter 7 presents the results including heavy flavor fraction and b -jet suppression.
7. Chapter 8 discusses the final results.

Chapter 2

Heavy Ion Physics

Nuclear physics studies the basic properties of nuclear matter. By the late 1960's, physicists had discovered a wide variety of hadrons, i.e., particles that carry and interact via the strong interaction. Gell-Mann and Ne'eman were able to systematize the various hadrons into multiplets by assuming that each baryon was formed from three quarks and each meson from a quark-antiquark pair [3], leading to the prediction of the Ω^- baryon. The observation of the Ω^- validated their approach [4], but implied that in addition to their "flavor" quantum numbers, quarks must also carry another quantum numbers, which was called color, which later became a key component in constructing the quark-based model [5] of the strong interaction called Quantum Chromodynamics (QCD).

The structure functions which express the internal structure of hadrons, are independent of high momentum Q^2 transfer as well as the functions of a single scaling variable, x by Bjorken Scaling [6]. The deep inelastic scattering (DIS) experiment at the Stanford Linear Accelerator Center (SLAC) provides validation for this scaling behavior [7, 8], and at the same time leads to the interpretation of the Parton Model [9, 10] which explains the point-like constituents within the nucleon.

Bjorken Scaling suggested that the coupling strength becomes relatively weak for high energies, which is the property of asymptotic freedom possessed by a non-Abelian gauge

theory, as can be demonstrated using renormalization group techniques [11–14]. When calculating the running of the coupling, the β -function is negative due to the requirement of the SU(3) gauge symmetry [15, 16]. The renormalization criteria and the negative property are satisfied by the theories mentioned above. Moreover, further calculation of DIS structure functions ensured the consistency between the scaling properties of these non-Abelian gauge theories and experimental observations [17–20].

The strong interaction between spin- $\frac{1}{2}$ quarks and spin-1 gluons can be described by QCD. Various experimental results provide demonstration for the correctness of QCD being the theory for the description of strong interaction. Moreover, the mass of visible matter can be explained by the chiral symmetry (possessed by the QCD Lagrangian) that is broken by the QCD vacuum. However, the non-perturbative features of QCD bring big challenges in theoretical calculations due to the relatively large coupling in low momentum range, and further work has been done to study these challenges for a better and more comprehensive understanding of strong interaction.

2.1 Fundamentals of QCD

There are six $N_f = 6$ fermions (quarks) of different quark flavors with spin- $\frac{1}{2}$ and eight $N_c^2 - 1 = 8$ gauge bosons with spin-1 in QCD. The gauge-invariant Lagrangian density can be written as [21]:

$$\mathcal{L}_{QCD} = \sum_f \bar{q}_f^\alpha (i \gamma^\mu D_\mu - m_f)_{\alpha\beta} q_f^\beta - \frac{1}{4} F_{\alpha\beta}^a F_a^{\alpha\beta} \quad , \quad (2.1)$$

where f represents the quark flavor of u (up), d (down), s (strange), c (charm), b (bottom), t (top). The symbols $(D_\mu)_{\alpha\beta}$, $(m_f)_{\alpha\beta}$ and $F_{\alpha\beta}^a$ represent covariant derivative, quark mass

term and field strength tensor respectively, and they are defined as

$$\begin{aligned}
 (D_\mu)_{\alpha\beta} &\equiv \partial_\mu \delta_{\alpha\beta} + ig(T_a)_{\alpha\beta} A_\mu^a \\
 (m_f)_{\alpha\beta} &\equiv m_f \delta_{\alpha\beta} \\
 F_{\alpha\beta}^a &= \partial_\alpha A_\beta^a - \partial_\beta A_\alpha^a - gf^{abc} A_\alpha^b A_\beta^c .
 \end{aligned}
 \tag{2.2}$$

$q_f^{\alpha=1,2,3}$ represent quark fields in an $SU(3)$ triplet, and $A_\mu^{a=1,\dots,8}$ represents gluon field. They are in an $SU(3)$ octet. g is the coupling constant representing the gauge coupling strength. The group generators T_a are hermitian 3×3 matrices which satisfy the following relation:

$$[T_a, T_b] = if_{abc} T_c . \tag{2.3}$$

Here f_{abc} ¹ represent structure constants which are antisymmetric for all indices.

The significant difference between non-Abelian QCD and Abelian Quantum Electrodynamics (QED) is that the Lagrangian of QCD introduces a self-coupling term for gauge bosons.

2.1.1 Asymptotic Freedom

QCD is a $SU(N_c)$ non-Abelian group theory, where the N_c is the number of colors. It is asymptotically free since the coupling for strong interaction decreases as we increase the energy scale. The beta function, which is defined as the derivative of the coupling constant with respect to the logarithm of the energy scale, is negative. The one loop calculation gives:

$$\beta(g) = \frac{\partial \alpha}{\partial \ln \mu} = -\frac{g^3}{48\pi^2} [11T(A) - 4T(R_{DF})] + \mathcal{O}(g^5). \tag{2.4}$$

¹Note that the rules to raise or lower the a, b, c indices are trivial (+, \dots , +) so that $f_{abc} = f^{abc}$. On the other hand, for Lorentz μ, ν indices, one transforms according to the metric signature, for what Minkovski (+, -, -, -) is used throughout this thesis.

The T in the above equation is the index of a representation R . For the gauge field in the $SU(3)$ representation, we have $T(A) = 3$, and for the $n_F = 6$ different flavors of Dirac fermions in the fundamental representation, we have $T(R_{DF}) = n_F/2$. We can see the beta function is negative for $n_F < 16$. Consequently, the strong interaction coupling constant will drop as we increase the energy scale μ and vanishes as μ approaches infinity (we commonly use Q as the energy scale instead of μ):

$$\alpha_s(Q^2) = \frac{4\pi}{(11 - \frac{2}{3}N_f) \log(Q^2/\Lambda_{QCD}^2)} . \quad (2.5)$$

In the following figure, we have shown the strong interaction coupling constant α_s as we vary the energy scale Q , and the asymptotic freedom can be seen.

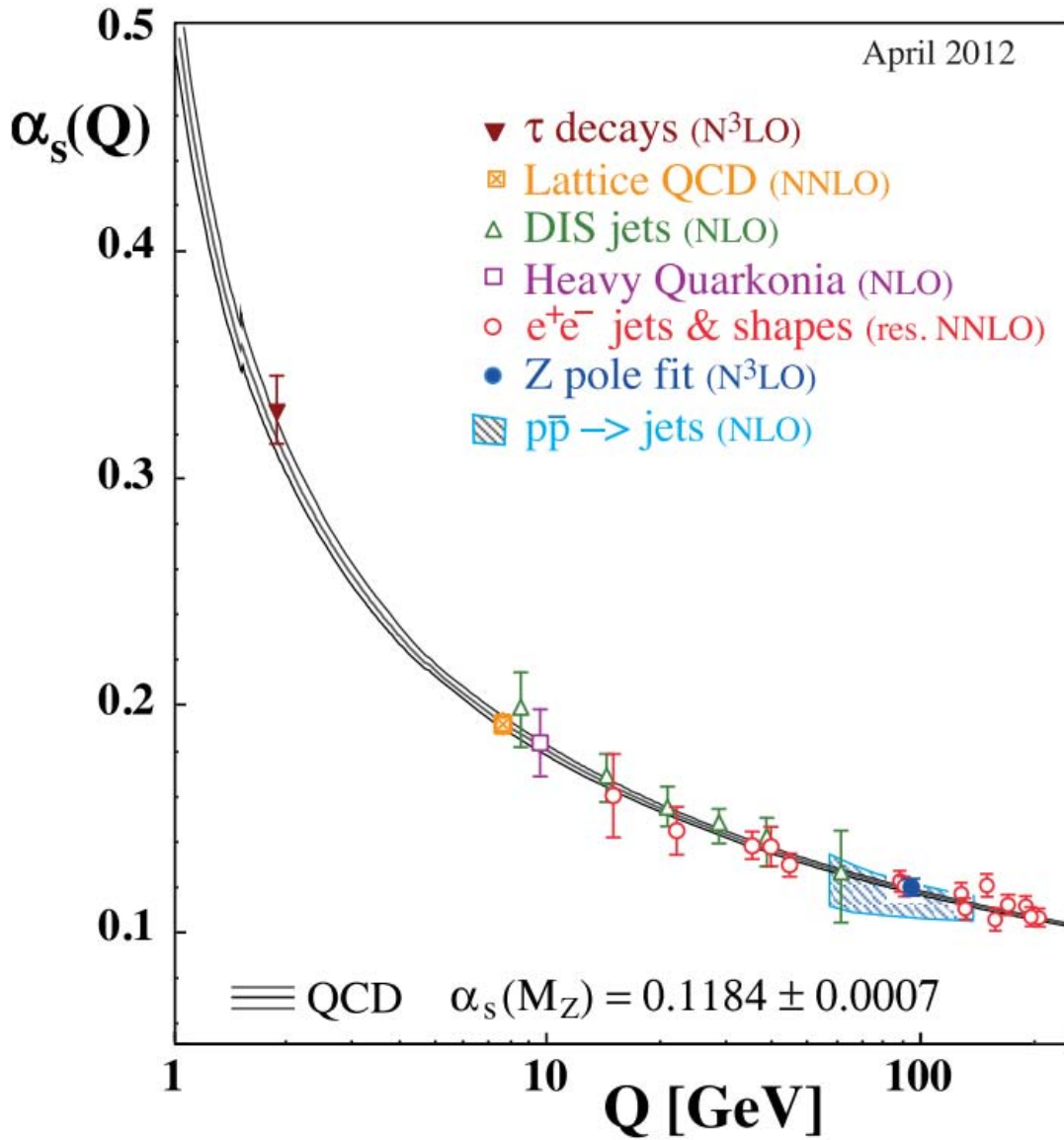


Figure 2.1: Summary of measurements of α_s as a function of the respective energy scale Q from [22]. The strong coupling strength clearly goes down as the momentum transfer increases.

2.2 Phase Structure of QCD Matter

Statistical methods are used for analyzing high multiplicities of particles in heavy ion collisions before QCD was introduced [23]. Rolf Hagedorn introduced the Statistical Bootstrap Model to describe hadronic resonance states with increasing energy which consist of lower

mass resonances, and it is very useful to analyze nuclear matter in the high temperature limit in the circumstances under which these resonances happen. The density and the thermodynamic energy density of resonance states are close to each other, and this leads to the divergence of partition function. There is a critical value of temperature where the hadronic matter is no longer stable, which is introduced by Hagedorn as the Hagedorn temperature. The increase in energy will produce more resonances instead of increasing the kinetic energy at Hagedorn temperature [24].

However, this picture is in contract to asymptotic freedom, which suggests the coupling strength is weak at high enough temperatures and perturbative QCD provides good description of nuclear matter kinematics [25]. It converts hadronic matter into quark matter at that temperature level. The state of nuclear matter is represented by the Quark Gluon Plasma (QGP) for the beginning stages of the Universe [26]. The relationship between the energy density ε and pressure p under the assumption of asymptotic freedom is expressed as:

$$\varepsilon - 3p = 0. \quad (2.6)$$

The energy density is proportional to T^4 with the proportionality constant consisting of g_{BE} (particles degeneracy follows Bose-Einstein) and g_{FD} (Fermi-Dirac), it is shown as the follows:

$$\varepsilon = (g_{BE} + \frac{7}{8}g_{FD})\frac{\pi^2}{30}T^4. \quad (2.7)$$

For low temperature limit, the system is composed of the lowest state of pion gas. And there are deconfined quarks and gluons in the context of high temperature limit. The following table lists the g_{BE} and g_{FD} values at different temperature limit:

Table 2.1: g_{BE} and g_{FD} values at different temperature

Constant	$T \sim 0$	$T \rightarrow \infty$
g_{BE}	$3_{isospin}$	$8_{color} \times 2_{spin}$
g_{FD}	0	$3_{color} \times 2_{spin} \times 2_{q\bar{q}} \times N_f$

With the information of table 2.1, the final energy density can be calculated as:

$$\varepsilon = \frac{\pi^2}{30} T^4 \begin{cases} 3 & \text{if } T \sim 0 \\ 16 + \frac{21}{2} N_f & \text{if } T \rightarrow \infty \end{cases} \quad (2.8)$$

The energy density can be significantly different in the different phases, due to the factor we get from the above equation and it is up to 9.

This transition can be indicated by the potential thermodynamics divergences, as well as the temperature limits where the transition can happen. Chiral symmetry is respected by QCD Lagrangian in the zero quark mass limit, however it is broken by non-perturbative effect. At high temperatures, chiral symmetry should be conserved and deconfinement should appear. Analytic QCD calculations cannot provide a clear description of a definite phase transition related to these phenomena [26], and Lattice QCD (lQCD) is introduced to address these issues.

2.2.1 Lattice QCD predictions

The lattice is introduced as a space-time grid in Euclidean space. The strong force is exchanged by gluons located along the lines between lattice vertices, where the quarks are located. Statistical mechanics is used for finite temperature calculations in the system, and the Feynman path integral is introduced cover all quantum effects. In lQCD, in order to understand the physics phenomena, calculations with different lattice spacings from discrete to continuum (infinitesimal lattice size) are used to extrapolate physical results.

The fact that the chemical potential of baryons can be finite ($\mu_B > 0$) has been resolved by reducing the size of space-time lattice at high temperature limit in the prediction of QCD phase transition. Moreover, the realistic masses of light quark are used. The energy density ε/T^4 as a function of temperature T is shown on Fig. 2.2.

The relationship plotted is for 2+1 staggered flavors state with the chemical potential

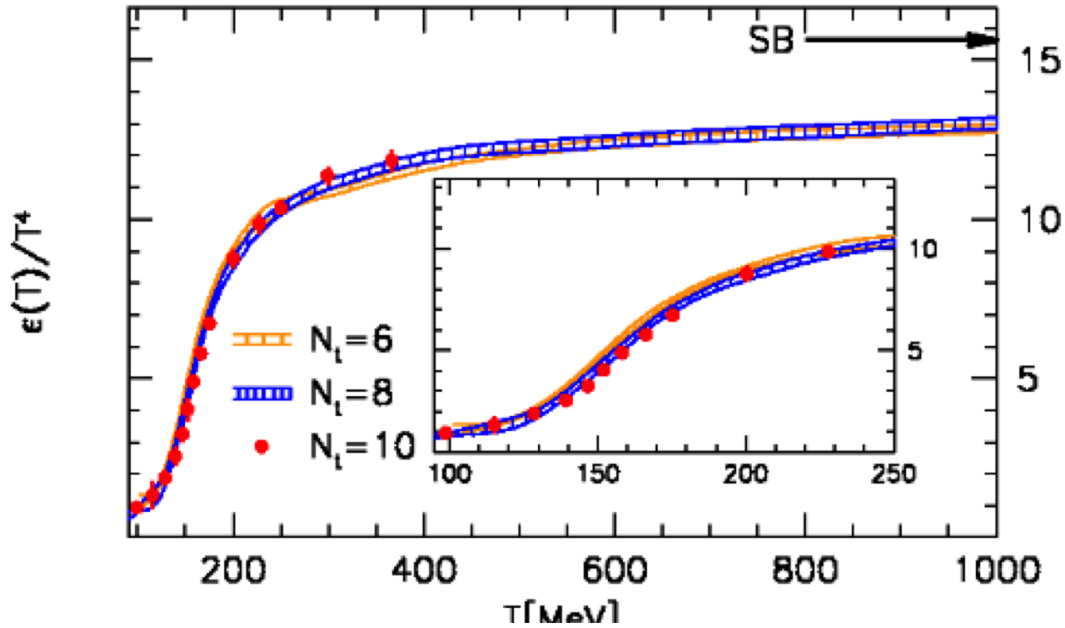


Figure 2.2: Energy density divided by T^4 as a function of temperature in a lattice calculation using physical quark masses [27]

$\mu_B = 0$. The results are calculated for different number of points in the temporal directions (N_t) with physical dynamic quark mass [28]. The quark flavor number leads to the principal uncertainty in the calculation. The Boltzmann factor $e^{-m/T}$ results in the suppression for the heavy quarks with large masses, such as the charm, the bottom and the top quark under the ideal gas of QGP assumption. The energy density distribution increases sharply at a certain temperature value, which is the critical temperature (173 MeV) for the phase transition from hadronic matter to the QGP [29]. This rapid but continuous energy density transition is expressed by the equation derived before 2.8. However, it implies a smooth crossover between phases rather than a first or second order phase transition.

The lQCD calculation indicates a lower energy density ε/T^4 around the critical temperature $T = 173\text{MeV}$ compared to Stefan-Boltzmann predictions, which implies the QGP is not strict equilibrium ideal gas due to the presence of partons interactions at $T \sim 173\text{MeV}$.

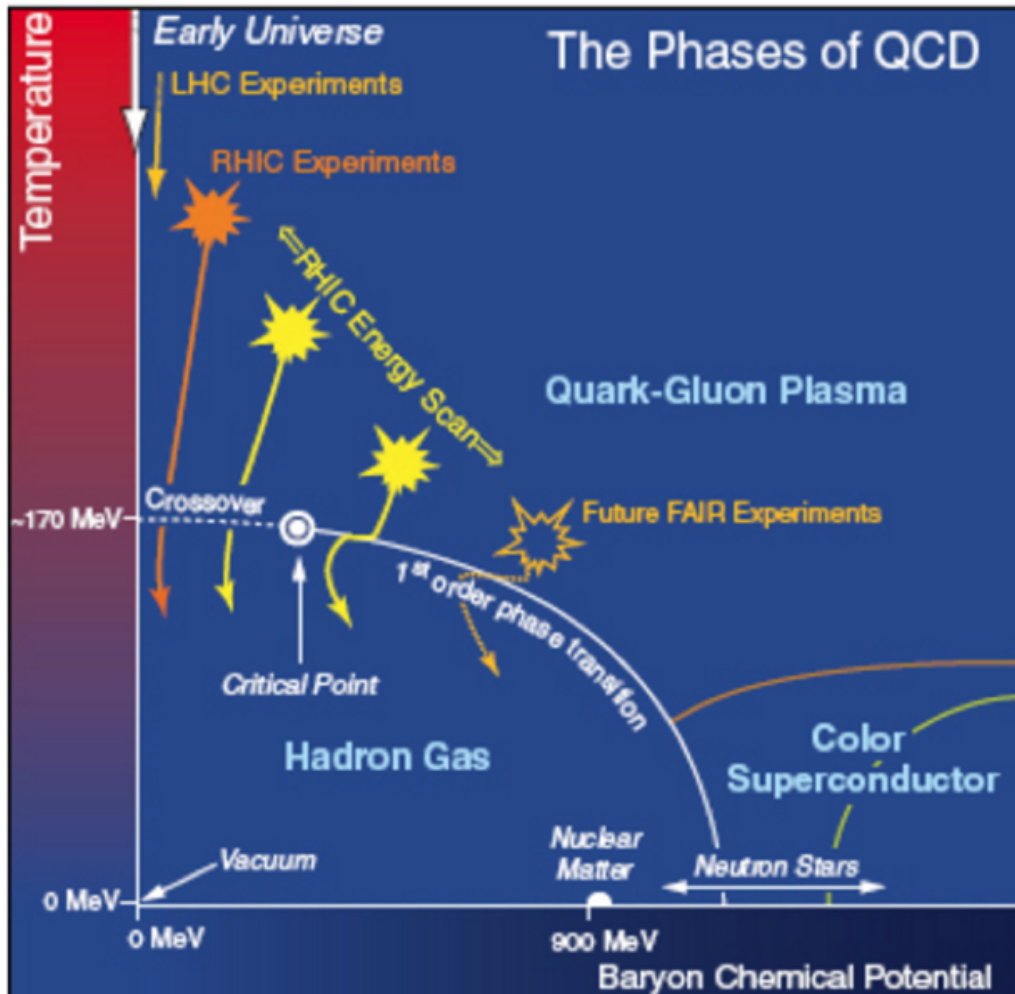


Figure 2.3: QCD Phase diagram represented in the direction of temperature and baryon chemical potential. Taken from NSAC Long Range Plan 2007 [30].

2.2.2 QCD Phase Diagram

The phase transition at different temperature T and chemical potential μ_B are shown on the QCD phase diagram 2.3, which represents the mixture of results of IQCD calculation from first principle, the experiment and the conjecture from various models. Since the finite μ_B leads to problems in IQCD calculations, the result of IQCD shown is with $\mu_B = 0$, and it describes the crossover transition from hadronic matters to QGP smoothly.

The QCD phase structure for high chemical potential can be understood well in neutron stars experiments. However there are insufficient measurements available for the study. Moreover, various research facilities and colliders provide huge amount of experimental data from heavy ion collisions at extreme high energy for the QCD phase study, in the high temperature T and low chemical potential range. Examples are the Relativistic Heavy Ion Collider (RHIC) in Brookhaven National Laboratories (BNL), the Large Hadron Collider (LHC) at European Organization for Nuclear Research (CERN), and the Facility for Antiproton and Ion Research (FAIR).

The first order transition takes place in the transition from hadronic matter to the QGP at higher μ_B . There is an important point where the first order transition starts to happen, and it is called the critical end point (CEP), which is essential for theorists to predict the phase structure of QCD matter. The experimental frontier for analyzing the CEP is implemented in the RHIC Beam Energy Scan (BES).

In the early universe stage, when the time scale is less than 10^{-5} seconds after the Big Bang, the universe is in a hot state and filled up with QGP. This is implied by Fig. 2.3, which shows the QGP takes up most of the phase space for high temperature limit ($T > 170$ MeV). Enormous attempts have been made to seek observations of the earliest transition between confinement and deconfinement but failed due to the feeble signature left. The laboratory is necessary for further study on the primordial QCD matter. Facilities such as the RHIC (with center of mass energy at 200 GeV) and the LHC (with center of mass energy at 2.76 TeV) can provide a crucial environment to reproduce the QGP state in ultra-relativistic nucleus-nucleus collisions successfully. Fig. 2.4 shows the event display of the nucleus collisions at the A Toroidal LHC ApparatuS (ATLAS) detector of LHC.

There is plentiful information embedded in the multiple particles coming out of these heavy ion collisions. The main purpose of this thesis is to interpret such fundamental information based on the experimental observations at the LHC. The following section describes

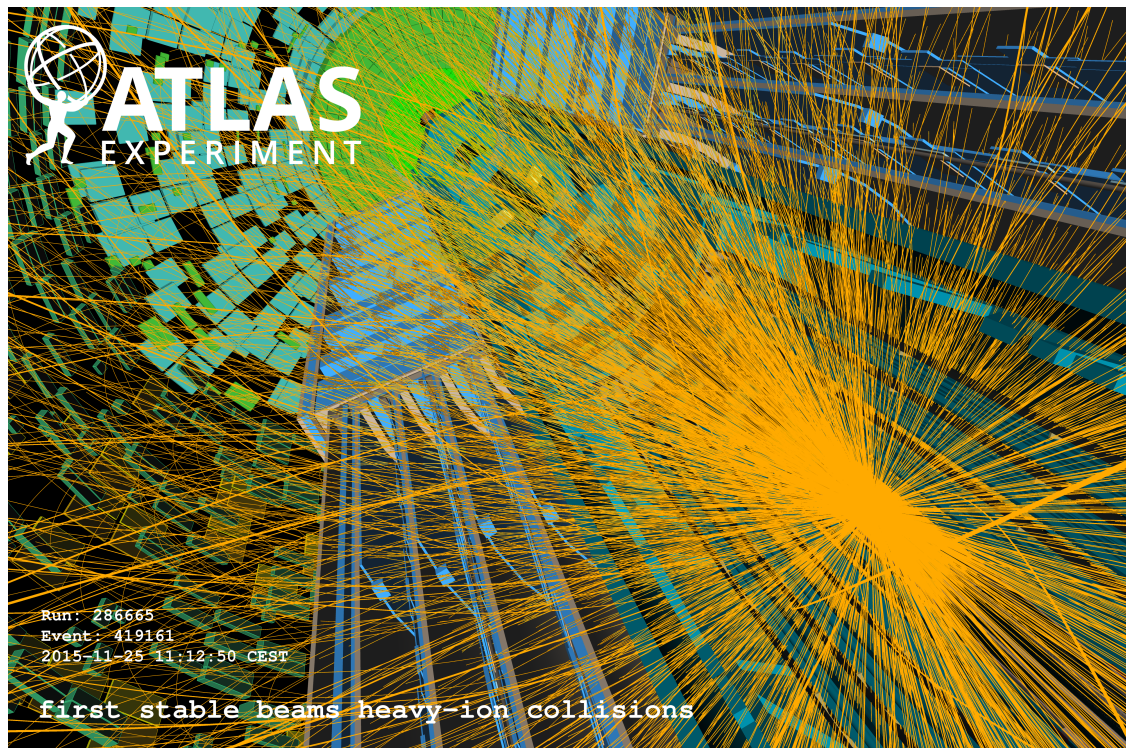


Figure 2.4: Event display of a heavy ion collision at LHC (ATLAS collaboration). Taken from [31].

the QGP phenomenology at the LHC in general.

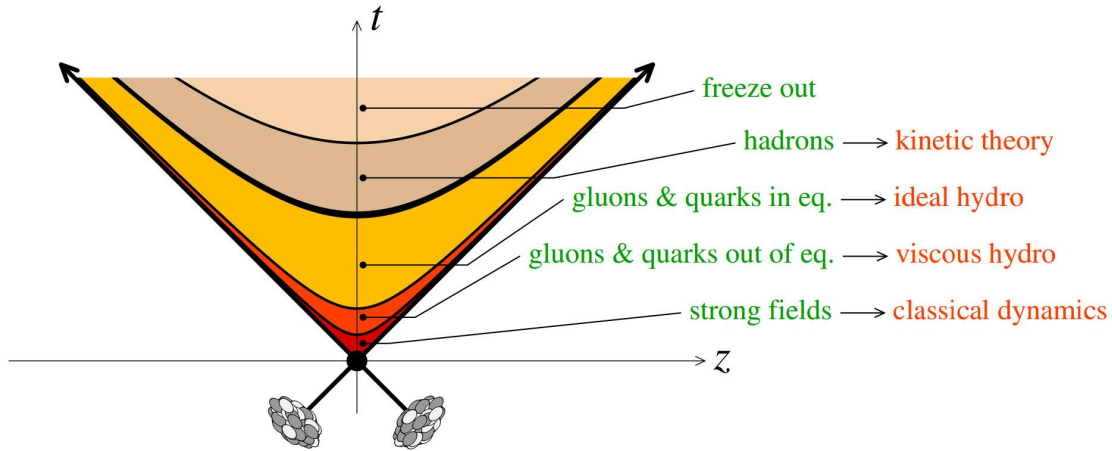


Figure 2.5: Schematic representation of the various stages of a Heavy Ion Collision as a function of time t and the longitudinal coordinate z (the collision axis). Taken from [33].

2.3 QGP phenomenology at LHC

The whole process of the evolution of a heavy ion collision provides useful information for understanding the QGP phenomenology. Bjorken [32] suggested that heavy ion collisions evolve in both longitudinal space and time. Both theoretical and experimental efforts have been made to demonstrate it. The schematic evolution of heavy ion collisions is shown in Fig. 2.5. There are four stages in heavy ion collisions evolution: pre-equilibrium, QGP state, hadronization and freeze-out and they will be described in detail in the following sections.

2.3.1 Pre-equilibrium

When two heavy ion beams collide with each other, both of them are squeezed in the lab frame along the z direction due to the high energy (GeV or TeV). Soft processes happen immediately after the hard processes. Objects with high p_T and low p_T are created during the parton interaction process. The system will reach equilibrium in the end due to the increasing entropy caused by multiple scatterings among the particles and massive quarks and gluons. The collisions in this process can be analyzed in several ways.

The Glauber Model [34] is one of the methods that are used to analyze this process and it addresses the problem of composite particles scattering in high energy. Under this model's assumption, the nucleons move independently within the nucleus and carry sufficient momentum at high enough energies to avoid being deflected as the nuclei passing through each other. At the same time, this model takes the collisions at the baryon level and describes the system geometrically. The heavy ion collisions of two nuclei are considered in terms of the individual interactions of the constituent nucleons. The nucleons normally have a continuous density distribution which is a parameterized Woods-Saxon distribution, and the nuclear density is calculated as follows:

$$\rho(r) = \rho_0 \frac{1}{1 + \exp(\frac{r-a}{R})}, \quad (2.9)$$

where ρ_0 represents the nucleon density in the center of the nucleus and ensures the normalization of this density distribution is equal to the number of nucleons. R and a represent the nuclear radius and “skin depth”, respectively. The parameters for Pb^{208} are $R = 6.62 \pm 0.06$ fm, $a = 0.546 \pm 0.01$ fm [35]. The schematic view of two nuclei colliding is shown in Fig. 2.6.

From Fig. 2.6, the distance from the center of nucleus A (target) to the center of nucleus B (projectile) is denoted by a impact parameter vector \vec{b} in the transverse plane. \vec{s} represents the vector from the center of A to one nucleon, and $\vec{s} - \vec{b}$ represents the distance vector from the center of B to the same nucleon. The two flux tubes indicated in Fig. 2.6 are analyzed and they overlap with each other during the collisions. $T_A(\vec{s})$ is defined as the probability per unit transverse area of a given nucleon being located in the target flux tube:

$$T_A(\vec{s}) = \int \rho_A(\vec{s}_A, z_A) dz_A, \quad (2.10)$$

where $\rho_A(\vec{s}_A, z_A)$ represents the probability of finding the nucleon located at (\vec{s}, z_A) per unit

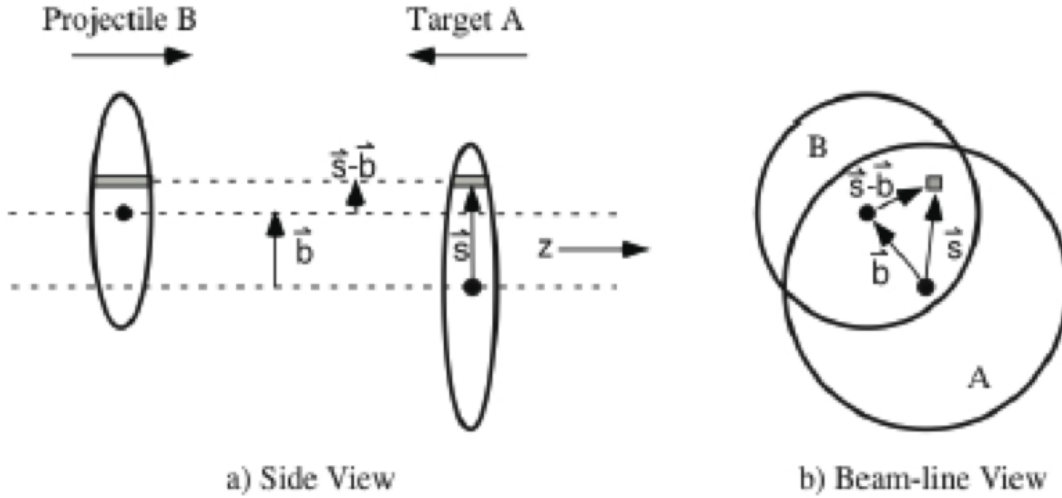


Figure 2.6: Schematic view of two colliding nuclei with left side presents transverse and right side presents longitudinal views. Taken from [34].

volume, and it has a normalization of unity. Similarly for projectile nucleon B, we define:

$$T_B(\vec{s}) = \int \rho_B(\vec{s}_B, z_B) dz_B \quad (2.11)$$

Then $T_{AB}(\vec{b})$ is defined as the joint probability of finding nucleons in both nuclei A and B at the same time and location \vec{s} :

$$T_{AB}(\vec{b}) = \int T_A(\vec{s}) T_B(\vec{s} - \vec{b}) d^2s \quad (2.12)$$

The thickness function $T_{\vec{b}}$ is the same as $T_{AB}(\vec{b})$, and it has the unit of inverse area. It should be ϕ independent due to the fact that nucleus is unpolarized, which gives $T(\vec{b}) = T(b)$. This can be interpreted as the effective overlap area for which a specific nucleon in A can interact with a given nucleon in B. Then the interaction occurs with a probability of $T(b)\sigma_{in}$, where σ_{in} represents the cross-section of this non-diffractive inelastic collisions between nucleon-nucleon.

For n nucleon-nucleon collisions out of A^*B nucleons, the probability of interaction happening follows the Binomial distribution and it is also a function of the impact parameter b . The probability can be expressed as follows:

$$p(n, b) = \binom{AB}{n} p^n (1-p)^{AB-n} = \binom{AB}{n} (T(b)\sigma_{in})^n (1-T(b)\sigma_{in})^{AB-n}. \quad (2.13)$$

Then in the collision between nucleus A and B, the total probability of having one inelastic event can be expressed as:

$$\frac{d\sigma_{in}^{AB}}{d\vec{b}} = \sum_{n=1}^{AB} p(n, b) = \sum_{n=0}^{AB} p(n, b) - p(0, b) = 1 - (1 - T(b)\sigma_{in})^{AB}. \quad (2.14)$$

The total inelastic cross section for nucleus A and B collision can be expressed as:

$$\sigma_{in}^{AB} = \int (1 - (1 - T(b)\sigma_{in})^{AB}) d\vec{b}. \quad (2.15)$$

There are two parameters that provide a description of the geometry of nucleus collisions, the $\langle N_{part} \rangle$ represents the average number of participants and the $\langle N_{coll} \rangle$ represents the average number of binary collisions. $\langle N_{coll} \rangle$ can be expressed as the average of n :

$$\langle N_{coll} \rangle(b) = \langle n \rangle = \sum_{n=0}^{AB} np(n, b) = AB \cdot T(b)\sigma_{in}. \quad (2.16)$$

The average number of nucleons in the target and projectile nuclei that interact (or the number of wounded nucleus) $\langle N_{part} \rangle$ can be expressed as:

$$\begin{aligned} \langle N_{part}(\vec{b}) \rangle &= A \int T_A(\vec{s}) 1 - [1 - T_B(\vec{s} - \vec{b})\sigma_{in}]^B d^2s \\ &+ B \int T_B(\vec{s} - \vec{b}) 1 - [1 - T_A(\vec{s})\sigma_{in}]^A d^2s. \end{aligned} \quad (2.17)$$

The ‘‘Optical Glauber Model’’ is used for the above calculation. Monte Carlo (MC) sim-

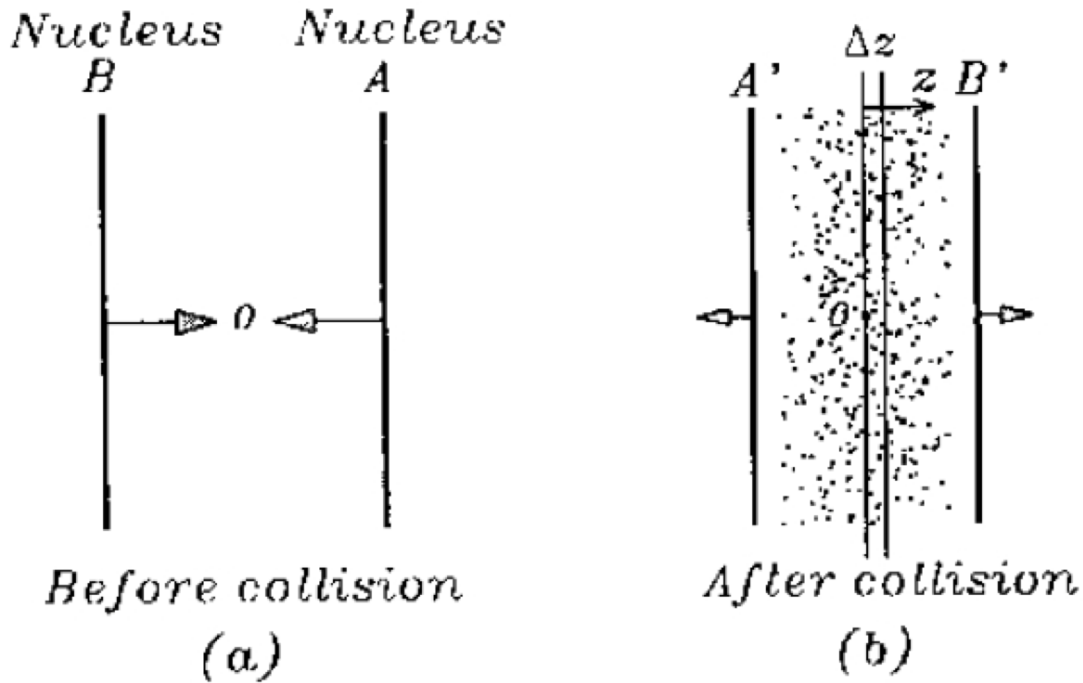


Figure 2.7: Left: Two nuclei A and B before collisions. Right: Nuclei A and B after collisions with energy deposited in region $z \sim 0$. Taken from [36].

ulation is used as other methods for this calculation and details are described in [34]. The $\langle N_{part}(\vec{b}) \rangle$, $\langle N_{coll}(\vec{b}) \rangle$ and impact parameter \vec{b} cannot be observed directly in experiments normally. A “Centrality” term is defined in both phenomenological Glauber Model and the experiment to calculate those quantities. The mapping between centrality and the parameters is needed and it only works if there exists a monotonic relationship between variables in the experiments and the Glauber Model calculation.

The estimation of the initial energy density by Bjorken [32] brought up the idea that, in the collision of two nuclei with little transverse overlap, there is only part of their kinematic energy stored for the heating up for central rapidity range. Fig. 2.7 shows the procedure of two nuclei collision. The particle density can be calculated in the central region around $z \sim$

0:

$$\begin{aligned}\frac{\Delta N}{\mathcal{A}\Delta z} &= \frac{1}{\mathcal{A}} \frac{dN}{dy} \frac{dy}{dz} \Big|_{y=0} \\ &= \frac{1}{\mathcal{A}} \frac{dN}{dy} \frac{1}{\tau_0 \cosh y} \Big|_{y=0},\end{aligned}\tag{2.18}$$

the transverse area is denoted by \mathcal{A} , y represents rapidity and τ_0 represents the time it took to produce a quark gluon plasma. Therefore the estimation for initial energy density can be expressed as:

$$\epsilon_0 = m_T \cosh y \frac{\Delta N}{\mathcal{A}\Delta z} = \frac{m_T}{\tau_0 \mathcal{A}} \frac{dN}{dy} \Big|_{y=0},\tag{2.19}$$

m_T represents the transverse mass of particles. The final energy density which can be measured in experiments is used for calculation of the initial energy density in this equation. The equilibrium time τ_0 is the only unknown variable which is estimated on the scale of 1 fm/c by Bjorken's assumption.

The Color Glass Condensate (CGC) also provides an important perspective on a heavy ion collisions' initial condition. At the beginning stage of nucleus collisions, for high enough energy, the degrees of freedom involved are partons [37]. The majority of these partons are gluons whose energy density is positively correlated to the energy transfer (Q^2) and negatively correlated to their momentum fraction (x). Fig. 2.8 shows the gluon distribution for different Q^2 and x range. In figure 2.9, it shows the parton energy density on transverse area is high and could result in gluon saturation for high energy and small x .

Q_s denotes the saturation scale, which is big ($Q_s \gg \Lambda_{QCD}$) and the coupling constant is small ($\alpha(Q_s) \ll 1$) when the scale close to the density on transverse area is taken into account. In this system, perturbation theory can be used for study, and there are mainly high density gluons with color degrees of freedom. The system behaves as liquid most of the time and behaves as solid otherwise, also the evolution is much slower compared to the natural time scales. All those properties explain the name of CGC. The gluon density can

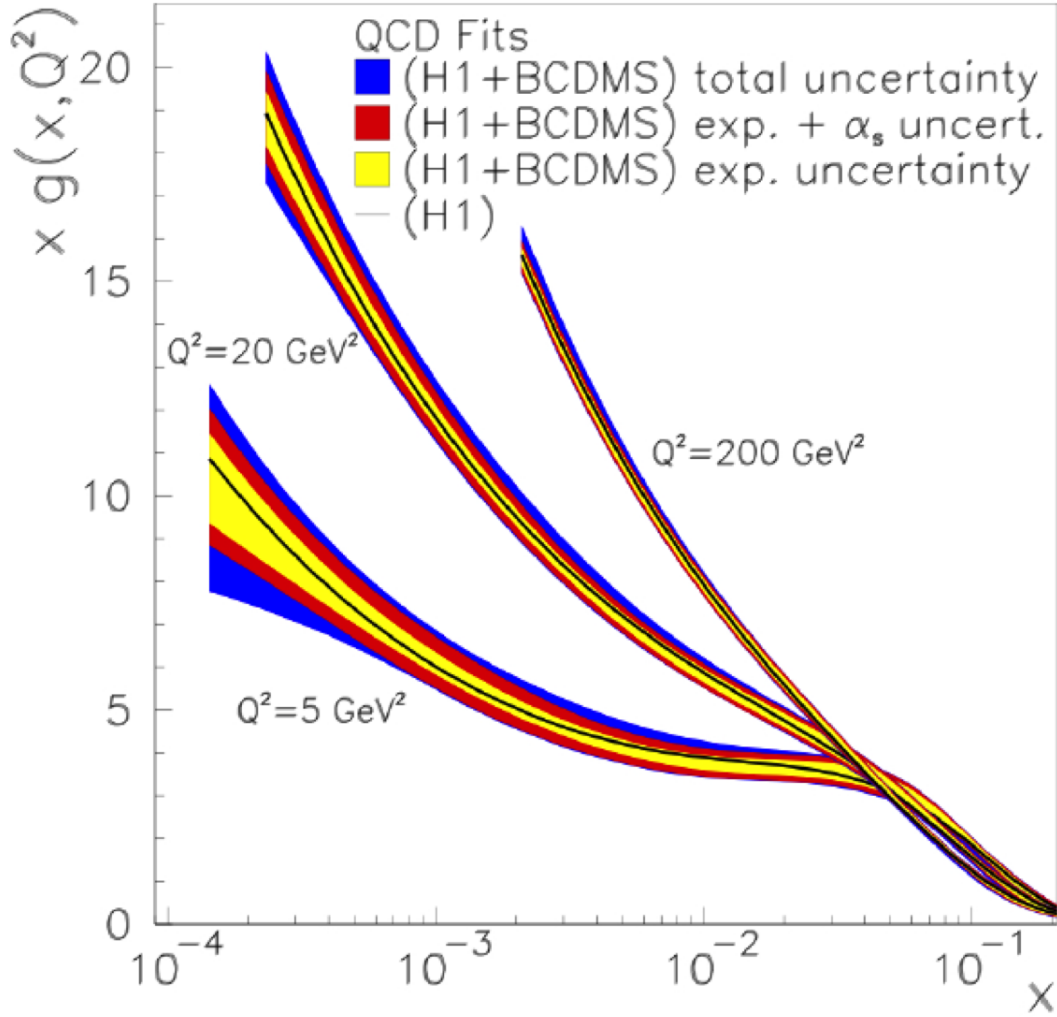


Figure 2.8: Gluon distributions from HERA experiment as a function of x at three different Q^2 [37]

be expressed as [39]:

$$\begin{aligned} \frac{dN}{dyd^2p_T} &\sim \frac{\pi R^2 Q_s^4}{\alpha_s p_T^4}, \text{ with } p_T > Q_s \\ \frac{dN}{dyd^2p_T} &\sim \frac{\pi R^2}{\alpha_s}, \text{ with } p_T < Q_s \end{aligned} \quad (2.20)$$

Since the final particle density is related, the collisions between nucleon and nucleus as well as electron and nucleus can provide more promising approaches because they are not

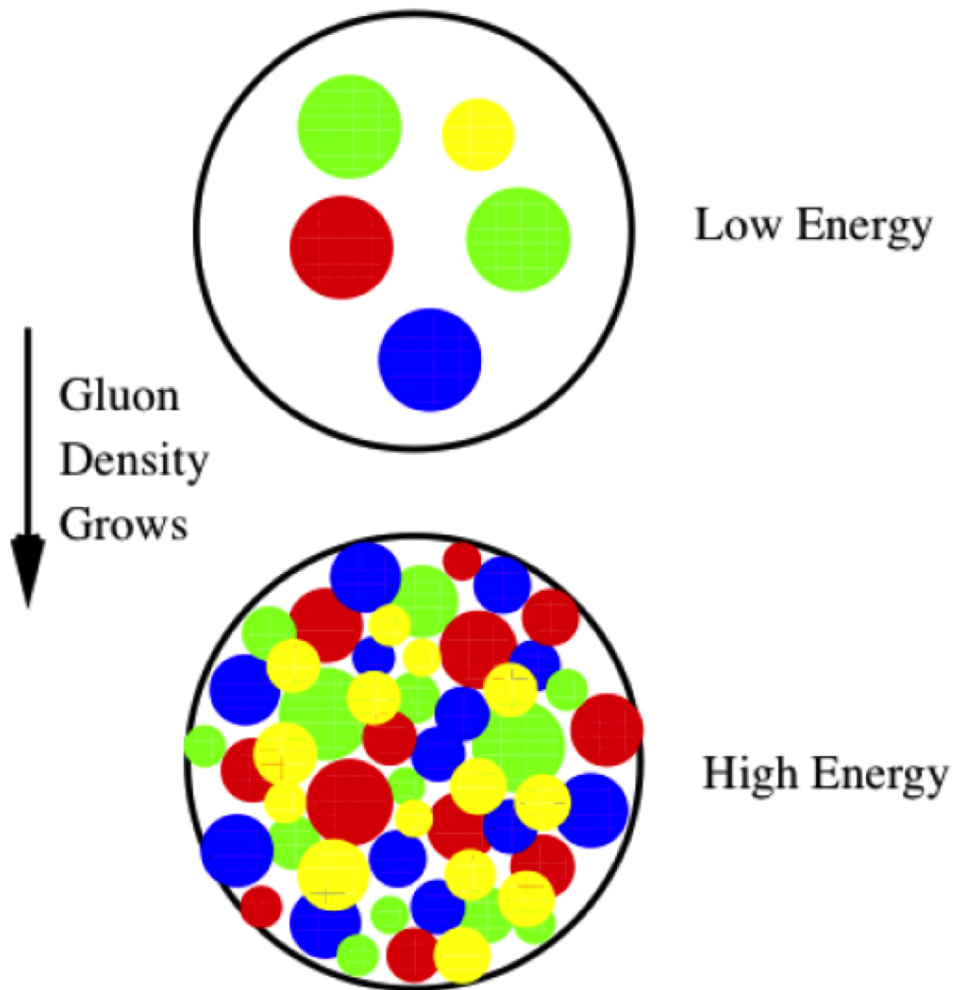


Figure 2.9: Gluon saturation in a hadron as x decreases [38]

influenced by the final state of collisions between nucleon-nucleon. Since high energy particles are produced during a short time due to the uncertainty principle ($\Delta t \sim 1/\Delta E$), the heavy quarks are produced at the early stage of heavy ion collisions, the interaction between these particles and the medium during the collisions provides a powerful tool for the understanding of QGP medium,

2.3.2 Collective Flow and Perfect Fluidity of QGP

The deconfined quarks and gluons produce QGP through the collisions. If it is not a central collision, where the impact parameter is not zero, the transverse plane ($x - y$) does not have a symmetric distribution after the collision. This feature is shown in Fig. 2.10, also the reaction plane is denoted by the expansion of beam direction and impact parameter vector. There is a almond shape interaction region in Fig. 2.10, which is asymmetric in space. Thus the anisotropic flow is introduced as another strong evidence for the existence of QGP.

The relativistic hydrodynamics can be used to study this system due to the achievement of local thermodynamic equilibrium. It is very popular for the physicists to apply the hydrodynamics in their analysis because there is no requirement for the assumption on the nature of the particles and the fields. However, the local equilibrium is rather a strong assumption that we should keep in mind. The initial condition, together with the equation of state can provide a thorough description. The following equation describes the motion of an ideal fluid without viscosity [40]:

$$\begin{aligned}\partial_\mu(nu^\mu) &= 0 \\ \partial_\mu(T^{\mu\nu}) &= 0,\end{aligned}\tag{2.21}$$

where $n = \frac{N}{V}$ denotes the baryon number density, $u^\mu = (\gamma, \gamma\vec{v})$ denotes the velocity vector, $T^{\mu\nu} = (\epsilon + P)u^\mu u^\nu - Pg^{\mu\nu}$ denotes the energy-momentum tensor. The equation represents the conservation of both baryon number and energy, and provides description of momentum and baryon density. Lattice QCD or phenomenological models [41] are used to calculate the equation of state for this dense system. The EOS under assumptions of different models with $n = 0$ is shown in Fig. 2.11

Different choices of equation of state can introduce various sensitivity to the final result based on the observables. Taking the nature of the phase transition as well as the non zero n (baryon density) into account can provide a better understanding of the system, and also

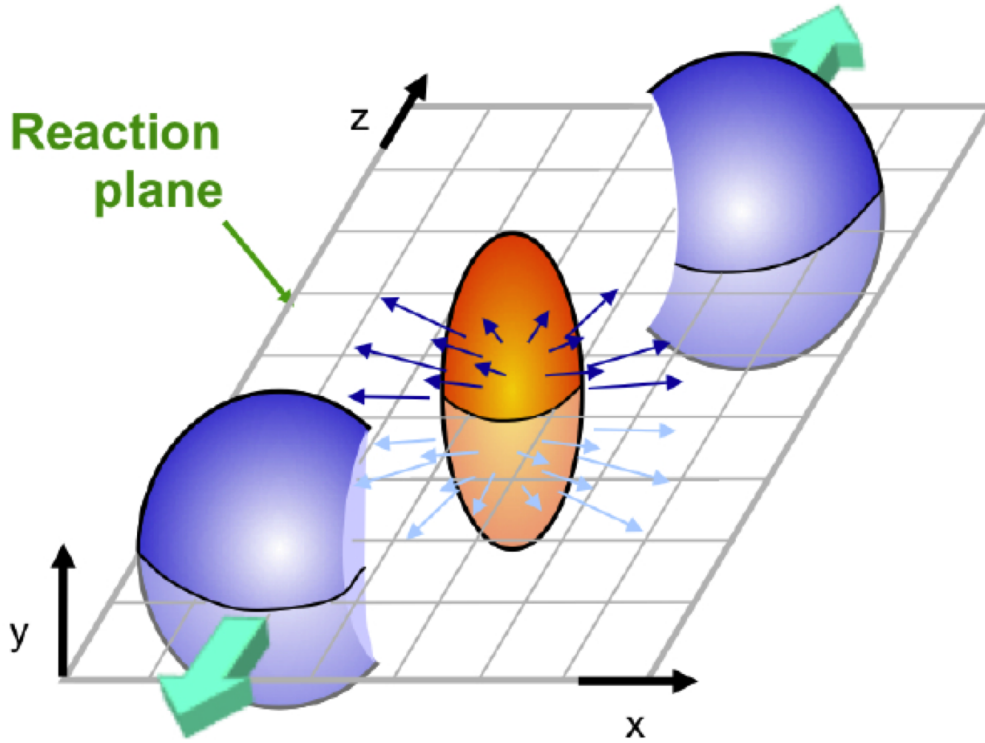


Figure 2.10: Geometry of a non-central heavy ion collisions. Taken from [42].

reduce the uncertainties. The initial conditions are beyond hydrodynamics, and they are treated as inputs to the calculation. The initial conditions can be derived through multiple methods ([44], [45], [46], [47]). There are two parts that comprise the initial entropy density. The hard part which is proportional to the $\langle N_{coll} \rangle$ and the soft part which is proportional to the $\langle N_{part} \rangle$, and they are linearly combined. Since the system reaches local equilibrium, the evolution of the system, like equation of state and motion can be described well using the information of initial condition. However, as the system evolves to the final stage, it cannot provide sufficient information. Thus more phenomenological models are introduced for the description of the freeze-out stage, which will be described in the following section.

The asymmetry in space can result in the corresponding asymmetry in momentum space, which can lead to faster expansion along the reaction plane compared to the y axis 2.10. This is supported in Fig. 2.12, which shows that the pressure gradient is higher along the

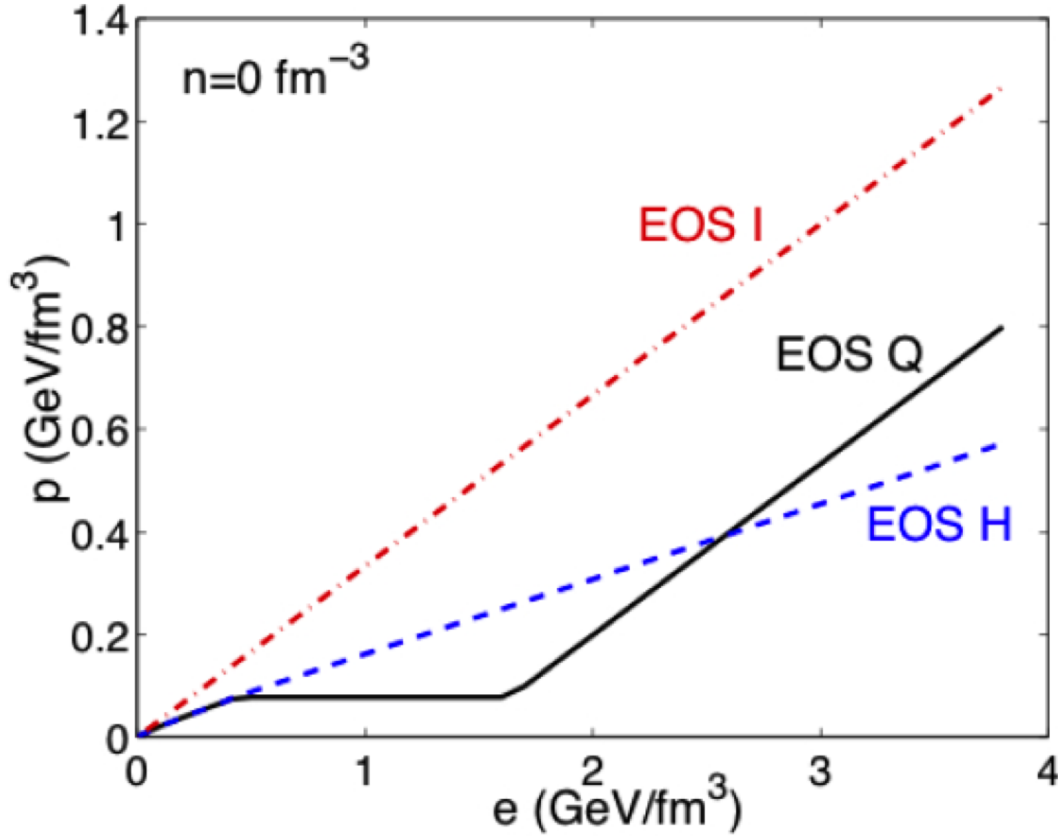


Figure 2.11: Nuclear EOS of Hagedorn resonance gas model [41] (EOS H), an ideal gas model (EOS I) and a connection of the two (EOS Q). [43]

reaction plane compared to the y axis. Due to the different expansion rate, collision space will evolve symmetrically as time goes by. The expansion process at different time scale derived by hydrodynamics is shown in Fig. 2.13, each contour represents the constant energy density. The left plot shows a elliptical shape at the beginning and is the most asymmetric, it evolves into a circular which is shown on the right plot at later time due to the faster expansion along the x direction. The spatial eccentricity parameter are defined to describe the amount of deformation in the reaction region:

$$\epsilon_x(b) = \frac{\langle y^2 - x^2 \rangle}{\langle y^2 + x^2 \rangle}. \quad (2.22)$$

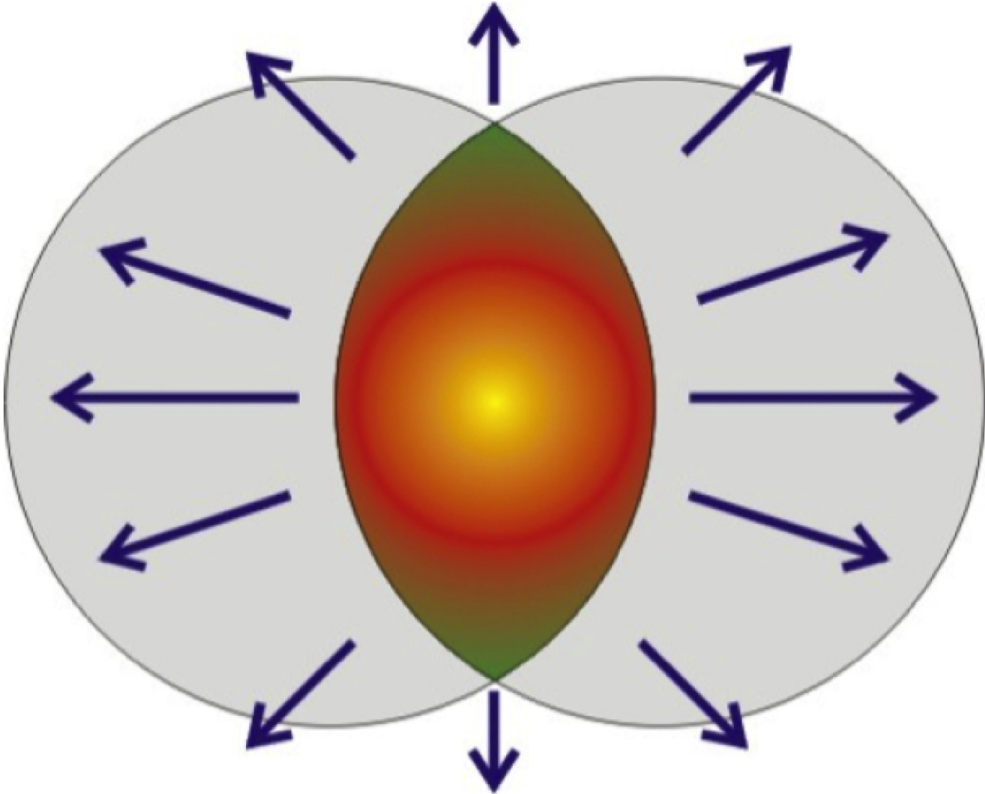


Figure 2.12: In an off-central collision between two heavy nuclei, the overlap region is almond-shaped with the length of the arrow indicates the expansion rate. The large pressure gradient in the horizontal direction (the collision plane) causes a faster expansion than in the vertical direction. Taken from [48].

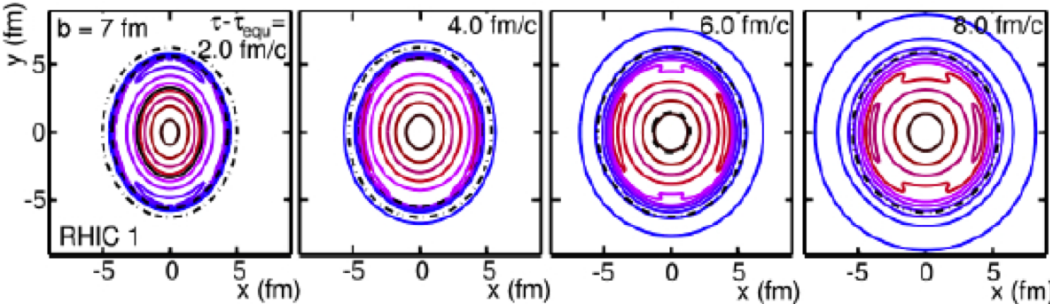


Figure 2.13: Contours of constant energy density in the transverse plan at different time after equilibrium [43]

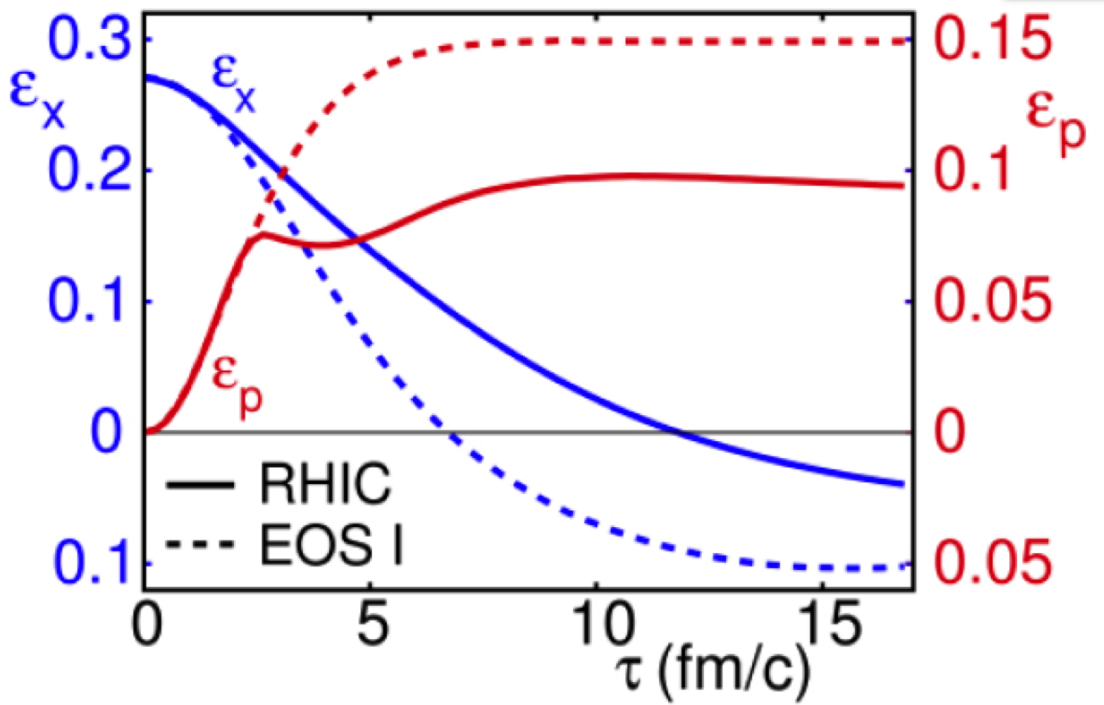


Figure 2.14: Time evolution of spatial eccentricity and momentum anisotropy [43]

At the same time the momentum anisotropy can be expressed as:

$$\epsilon_p(\tau) = \frac{\int dx dy (T^{xx} - T^{yy})}{\int dx dy (T^{xx} + T^{yy})}. \quad (2.23)$$

Fig. 2.14 shows the transformation of space anisotropy to momentum anisotropy.

2.3.3 Hadronization and Freeze out

After the formation of QGP, the temperature can decrease significantly after 10 fm/c. Hadrons can be formed by the confinement of quarks and gluons when the temperature is below the critical value. The inelastic collisions can be reduced due to the slowing down of the expansion, this will continue until the species of hadron are stable and sufficient enough. The details can be found in [49, 50] and this is introduced as chemical freeze-out, where the major collisions are elastic instead of inelastic maintaining kinetic equilibrium. The “kinetic

freeze-out” [51, 52] happens after chemical freeze out when kinetic equilibrium is broken and the kinematic distribution is stable.

Chapter 3

Heavy Flavour Physics

This thesis focuses on the heavy flavor aspect of the physics, bottom quarks are good candidates for the approach due to their large masses compared to the u, s, d, c quarks. Moreover it has adequate longer life time compared to the heavier t quark, which is crucial for the hadrons' bound state formation.

3.1 Perturbative QCD and Hard Scattering

The hard scattering processes with large momentum and energy transfers are investigated through many experiments, and the parton model is introduced for the interpretation of these results. In the parton model, hard scattering takes place among different constituents which comprise the hadrons [53]. QCD theory is used to describe the strong interactions and the parton model is an appropriate candidate among different models for an approximation to the QCD theory for the hard scattering process. The following section will provide general introduction to the parton model and its applications.

3.1.1 Parton Models

The parton model is one of the fundamental applications of perturbative QCD. It provides a tree-level and an impulse approximation to the theory [54]. The constituents which participate in the hard scattering process are treated as point-like objects. The scattering cross section for two colliding hadrons are calculated in the following equation:

$$\sigma_{AB}(p_A, p_B) \sim \sum_{i,j} \int dx_i dx_j \hat{\sigma}(x_i p_A, x_j p_B) \phi_i^A(x_i) \phi_j^B(x_j), \quad (3.1)$$

where A, B represents the two hadrons, and i, j represents different types of parton respectively, x represents the parton momentum fraction. The probability density function for parton i existing in the hadron A is represented by ϕ_i^A , with momentum of $p_i = x_i p_A$. $\hat{\sigma}$ denotes the partonic matrix element, which can be calculated using perturbation theory due to the asymptotic freedom at hard enough scales. However, it develops into non-perturbative theory due to the initial and final states involved during hadronic scattering process in the physical world. The calculation of equation 3.1 can be considered separately with different scales. The behavior of short range in the QCD theory is incorporated with the long range behavior in $\hat{\sigma}$. This is achieved through factorization theorems which cannot be calculated by perturbative QCD theory. It has similar formulation to the equation 3.1, the scheme-dependent factorization scale F is introduced to describe the different kinetics aspects of distinct range components. The integrand terms in factorization theorems depend on the scale F, at the same time it prevents the quantum mechanical interference between short and long range interaction. Moreover, the parton distribution functions (PDFs) which represent the parton probability distributions do not depend on the particular scattering process. The scattering at the partonic level does not affect the calculation in the context of the PDFs and can be obtained from experiment, which makes the PDFs common among all the hadrons.

The following process provides an appropriate method to prove the factorization theo-

rems:

$$d\sigma(A + B \rightarrow C + D) = d\hat{\sigma} \oplus \Phi_A \oplus \Phi_B \oplus \Delta_C \oplus \Delta_D + p.s.c., \quad (3.2)$$

where Φ represents the parton distribution of each particle and Δ denotes the fragmentation function [55], which describes the final-state single particle energy distributions in hard scattering processes, \oplus denotes a convolution over parton momentum fraction with the summation of all parton species and color indices. The p.s.c. terms in this process represent the power suppressed corrections, which go through suppression by powers of a hard scale. The deep inelastic scattering (DIS) and the e^+e^- experiments provide demonstration for the factorization theorems. However, the Drell-Yan process is the only one that provides solid proof for the case of scattering among hadrons [56–58].

3.1.2 Deep Inelastic Scattering

The structure of hadron and the parton model are developed essentially by the experiment of scattering of charged (e, μ) leptons from a hadronic target. The electron interacts with the target via the exchange of a virtual photon, which is called neutral current process (NC). Q^2 denotes the squared transferred momentum, which is defined as the virtuality of the exchanged photon $Q^2 = -q^2$. M denotes the mass of the target and the momentum transfer is high in deep inelastic scattering (DIS), in the sense that $Q^2 \gg M^2$. The fraction of the momentum of the incoming target by the struck quark is defined as the Bjorken scaling variable:

$$x = \frac{Q^2}{2P \cdot q}, \quad (3.3)$$

where P represents the target's four momentum. Another parameter is introduced to describe the amount of energy lost by the electron measured in the rest frame of the target:

$$y = \frac{P \cdot q}{P \cdot k}, \quad (3.4)$$

where k represents the incoming electron's four momentum. The factorization theorem provides the applicability of the pQCD in hardon induced processes, and the cross section can be expressed as the convolution of the hard process with the soft part resolving long-range effects:

$$\sigma(x, Q^2) = \sum_{q, \bar{q}, g} \int_x^1 \frac{d\xi}{\xi} f_i(\xi, \mu_f^2, \alpha_s(\mu_r)) \hat{\sigma}_i\left(\frac{x}{\xi}, \frac{Q^2}{\mu_r^2}, \frac{\mu_r^2}{\mu_f^2}, \alpha_s(\mu_r)\right), \quad (3.5)$$

where ξ denotes the momentum fraction of the initial parton in the target. μ_f and μ_r denote the factorization scales and the renormalization scales respectively [59], and $f_i(\xi, \mu_f^2, \alpha_s)$ denotes the Parton Distribution Functions (PDFs) for parton i of the target. $\hat{\sigma}_i$ represents the partonic cross section depending on the incoming parton and its momentum fraction, and it is calculable in perturbation theory. The result depends on the factorization and renormalization scheme which are not set to be equal. At the same time this factorization feature of cross section shows a basic property of the QCD.

3.1.3 Jets

Partons cannot be directly observed at the LHC since QCD confinement prevents partons from existing as free particles. Instead, narrow cones of hadrons and other particles from the hadronization of a parton are experimentally studied to determine the properties of the original parton. These cones are identified as experimentally observed objects called jets. They are first observed at Stanford Linear Accelerator Center (SLAC) [60] through hard scattering processes, and they provide assessment of the theoretical application in experiment. Jet production is the dominant high transverse momentum (p_T) process and as such gives the first glimpse of physics at the TeV scale at the LHC. The jets cross sections and properties have been measured at the e^+e^- , ep , $p\bar{p}$, and pp colliders, as well as in the γp and $\gamma\gamma$ collisions. They provided precise measurements of the strong coupling constant, and have been used to obtain information about the structure of the proton and the photon. Jets have become important tools for understanding the strong interaction and searching

for physics beyond the Standard Model [61–72]. The observable in jet production needs to have accurate definitions in the measurement which are well-defined in theory due to the complicity of the final states [73]. The algorithms applied for jets reconstruction are established on clustering energy deposits nearby in angle, which will be described in detail in section 5.5.1.

In high energy experiments, jets become fundamental and important tools not only for testing QCD, but also for the reconstruction of more complicated physics objects. The results of theoretical predictions (which are provided by `fastNLO` with `NLOJET++` [74]) of inclusive jet cross section as a function of jet transverse momentum p_T are presented in Fig. 3.1, as well as the ratio of data/theory distribution for a wide range of experiments.

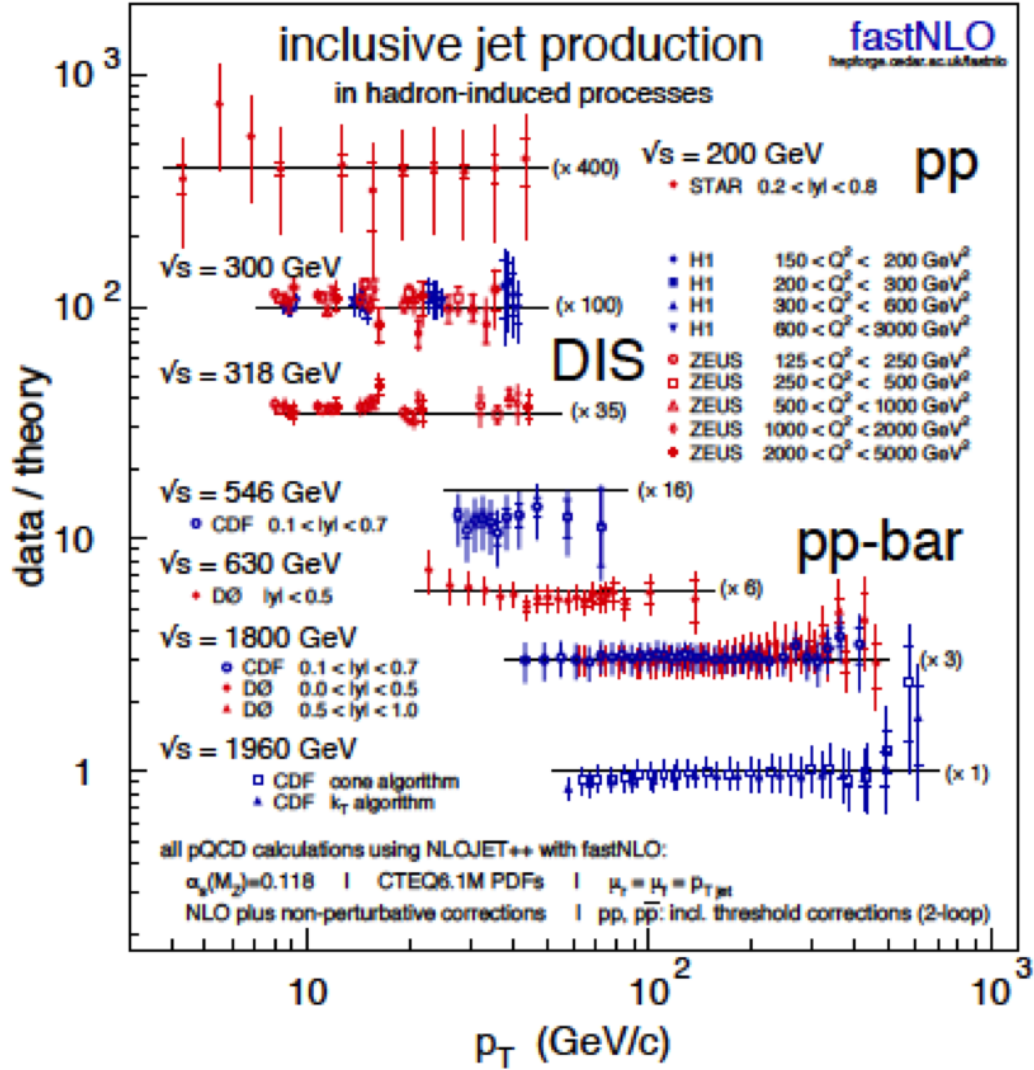


Figure 3.1: The single inclusive jet cross section ratio between data and theory at different energies [74, 75]

3.2 Hard Processes in Nuclear Collisions

In heavy ion collisions, particles with high transverse momentum p_T can provide useful insights in QGP studies using “external” source. This approach is referred to as “hard probes” and becomes one of the most powerful tools. In the early stage of a collision, partons with large virtualities and high momentum are produced even before the existence of the medium.

Those hard partons last for the entire evolution, and lose energy through the interaction with the medium (scattering processes) which is calculable due to the factorization of QCD. There are jets coming from the fragmentation and the hadronization of hard partons in the final stage. The important properties of the QGP can be learned thoroughly through the study of the modification of jet/leading hadron spectra in the presence of the medium.

3.2.1 Glauber Model to Experimental Data Mapping

In section 2.3.1 we introduced $\langle N_{coll} \rangle$ and $\langle N_{part} \rangle$, which represent the average number of binary collisions and the average number of participants in nucleus collisions, which cannot be observed directly in experiments. Centrality is defined for mapping between the distribution from experiment and the quantities in Glauber Model. This works under the assumption that the impact parameter \vec{b} has a monotonic relationship with the particle multiplicity. The *peripheral* collisions in centrality class definition represents the events with larger \vec{b} and lower multiplicity. At the same time *central* collisions represents the events with smaller \vec{b} and higher multiplicity. Here ξ can be defined as final-state observable with the integral of its minimum bias distribution known, and the range of its value is divided into sub-ranges where the integral of the distribution over that range is some fraction of the total.

The centrality is addressed as a percentage and the ξ integration normally goes from large value to small value. The centrality interval $a - b\%$ is defined by the boundary value of each sub-range in the distribution of ξ :

$$\begin{aligned}
 100 \left(\frac{\int_{\infty}^{n_a} \frac{dN_{evt}}{d\xi} d\xi}{\int_{\infty}^0 \frac{dN_{evt}}{d\xi} d\xi} \right) &= a[\%] \\
 100 \left(\frac{\int_{\infty}^{n_b} \frac{dN_{evt}}{d\xi} d\xi}{\int_{\infty}^0 \frac{dN_{evt}}{d\xi} d\xi} \right) &= b[\%],
 \end{aligned}
 \tag{3.6}$$

which is shown in Fig. 3.2 as an example of this division.

After the determination of centrality, the “two-component” model [77, 78] is introduced

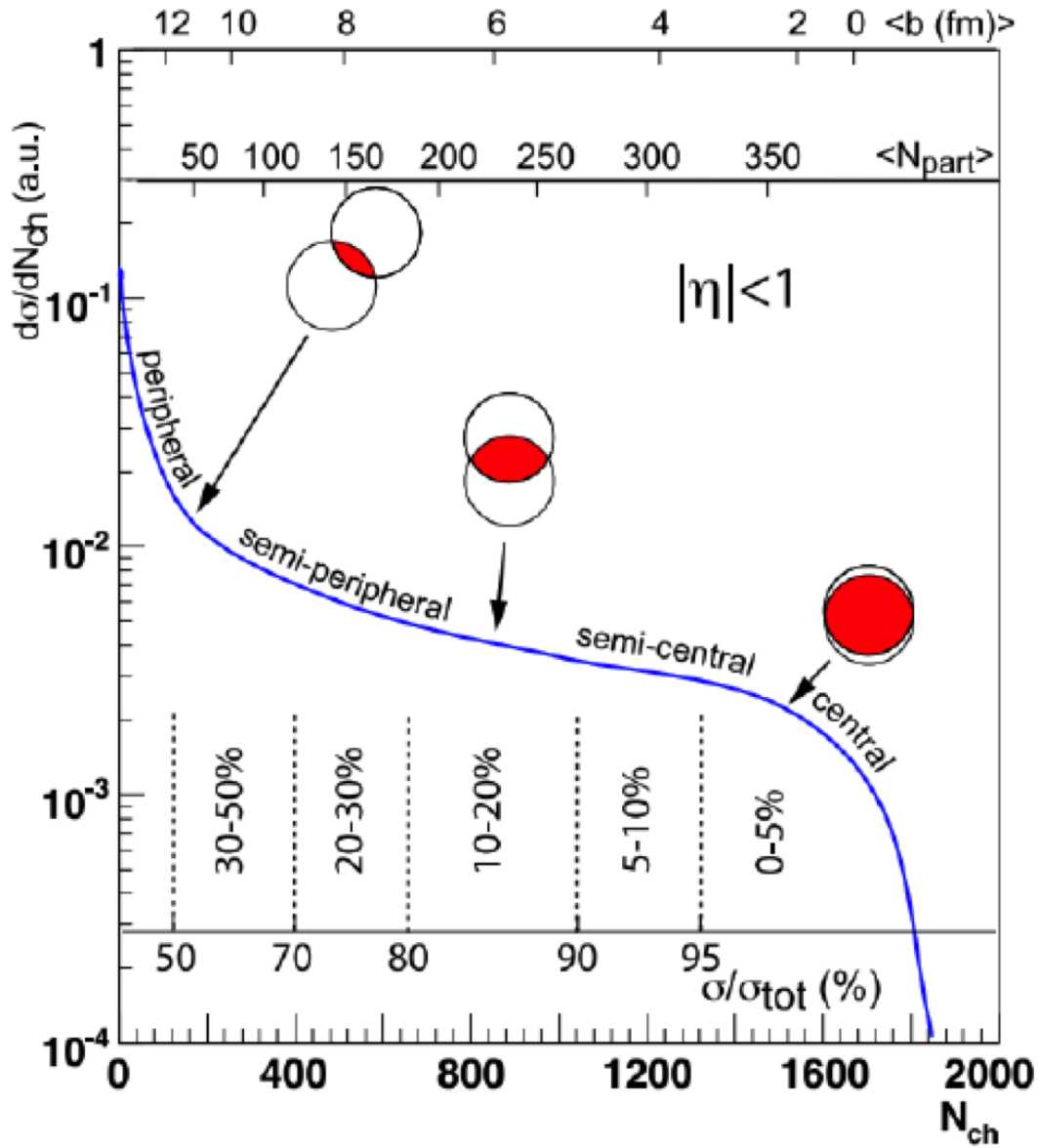


Figure 3.2: Schematic of the mapping of experimental observables (the number of charged particles N_{ch}) with Glauber quantities ($\langle \vec{b} \rangle, \langle N_{part} \rangle$) [76]

for the mapping between the Glauber quantities and each centrality interval. There are two components in nuclear collisions, one is the “soft” part and it is proportional to the variable N_{part} . The other component is the “hard” part and it is proportional to the variable N_{coll} . The new variable Glauber quantity ξ_G is defined in a way that it has similar distribution

to the experimentally observed variable ξ . The linear combination of two components turns out to be an appropriate choice for ξ_G :

$$\xi_G = \xi_{G0} \left((1-x) \frac{N_{part}}{2} + x N_{coll} \right), \quad (3.7)$$

where $0 < x < 1$, x and ξ_{G0} can be determined from the fitting of the $dN_{evt}/d\xi$ distribution measured in experiment with $dN_{evt}/d\xi_G$ distribution from a MC Glauber sample [79]. The centrality intervals for ξ_G are defined the same way as ξ , $\langle N_{coll} \rangle$ and $\langle N_{part} \rangle$ in each centrality interval are defined by averaging over the N_{coll} and N_{part} in the same centrality bin.

3.2.2 Nuclear effects

In 1980s, the bound nucleon systems were found to behave differently in momentum distributions for quarks and gluons compared to the nucleon with free or loosely bound systems [80]. It indicates that the nuclear structure functions are not just the simple combination of each individual nucleon's structure functions. Thus nuclear parton distribution functions (nPDFs) accommodate nuclear effects into the existing PDFs [81–84].

The nPDFs experience suppression at lower x value and enhancement at higher x value compared to the PDFs of nucleon. In addition, nPDFs have the same evolution based on the DGLAP (Dokshitzer–Gribov–Lipatov–Altarelli–Parisi) equation [85–87] as the PDFs of a free nucleon, except for a different initial parametrization. The nuclear modifications can be quantified through the ratio between the PDFs of bound and free proton:

$$R_i^A(x, Q^2) = \frac{f_i^{p/A}(x, Q^2)}{f_i^p(x, Q^2)}, \quad (3.8)$$

where A denotes the nuclear mass number, and i denotes the parton species: valence quark, sea quark or gluon. $f_i^{p/A}$ denotes the bound proton PDFs and f_i^p denotes the free proton PDFs. The nPDFs can be calculated from a parametrization of $R_i^A(x, Q^2)$ at an initial scale

with the PDF set of free proton as baseline [81]. The following lists the different nuclear effects in different x regions:

- Shadowing for $x \lesssim 0.01$: $R_i^A < 1$. The shadowing effect contains [88]: 1. Enhancement of shadowing with decreasing x ; 2. Enhancement of shadowing with A ; 3. Suppression of shadowing with increasing Q^2 . The effective nucleon-nucleon cross section is reduced due to the shadowing of elastic interactions and the destructive interference effect which makes the incoming flux decreases [89]. The experiments at the Large Hadron Collider (LHC) is specifically related to this shadowing effect at low x region according to the fact that it provides investigation of nuclear collisions at lower x and higher energies. The hadron yield will be reduced at high p_T region accordingly.
- Antishadowing for $x \sim 0.1$: $R_i^A > 1$. The antishadowing effect is required to restore the sum rule of momentum in nuclei, thus it balances the shadowing and the EMC-effects [90].
- EMC (European Muon Collaboration)-effect for $0.3 \lesssim x \lesssim 0.7$: $R_i^A > 1$. This effect can be described by the parton model, valence quarks in free nucleon carry larger momentum fraction compared to those within nucleus.
- Fermi-motion for $x \rightarrow 1$ and beyond: $R_i^A > 1$. This effect can be explained with non-stationary nucleons within the nucleus.

These effects are shown in Fig. 3.3 and there is no unique theoretical explanation for these nuclear effects at present. The description for these effects derived from several different models can be found in Ref [88, 91, 92].

3.2.3 Jet Quenching

In heavy ion collisions, the parton is expected to lose energy by passing through the QGP medium created in the Pb+Pb collisions. There are two energy loss mechanisms: radia-

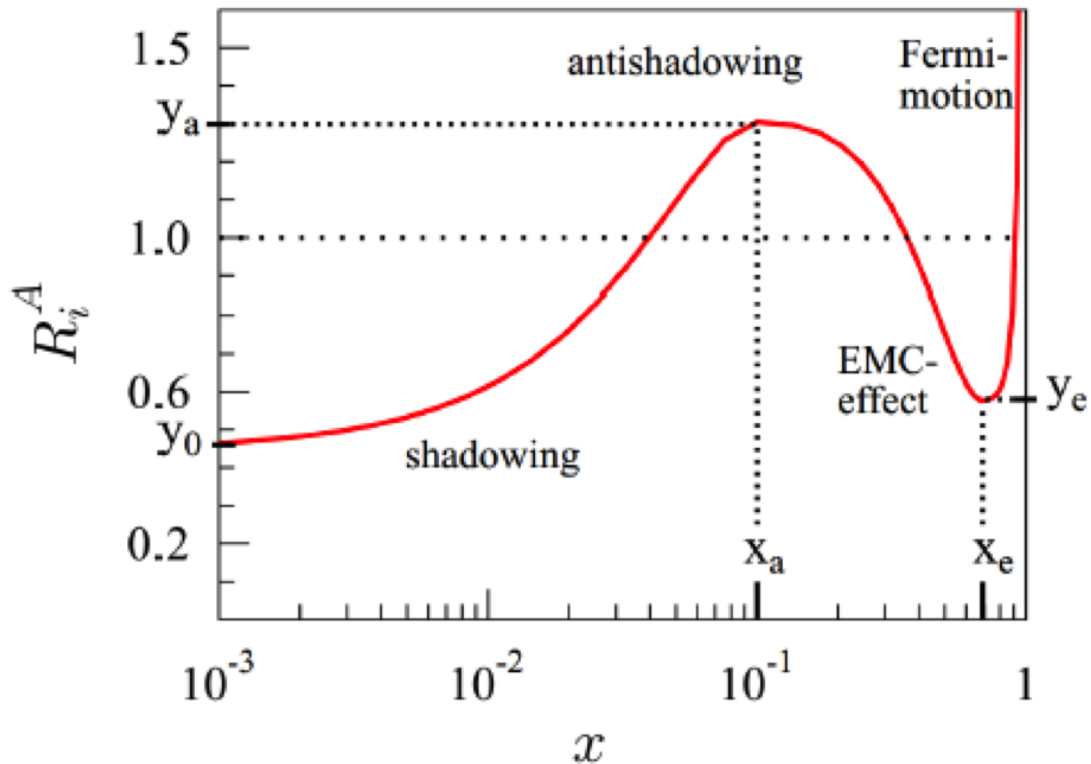


Figure 3.3: Schematic of $R_i^A(x, Q^2)$ distribution as a function of x and the different nuclear effects in each x region [81]. In this figure, y_0 is the height at which shadowing levels out as $x \rightarrow 0$, x_a and y_a are the position and height, respectively, at which antishadowing is maximum, and x_e and y_e are the position and height at which the EMC-effect is minimum.

tive energy loss coming from gluon bremsstrahlung and collisional energy loss coming from collisions with other partons in the medium [93, 94]. The particles with high transverse momentum are expected to experience suppression in yields compared to rescaled proton-proton collisions, where there is no medium effect present. Fig. 3.4 shows these two energy loss mechanisms: On the left side of Fig. 3.4, it represents the collisional energy loss stems from elastic scattering with the medium constituents which dominates at the low energy of particle. On the right side of Fig. 3.4, it represents the radiative energy loss stems from inelastic scattering within the medium which dominated at the higher energy region of particle.

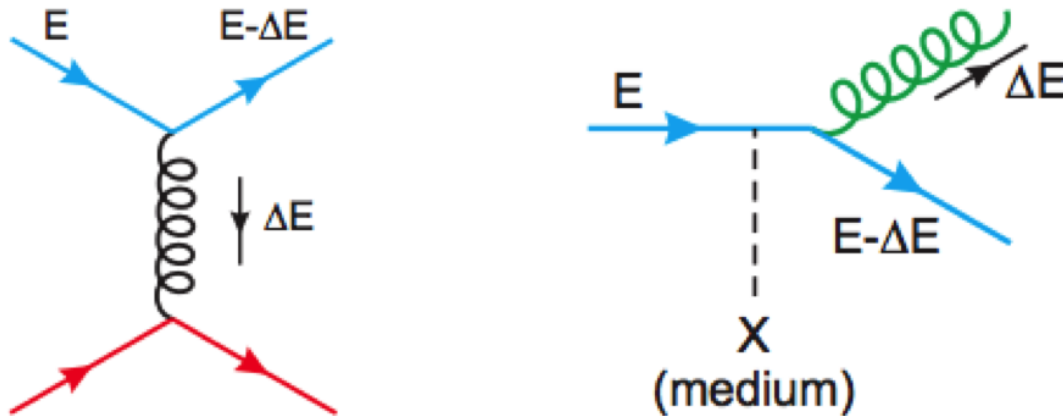


Figure 3.4: Diagrams for collisional (left) and radiative (right) energy loss of a quark with energy E passing through a QGP medium. Taken from [95].

Collisional Energy Loss

Unlike QED, energy loss in QCD should take the non-Abelian feature into account. There are several changes coming from the fact that gluons can also interact with themselves. The QCD coupling “constant” $\alpha_s(Q)$ has to be evaluated to the scale Q considered specifically. In addition, the difference between the coupling of quarks and gluons with the medium should be considered. In general, the average energy loss in one scattering can be expressed in the following equation:

$$\langle \Delta E_{coll}^{1scat} \rangle \approx \frac{1}{\sigma T} \int_{m_D^2}^{t_{max}} t \frac{d\sigma}{dt} dt, \quad (3.9)$$

where T denotes the temperature of the medium, $d\sigma/dt$ denotes the cross section of the scattering process, $t = Q^2$ denotes the squared transfer momentum, $m_D (\sim gT)$ denotes Debye mass which is the inverse of the screening length of the (chromo) electric fields in the medium.

Bjorken [96] and Braaten [97] first estimated the collisional energy loss of energetic partons within the QGP medium, and it is modified by other physicists later [98–100]. In equation 3.9, the integral limits can be expressed as $t_{min} = m_D^2(T) \sim 4\pi\alpha_s T^2(1 + N_f/6)$ and $t_{max} \sim ET$, where E denotes the parton energy and N_f denotes the flavor number. The

t -differential elastic parton-parton cross section is:

$$\begin{aligned} \frac{d\sigma}{dt} &\approx C_i \frac{4\pi\alpha_s^2(t)}{t^2} \\ \alpha_s(t) &= \frac{12\pi}{(33 - 2N_f)\ln(t/\Lambda_{QCD}^2)}, \end{aligned} \quad (3.10)$$

where C_i denotes the color factor and equals 4/9, 9/4, 1 for scattering process qq , gg , qg respectively. At the limit of $E \gg M^2/T$, the collisional energy loss per unit length for different mass of particles is:

$$\begin{aligned} -\frac{dE_{coll}}{dl}\Big|_{q,g} &= \frac{1}{4}C_R\alpha_s(ET)m_D^2\ln\left(\frac{ET}{m_D^2}\right), \text{ for gluon and light quarks} \\ -\frac{dE_{coll}}{dl}\Big|_Q &= -\frac{dE_{coll}}{dl}\Big|_q - \frac{2}{9}C_R\pi T^2[\alpha_s^2(M^2)\alpha_s^2(ET)\ln\left(\frac{ET}{M^2}\right)], \text{ for heavy quarks} \end{aligned} \quad (3.11)$$

where C_R denotes the quadratic Casimir of the hard parton and it equals 4/3 and 3 for quark and gluon respectively [99]. The initial parton energy has logarithmic impact on the collisional energy loss and it's also linearly correlated to the medium thickness.

Radiative Energy Loss

The radiative energy loss comes from the medium-induced multiple gluon emissions within the QGP medium [101–104]. Classically, the total energy loss per scattering can be calculated from the gluon bremsstrahlung spectrum:

$$\Delta E_{rad}^{1scat} = \int^E \int^{k_{Tmax}} \omega \frac{d^2 I_{rad}}{d\omega dk_{\perp}^2} d\omega dk_{\perp}^2 \quad (3.12)$$

where ω denotes the energy and k_{\perp} denotes the transverse momentum of the radiated gluon. For incoherent scattering the total energy loss is expressed as:

$$\Delta E^{tot} = N \cdot \Delta E^{1scat}, \quad (3.13)$$

where $N = L/\lambda$ denotes the medium opacity which is the number of scatterings experienced by the particle in a medium with thickness L . The energy loss per unit length is:

$$-\frac{dE}{dl} = \frac{\langle \Delta E^{tot} \rangle}{L}, \quad (3.14)$$

and for the incoherent scattering, the expression reduces to:

$$-\frac{dE}{dl} = \frac{\langle \Delta E^{tot} \rangle}{\lambda}. \quad (3.15)$$

The DGLAP splitting functions in the vacuum [85–87] can be used to calculate the radiation probabilities in QCD:

$$\begin{aligned} P_{q \rightarrow qg}(z) &= C_F \frac{1 + (1-z)^2}{z} \\ P_{g \rightarrow gg}(z) &= C_A \frac{1 + z^4 + (1-z)^4}{z(1-z)}, \end{aligned} \quad (3.16)$$

where $z = \omega/E$ denotes the fraction of the energy that the radiated gluon takes from its parent parton. The C_F denotes the fundamental representation of the color Casimir factor and the C_A denotes the adjoint representation. The final radiated gluon spectrum is proportional to these probabilities. Also the transport coefficient $\hat{q} = m_D^2/\lambda$ is introduced to describe the medium modifications in the radiative energy loss estimation. It encodes the “scattering power” of the medium through the average transverse momentum squared transferred to the traversing particle per unit path-length. For $L \ll \lambda$ case, which indicates the thin media, the gluonstrahlung spectrum can be described by the Bethe-Heitler expression [105]. The total collisional energy loss is:

$$\begin{aligned} \omega \frac{dI_{rad}}{d\omega} &\approx \alpha_s \hat{q} L^2 / \omega \\ \Delta E_{rad}^{BH} &\approx \alpha_s \hat{q} L^2 \ln(E/(m_D^2 L)). \end{aligned} \quad (3.17)$$

For the thick media case ($L \gg \lambda$), the spectrum can be described by the Landau-Pomeranchuk-Migdal (LPM) coherence effect [106]. Gluons with greater or smaller energy than the characteristic gluonstrahlung energy $\omega_c = \frac{1}{2}\hat{q}L^2$ should be treated separately:

$$\omega \frac{dI_{rad}}{d\omega} \approx \alpha_s \begin{cases} \sqrt{\hat{q}L^2/\omega} & \text{if } \omega < \omega_c \\ \hat{q}L^2/\omega & \text{if } \omega > \omega_c \end{cases} \quad (3.18)$$

$$\Delta E_{rad}^{LPM} \approx \alpha_s \begin{cases} \hat{q}L^2 & \text{if } \omega < \omega_c \\ \hat{q}L^2 \ln(E/(\hat{q}L^2)) & \text{if } \omega > \omega_c \end{cases} \quad (3.19)$$

From the formulas above there are two features need to be noticed: 1) The LPM gluon spectrum ($\omega \frac{dI_{rad}}{d\omega} \propto \omega^{-1/2}$) is suppressed in the infrared compared to the BH spectrum ($\omega \frac{dI_{rad}}{d\omega} \propto \omega^{-1}$). 2) The energy loss in QCD depends on the thickness of the medium specifically with the form of L^2 , which is a universal feature of the medium-induced energy loss of any in-medium newborn particle.

Nuclear modification factor in the Pb+Pb collisions

Jet quenching was first observed through two measurements in experiment. The suppression occurred significantly for single hadron at high p_T in central collisions [107–110]. In order to study the phenomenon of suppression more quantitatively, the perturbation theory techniques are used to calculate the production rate of a single high p_T parton, c in a parton-parton collision: $ab \rightarrow c + X$, since the QCD coupling constant α_s is small for high-energy (short distance) parton interactions. In high energy hadron-hadron collisions, the QCD “factorisation theorem” can be used for the calculation of high p_T particles’ production based on the underlying parton-parton processes [57]. The cross section of a hadron h with high p_T

can be expressed as follows:

$$d\sigma_{AB \rightarrow h}^{hard} = f_{a/A}(x_1, Q^2) \otimes f_{b/B}(x_2, Q^2) \otimes d\sigma_{ab \rightarrow c}^{hard} \otimes \mathcal{D}_{c \rightarrow h}(z, Q^2), \quad (3.20)$$

where $\sigma_{ab \rightarrow cX}(x_1, x_2, Q^2)$ denotes the perturbative partonic cross section, which is calculable up to a given order in α_s . $f_{a/A}(x, Q^2)$ is the PDF which represents the probability of finding a parton with flavor a and momentum fraction $x = p_{parton}/p_{nucleus}$ inside the nucleus A . $\mathcal{D}_{c \rightarrow h}(z, Q^2)$ denotes the fragmentation function (FF) which represents the ‘‘probability’’ that the outgoing parton c fragments into a final hadron h with fractional momentum $z = p_{hadron}/p_{parton}$. The two non-perturbative terms $f_{a/A}(x, Q^2)$ and $\mathcal{D}_{c \rightarrow h}(z, Q^2)$ are universal, and they can be determined from experiment. $\mathcal{D}_{c \rightarrow h}$ can be defined as $\delta(1 - z)$ for calculating the cross section of total parton (jet). Fig. 3.5 shows the sketch of dijet production in hadronic collisions.

Each nucleus can be treated as a collection of free partons, because during the hard scattering processes, partons are ‘‘frozen’’. For a nucleus with mass number of A , the parton density can be simply expressed as a superposition of A independent nucleons for high p_T production: $f_{a/A}(x, Q^2) \approx A \cdot f_{a/N}(x, Q^2)$. Hence the cross section of hadron h is:

$$d\sigma_{AB \rightarrow h}^{hard} \approx A \cdot B f_{a/p}(x, Q^2) \otimes f_{b/p}(x, Q^2) \otimes d\sigma_{ab \rightarrow c}^{hard} \otimes \mathcal{D}_{c \rightarrow h}(z, Q^2). \quad (3.21)$$

The inclusive hard cross sections for $A B$ interaction can be expressed simply as the pp cross sections times $A \cdot B$ from the implication of QCD factorisation in equation 3.20:

$$d\sigma_{AB}^{hard} = A \cdot B \cdot d\sigma_{pp}^{hard}. \quad (3.22)$$

In general, the yields are directly measured in the nucleus-nucleus experiments, the above

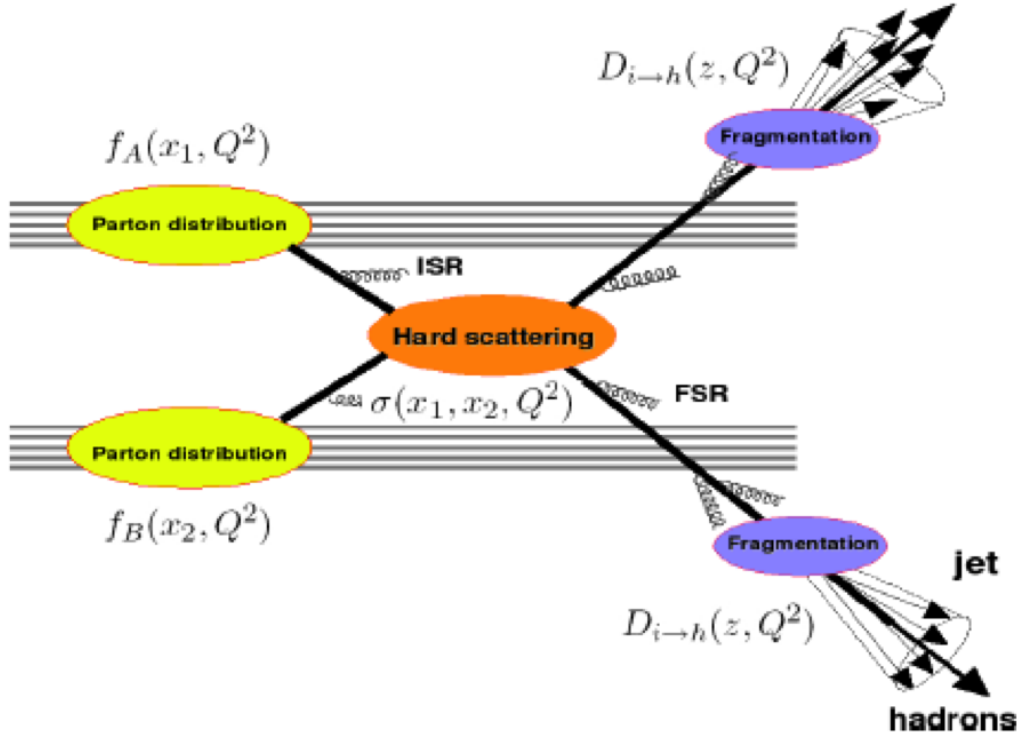


Figure 3.5: Sketch of dijet production and pQCD factorisation in hadronic collisions: $f_{a/A}(x, Q^2)$ are the PDFs, $\mathcal{D}_{i \rightarrow h}(z, Q^2)$ are the FFs and ISF (FSR) represents initial (final) state radiation. Taken from [95].

equation can be written as follows 2.3.1:

$$dN_{AB}^{hard}(b) = \langle T_{AB}(b) \rangle \cdot \sigma_{pp}^{hard}, \quad (3.23)$$

where the $T_{AB}(b)$ denotes the nuclear overlap function with impact parameter b . It can be determined from the measured Woods-Saxon distribution of the interacting nuclei within a geometric Glauber model [111]. The nuclear overlap function $T_{AA}(b)$ can be interpreted as the effective integrated “luminosity” of the partons in the collisions of two beams of nucleons. Since the $N_{coll}(b)$ is proportional to $T_{AB}(b)$: $N_{coll}(b) = T_{AB}(b)\sigma_{NN}^{in}$, equation 3.23 can be expressed as:

$$dN_{AB}^{hard}(b) = \langle N_{coll}(b) \rangle \cdot dN_{pp}^{hard}. \quad (3.24)$$

The nuclear modification factor is introduced to describe the effects of the medium on the yields of a hard probe in the AA (Pb+Pb) collisions quantitatively:

$$R_{AA}(p_T, y; b) = \frac{d^2 N_{AA}/dy/dp_T}{\langle T_{AA}(b) \rangle \times d^2 \sigma_{pp}/dydp_T}. \quad (3.25)$$

R_{AA} is the main observable of interests in this thesis. If there is no medium effects, the R_{AA} is expected to be equal to one. In case of suppression of the particles, the R_{AA} will be smaller than one in both intermediate and high transverse momentum.

3.3 Jet Phenomenology Involving Heavy Flavor

The heavy quarks we focused on in this analysis are bottoms quarks, which are not expected to be produced thermally in significant amounts in the QGP due to their large mass $m_b = 4.18_{-0.03}^{+0.03} GeV/c^2$. Bottom quarks are expected to be produced primarily in the hard scattering of partons in the initial stages of the collision, and live much longer ($\sim 10^{-11} sec$) than the duration of the QGP ($\sim 10^{-33} sec$) [112]. Thus they can experience the whole evolution of the system. The production for bottom quarks is perturbative in QCD process due to the requirement of the higher energy transfer.

3.3.1 Heavy Flavour Production

The open heavy-flavor production can be studied through the approach of semi-leptonic decay process. The direct b -decay channel: $b \rightarrow lX$ and the cascade decay channel: $b \rightarrow c \rightarrow lX$ are with branching ratio of $(10.69 \pm 0.22)\%$ and $(9.62 \pm 0.53)\%$ respectively [75], where l denotes leptons, like electrons or muons.

There are three heavy-flavor production in high energy particle collisions:

- Pair creation: The two Leading Order (LO) processes which produce the hard sub-process are shown in Fig. 3.6a and 3.6b. As shown in Fig. 3.6a, the process is $gg \rightarrow Q\bar{Q}$,

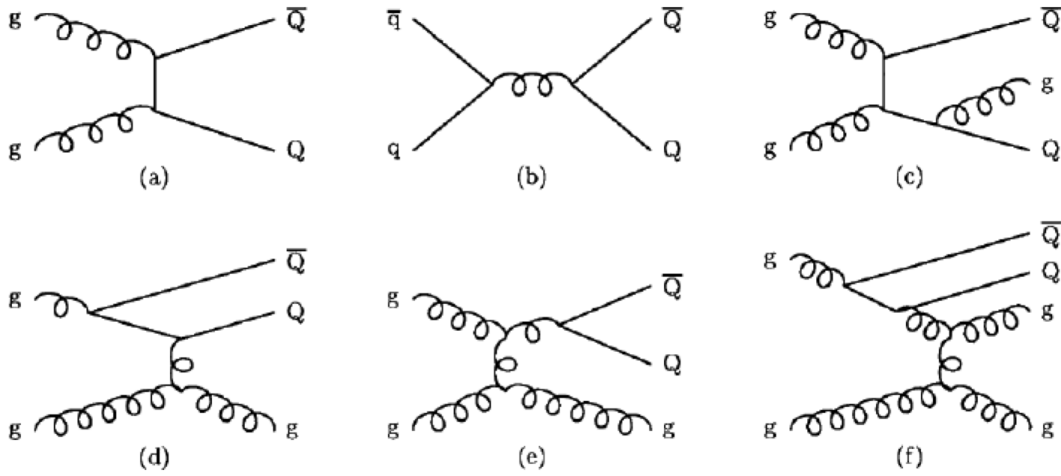


Figure 3.6: Diagrams for examples of heavy-flavor production: Pair creation (a,b with leading order. c, with gluon emission), Flavour excitation (d), Gluon splitting (e), Events classified as gluon splitting but of flavor-excitation character. [113]

where Q represents the heavy quark. Fig. 3.6b shows the process of $q\bar{q} \rightarrow Q\bar{Q}$ and Fig. 3.6c represents the same process with the gluon shower emission. This additional gluon shower does not have effect on the cross section of the production; however, it can contribute to the alteration of kinematics. The parton shower in Fig. 3.6a and Fig. 3.6b must come out back-to-back due to the momentum conservation, while there is a net recoil allowed for the emerged parton shower in Fig. 3.6c [113].

- Flavour excitation: Fig. 3.6d shows the flavor excitation process, where the heavy quark Q is excited by the exchange of a gluon with the other hadron, and Q is on the mass shell of the particle in the final state. Since Q is not a valence flavor, it has to be generated from gluon splitting $g \rightarrow Q\bar{Q}$ inside the incident particle before the scattering [113].
- Gluon splitting: Fig. 3.6e shows the occurrence of heavy quarks in $g \rightarrow Q\bar{Q}$ process in the initial or the final state shower, and not in the hard scattering. There is a large combined transverse momentum in the final state. Thus the shower is constrained

within a small cone of angular separation [113].

Fig. 3.6f shows the flavor excitation feature; however, it's considered as a gluon splitting process due to the gluon participation in hard scattering. During the process a gluon branches to $Q\bar{Q}$ at first, and one of the heavy quarks emits another gluon later [113].

3.3.2 Semi-leptonic Decay

Semi-leptonic decays of hadrons contain a single charged lepton in the final state particles. From the theoretical perspective, these decays are relatively simple and clear. Thus they provide means not only to measure fundamental standard-model parameters, but also to perform detailed studies of decay dynamics. In experiments, the hadrons containing heavy quarks can decay to leptons or lighter hadrons through weak interaction. There are transitions across quark generations even though the same generation of quark transitions has high probability. The 3×3 unitary matrix Cabibbo-Kobayashi-Maskawa (CKM) is introduced to describe the strength of flavor-changing weak decays [114, 115]:

$$V = \begin{bmatrix} V_{ud} & V_{us} & V_{ub} \\ V_{cd} & V_{cs} & V_{cb} \\ V_{td} & V_{ts} & V_{tb} \end{bmatrix} \quad (3.26)$$

The mixing angles and irreducible phase can provide information in the universality of the weak decay and the CP violation in the Standard Model. The amplitudes for the processes $b \rightarrow c \rightarrow lX$ and $b \rightarrow ulX$ are proportional to V_{cb} and V_{ub} respectively [22]:

$$\begin{aligned} |V_{cb}| &= 40.9 \pm 1.1 * 10^{-3} \\ |V_{ub}| &= 4.14 \pm 0.19 * 10^{-3} \end{aligned} \quad (3.27)$$

From this result, the b quark has relatively longer life time ($\tau \sim 10^{-12}\text{s}$) due to the high suppression in decay. The decay channel $b \rightarrow c$ is highly preferred over the $b \rightarrow u$ decay, since $|V_{cb}|$ is much larger than the value of $|V_{ub}|$. Because muon is experimentally accessible in an easier way and provides clean environment to study, b quarks semi-leptonic decay into muons is considered for heavy flavor study in this thesis.

3.4 Heavy Flavor Quenching

Heavy quarks are not valence flavor in the beam particle as light quarks (u, d, s), there is no ambiguous information in the identification of heavy flavor hadrons through the interaction with the QGP medium [113]. Quark energy loss can occur due to gluon radiation or (hard or soft) collisions. Heavy quarks are of a great interest in heavy ion collisions because parton showers initiated by heavy quark hadrons are expected to be sensitive to the medium in a different way, for which the dominant energy loss mechanism are the collisions of the heavy quark with the constituents of the QGP.

The gluon bremsstrahlung distribution of heavy quarks is $[1 + (M^2/E^2) \cdot \theta^{-2}]^{-2}$ factor less than the light quarks case, where M denotes the mass of the heavy quark and E denotes the energy. θ denotes the angle of gluon emission (with respect to the heavy quark's momentum). This factor mentioned above is always smaller than 1, and close to zero for small angles ($\theta \lesssim M/E$, this different pattern of the small angle gluon radiation induced by medium is called “dead-cone” effect [2]). It suggests that the heavy quarks will lose less energy to the medium than the light quarks. However, there is proof later showed the non-negligible energy loss for heavy flavors due to the fact that dead-cone can be filled by gluon radiation from Armesto et al. [116]. During the transverse momentum range $p_T \leq M$, the collisional energy loss dominates the total energy loss. During the range of $p_T \gg M$, which is the ultra-relativistic case, the dominant energy loss is radiative and the mass of the quark behaves as a collinear regulator generally.

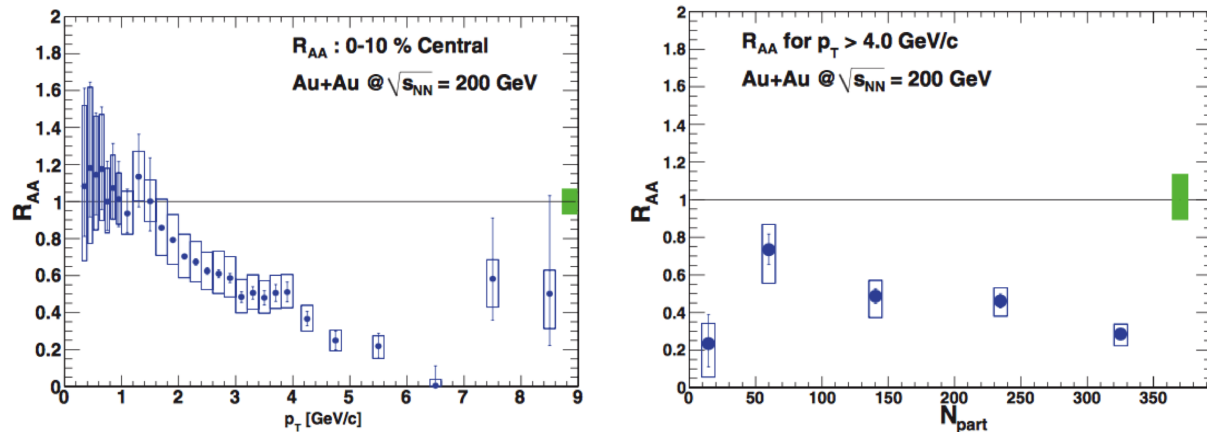


Figure 3.7: Left: Nuclear modification factor R_{AA} for electrons from heavy quark decays as function of p_T for the 10% most central Au + Au collisions at $\sqrt{s_{NN}} = 200$ GeV. The boxes show the point-to-point correlated systematic uncertainty. Right: Nuclear modification factors R_{AA} for open heavy-flavor electrons vs centrality, integrated above the $p_T^e > 4$ GeV range. Taken from [117]

Open heavy flavor measurements in nuclear collisions were pioneered at the RHIC, where heavy flavor energy loss was discovered via the observation of the suppression of the yield of electrons from heavy flavor hadron decays, which is in high transverse momentum range in central Au+Au collisions at $\sqrt{s_{NN}} = 200$ GeV with respect to pp collisions. Fig. 3.7 shows the nuclear modification factor of electrons from heavy quarks decays in the Pioneering High Energy Nuclear Interaction eXperiment (PHENIX) experiment at the RHIC [117], where a non-photonic e^\pm is defined to be an e^\pm produced with an (anti)neutrino in a charged-current weak decay. It is measured in the range of $0.3 < p_T < 9.0$ GeV/ c at the mid-rapidity ($|y| < 0.35$). In Fig. 3.7, we can see that the suppression level in the most central collisions (0-10%) for electrons with p_T above 4 GeV is at around 0.3. The non-photonic electron nuclear modification factor R_{AA} has also been studied with the Solenoidal Tracker at RHIC (STAR) experiment. Fig. 3.8 shows the measurement of non-photonic electron and its elliptic flow v_2 in central Au+Au collisions at $\sqrt{s_{NN}} = 200$ GeV. It has similar suppression level compared to the PHENIX results. This suppression can be interpreted in terms of parton energy loss in the plasma.

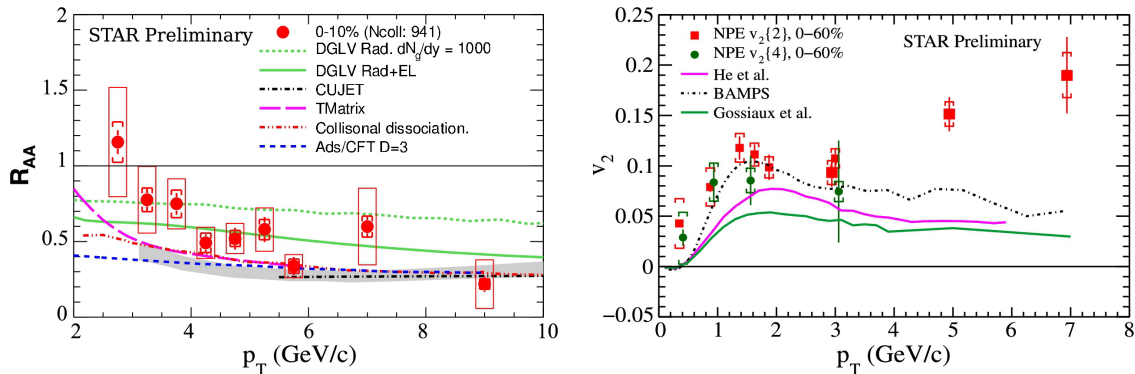


Figure 3.8: Non-photonuclear electron nuclear modification factor R_{AA} (left) and elliptic flow v_2 (right) measured for 0–10% and 0–60% centrality intervals, respectively, in Au+Au collisions at $\sqrt{s_{NN}} = 200$ GeV. The vertical bars on data points indicate statistical uncertainties. The brackets and boxes around data points represent the systematic uncertainties from Au+Au and p+p collisions, respectively. Taken from [118].

Measurements conducted at the LHC can exploit the larger heavy flavor production cross sections compared to the RHIC. Furthermore, the LHC experiments profited from the availability of high resolution vertex spectrometers, which allows the decay topology of heavy-flavor hadrons to be utilized. In addition, jet-medium interaction does not need strict separation between medium effects and jet fragmentation, which is more general and it provides direct sensitivity for the medium effects study. Measurements of full jets at the RHIC are restricted by the bounded acceptance of the detectors, However, this issue does not exist for the experiments at the LHC. The production of jets associated to the bottom quarks is measured for the first time in the Pb+Pb collisions at $\sqrt{s_{NN}} = 2.76$ TeV per nucleon pair in the Compact Muon Solenoid (CMS) experiment at the LHC [119]. The transverse momentum p_T of b -jet is in the range of 80 - 250 GeV, and the centrality integrated b -jet suppression as a function of p_T is shown in Fig. 3.9.

The muon tagged b -jet suppression measurement in the ATLAS experiment discussed in this thesis is in lower transverse momentum range of p_T between 30 - 150 GeV, it provides more sensitivity to the quenching effects in different kinematic region, and also provides different systematic study.

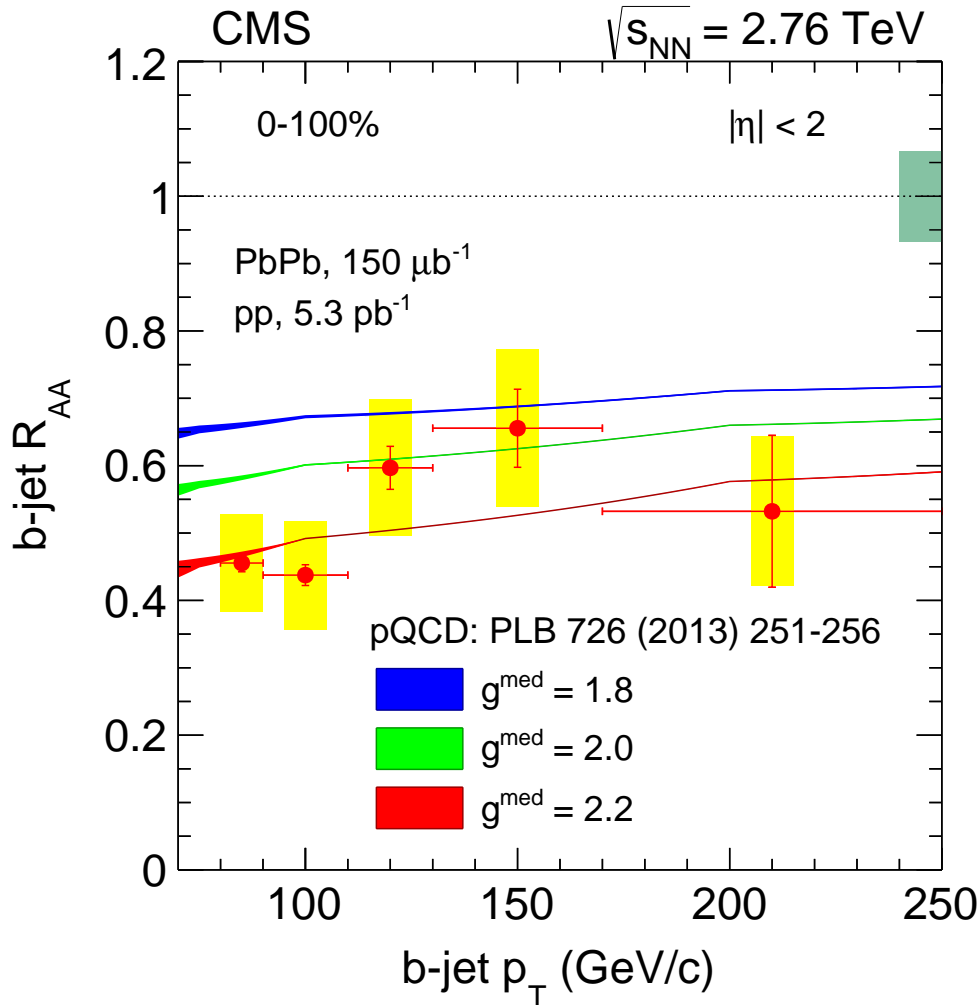


Figure 3.9: The centrality integrated (0–100%) b -jet R_{AA} as a function of p_T . The normalization uncertainty from the integrated luminosity in pp collisions and from T_{AA} is represented by the green band around unity. The data are compared to pQCD-based calculations from Ref. [120]. Taken from [119]

Heavy quarks are very powerful probes because they will interact strongly with the medium. Due to the large masses relative to their light counterparts, the differences in the degree of energy loss are expected. The measurement of heavy flavor suppression can provide valuable insight into the real mechanism .

Chapter 4

Experimental Setup

4.1 The Large Hadron Collider

The Large Hadron Collider (LHC) is the largest and the most powerful particle accelerator in the world. It is located at the European Organization for Nuclear Research (CERN) in Geneva, Switzerland. This machine is able to collide heavy ions although it is primarily designed for colliding protons, this program started to collect first lead ion collisions in November 2010.

The LHC machine had a 27 kilometres circumference that extends to the France-Switzerland border, and lies as deep as 175 metres beneath it. Unprecedented collision energies can be run on this massive accelerator, there are two parallel beam lines circulating particles traveling in opposite directions, and intersecting at designated interaction points (IPs). Pb^{208} ions are extracted from a source and accelerated through a sequence of injection chain elements before being injected to the LHC. The particles are prepared by a series of linear particle accelerators (LINAC3), the Low Energy Ion Ring (LEIR), the Proton Synchrotron (PS) and the Super Proton Synchrotron (SPS). The ions with charge state Pb^{+27} are generated in the LINAC3, where they are stripped to Pb^{+42} via carbon foil and are accelerated to 4.2 MeV

per nucleon. They reach 72 MeV per nucleon in the LEIR, and 6 GeV in the PS. The lead beam is fully stripped with an aluminum foil to Pb^{+82} as it is transferred from the PS to the SPS, and then accelerated to 177 GeV per nucleon.

There are seven detectors located at the LHC: A Toroidal LHC ApparatuS (ATLAS), Compact Muon Solenoid (CMS), A Large Ion Collider Experiment (ALICE), LHC-beauty (LHCb), TOTAl Elastic and diffractive cross section Measurement (TOTEM), LHC-forward (LHCf) and Monopole and Exotics Detector At the LHC (MoEDAL). Two of them, the ATLAS experiment and the CMS, are large, general purpose particle detectors. They also have the ability for the heavy ion physics study. The ALICE is a detector aim for heavy ion study. The LHCb has other specific roles such as the missing antimatter investigation. And the last three, the TOTEM, the MoEDAL and the LHCf, are much smaller and are for very specialized research. The TOTEM detector aims at the measurement of total cross section, elastic scattering, and diffractive processes. The LHCf provides better measurement of the particles generated in the forward region of collisions. The MoEDAL has the main goal of highly ionizing massive particles and magnetic monopole searching.

The proton beams were first circulated at the LHC in September 2008. However, it was intermittent due to an incident of magnet quench 9 days later. After the repair of the damage of the superconducting magnets, the proton beams with the center of mass energy at 900 GeV were circulated again on November 20 2009, and the first proton proton collisions were recorded in 3 days. The center of mass energy is increased to 7 TeV on March 30 2010. The LHC observed the first heavy ion collisions with the center of mass energy at 2.76 TeV per nucleon on November 8 2010. The center of mass energy of proton collisions achieved at 8 TeV in April 2012.

4.2 The ATLAS Experiment

The ATLAS experiment [121] at the LHC is a multi-purpose particle detector with a forward-backward symmetric cylindrical geometry, and a near 4π coverage in solid angle. It consists of an inner tracking detector, which is surrounded by a thin superconducting solenoid. It provides a 2 T axial magnetic field, electromagnetic and hadron calorimeters, and a muon spectrometer. The inner tracking detector covers the pseudorapidity range of $|\eta| < 2.5$. It consists of silicon pixel, silicon micro-strip, and transition radiation tracking detectors. Lead/liquid-argon (LAr) sampling calorimeters provide electromagnetic (EM) energy measurements with high granularity. A hadron (iron/scintillator-tile) calorimeter covers the central pseudorapidity range ($|\eta| < 1.7$). The end-cap and forward regions are instrumented with the LAr calorimeters for both EM and hadronic energy measurements up to $|\eta| < 3.2$. The forward region $3.2 < |\eta| < 4.9$ will be covered in the ATLAS forward calorimeter (FCAL) part. The FCAL consists of two calorimeter modules, and they locate forward and backward roughly 4.7 m from the center of the detector. They cover the pseudorapidity region of $3.2 < |\eta| < 4.9$. Each FCAL module consists of three longitudinal sampling layers. They are divided into transverse segments with approximate size $\Delta\eta \times \Delta\phi \approx 0.2 \times 0.2$. The total transverse energy, ΣE_T , measured in the FCAL is used to characterize the geometry or the “centrality” of the Pb+Pb collisions. The Minimum Bias Trigger Scintillators (MBTS) covers the pseudorapidity range of $2.09 < |\eta| < 3.84$. Minimum bias event is triggered and the event is selected by the MBTS. A graphical representation of the ATLAS highlighting the various subsystems is shown in Fig. 4.1.

4.2.1 Inner Detector

The Inner Detector (ID) is the innermost detector system in the ATLAS, it contains the Semiconductor Tracker (SCT), the pixel detector and the Transition Radiation Tracker (TRT). The barrel region of the ID is shown in Fig. 4.2. The pixel detector and the SCT are lo-

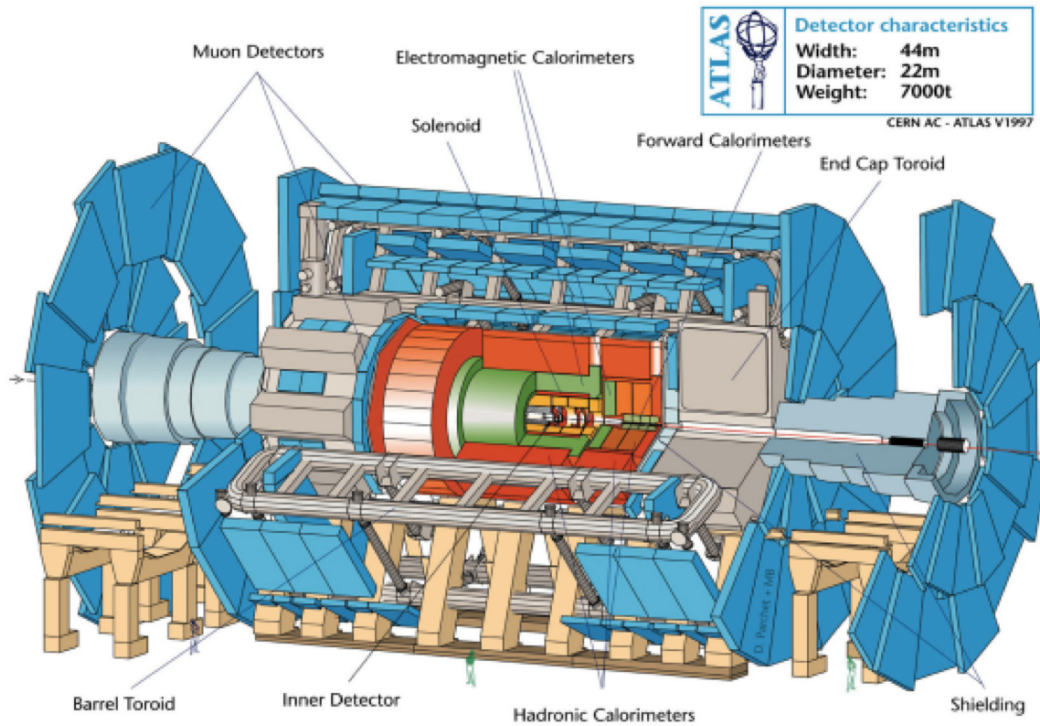


Figure 4.1: A diagram of the ATLAS detector showing the major detector systems. Taken from [122].

cated at inner radii. At larger radii, the detector which consists of many layers of gaseous straw tube elements and criss-cross with transition radiation material (TRT) is used. The ID can cover the measurement of the trajectories of charged particles which are bent in 2 Tesla solenoidal magnetic field provided by the central solenoid. It can provide robust pattern recognition and precise momentum resolution for charged particle above some certain transverse momentum (p_T) threshold (nominally 0.5 GeV) and within pseudorapidity range of $|\eta| < 2.5$.

In the pixel detector, there are three barrel layers and two end-caps each with three disk layers oriented with the plane of the disk perpendicular to the z axis for pixel modules. For each barrel, the layers have radii of 50.5 mm (layer-0), 88.5 mm (layer-1) and 122.5 mm (layer-2), respectively. The disk plane of the end-cap pixel are $\pm 495\text{mm}$, $\pm 580\text{mm}$ and $\pm 650\text{mm}$

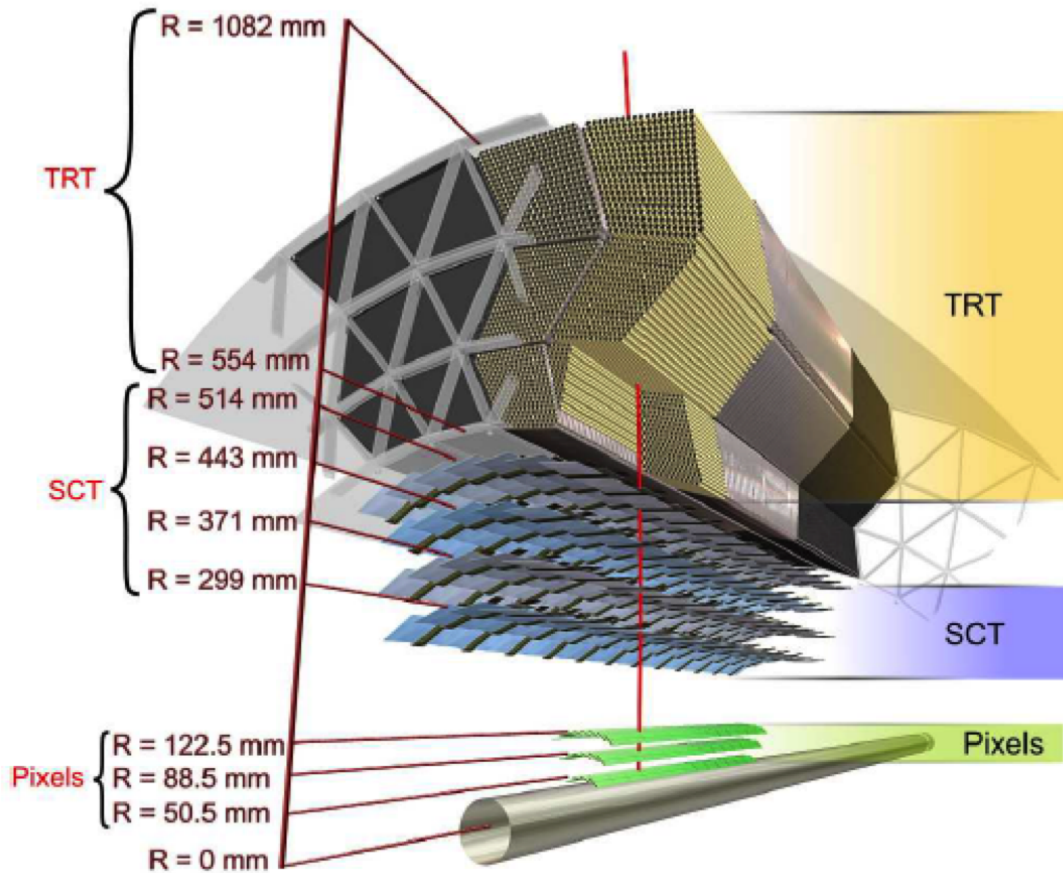


Figure 4.2: A diagram of the ATLAS inner detector barrel region. Taken from [123].

respectively away from the center of the detector, and they are placed symmetrically forward and backward along the z axis. The pixel barrel layers are composed of 22, 38 and 52 staves for the inner, middle, and outer layers, respectively. There are 13 pixel sensor modules on each stave. Each pixel module has 16 front-end electronic chips (FE) from the bottom up. It contains stack, bump bonds (connecting the electronic channels to pixel sensor elements), the sensor tile, flexible polyimide printed circuit board, and polyimide pig-tail with Cu lines and a connector (barrel modules) or a wire micro-cable (end-cap modules). There are 1744 pixel sensors in the Inner Detector and each sensor has 47232 pixels.

The SCT contains 4088 modules in the barrel, which is made of four coaxial cylindrical

layers and two end-caps each with nine disk layers. The barrel SCT modules consist of four sensors, two each on the top and bottom side, which are glued on thermal pyrolytic graphite (TPG) baseboard. For the end-caps SCT modules, they have two sets of sensors glued back-to-back around a central TPG spine. There are 15912 SCT sensors in the Inner Detector and each sensor has 768 active strips.

The TRT is a combination of the straw tracker and transition radiation detector. The TRT contains up to 73 layers of straws interleaved with polypropylene fibres (in the barrel), each straw is 4 mm in diameter and up to 144 cm long. There are about 50000 straws and each divided in two at the center region and read out to reduce the occupancy. The end-cap contains 160 straw planes interleaved with polypropylene radiator foils separated by a polypropylene net, and there are 320000 radial straws in total at the outer radius. The total number of channels is 420000. Each channel has a spatial resolution of 170 mm per straw and provides a drift time measurement, also there are two independent thresholds. These will let the detector have good discrimination between tracking hits, which pass the lower threshold, and transition radiation hits, which pass the higher one. The straws contain polyimide drift tubes of 4 mm diameter and anodes (31 μm diameter tungsten wires plated with 0.5–0.7 μm gold). The straw tube wall consists of two multi-layer films bonded back-to-back and have thickness of 35 μm . The straws are mechanically stabilised using carbon fibres and are filled with a mixture of gas (70% Xe , 27% CO_2 and 3% O_2), it operated in an environment of CO_2 . The precision of the TRT is not as good as the pixel detector and the SCT, but it was necessary to reduce the cost of covering a larger volume and to have capability of transition radiation detection.

4.2.2 Calorimeters

In the ATLAS experiment, the calorimeters use two kinds of active medium: scintillating tiles and liquid argon. For liquid argon, there are several kinds of calorimeters. For example,

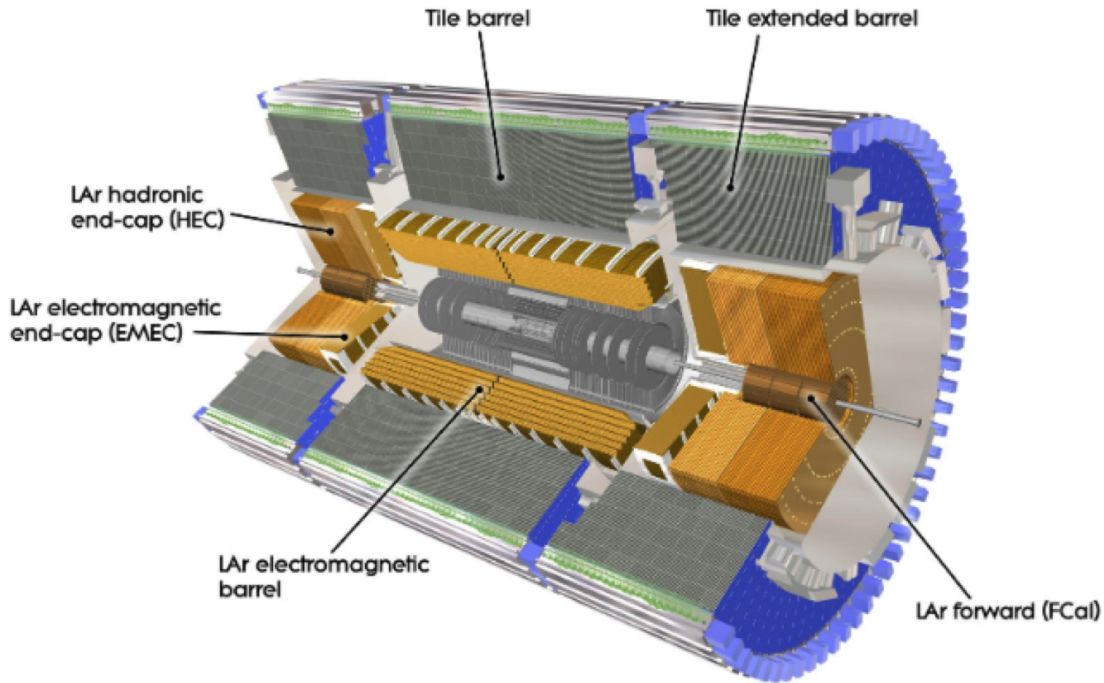


Figure 4.3: A cut-out view of ATLAS calorimeter detectors. Taken from [124].

the electromagnetic calorimeter is located in the barrel region. In the end-caps, there are an electromagnetic end-cap calorimeter (EMEC), a hadronic end-cap calorimeter (HEC), and a forward calorimeter (FCal). As for calorimeters using scintillating tiles, there is TileCal (tile calorimeter). The inner electromagnetic calorimeter absorbs energy mainly by electromagnetic interaction, while the outer hadronic calorimeter absorbs energy mainly by hadronic interaction. The calorimeters cover the pseudorapidity range of $|\eta| < 4.9$ in total. The overall layout of calorimeters system in the ATLAS detector is shown in Fig. 4.3.

Electromagnetic Calorimeters

The electromagnetic (EM) calorimeter is used for the identification and measurements of electron and photon [40]. It provides high precision, not only in the amount of energy absorbed, but also in the measurement of where the energy is deposited. Layers of lead

covered by stainless steel sheets and liquid argon are interleaved. The shower gets developed by lead with its short radiation length, at the same time, the secondary electrons help create ionization in the narrow gaps of liquid argon. The ionization electrons produce an inductive signal, after drifting in the electric field across the gas gap and got captured by the copper electrodes. The EM calorimeters consist of one barrel and two end-cap regions.

There is a liquid argon pre-sampler detector with thickness of 1.1 cm and 0.5 cm in barrel and end-cap region inside the EM calorimeters. There is no lead absorber in front of the pre-sampler. The energy lost by electrons and photons can be corrected by this pre-sampler in the inner detector, solenoid and cryostat wall. The barrel of EM calorimeter consists of three sampling layers. The first layer consists of very thin η strips with $\Delta\eta = 0.0031$ and each layer has a depth of 4.3 radiation lengths. This provides an excellent resolution in the distinguish of the direction between photon and π^0 . The second sampling has a depth of 16 radiation lengths, and most of the energy is deposited in this layer. The noise can be reduced if there is no third sampling layer, also the clusters with energy below 50 GeV will be fully contained. This layer has square cells with size of 0.0245 in both η and ϕ direction. The third sampling layer contains cells with size $\Delta\eta \times \Delta\phi = 0.05 \times 0.0245$.

There are two co-axial wheels located at $|\eta| = 2.5$ for the end-caps of the EM calorimeter. The inner wheel is divided into three longitudinal layers in order to achieve more precise measurement in the lower pseudorapidity region. The three layers have similar structure to the barrel region, the first layer has long, thin strips in η direction, the second layer consists of square cells with the same size of that in the barrel region and the cells are twice coarser granularity in η direction for the third layer. In the transition region between the barrel and end-cap, which is in the pseudorapidity range of $1.37 < |\eta| < 1.56$, the energy resolution can change significantly. This crack region is used neither for photon identification nor for precision measurements with electrons.

Hadronic Calorimeters

The hadronic calorimeters are located outside EM calorimeters and they measure particle energy by hadronic interactions. They contain three parts: tile calorimeters, liquid argon end-cap calorimeters and liquid argon forward calorimeters. The tile calorimeters are placed in the barrel region, and the liquid argon is used in the end-cap region to withstand the high level of radiations. The details of those three kinds of calorimeters will be explained as follows: The hadronic end-cap calorimeter uses copper as absorber and liquid-argon as the active medium. It covers pseudorapidity range of $1.5 < |\eta| < 3.2$. It consists of two wheels in each end-cap. Three electrodes divide the gaps between absorbers into four separate LAr drift zones. The middle electrode is the readout electrode. The space between the electrodes is maintained using a honeycomb sheet. The hadronic end-cap calorimeter has 5632 readout channels.

Tile Calorimeters Tile calorimeter consists three parts, the central barrel region covers pseudorapidity range of $|\eta| < 1.0$, and the other two extended barrel regions are located at $0.8 < |\eta| < 1.7$. It uses scintillator tiles as active materials. The scintillator tiles are placed in a way such that the $\frac{e}{h}$ ratio is improved if the shower passes through the tiles from the side. The tile calorimeter has a designed energy resolution of $\frac{50\%}{\sqrt{E}} \oplus 3\%$.

Liquid argon endcap Calorimeters The HEC is composed of two independent wheels per end-cap, which are located behind the end-cap EM calorimeter. It is placed between the tile calorimeter and forward calorimeter and covers the range of $1.5 < |\eta| < 3.2$. The copper plates are used as the absorbers placed perpendicular to the beam. The HEC has a designed energy resolution of $\frac{50\%}{\sqrt{E}} \oplus 3\%$.

Liquid argon forward Calorimeters The FCal contains three modules in each end-cap: the first module focuses on electromagnetic measurements and uses copper as material, while

the other two are for hadronic measurements and are made of tungsten. Copper/tungsten are selected because when the high energy jets close to the beam pipe, the background level in the surrounding calorimeters can be suppressed from the limitation of the width and depth of the showers from them. The calorimeter consists of cylindrical holes which are filled with liquid argon, and they form a metal matrix. The gaps can be controlled precisely as small as $250\mu\text{m}$, which can help in the sensitivity to the pileup effects and ion buildup. The FCal covers the pseudorapidity range of $3.1 < |\eta| < 4.9$. In the Pb+Pb collisions, we use the total transverse energy deposited in the FCal to characterize the geometry (centrality). The FCal has a designed energy resolution of $\frac{100\%}{\sqrt{E}} \oplus 10\%$.

4.2.3 Muon Spectrometer

The muon spectrometer is located at the outmost part in the detector, it focuses on muon particle tracking. There are three parts covering different pseudorapidity range: the barrel part has coverage over $|\eta| < 1.05$, the two end-cap parts have coverage over $1.0 < |\eta| < 2.7$, Fig. 4.4 shows a $x - y$ view of the muon spectrometer (MS).

The muon spectrometer surrounds the calorimeters and is based on three large air-core toroid superconducting magnets with eight coils each [40]. Its bending power is in the range from 2.0 to 7.5 T m. It includes a system of precision tracking chambers and fast detectors for triggering, each contains two parts. Fig. 4.5 shows the $z - y$ view of these four parts chambers.

There are Monitored Drift Tube (MDT) and Cathode Strip Chamber (CSC) that constitute the precision tracking chambers. MDT is responsible for $|\eta| > 2.7$ and CSC covers $2.0 < |\eta| < 2.7$. They focus on the precise measurement of muon p_T below 100 GeV with an accuracy of 2-3%, and the accuracy for muon p_T at 100 GeV is around 10%. The trigger chambers consist of Resistive Plate Chamber (RPC) and Thin Gap Chamber (TGC), covering $|\eta| < 1.05$ and $1.05 < |\eta| < 2.4$, respectively. They focus on the fast muon trigger.

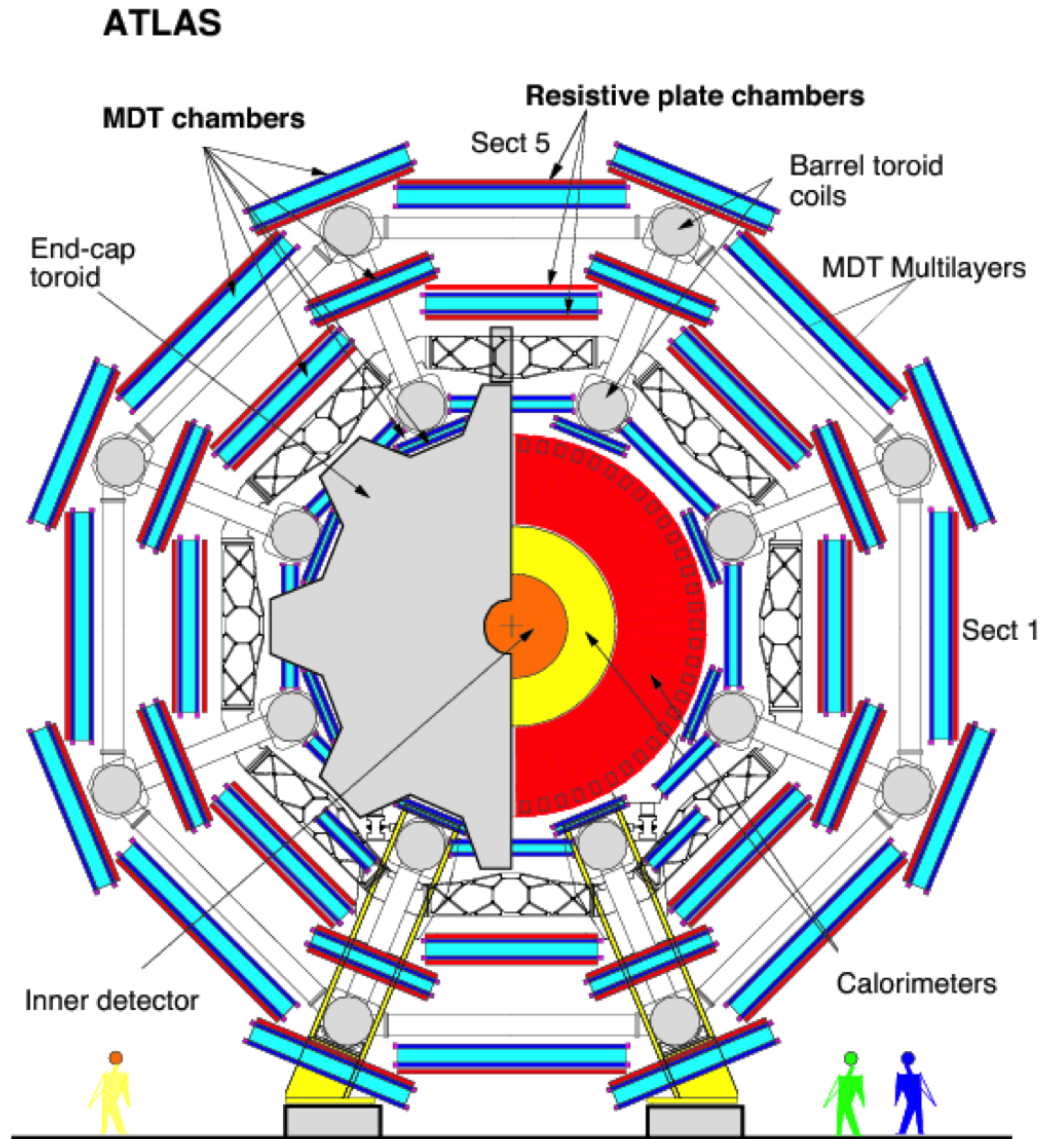


Figure 4.4: Schematic view of the muon spectrometer in the $x-y$ projections. Inner, Middle and Outer chamber stations are denoted BI, BM, BO in the barrel and EI, EM, EO in the end-cap. Taken from [125].

MDT

There are three barrel layers and four end-cap layers in MDT, each layer is composed of 16 chambers with 8 small and 8 large placed alternatively with a small ϕ overlap. This structure could minimize the gaps in the detector system. The barrel layers cover the pseudorapidity

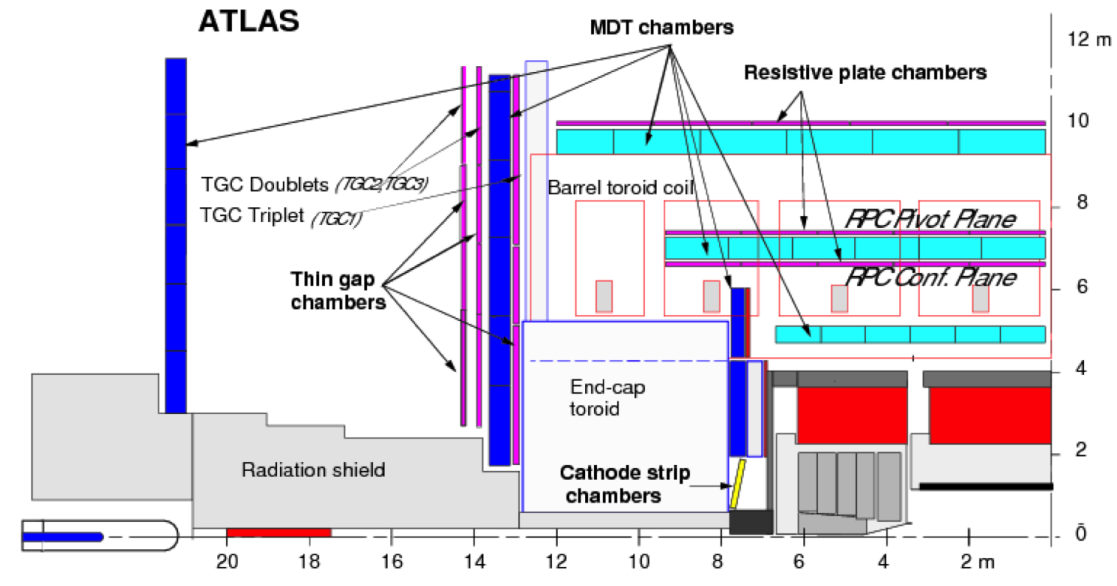


Figure 4.5: Schematic view of the muon spectrometer in the $z - y$ projections. Taken from [125].

range of $|\eta| < 1.05$, except for the central detector part at $\eta \approx 0$. The three barrel layers are placed at radii of 5m, 7.5m and 10m concentrically around beam axis. The large wheels are perpendicular to the z-axis with a distance of $|z| \approx 7.4m, 10.8 m, 14 m$ and $21.5 m$ from the primary vertex in the two end-cap regions. The pseudorapidity coverage is $1.05 < |\eta| < 2.7$ except for $|\eta| > 2.0$, which is in the region of inner most end-cap layer. The CSC is responsible for that part due to the consideration of muon track density.

CSC

In the end-cap region, each side contains two CSC layers with the pseudorapidity range of $2.0 < |\eta| < 2.7$ with high particle density. Similar to the MDT's case, there are 8 large and 8 small chambers in different ϕ direction inside CSC with them alternating each other. Inside the chamber, four CSC planes will provide four independent measurements in η and ϕ along each track. The CSC is multi-wire proportional chambers with the wires oriented in the radial direction. The good feature of CSC is that it can provide good two-track separation

and resolution, as well as time resolution and low neutron sensitivity. This is helpful for doing precision tracking in the forward pseudorapidity region with high particle density.

RPC

The RPC is mostly used for the fast trigger. It consists of three barrel stations with a coverage of $|\eta| < 1.05$. The three concentric cylindrical stations are located around the beam axis at radii of approximate 7.8 m (RPC1), 8.4 m (RPC2) and 10.2 m (RPC3) (see Fig. 4.6 for location of RPC). The large lever arm between RPC3 and RPC1 permits the trigger to select high momentum tracks in the range of 9-35 GeV, while the two inner stations (RPC1 and RPC2) provide the low p_T trigger in the range of 6-9 GeV. Each RPC station consists of two independent detector layers, and each with measurement of η and ϕ . A track going through all three stations thus delivers six measurements. The redundancy in the track measurement can be used to reject fake tracks from noise hits and greatly improve the trigger element sufficiency in the presence of small chamber inefficiencies. The RPC is a gaseous parallel electrode-plate detector without wires.

TGC

The TGC consists of six wheels in the end-cap region, with three wheels on each side. It provides both the trigger capability and the azimuthal coordinate measurement to complement the measurement of the MDT in the bending direction. The inner most wheel (MDT1 in Fig. 4.6) is composed of two layers and radially segmented into two non-overlapping regions. The middle wheel (MDT2) is composed of seven layers. The outer wheel (MDT3) does not provide independent coordinate measurement because there is no magnetic field between MDT2 and MDT3. Instead, the azimuthal coordinate in the outer MDT wheel is obtained by linear extrapolation of the track from the middle wheel. Like CSC, the TGC is a multi-wire detector.

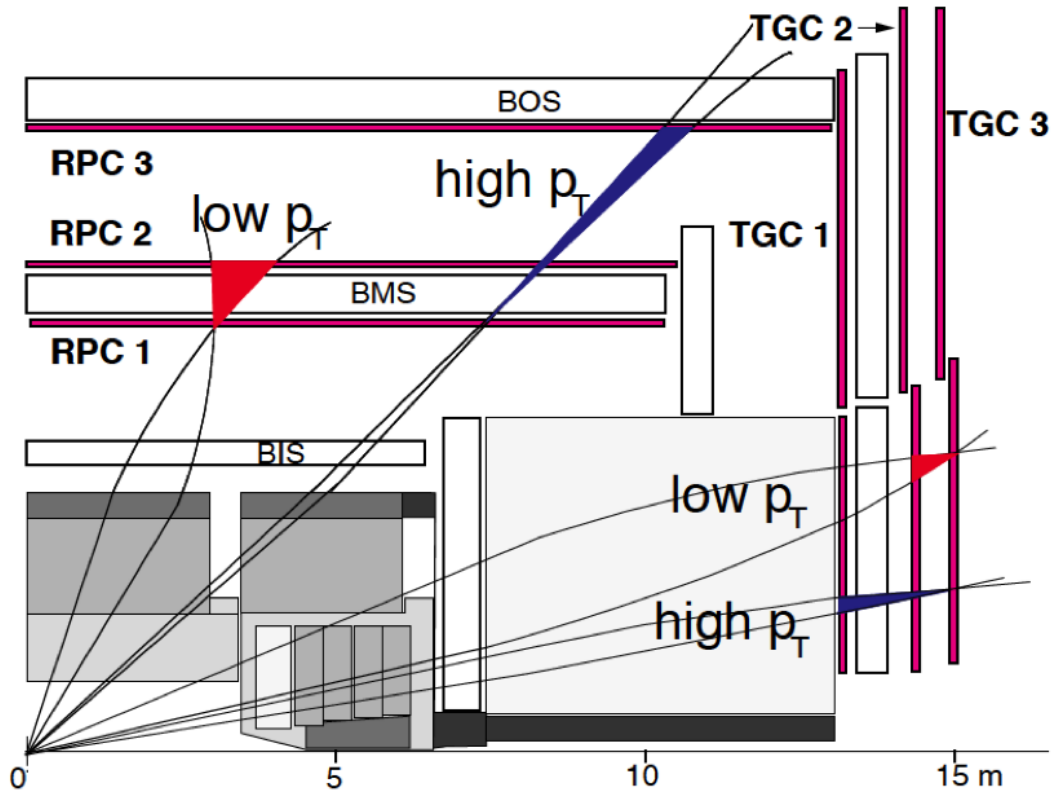


Figure 4.6: Muon Spectrometer as both high and low momentum trigger. Taken from [40].

4.2.4 Zero Degree Calorimeters

The Zero Degree Calorimeters (ZDC) in ATLAS are located at $|z| = 140$ m from the interactions points. Because the charged particles are influenced by the magnetic fields and deflected before they arrive at ZDC, the detector provides measurement for neutral particles with $|\eta| < 8.3$. There are four modules on each side, one of them is electromagnetic module and the rest three are hadronic modules. There are 11 plates along the direction which is perpendicular to the beam, they consist of tungsten with stainless steel quartz rods embedded. Quartz strips with length 1.55 mm are placed between these plates. The quartz rods produce Cerenkov light into the photo multiplier tubes.

In heavy ion collisions, ZDC was used as a minimum bias trigger due to the fact that

it rejects large background from photo-nuclear collisions efficiently by requiring a single neutron on both sides. The logical AND of one-sided triggers ZDC_A and ZDC_C produce ZDC_A_C, the coincidence trigger.

4.2.5 Minimum Bias Trigger Scintillators

The Minimum Bias Trigger Scintillators (MBTS) detector is located at $|z| = 3.56$ m and consist of two sets of 16 scintillator counters placed on the end-cap calorimeter cryostats. The counters are divided into 2 units along the η direction and 8 units along the ϕ direction. The radii from the innermost set has a range from 153 mm to 426 mm, corresponding to the pseudorapidity range of $2.82 < |\eta| < 3.84$. For the outermost set the radii is from 426 mm to 890 mm, with the pseudorapidity range of $2.09 < |\eta| < 2.82$.

4.2.6 Trigger System

The triggering system is used to select different types of events which are expected to have a particular physics object of interest. The events are sampled into multiple categories with a combination of hardware and software elements in trigger system. There are three different levels in ATLAS trigger system. The Level-1 (L1) trigger is hardware-only trigger. Objects with high transverse energy (E_T) such as electrons, jets, τ leptons decaying into hadrons, as well as events with high missing transverse energy E_T^{miss} are identified by the L1 trigger using reduced-granularity calorimeter information. The L1 muon trigger aims to identify muons by using information from RPC and TGC as explained in 4.2.3. The collision events without biasing toward any specific physics are selected by minimum bias trigger. The Central Trigger Processor (CTP) makes decisions based on the combined information of transverse energy (E_T) and transverse momentum (p_T). The L1 trigger is mainly for coarser and faster signal processing and the overall rate is reduced to at most 75 kHz.

The Level-2 (L2) and Event Filter (EF) triggers are both hardware- and software-based,

and they compose the High Level Trigger (HLT) system, which receives the information from the L1 selection. The L2 trigger assembles the full detector information from L1 Regions-Of-Interest (ROI), which is identified as having an L1-triggered object and performs an event selection. L2 event selection process uses algorithms like tracking and calorimeter clustering and etc. The overall rate is reduced to 3.5 kHz at this level. Finally, the properties of an offline event reconstruction is used to perform a selection by the Event Filter (EF) trigger. It is seeded by the decisions of the L2 event event selection that passed, events are categorized into different data streams by selected objects: jet, muon, electron, photon tau and etc. The final rate is reduced to 200 Hz at this level, and it provides seed events for offline analysis.

The rate of less interesting triggers relative to the rarer ones are reduced by prescales. The same L1 and L2 items can seed multiple chains, and prescales can be applied at any of the three levels. If an event has been selected by any one of its chains after the application of all prescales, then it is recorded and reconstructed.

Jet trigger

The jet trigger is an integral part of the ATLAS trigger system, processing events based on consecutively more detailed detector information at the L1, the L2 and the EF stages [126]. Jets are reconstructed by energy deposited in the hadronic and electromagnetic calorimeter subsystems. At the L1 and the L2, the fast, custom jet algorithms are used for the jets reconstruction, and the anti- k_t algorithm [127] in the four-momentum recombination scheme, which is implemented in the FASTJET [128] package is used for the jets reconstruction at the EF.

The first stage of jet trigger is the L1 calorimeter trigger system (L1Calo) [129]. Jets are reconstructed from the combined energy deposits in the LAr and tile calorimeters by this system. The collections of calorimeter cells are projected back to the nominal interaction point and is known as trigger towers. The transverse energy E_T of jet candidate is used

to compare to a set of predefined E_T thresholds for the decision of which candidates can produce an ROI. The central trigger processor (CTP) receives the information about the regions of the detector, which contain jet candidates and the generation of the L1 decision is based on that. After the L1 selection, the L2 trigger will process the events and it has access to the calorimeter cells within the ROIs identified by the L1. The extraction algorithm which contains a simple iterative cone algorithm [130] is used by the L2 jet trigger for the jets reconstruction using the full detector granularity. The L2 processing in the HLT is seeded off the L1 ROI corresponding to the jets. A hypothesis algorithm is used to test the characteristics of jet candidates to decide whether they meet the predetermined selection requirement of the L2 trigger. Various fragments which are temporarily stored in memory in the data acquisition system are used to build each event selected at the L2. The standard ATLAS event reconstruction algorithms is used at the EF for both offline analysis and final offline detector calibrations. The EF can access the full detector information due to the fact that it runs after the event builder. Similar to the reconstruction of standard offline jet, the $anti k_t$ jets are reconstructed in the complete calorimeter by the EF jet trigger. This feature allows EF triggers to select some portion of events at L1 randomly irrespective of whether any ROI is present. Any bias which is introduced by the jet reconstruction at either the L1 or the L2 stages can be avoided by triggering jet candidates in this way at the EF.

In 2011 Pb+Pb data analysis, the trigger used for selecting qualified jets is JET20. It has a nominal threshold of $p_T^{\text{jet}} > 20$ GeV and was unrescaled for the duration of the run. This trigger is seeded off the L1TE10 trigger, which is fully efficient in the centrality range analyzed, and utilized a full-scan jet reconstruction algorithm in the event filter that included elements of the background subtraction procedure used in the offline heavy-ion jet reconstruction. For the full-scan mode, the EF runs the jet finding algorithm once per event for each configured jet radius, and using data from the complete calorimeter. The primary HLT trigger requires the total transverse energy measured in calorimeter greater than 10 GeV

(TE10) at the L1 and at least one $R = 0.2$ jet with $E_T > 20$ GeV at the electromagnetic scale.

Muon trigger

The L1 muon trigger is based on signals in the muon trigger chambers: RPC's in the barrel and TGC's in the end-caps [131]. The trigger searches for patterns of hits consistent with high- p_T muons originating from the interaction region. The logic provides six independently-programmable p_T thresholds, which seed the HLT algorithms. The information for each bunch-crossing used in the L1 trigger decision is the multiplicity of muons for each of the p_T thresholds. Muons are not double-counted across the different thresholds.

The HLT is composed of the fast L2 and EF muon algorithms which rely on the software of offline muon reconstruction [121, 130, 132]. The trigger decision algorithms use the muon reconstruction result at each step of the HLT to determine whether this muon candidate can be accepted or discarded. The precision data from the MDT's is used to refine the candidate from L1 at L2. The L2 standalone algorithm (SA) has access to the data in a ROI defined by the L1 muon candidate and uses MS data within this region to construct a track. The fast fitting algorithms and Look-Up-Tables (LUTs) are used to refine and improve the muon candidate's track parameters and momentum. After the hits from the MDT are selected by a pattern recognition algorithm on a region identified by the L1, a track fit is performed using the MDT drift times. At the same time the p_T measurement is assigned from LUTs [130]. The track parameter resolution is refined by a fast track combination algorithm (CB), which combines the reconstructed tracks in the ID with the tracks found by the L2 SA. The muons from in-flight decays of light mesons or cosmic radiation will be rejected by this combination. In addition, the third algorithm, L2 isolated muon algorithm is seeded by the CB algorithm and incorporates the calorimetric and the ID tracking information to discover the isolated muon candidates. Thus there are SA, CB, and isolated three kinds of triggers at the L2.

At the EF level the full event data are accessible. The ROI identified by the L1 and the L2 is used for the start of muon reconstruction, also it uses the information from the trigger and precision chambers to reconstruct segments and tracks. A muon candidate using data only from the MS can be identified by extrapolating the track to the interaction region, resulting in the EF MS only trigger. The muon candidate is combined with the tracks from the ID to produce the EF muon combined (CB) trigger, which is similar to the L2 algorithms. Another algorithm that starts from tracks from the ID and extrapolates them to the muon detectors complements this “outside-in” strategy and resulting in the EF muon “inside-out” triggers. These three EF algorithms are all based on offline tools to reconstruct the muons online in the trigger system [130].

In the 2011 Pb+Pb data analysis, the trigger used for selecting qualified muons are MU4, which requires muon transverse momentum greater than 4 GeV at the L2. The EF trigger decision is based only on MS reconstruction, and it’s seeded off the L1TE50 with requirement of total transverse energy measured in the calorimeter greater than 50 GeV at the L1. In the 2013 *pp* data analysis, the trigger used for selecting qualified muons are the muon and jet combined trigger MU4_JET30, which is a combination of the muon trigger EF_MU4 and the jet trigger JET30. This trigger requires primary vertex and events to have one jet-muon pair (which means one muon and one jet within $\Delta R < 0.4$) with the muon and jet’s p_T of at least 4 and 30 GeV at the L2, respectively. In addition, the EF is in full-scan mode for the JET30 trigger and it’s seeded off the L1J5, which requires the transverse momentum of jet greater than 5 GeV at the L1.

Minimum bias trigger

In section 4.2.5, there is a brief introduction about the MBTS. The minimum bias events are selected by the MBTS for early runs, and the trigger provides not only energy, but also timing information. In the 2011 Pb+Pb data sample, the minimum bias events were selected using

either the MBZDC_L1VTE50 or the MB_L1TE50 triggers and they are mutually exclusive. The MBZDV_L1VTE50 indicates the total transverse energy lower than 50 GeV at the L1 and at least one neutron is required in both the A and C sides of the ZDC. In addition, the online tracking is used to search for tracks within the triggered event. At the same time, the MB_L1TE50 indicates the total transverse energy greater than 50 GeV at the L1 and there is no further event processing performed from the L1 to the HLT for this trigger. The combination is fully efficient except for the most peripheral centrality bins, which are not analyzed as part of this analysis. This trigger was prescaled throughout data taking with a luminosity-averaged scale down of approximately 20.

Chapter 5

Data Analysis

In this analysis, we present a measurement of b -jet production rates in Pb+Pb and pp collisions with center of mass energy at $\sqrt{s_{NN}} = 2.76$ TeV. The measurement is done using fully reconstructed jets using anti- k_t algorithm with $R = 0.2$ and a per-event background subtraction procedure, both of which will be described in the section 5.5.1.

5.1 2011 Pb+Pb Data samples

The experimental data used for this analysis are from 2011 Pb+Pb LHC heavy-ion runs at $\sqrt{s_{NN}} = 2.76$ TeV using jet triggers, muon triggers and minimum bias trigger. The total integrated luminosity is $140 \mu b^{-1}$. There are 42 runs in total of the full 2011 data set [133]. The event selection criteria for 2011 Pb+Pb collisions are listed as follows to select good events for this analysis:

1. Good luminosity block provided by 2011 heavy ion good run list [134].
2. At least one reconstructed primary vertex.
3. Both MBTS sides A and C record valid time, $time_A \neq 0$ and $|time_A| \neq 75$, at the same time $time_C \neq 0$ and $|time_C| \neq 75$

4. The time difference between two sides, $\Delta t_{MBTS} = |time_A - time_C|$, should be smaller than 5 ns , $\Delta t_{MBTS} < 5$.
5. For minimum bias events, they are required to pass either the MBZDC_L1VTE50 or the L1TE50 (Section 4.2.6) trigger.
6. Pass the JET20 (Section 4.2.6) trigger for jet triggered events.
7. Pass the MU4 (Section 4.2.6) trigger for muon triggered events.

The event selection criteria for 2013 pp collisions are listed in the following:

1. Good luminosity block provided by the good run list [134].
2. At least one reconstructed primary vertex.
3. Pass the MU4_JET30 (Section 4.2.6) muon jet combined trigger.

In 2011 Pb+Pb collisions, the jet trigger JET20 (Section 4.2.6) is used for jet p_T above 50 GeV, and the muon trigger MU4 (Section 4.2.6) is used for jet p_T below 50 GeV. The efficiency of MU4 is shown on Fig. 5.1 as a function of p_T in different centrality intervals and different pseudorapidity regions. The plot shows that trigger efficiency is different at the barrel (mid pseudorapidity) region and the end-cap (forward pseudorapidity) region: The latter shows a higher plateau at around 90% while the former peaks at around 78% for muon p_T at around 6 GeV. Since this trigger is a TE50 trigger which is efficient for low central bins, there are big fluctuations for very peripheral bins above 60%. When evaluating this trigger efficiency, we applied a cut of momentum balance on the muons between the track momentum measured by the inner detector and the muon spectrometer. Details about this cut and the reason for applying it will be described in section 5.3.

The reason for using different triggers for different jet p_T range is explained in the section 5.5.1

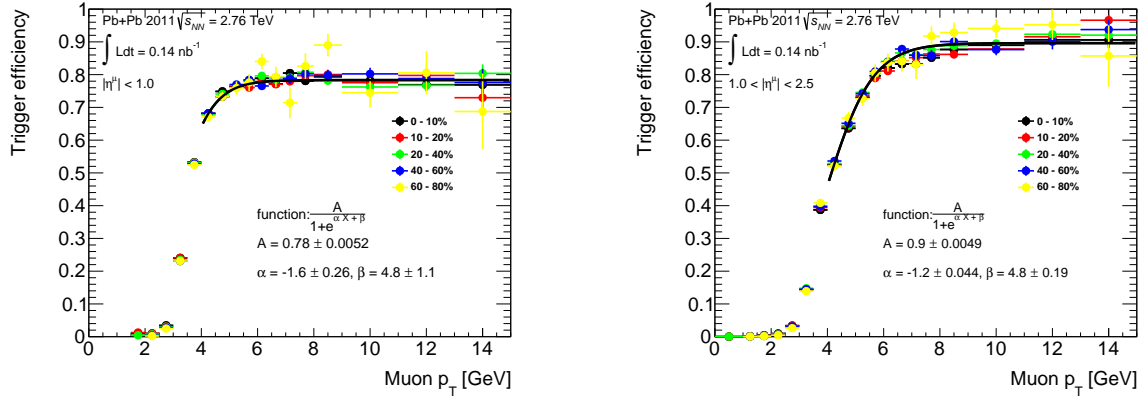


Figure 5.1: The MU4 trigger efficiency distributions in mid and forward pseudorapidity region are shown in different centrality intervals in 2011 Pb+Pb collisions.

5.2 Collision geometry and centrality definition

In this analysis, events were required to satisfy the standard heavy-ion minimum bias event selection criteria of a single reconstructed vertex and MBTS timing cut $\Delta t_{MBTS} < 5$ ns [135]. Only events recorded during luminosity blocks with good data quality were selected, with valid luminosity blocks specified in the heavy-ion 2011 good run list [134].

We define the centrality for each event in bins of the fraction of the transverse energy deposited in forward calorimeter (ΣE_T^{FCal}). The centrality definition has been applied in the 2011 Pb+Pb data analysis [135]. These intervals are expressed in percentiles of the total inelastic non-Coulomb lead-lead cross section (0-10%, 10-20%, ...60-80%), with the most central interval (0-10%) corresponding to the 10% of events with the largest values of ΣE_T^{FCal} .

An analysis of the minimum bias ΣE_T^{FCal} distribution for 2011 indicated a 4% change in the FCal energy scale relative to 2010, which is consistent with the improvements made to the energy scale calibration between 2010 and 2011. The 2011 centrality definitions were derived by simply rescaling the bin boundaries in the 2010 definition by a factor of 1.04. A standard Glauber model analysis [34, 79] of the ΣE_T^{FCal} distribution [136] was used to evaluate the average number of participating nucleons, $\langle N_{part} \rangle$, and nuclear overlap function

$\langle T_{AA} \rangle$ in each centrality interval. The centrality intervals used in this measurement are indicated in Table 5.1 along with the values of $\langle T_{AA} \rangle$ and $\langle N_{\text{part}} \rangle$ for those intervals.

Table 5.1: The $\langle T_{AA} \rangle$ and $\langle N_{\text{part}} \rangle$ values and their uncertainties in each centrality bin

Centrality(%)	$\langle T_{AA} \rangle [\text{mb}^{-1}]$	$\langle N_{\text{part}} \rangle$
0-10	23.447 ± 0.370	356.21 ± 2.163
10-20	14.426 ± 0.296	260.7 ± 3.191
20-40	6.885 ± 0.242	157.82 ± 3.694
40-60	2.017 ± 0.145	69.275 ± 3.297
60-80	0.410 ± 0.050	22.6 ± 2.1

5.3 2013 pp data samples

The pp data used in this study is from 2013 collisions at $\sqrt{s_{NN}} = 2.76$ TeV. The total collected luminosity is 4.1 pb^{-1} and it consists of six runs. The events were selected with the trigger MU4_JET30 (Section 4.2.6) which is a combination of the muon trigger EF_MU4 and the jet trigger JET30.

This trigger shows inefficiency at low muon p_T . After studying this effect, a cut on muon momentum balance is applied to remove the background of fake muons and improve the trigger efficiency performance. The momentum balance is defined as follows [137]:

$$\frac{\Delta p}{p_{ID}} = \frac{p_{ID} - p_{MS} - p_{param}(p_{MS}, \eta, \phi)}{p_{ID}} \quad (5.1)$$

where p_{ID} is the track momentum measured by the inner detector, p_{MS} is the track segment momentum measured by the muon spectrometer, $p_{param}(p_{MS}, \eta, \phi)$ is the parametrized estimation of the minimum ionizing energy loss by a muon crossing the material in the calorimeter. The parametrized estimation is preferred rather than the measured energy in the calorimeter because the muons considered are usually not isolated.

The momentum balance quantifies the momentum difference between the inner detector

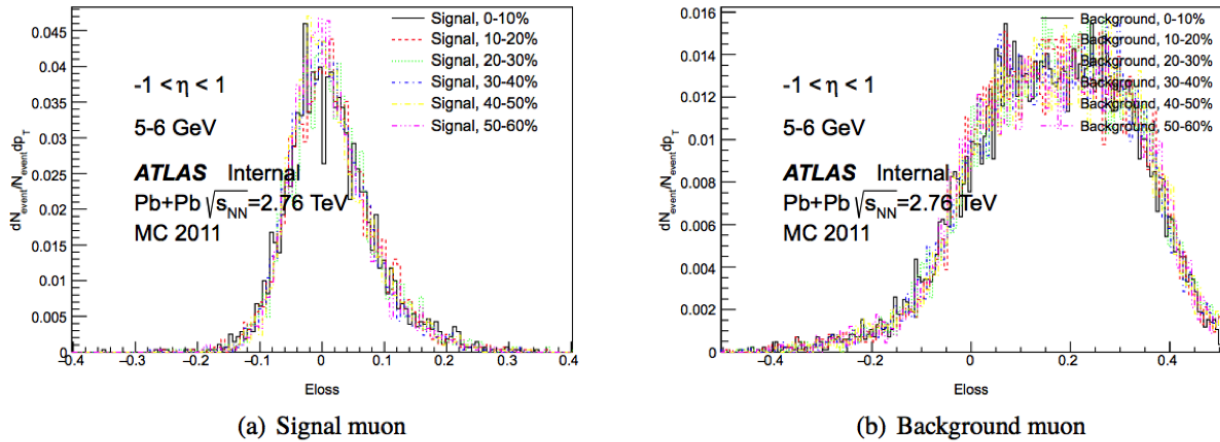


Figure 5.2: Signal muon (a) and background muon (b) momentum balance distribution in different centrality intervals from 2011 Pb+Pb MC sample. Taken from [137].

and muon spectrometer and a cut that removes the value highly deviated from zero can improve the performance of muons.

In the study of heavy flavor muon suppression in the 2011 Pb+Pb collisions [137], Fig. 5.2 shows the distribution of $\frac{\Delta p}{p_{ID}}$ (which is denoted as Eloss in the plots) in different centrality intervals. The signal muon denotes the prompt muons decayed from heavy flavor quarks (b or c), and the background muon denotes the muons decayed in-flight from other particles (pions or kaons). The $\frac{\Delta p}{p_{ID}}$ distribution shows no centrality dependence. Fig. 5.3 shows the distribution of $\frac{\Delta p}{p_{ID}}$ between the Pb+Pb 2011 data and the pp 2013 data for both signal muons and background muons. The fact that they are in agreement shows the same cut on the $\frac{\Delta p}{p_{ID}}$ can be applied to both the Pb+Pb and the pp sample.

In this analysis, we show the $\frac{\Delta p}{p_{ID}}$ distribution of different flavor jets in pp 2012 MC sample in Fig. 5.4. The flavor of jets is identified by the different sources that muons decayed from. The b -, c - and light-jets denotes muons coming from the b quark or the c quark or light mesons respectively, with details described later in section 6.3. In this analysis, b -jets are identified as signal, while other kinds of jets are classified as background. In Fig. 5.4, a cut on $\frac{\Delta p}{p_{ID}}$ at the positive side at around 0.15 can cut off almost half of the light-jet background,

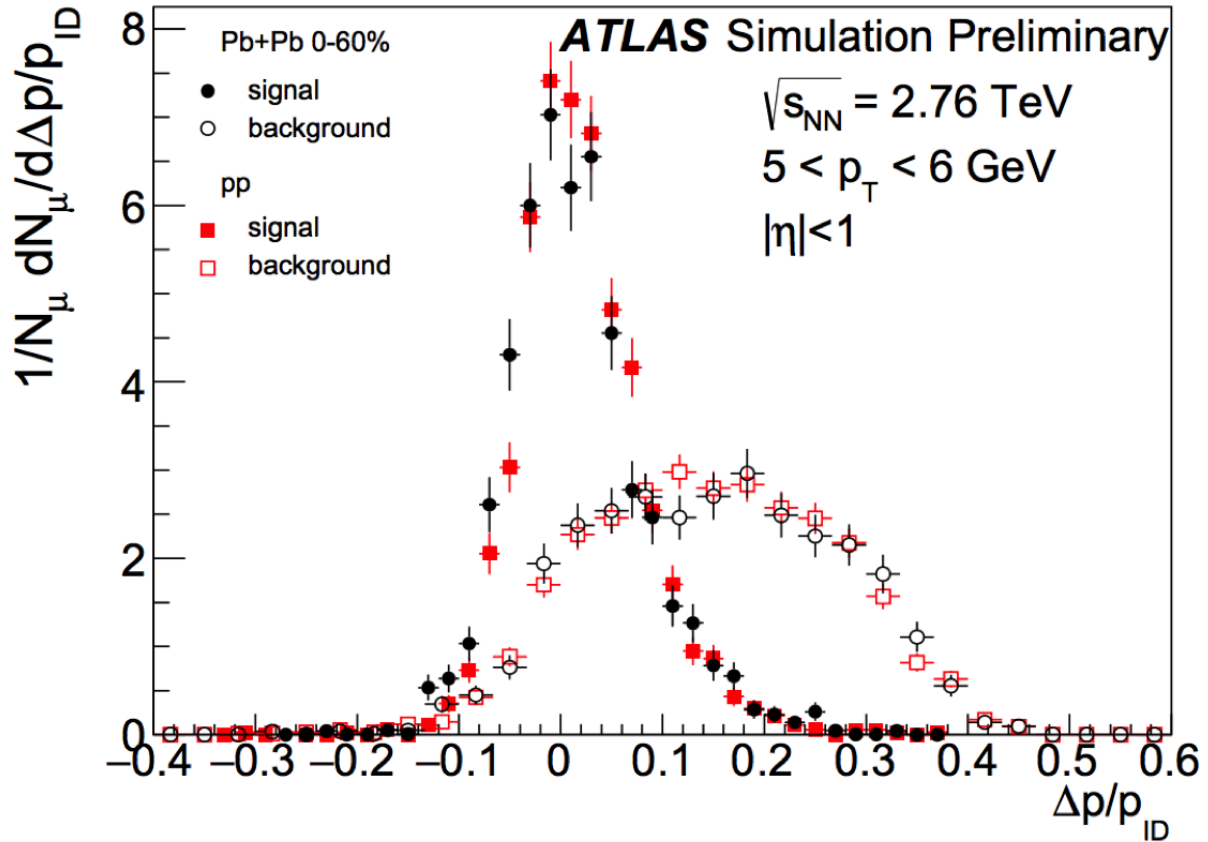


Figure 5.3: Signal and background muon momentum balance distribution in pp collisions (red points) and Pb+Pb collisions (black points) in the 0-60% centrality interval. The signal and background distributions are separately normalized such that their integral is unity. The background distribution is binned more coarsely because of the limited statistics available in the background sample. Taken from [137].

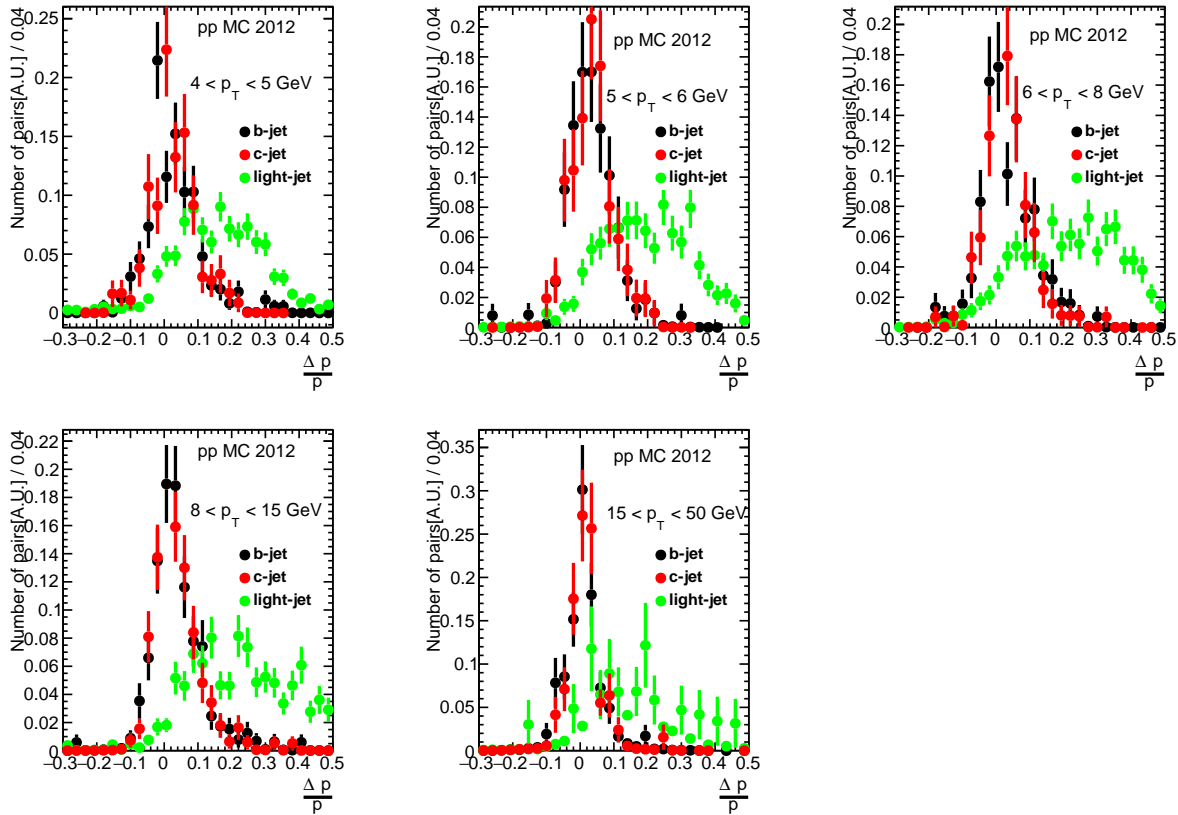


Figure 5.4: $\frac{\Delta p}{p_{ID}}$ distribution for b -, c - and light-jets in different muon transverse momentum p_T intervals in the 2012 pp MC sample.

and keep most of the b -jet template for study.

Due to the fact that b -jet and c -jet have very similar $\frac{\Delta p}{p_{ID}}$ distribution and the shape resembles gaussian distribution, these two contributions are combined to be fitted to a gaussian function, and the σ values at each muon p_T interval are shown in the following table:

Table 5.2: σ of the gaussian fit of $\frac{\Delta p}{p_{ID}}$ distribution from b, c - jets

p_T^{muon} GeV	4-5	5-6	6-8	8-15	15- 50
σ	0.05	0.052	0.049	0.05	0.055

We applied a cut on the $\frac{\Delta p}{p_{ID}}$ with the value of 2.5σ for each muon p_T interval with the σ value from table 5.2. The specific 2.5 is chosen because it can remove the background muons

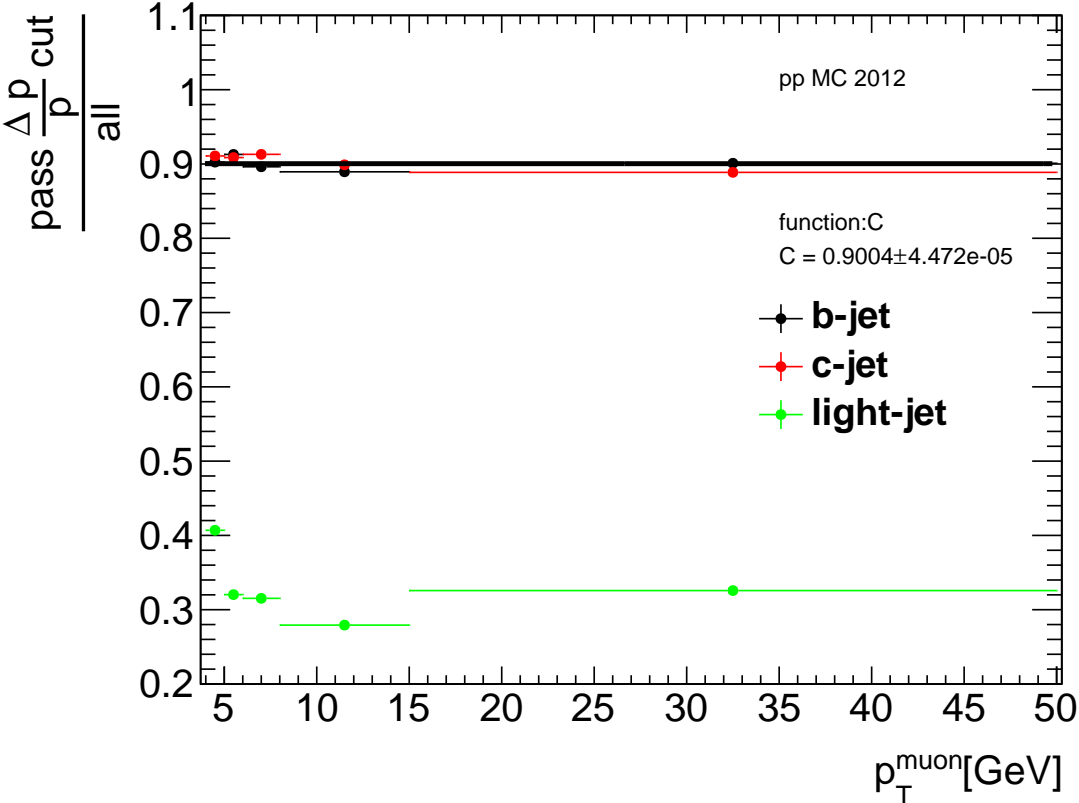


Figure 5.5: Fraction for b -, c - and light-jets that pass the $\frac{\Delta p}{p_{ID}}$ cut as a function of muon p_T in the 2012 pp MC sample.

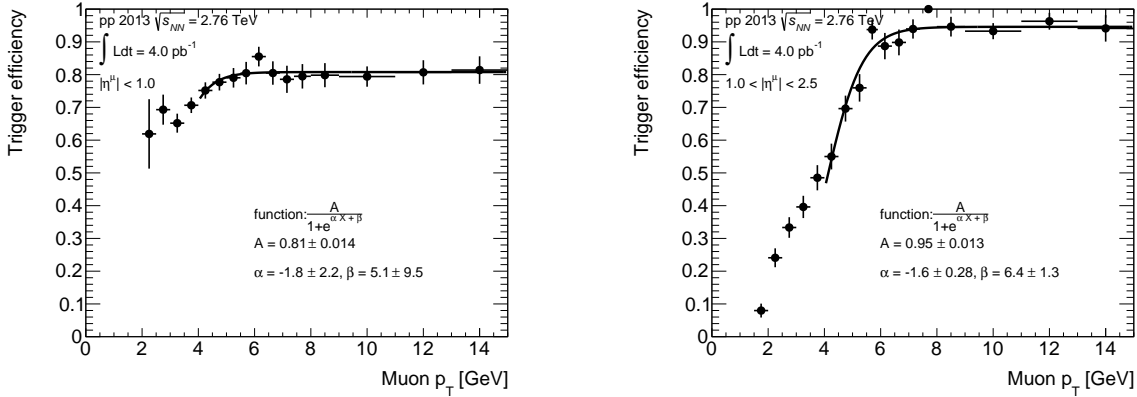


Figure 5.6: The MU4_JET30 efficiency distributions at the L1 level in the mid and the forward pseudorapidity region are shown on the left and right, respectively, in 2013 pp collisions.

and improve the MU4_JET30 trigger efficiency effectively. Fig. 5.5 shows the fraction of different flavor of jets that pass the $\frac{\Delta p}{p_{ID}}$ cut, the b -jets exhibit flat fraction distribution as a function of muon p_T . This fraction is fitted with a constant, with the fitted value being 0.90, and the final b -jets yield will be corrected with this value. Since the cut of $\frac{\Delta p}{p_{ID}}$ is necessary for this study, it will be applied throughout the following analysis.

Fig. 5.6 and 5.7 show the MU4_JET30 trigger efficiency as a function of p_T in the mid and forward-pseudorapidity region at the L1 and HLT level separately. We can see the efficiency at the L1 level reaches a plateau of 0.81 for the mid pseudorapidity and reaches a plateau of 0.95 for the forward pseudorapidity for muon transverse momentum p_T above 6 GeV, while for the HLT level it reaches a plateau of 0.97 for the mid pseudorapidity and reaches a plateau of 0.98 for the forward pseudorapidity. The final combined trigger efficiency in pp is shown in Fig. 5.8, which is the product of these two efficiencies at the L1 and HLT level.

The average number of pp collisions in a typical crossing (pile-up) was small during this data taking, and varied between 0.3 and 0.6.

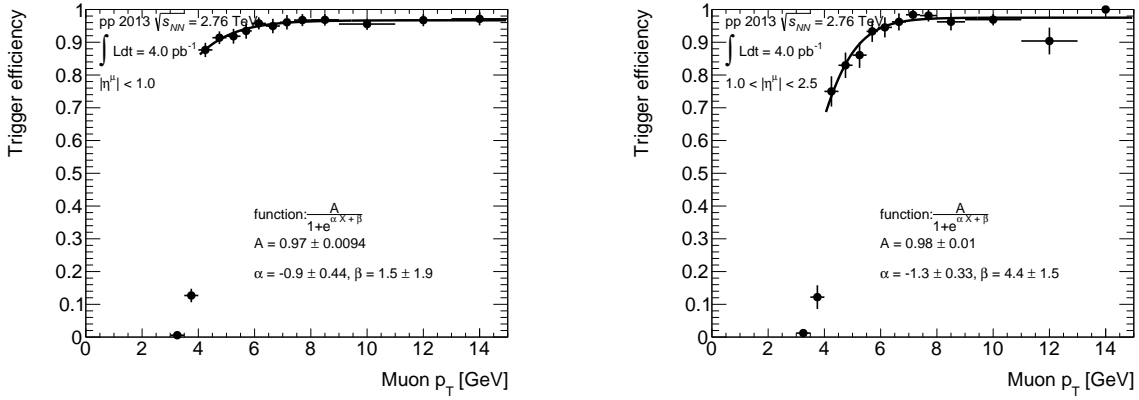


Figure 5.7: The MU4_JET30 trigger efficiency distributions at HLT in mid and forward pseudorapidity region are shown on the left and right, respectively, in 2013 pp collisions.

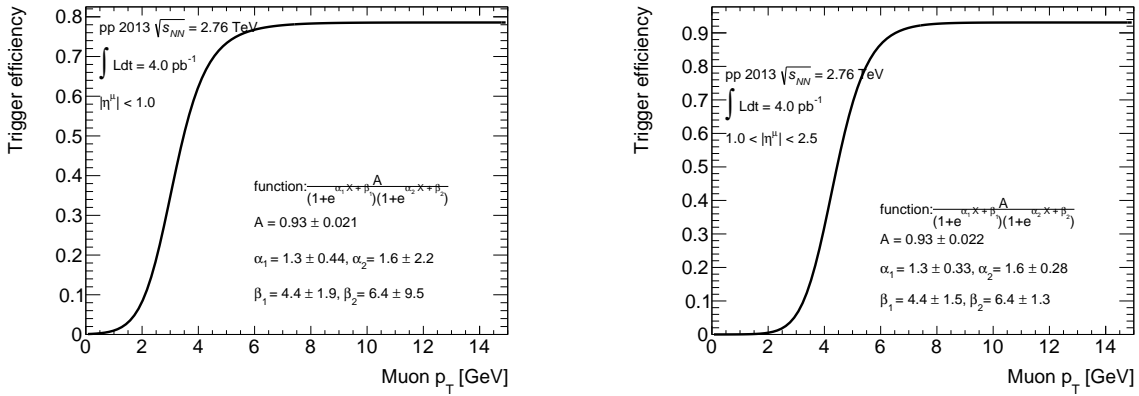


Figure 5.8: The MU4_JET30 trigger efficiency distributions in the mid and the forward pseudorapidity region are shown on the left and right, respectively, in 2013 pp collisions.

5.4 Monte Carlo Simulation

Monte Carlo (MC) samples used in the Pb+Pb analysis were generated by combining minimum bias Pb+Pb data with PYTHIA [138] dijet samples and performing reconstruction on the combined signal. There are two MC samples used in this analysis, one is an inclusive sample used for the background light jet template building. The second is a muon filtered sample used for the signal b -jet and background c -jet template building. The J1 to J3 dijet samples are sampled with non-overlapping \hat{p}_T (parton p_T) between 17 GeV and 140 GeV. The J1-J3 muon-filtered dijet samples, referred to as the $JX\mu$ dijet samples, are required to have a muon with $p_T > 3.5$ GeV in addition. These $JX\mu$ samples thus contain muons from b - and c -decays, but they do not simulate realistically muons from in-flight decays since pions and kaons are treated as stable particles on generator level. The contribution from muons produced in hadronic showers in calorimeter is also absent for this reason. Table 5.3 shows the Pb+Pb MC samples used and their properties.

Table 5.3: MC samples used in Pb+Pb

Sample	Number of events	Cross section[nb]	Filter efficiency	\hat{p}_T range
J1 dijet	4500000	1.8760e+05	1.0	$17 < \hat{p}_T < 35$ GeV
J2 dijet	4500000	8.2787e+03	1.0	$35 < \hat{p}_T < 70$ GeV
J3 dijet	4500000	2.9419e+02	1.0	$70 < \hat{p}_T < 140$ GeV
J1 μ dijet	650000	1.8760e+05	6.6523e-03	$17 < \hat{p}_T < 35$ GeV
J2 μ dijet	650000	8.2787e+03	1.4941e-02	$35 < \hat{p}_T < 70$ GeV
J3 μ dijet	650000	2.9419e+02	2.4284e-02	$70 < \hat{p}_T < 140$ GeV

A separate PYTHIA MC sample was produced for the pp cross section analysis. This sample utilized the same generator and tune but was simulated with the 2013 detector conditions. The small pile-up contribution in pp collisions was accounted for by overlaying the signed events at the same rate as present in the data. Table 5.4 shows the pp samples used and their properties.

Table 5.4: MC samples used in pp

Sample	Number of events	Cross section[nb]	Filter efficiency	\hat{p}_T range
JZ1 dijet	5000000	2.6664e+06	1.4737e-04	$20 < \hat{p}_T < 80$ GeV
JZ2 dijet	5000000	3.2262e+03	6.8739e-04	$80 < \hat{p}_T < 200$ GeV
JZ1 μ dijet	400000	2.6664E+06	6.6523E-03	$17 < \hat{p}_T < 35$ GeV
JZ2 μ dijet	400000	3.2262E+03	1.4941E-02	$35 < \hat{p}_T < 70$ GeV
JZ3 μ dijet	400000	3.3335E+01	2.4284E-02	$70 < \hat{p}_T < 140$ GeV

5.5 Jet Reconstruction and Performance

5.5.1 Jet Reconstruction

Jets are generally defined by the energy deposition from hadrons in different calorimeters (electromagnetic and hadronic calorimeters). The topological clustering algorithm is applied for clustering the energy in each calorimeter cells. The anti- k_t clustering algorithm [127] applied to calorimeter towers of size $\Delta\eta \times \Delta\phi = 0.1 \times 0.1$ are commonly used in ATLAS. Clustering different proto-jet objects sequentially with their four momentum p_i^μ is the crucial principle of this algorithm. The decision for grouping each calorimeter cells is based on the measurement of distance between two proto-jets objects d_{ij} , and the distance between each single proto-jet and the beam d_{iB} . The d_{ij} and d_{iB} are defined in the following:

$$d_{ij} = \min\left(\frac{1}{k_{Ti}^2}, \frac{1}{k_{Tj}^2}\right) \left(\frac{(y_i - y_j)^2 + (\phi_i - \phi_j)^2}{R^2} \right), \quad (5.2)$$

$$d_{iB} = \frac{1}{k_{Ti}^2}.$$

Here the y denotes the rapidity of the proto-jet, k_T denotes the transverse energy and R denotes the cutoff cone radius parameter in y and ϕ space. For each proto-jet, the comparison among different d_{ij} and d_{iB} is made for clustering decisions: if a d_{ij} is the minimum among all the distances, the i and j jets are combined as one jet and start over, while if the minimum is d_{iB} , the object is classified as a jet and removed from the subsequent clustering. The

distances are recalculated and the procedure repeated until no jets are left.

The candidates for proto-jet can be calorimeter clusters or tracks, with the jets named *calorimeter jets* or *track jets*, respectively. Tracks are used when the analysis focuses on the structure of the jet, like in boosted final states. Only the calorimeter jets are considered in this analysis.

Jets generated by this algorithm are near the largest energy deposits. The radius parameter R of the jets restricts the amount of the smaller energy deposits around added in the clustering procedure.

Subtraction

In Pb+Pb collisions, the calorimetric measurement of jet transverse energy E_T contains both the real signal of jet and the underlying event (UE) contributions [139]. A background subtraction technique is introduced to correct jet kinematics for the presence of an uncorrelated UE within the jet cone. This technique is applied per calorimeter sampling layer in order to take the variation of detector response in different longitudinal layers into account. For each layer i , the background transverse energy density $\rho_i(\eta, \phi)$ is defined to describe the UE distribution. For each cell clustered within the jet, the background was evaluated at the cell's coordinates. The cell's energy is corrected as follows:

$$E_T^{cell} \Big|_{\text{subtracted}} = E_T^{cell} \Big|_{\text{unsubtracted}} - \rho_i^{cell}(\eta^{cell}, \phi^{cell}) \Delta\eta^{cell} \Delta\phi^{cell} \quad (5.3)$$

The UE contribution to jets is subtracted on an event-by-event basis at the cell level since UE can vary over a wide range of magnitude. The background transverse energy density is estimated as:

$$\rho_i(\eta, \phi) = \varrho_i(\eta)[1 + 2v_2 \cos(2(\phi - \Phi_2))] \quad (5.4)$$

where v_2 is the second Fourier coefficient of the Fourier decomposition of the angular distribution of particles [140], and it is used to describe the anisotropy of the distribution and provides sensitivity to the correlations in the UE. Φ_2 denotes the event plane angle and $\rho_i(\eta) = \langle \frac{dE_{Ti}|_{\text{unsubtracted}}}{d\eta d\phi} \rangle$ denotes the average E_{Ti} density measured in layer i with the full azimuth range of 2π . The four vector sum of the individual cell four vectors is used to determine the jet's four vector, which were taken to be massless.

The subtraction will introduce a bias to the jet energy if the energy of a jet itself is allowed to contribute to the calculation of ρ . The background will be overestimated, and this leads to the jet being applied with an over-subtraction. This effect is called self-energy bias. The jet energy scale (JES) can be shifted by nearly 10% for the jets which are associated by the self-energy bias. Starting from the reprocessing of the data in 2010, an iterative background determination procedure is applied to address this problem. Additional jet collections were introduced with extra iteration step during the reprocessing of the 2011 data. This method effectively reduces the residual self-energy bias in both the background and the subtracted jets at the analysis stage. In addition, the reconstructed jets were required to pass the UE jet rejection which rejects the background that is falsely reconstructed as jets. This requirement suppresses the contribution from UE fluctuations to the jet spectrum [133].

This anti- k_t algorithm with radius parameter $R = 0.2$ jet is used in this analysis since the UE contribution is much lower compared to $R = 0.3$ or 0.4 jets (UE contribution is proportional to the jet area [141]). Thus the performance of E_T measurement is better for the smaller R values.

Calibration

The calibration is applied for jets produced in Pb+Pb collisions to account for the inefficiencies in the energy measurement of calorimeters. Due to the non-compensation of the hadronic calorimeter, the EM+JES calibration scheme applies corrections as a multiplicative

factor depending on the jet energy (p_T) and pseudorapidity (η) to jets reconstructed at the electromagnetic scale. Numerical Inversion procedure can be applied to get these factors from MC for heavy ion jets using the same procedure as pp jets reconstruction [142].

A final cross calibration, that accounts for the residual differences in the calorimetric response between data and Monte Carlo has been applied to data. In pp collisions, the events where jets are measured while recoiling against objects whose energy scale is well known are used for the so called *insitu* studies. The difference between the recoil of the jet with respect to the reference object in data sample and MC sample is used as a final correction. The cross calibration was defined where heavy ion jets and pp jets are compared in the same events in 2012 8 TeV pp data where the pp JES has been studied the most largely. The cross calibration factors are defined in the same way as the standard *insitu* factors by comparing the energies of these two kinds of jets in data and MC, respectively, except that the pp jets were used as a reference in the cross calibration case. The calibration of heavy-ion jets is described in details in Ref. [143].

Jet selection

Jet selection requirements are:

1. $p_T > 30$ GeV
2. $|\eta| < 2.1$
3. Have highest p_T of all the jets within cone size $\Delta R < 0.8$ of itself (isolation cut)
4. Match to jet fires the jet trigger ($\Delta R < 0.4$)

In addition, since the calorimetric jet's η position is not corrected for to account for displacement of the primary vertex, truth jets from MC samples are used to study the jet angular resolution and improve the jet position measurement.

5.5.2 Jet Performance

Jet pseudorapidity correction

The procedure for jet η position correction from previous section. 5.5.1 finds the relationship between the $\Delta\eta$ and the primary vertex displacement position vx_z , where the $\Delta\eta$ is defined as the difference between the reconstructed jet η and the truth jet η . Normally it is a linear relationship that the average value of $\Delta\eta$ increases when vx_z goes up, the slope of this linear relationship depends on which jet η or p_T bin it belongs to. Since it is symmetric for jet η distribution, we focus on the slope variation in different jet $|\eta|$ bins.

Fig. 5.11 shows the relationship in different jet p_T and $|\eta|$ bins, and from the plots we can see that it depends more on jet $|\eta|$ than p_T . The black points are $\Delta\eta$ mean value in each vx_z bin, and linear function is used to fit this relationship for vx_z within -100 mm and 100mm, and the slope is extracted from the fit. Fig. 5.12 upper plots shows linear dependence between slope and jet p_T . The lower plot shows linear dependence for jet $|\eta| < 2.0$, and for the very forward pseudorapidity region where $|\eta| > 2.0$, the relationship is complicated and the slope remains 0.0002. We applied a correction to calorimetric jet η distribution to account for the influence caused by the displacement of the primary vertex, and this correction can be described as follows:

$$\eta_{\text{jet}}^{\text{correct}} = \begin{cases} \eta_{\text{jet}}^{\text{original}} - \text{slope}(\eta_{\text{jet}}^{\text{original}}) \times vx_z & \text{if } |\eta_{\text{jet}}^{\text{original}}| \leq 2.0 \\ \eta_{\text{jet}}^{\text{original}} - 0.000218 \times vx_z & \text{if } |\eta_{\text{jet}}^{\text{original}}| > 2.0 \end{cases} \quad (5.5)$$

The comparison between the jet η resolution before and after this correction will be shown in section. 5.5.2.

Jet angular resolution

This section focuses on the study of jet angular resolution in different centrality intervals for calorimetric jets.

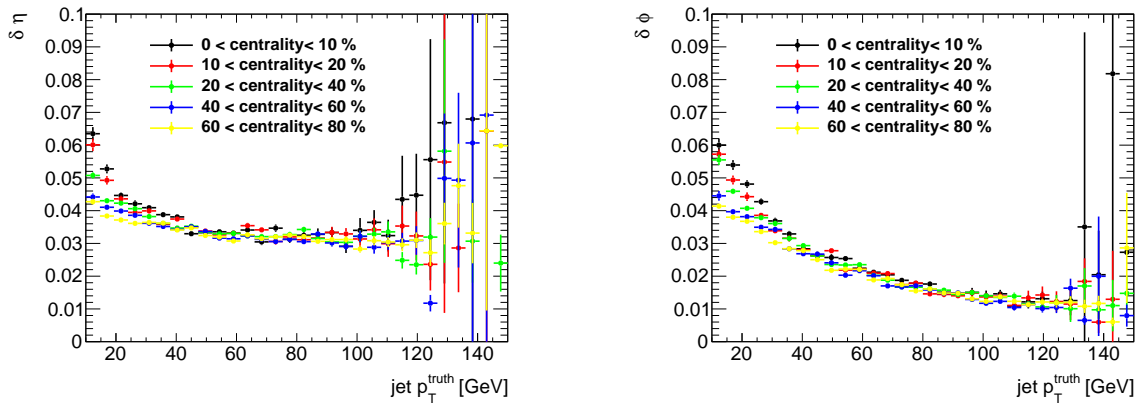


Figure 5.9: Left: Jet η and Right: Jet ϕ resolution distribution for the full jet p_T range.

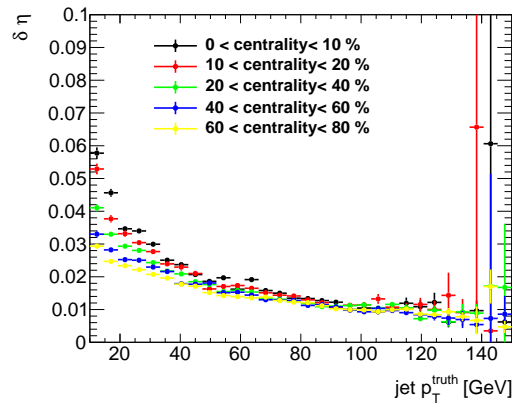


Figure 5.10: Jet η resolution distribution with vertex correction for the full jet p_T range.

Fig. 5.9 presents η and ϕ resolution separately.

The resolution is the standard deviation σ from the gaussian fit result of the 2D distribution of $\Delta\eta$ vs truth jet p_T and $\Delta\phi$ vs truth jet p_T . We can see the resolution of calorimetric jets has strong centrality dependence for low jet p_T range, which proves what we have got on Fig. 6.18. Fig. 5.10 shows the jet η resolution after primary vertex displacement correction, where the resolution becomes better especially for the high jet p_T region. Compared to Fig. 5.9, the resolution is improved by almost a factor of 2.

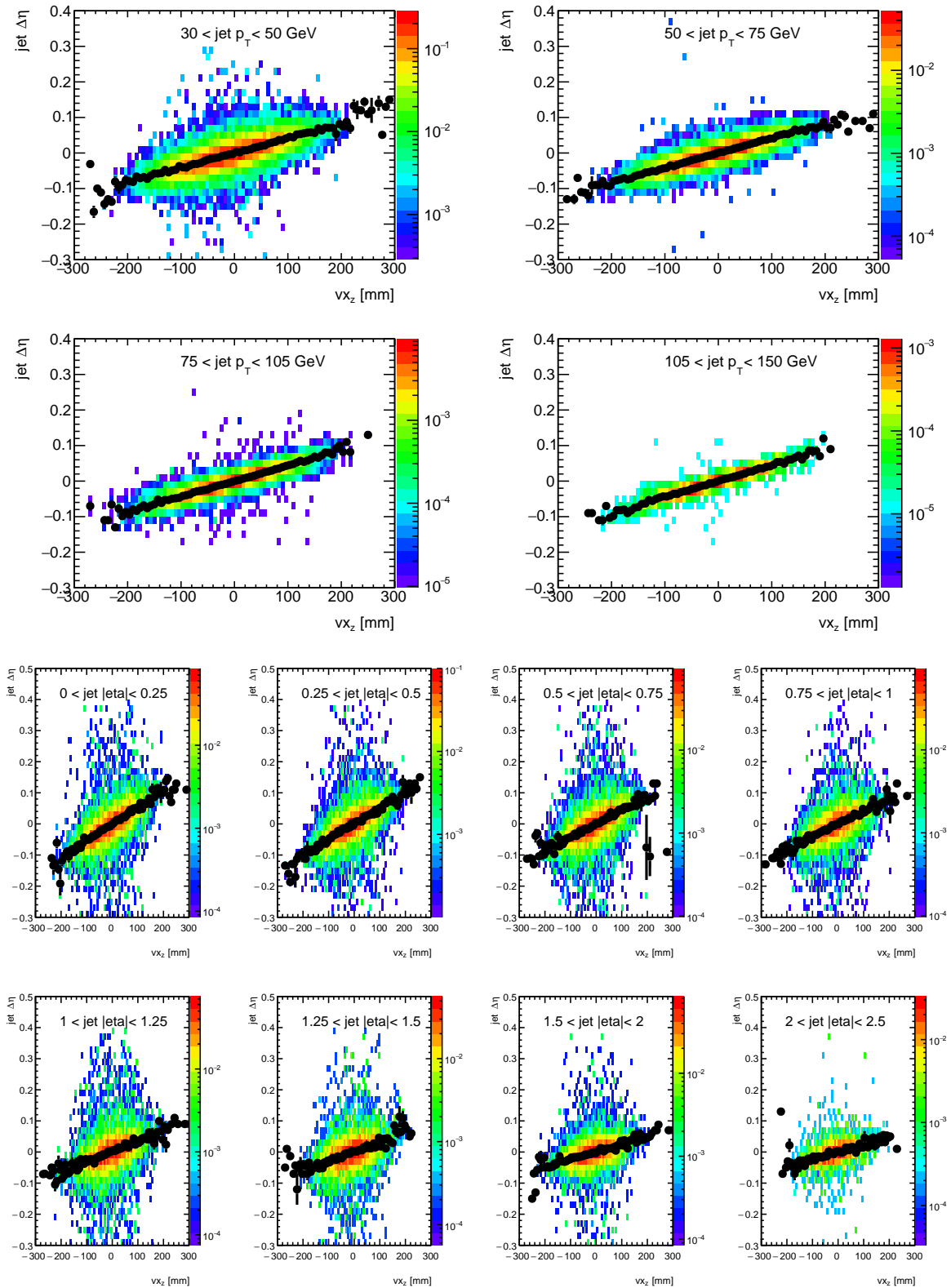


Figure 5.11: The relationship between jet $\Delta\eta$ and vx_z in different jet top : p_T and bottom: $|\eta|$ bins in MC sample for the full centrality range.

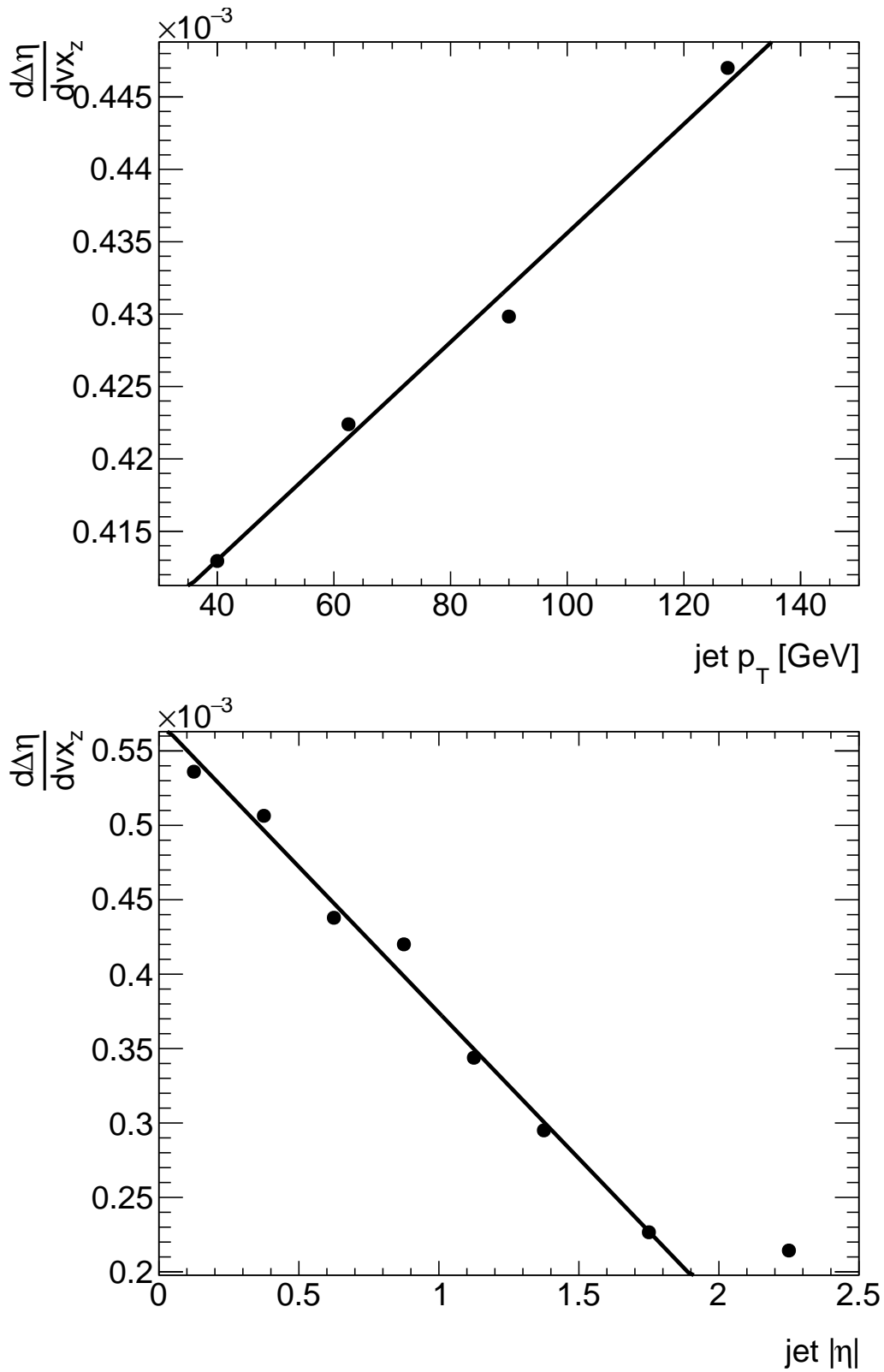


Figure 5.12: The relationship between jet $\Delta\eta$ and vx_z as a function of jet top: p_T and bottom: $|\eta|$ used for jet η correction in MC sample for the full centrality range.

General kinematics of jet

This section presents general kinematics performance of jets, such as their transverse momentum p_T and pseudorapidity η distribution. The left side of Fig. 5.13 shows jet p_T distribution for jet triggered sample. The spectrum starts to drop for jet p_T below 40 GeV because of the jet trigger (JET20) inefficiency for that range. Muon trigger MU4 is used to correct for that inefficiency. The left side of Fig. 5.14 shows jet transverse momentum p_T distribution from this muon triggered sample, which goes up for the lower jet p_T range. The comparison between jet p_T distribution from jet triggered events and muon triggered events is shown on the right side of Fig. 5.14, the muon triggered sample has a momentum spectrum lower than jet triggered sample in general due to the muon trigger efficiency is less than 1 (Section 5.1). Therefore, we correct muon triggered sample by the muon trigger efficiency, so that it can provide productive measurement for low jet transverse momentum range. Thus it is used for $30 < \text{jet } p_T < 50$ GeV bin in this analysis, while the other bins use jet triggered sample.

The right side of Fig. 5.13 shows the pseudorapidity η distribution of selected jets from jet triggered sample. Since the inefficiency of jet trigger does not depend on η , η distribution is symmetric around zero and smooth, except the hole region ($|\eta| < 0.1$) and the region between barrel and end-cap transition ($|\eta| \sim 1.05$), where the acceptance is low.

For jets in the 2013 pp sample, we include the following requirement, in addition to the same jet reconstruction requirements as the Pb+Pb data sample:

1. `antikt2HIItrEM_isUgly` is equal to false
2. `antikt2HIItrEM_isBadMedium` is equal to false

These cuts remove the jet candidates that are not originated from the hard-scatter primary vertex of interest in the event. Instead they can come from protons interacting with the residual beam gas or in the beam halo, and electronic noise in the calorimeter. The cuts ensure the quality of the reconstructed jets and Fig. 6.24 shows the kinematics distribution

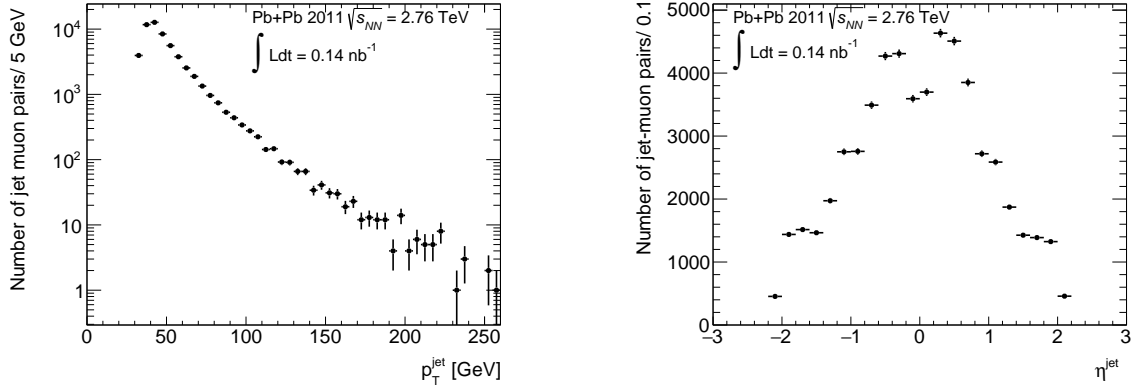


Figure 5.13: The jet transverse momentum p_T and pseudorapidity η distributions from selected jet muon pairs are shown on the left and right, respectively, in 2011 Pb+Pb collisions for the full centrality range.

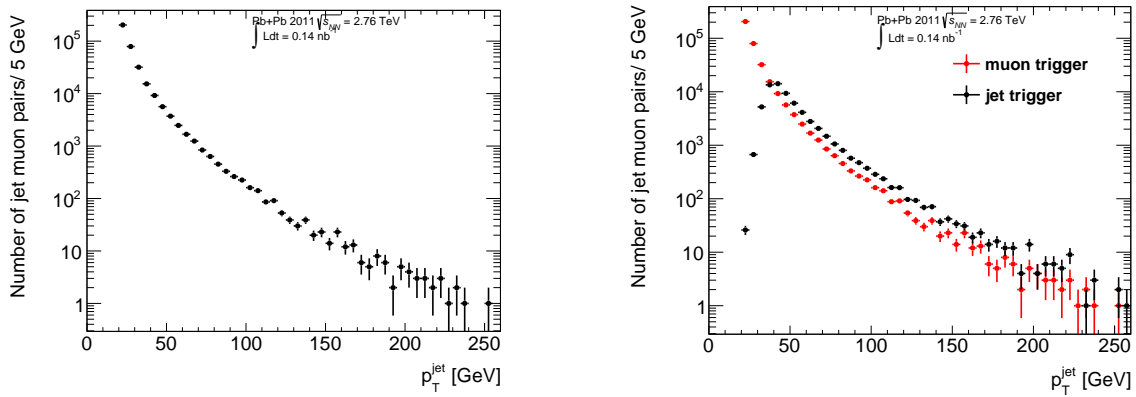


Figure 5.14: The jet transverse momentum p_T distributions from selected jet muon pairs in 2011 Pb+Pb muon triggered sample for the full centrality range on the left and jet p_T comparison between jet trigger and muon trigger sample on the right.

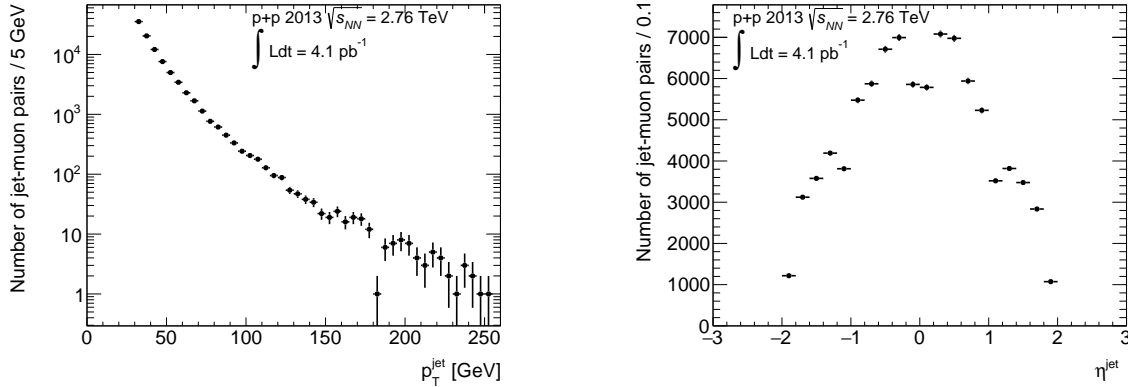


Figure 5.15: The jet transverse momentum p_T and pseudorapidity η distributions from selected jet muon pairs are shown on the left and right, respectively, in 2013 pp collisions.

from selected jets in 2013 pp sample. The left side of Fig. 6.24 shows the jet transverse momentum distribution is smooth and efficient for low jet p_T range.

5.6 Muon Selection and Reconstruction Efficiency

5.6.1 Muon Reconstruction

As discussed in section. 4.2.3, muons are reconstructed by matching tracks from the muon spectrometer (MS) to a track in the inner detector. The TGC and RPC measure the information in muon direction except for the deflection in magnetic field. The measurement of deflection is covered by the MDT and the CSC components in the MS and they provide improvement in measurement of muon's energy and momentum. The combination of different information from the MS, the inner detector and calorimeters produces four different kinds of reconstructed muons.

Stand-alone muon (SA): Only the hits in the MS are used for SA muon reconstruction. They are used for the reconstruction of muon with the pseudorapidity range of $2.5 < |\eta| < 2.7$ covered only by MS. Combined muon (CB): The hits in the MS and inner detector are both used for CB muon reconstruction. CB muons are required to match the tracks reconstructed

in these two detectors and make up most part of the reconstructed muons. Therefore they are chosen to be the muon candidates analyzed in this thesis. Segment-tagged muon (ST): Reconstructed tracks in the inner detector that are matched to hits or track segments in the MS are used for ST muons reconstruction. They provide good measurement for low p_T muons or those in a low-acceptance region of the MS. Calorimeter-tagged muon (CaloTag): A track reconstructed in the inner detector are used for CaloTag muons reconstruction if the hypothesis of a minimum ionizing muon is consistent with the associated energy deposit in the calorimeter. They provide measurement for the pseudorapidity range of $|\eta| < 0.1$ in the MS.

There are two chains for the muon reconstruction based on the tracks in the MS: Staco and Muid [144], and they provide different strategies for each specific type of reconstructed muons. The track segments in the MS are built first and combined into full tracks for both chains. To combine MS tracks with inner detector tracks for CB muon reconstruction, Muid performs a fit of the information used to reconstruct the MS track starting with inner detector track, while Staco provides a statistical combination of the two tracks weighted by their covariance matrices. Muid is used in this analysis.

Reconstructed muons are required to have [145] for both Pb+Pb and pp data sample:

1. Combined Muon
2. $p_T > 4$ GeV
3. $|\eta| < 2.5$
4. Number of pixel hits greater or equal to one
5. Number of B layer hits greater or equal to one
6. Number of SCT hits greater or equal to seven
7. The sum of pixel holes and SCT holes less than two

8. No SCT holes
9. $|d0_{PV}| < 5\text{mm}$, $|z0_{PV}| < 5\text{mm}$
10. Momentum measured by ID $p_{id} > 3\text{ GeV}$, momentum measured by MS $p_{me} > 0.1\text{ GeV}$
11. Match $\chi^2/\text{ndof} < 10$

5.6.2 Muon reconstruction efficiency

The muon reconstruction efficiency is calculated using information in the MC sample as follows:

$$\epsilon_{muon_reco} = \frac{\#\text{reconstructed muons matched to truth muon}}{\#\text{true muons}}. \quad (5.6)$$

True muons are all truth muons with $|\eta| < 2.5$. Reconstructed muons are those that satisfies the reconstruction cuts as listed in the section. 5.6.1. The resulting muon reconstruction efficiency as a function of the truth muon p_T in different centrality intervals is shown in Fig. 5.16 for Pb+Pb sample and in Fig. 5.17 for pp sample. The efficiency reaches the plateau of 80% very quickly at around muon $p_T > 6\text{ GeV}$ and shows little centrality dependence.

5.6.3 Muon performance

Fig. 5.18 and 5.19 shows kinematics distribution for muon after reconstruction selection for the Pb+Pb and the pp sample respectively. In the Pb+Pb sample, the muon transverse momentum p_T distribution (left side of Fig. 5.18) from jet triggered events decreases smoothly as the muon p_T increases, since the jet trigger inefficiency does not depend on muon momentum spectrum, the muon p_T is not biased. The pseudorapidity η distribution (left side of Fig. 5.18) shows same feature as jet η distribution 5.13. In pp sample, the muon transverse

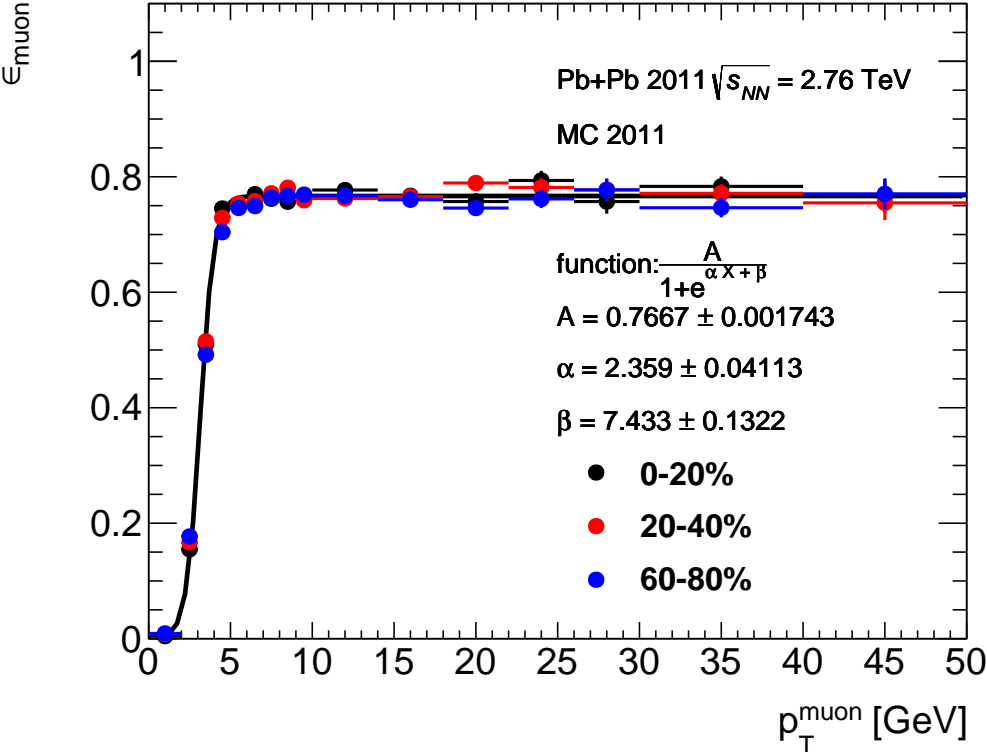


Figure 5.16: Muon reconstruction efficiency in different centrality intervals in the Pb+Pb sample.

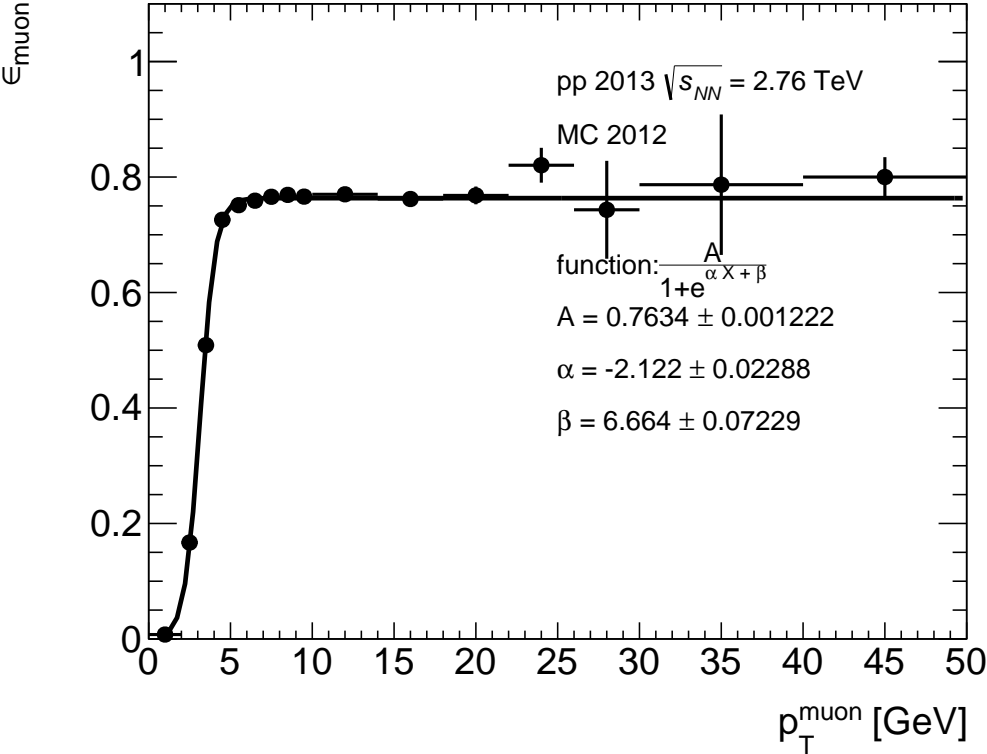


Figure 5.17: Muon reconstruction efficiency in the pp sample.

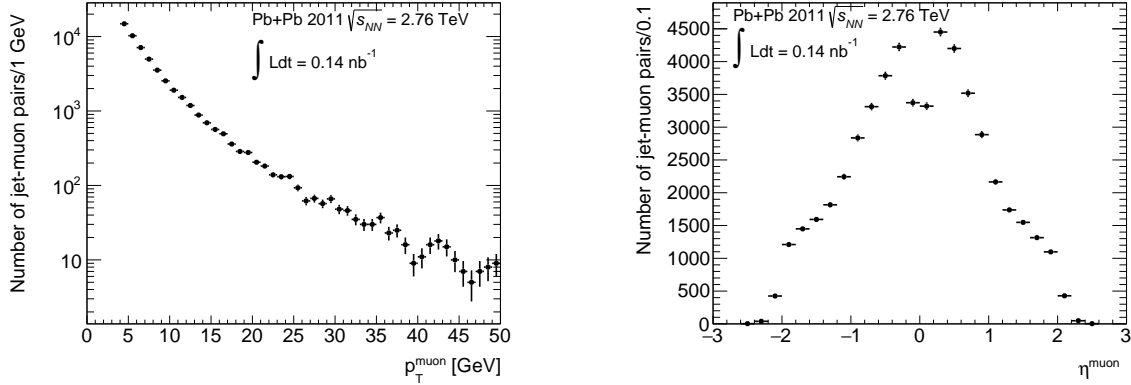


Figure 5.18: The muon transverse momentum p_T and pseudorapidity η distributions from selected jet muon pairs are shown on the left and right, respectively, in 2011 Pb+Pb collisions for the full centrality range.

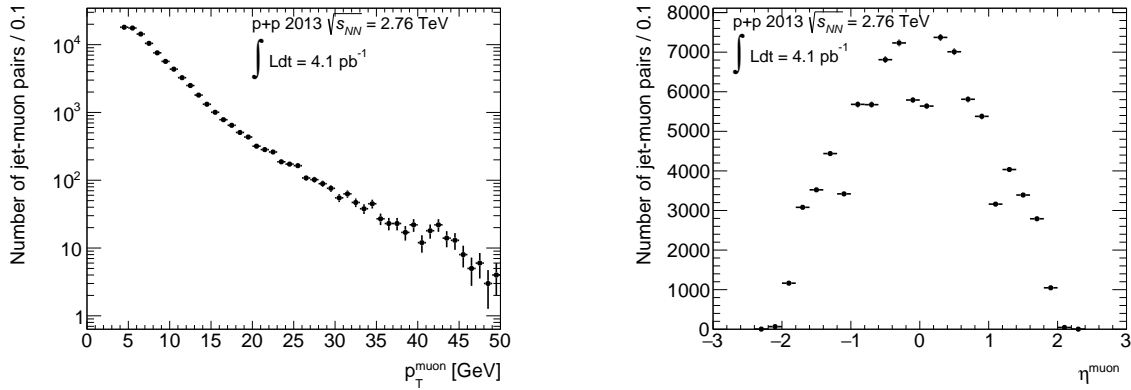


Figure 5.19: The muon transverse momentum p_T and pseudorapidity η distributions from selected jet muon pairs are shown on the left and right, respectively, in 2013 pp collisions.

momentum p_T distribution (left side of Fig. 5.19) starts to drop for low muon p_T region (< 5 GeV), because of the inefficiency of the EF_MU4 muon trigger, which is embedded in the muon jet combined trigger (MU4_JET30) used in pp sample.

Chapter 6

B-tagging Analysis

6.1 p_T^{rel} analysis

The flavor of jets is identified using muons that associated with the jets and the b -fraction is extracted from a template analysis of the p_T^{rel} distribution. The p_T^{rel} [146] is the momentum of the muon relative to the jet axis, it is expressed as:

$$p_T^{\text{rel}} = \frac{|\vec{p}^\mu \times \vec{p}^{\text{jet}}|}{\vec{p}^{\text{jet}}} \quad (6.1)$$

where \vec{p}^μ is the muon momentum and the \vec{p}^{jet} is the jet momentum. The p_T^{rel} distribution for b -jets is generally broader due to the effect of the large b mass on the decay kinematics. The measurement of b -jet suppression is carried out within an pseudorapidity region of $|\eta| < 2.1$, and in four bins of jet transverse momentum p_T in the range of $30 \text{ GeV} < p_T^{b\text{-jet}} < 150 \text{ GeV}$.

6.2 Jet Muon Pair Selection

This measurement is performed by analyzing jet muon pair distribution after passing all the selection requirements mentioned above (section. 5.5.1, 5.6.1). Pairs are formed from

selected jets and muons within $\Delta R < 0.4$.

Fig. 5.13 - 5.18 show basic kinematics distributions for the pairs in the Pb+Pb data. At last there are 48800 jet muon pairs from the Pb+Pb sample and 64679 jet muon pairs from the pp sample passing all requirements. Table 6.1 shows the number of jet muon pairs in each jet transverse momentum p_T bin used in this analysis.

Table 6.1: Number of jet muon pairs after jet and muon selection

Jet p_T	Centrality(%)	0-10	10-20	20-40	40-60	60-80	pp
30-50		15099	9317	9421	3240	752	53361
50-75		3083	2208	2349	853	177	9229
75-105		637	421	484	183	44	1627
105-150		153	122	118			417

In order to take the difference of spectrum between MC and data into account, the ratio of jet transverse momentum p_T from data over MC is shown in Fig. 6.1 in Pb+Pb and pp samples, respectively. The linear function is used to fit to the ratio distribution and it is applied as weight when building the templates from the MC sample.

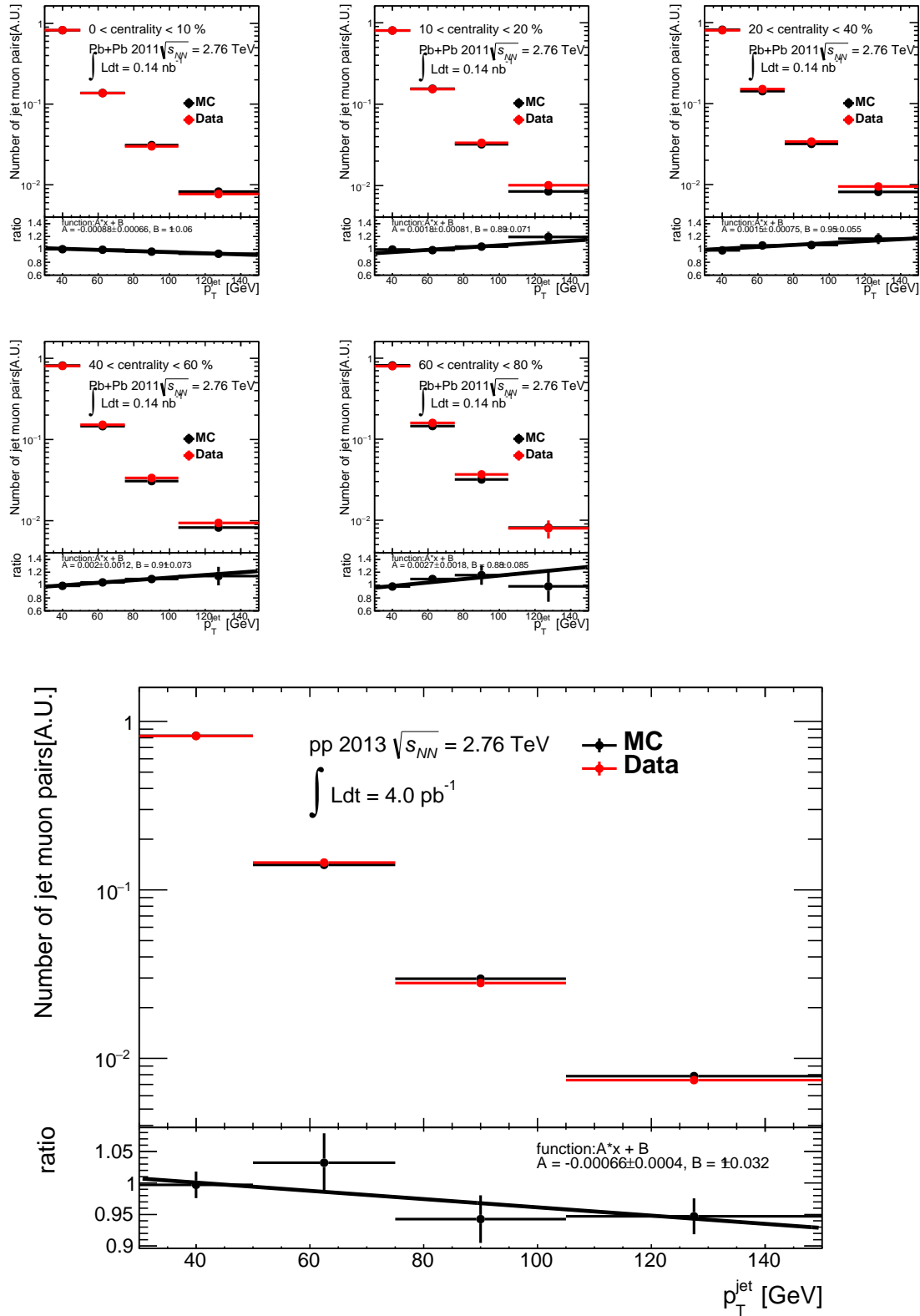


Figure 6.1: The jet transverse momentum p_T distributions from selected jet muon pairs in MC and data and their ratio in Pb+Pb and pp collisions are shown on the top and bottom, respectively.

6.3 Muon Tagged Jets

In the MC samples, the truth-level flavor of each jet muon pair is identified as either b , c , or light-jets, using the following procedure. Reconstructed jets meeting the criteria (section 5.5.1) are required to match to a truth jet within $\Delta R < 0.4$, at the same time the truth jet is required to have jet transverse momentum p_T above 10 GeV and $|\eta| < 2.1$. On the basis of the truth match jet, we try to find whether there is a reconstructed muon within $\Delta R < 0.4$. And if there is, then the muon is required to match to a truth particle (can be truth μ or π etc.). The truth particle is used to define the flavor of the jet. The b -jet template consists of the direct decay component $b \rightarrow \mu$ and the cascade component $b \rightarrow c \rightarrow \mu$. Other c hadron decays form the c -jet template. If the jet is neither a b -jet nor c -jet, it is included in the light-jet template.

Fig. 6.2 is p_T^{rel} distribution of different flavor jets in different jet p_T intervals. The following plot Fig. 6.3 is p_T^{rel} distribution from the 2012 pp MC sample. In these figures b, c -jet templates are from the MC sample and light-jet are from the data driven template and the reason for that will be explained in section 6.4.1. As the jet transverse momentum p_T goes higher, the muons are more likely to be collimated with jets and the p_T^{rel} shows narrower distribution in general. From p_T^{rel} distribution of different templates, the signal b -jet has broader p_T^{rel} distribution than other background templates, which makes p_T^{rel} the appropriate discriminants in this analysis. Other than that, we notice the light-jet and c -jet templates have similar p_T^{rel} shape, which can result in difficulty in differentiating between those two background templates. In order to cope with that, we fix the relative c -jet to light-jet ratio using the information from the MC sample which will be described in details in section 6.4.

6.3.1 Combinatoric Background Subtraction

In the Pb+Pb data the p_T^{rel} distribution has bump at around 1.6 GeV, which arises from the combinatoric contribution. In other words, it comes from the random association between

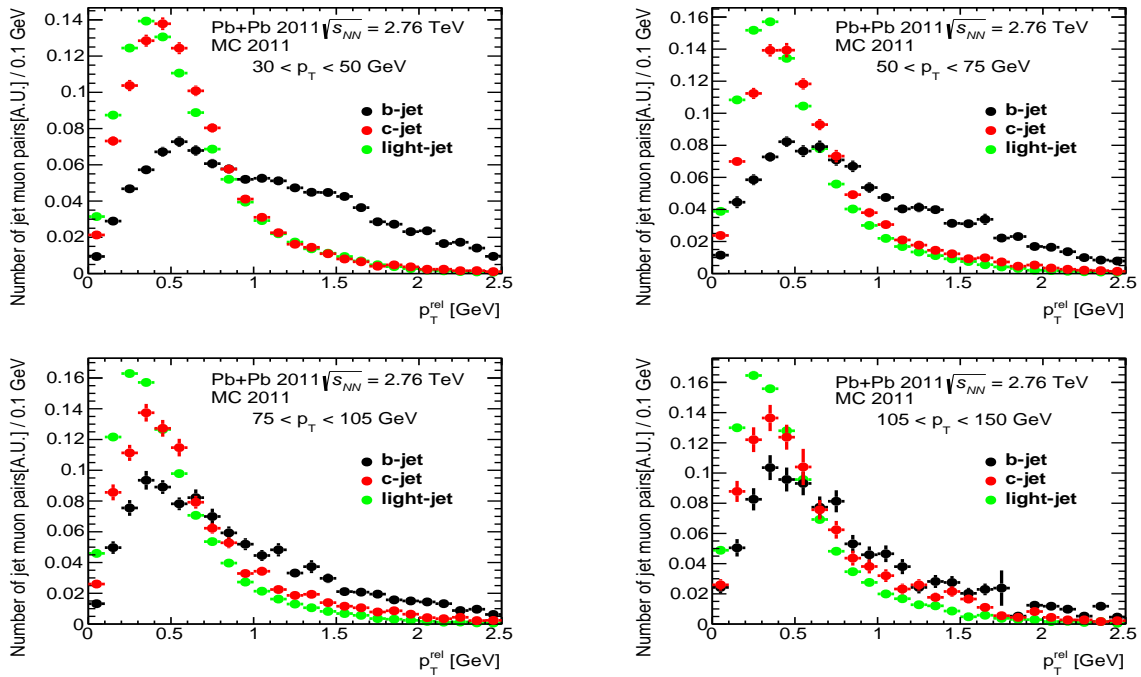


Figure 6.2: p_T^{rel} distribution for b -, c - and light-jets (data driven) in different jet p_T intervals for the full centrality range in 2011 Pb+Pb MC and data sample respectively.

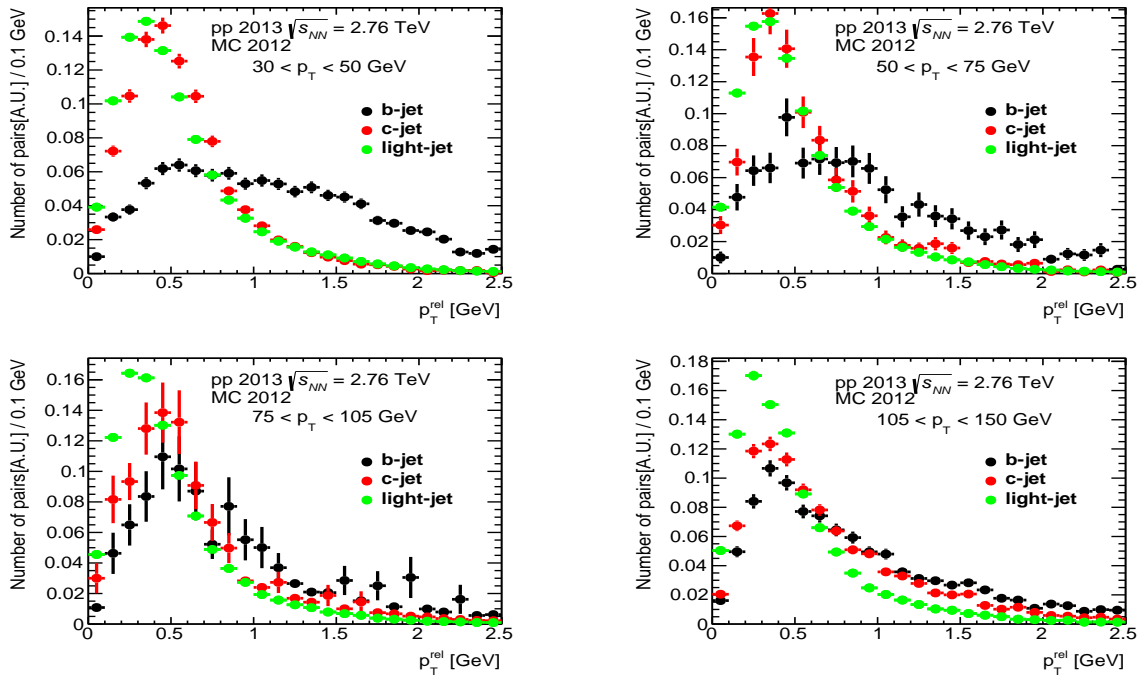


Figure 6.3: p_T^{rel} distribution for b -, c - and light-jets (data driven) in different jet p_T intervals in 2012 pp MC and data sample respectively.

uncorrelated jet muon pairs. This effect is studied by performing an event mixing: The jet muon pairs are formed using muons from a different event of the same centrality chosen at random. The ΔR distributions for the Pb+Pb data are shown in Fig. 6.5. The distributions for ΔR after combinatoric subtraction are also shown in Fig. 6.6. Both distributions are normalized to the per jet basis, which shows the probability distribution of a muon being within the ΔR value for each single jet. The data distribution shows a tail at large ΔR consistent with the random overlay, which is described well by the event mixed distributions. Fig 6.6 can be compared with the same distribution in pp shown in Fig 6.11, where such combinatoric contribution is expected to be negligible.

To study this, event mixing techniques are used in the minimum bias Pb+Pb data sample to estimate the random mixture of the jet muon pairs, Muons in the minimum bias sample are used since we only care about the intrinsic rate of the random association. One thing needs to be noticed is that events in minimum bias has a different centrality distribution compared to the data events used in jet triggered sample. To ensure the correct mixture of centrality-dependent effects, each event in the minimum bias was reweighted when being analyzed. The reweighting was performed by comparing the ΣE_T^{FCal} distributions in the jet-triggered and the minimum bias events and the events of a given ΣE_T^{FCal} in the minimum bias sample are reweighted by the ratio. The two ΣE_T^{FCal} distributions and the consequent reweighting factors are shown in Fig. 6.4. Both distributions begin to fall sharply near $\Sigma E_T^{\text{FCal}} \simeq 3.5$ TeV, where the intrinsic distribution falls off and beyond this point the distribution is influenced by the pile up. No attempt was made to reweight the contribution of these collisions which comprise less than 0.1% of the collisions, thus reweighting factors were fixed to unity for $\Sigma E_T^{\text{FCal}} > 3.5$ TeV.

For each jet in the hard probes sample (which select events with reconstructed jets over threshold using the pp version of the event filter jet algorithm), we check whether the muon from the minimum bias sample is within $\Delta R < 0.4$ of the jet, that will require the muon

and jet to be both in the event with the same centrality. This explores the combinatoric distribution since muon and jet are in totally different events, and the association only happens for uncorrelated jet muon pairs. Also, to increase the statistics, we match five different muons to one jet and then scale the final distribution down by a factor of 5, this would give the right normalization to the final distribution. This can be seen more clearly in the following formula:

$$\text{Number of combinatoric background} = \frac{\#\text{jet muon pairs}}{\#\text{jets mixed}} \times \#\text{jets analysed}, \quad (6.2)$$

where $\#\text{jets mixed} = 5 * \#\text{jets analysed}$.

The same procedure is repeated for the muon triggered sample for jet transverse momentum p_T between 30 - 50 GeV. Due to the fact that the sample is triggered on muons, jets in minimum bias sample are used to randomly mix with each muon from hard probes sample. The previous equation is expressed as follows for the event mixing in muon triggered sample:

$$\text{Number of combinatoric background} = \frac{\#\text{jet muon pairs}}{\#\text{muons mixed}} \times \#\text{muons analysed} \quad (6.3)$$

where $\#\text{muons mixed} = 5 * \#\text{muons analysed}$ and the combinatoric background is evaluated in the same way.

From Fig. 6.5 and Fig. 6.8, we can see that the combinatoric distribution is well estimated since it can describe the tail in ΔR distribution in different centrality and jet p_T bins. Fig. 6.6 and Fig. 6.9 are the ΔR distribution after the combinatoric subtraction. This provides a method for the underlying event background estimation. We subtract the background from the original p_T^{rel} distribution, see Fig. 6.7 and Fig. 6.10, the red distribution is after the combinatoric subtraction, which gives a more steeply falling tail compared to the original

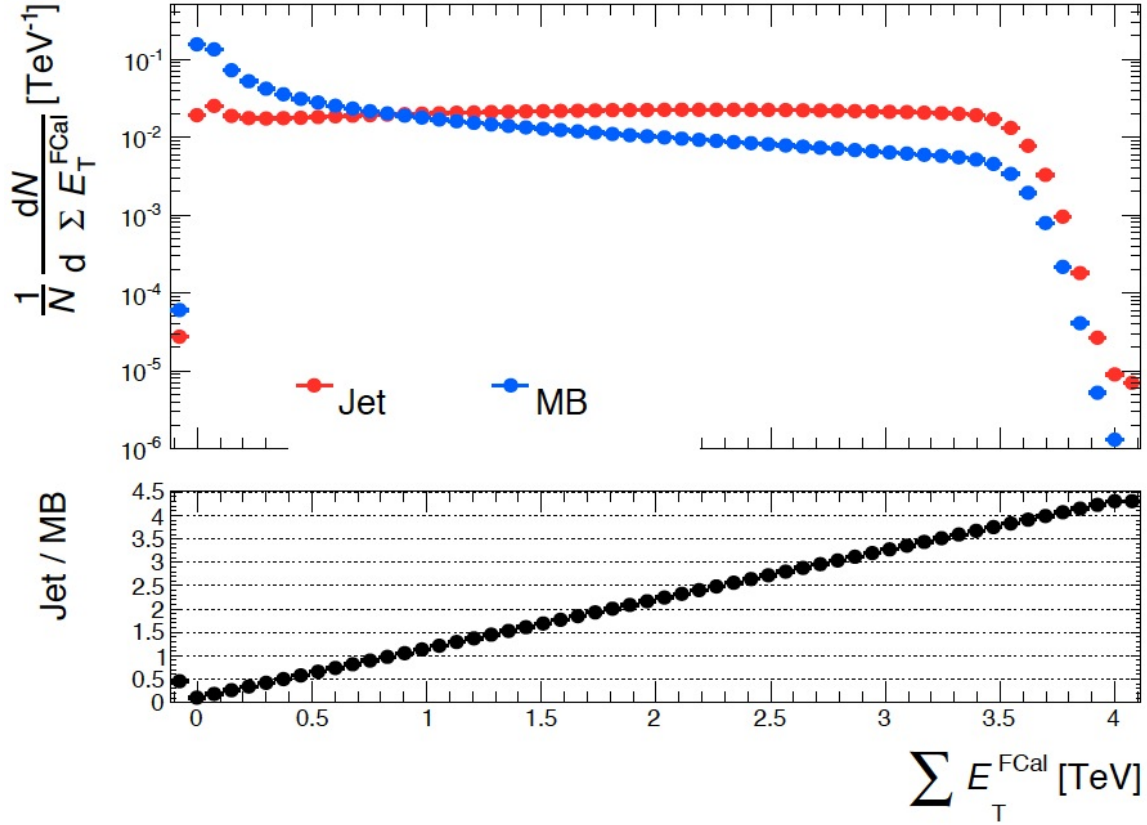


Figure 6.4: The ΣE_T^{FCal} distributions in minimum bias (blue) and jet-triggered (red) events. The ratio, which defines the reweighting factors in the MC, is shown below and is fixed to unity above $\Sigma E_T^{\text{FCal}} > 3.5$ TeV. Taken from [133].

black distribution.

The following figures Fig. 6.11 and Fig. 6.12 show the p_T^{el} distribution of pp data. We can see it has tail similar to what we got from Pb+Pb but after combinatoric subtraction.

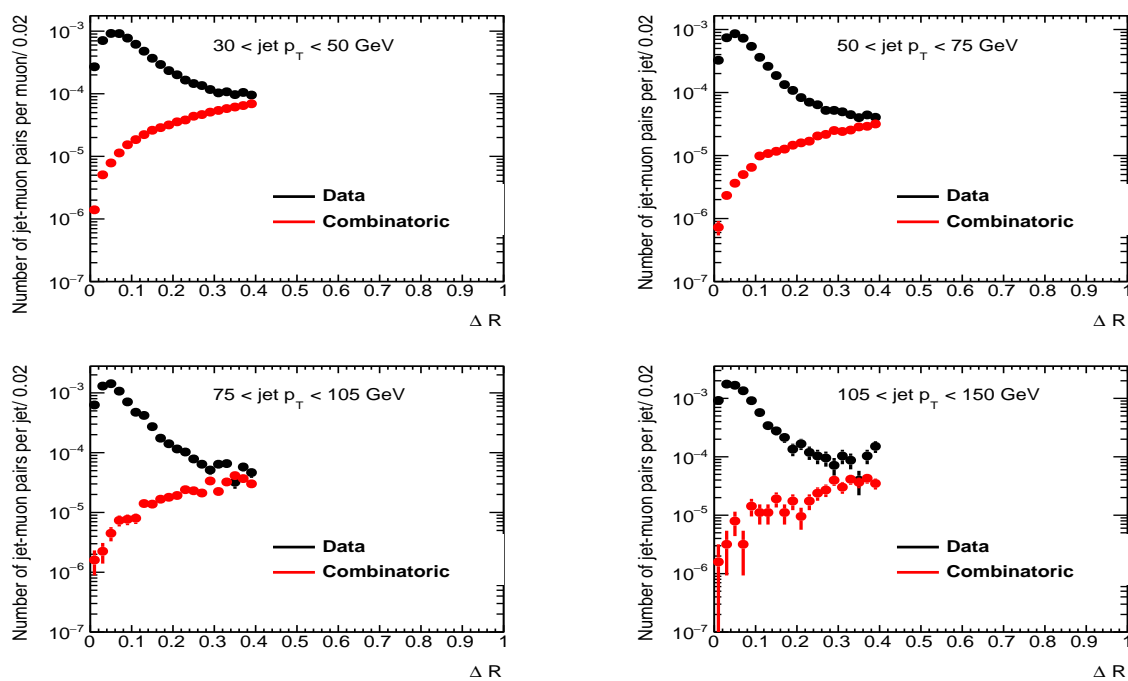


Figure 6.5: ΔR in different jet p_T bins for the full centrality range in 2011 Pb+Pb data, black is original distribution, red is from combinatoric background.

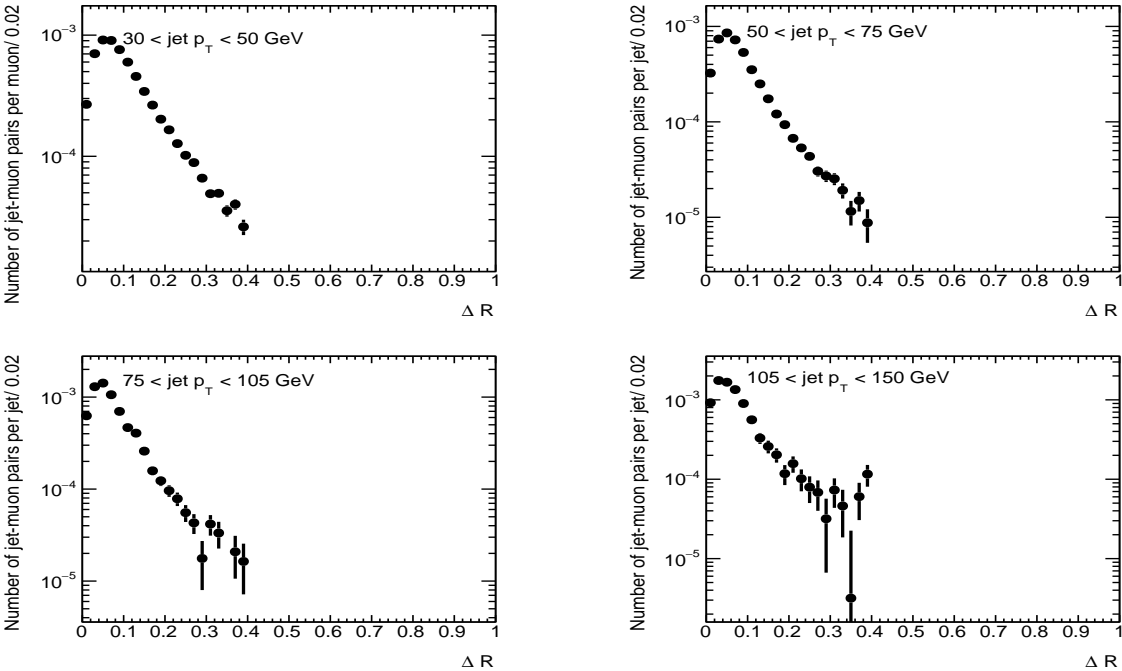


Figure 6.6: ΔR in different jet p_T bins after combinatoric subtraction for the full centrality range in 2011 Pb+Pb data.

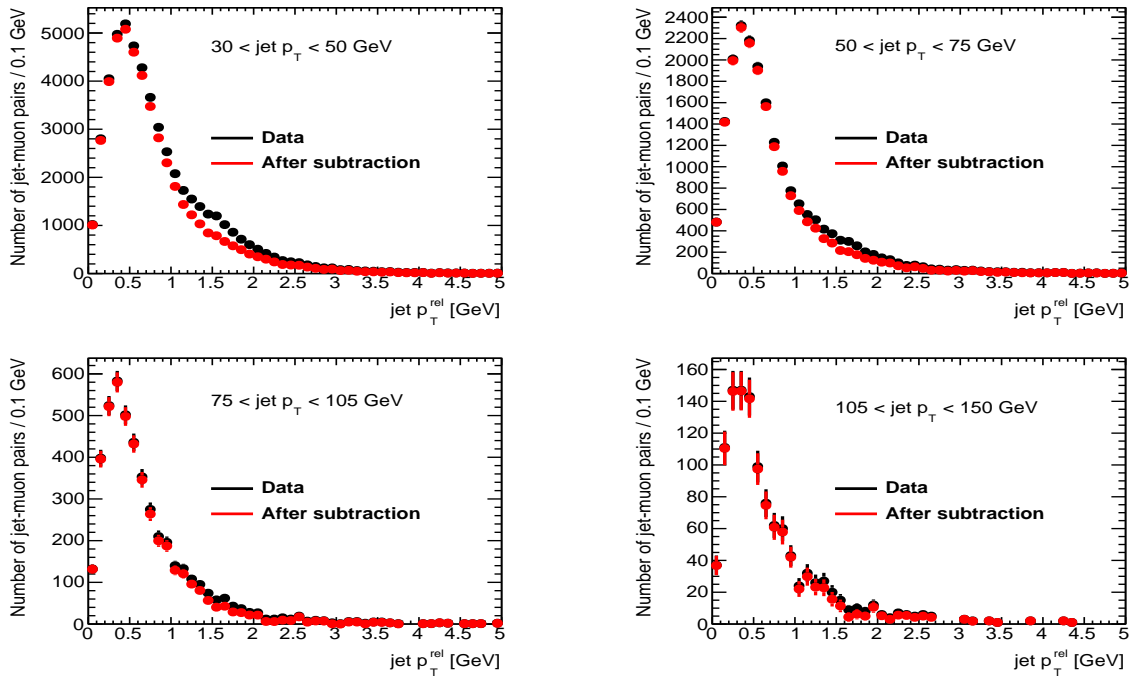


Figure 6.7: p_T^{rel} in different jet p_T bins for the full centrality range in 2011 Pb+Pb data, black is original distribution, red is after combinatoric background subtraction.

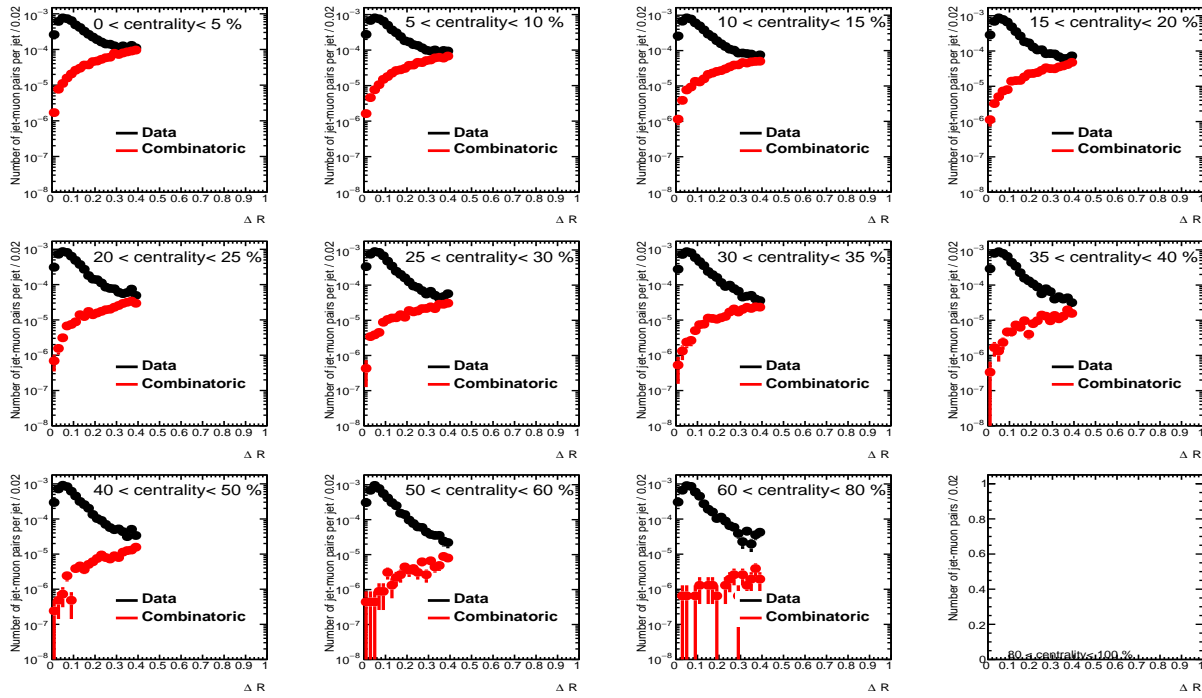


Figure 6.8: ΔR in different centrality bins for the full jet p_T range in 2011 Pb+Pb data, black is original distribution, red is from combinatoric background.

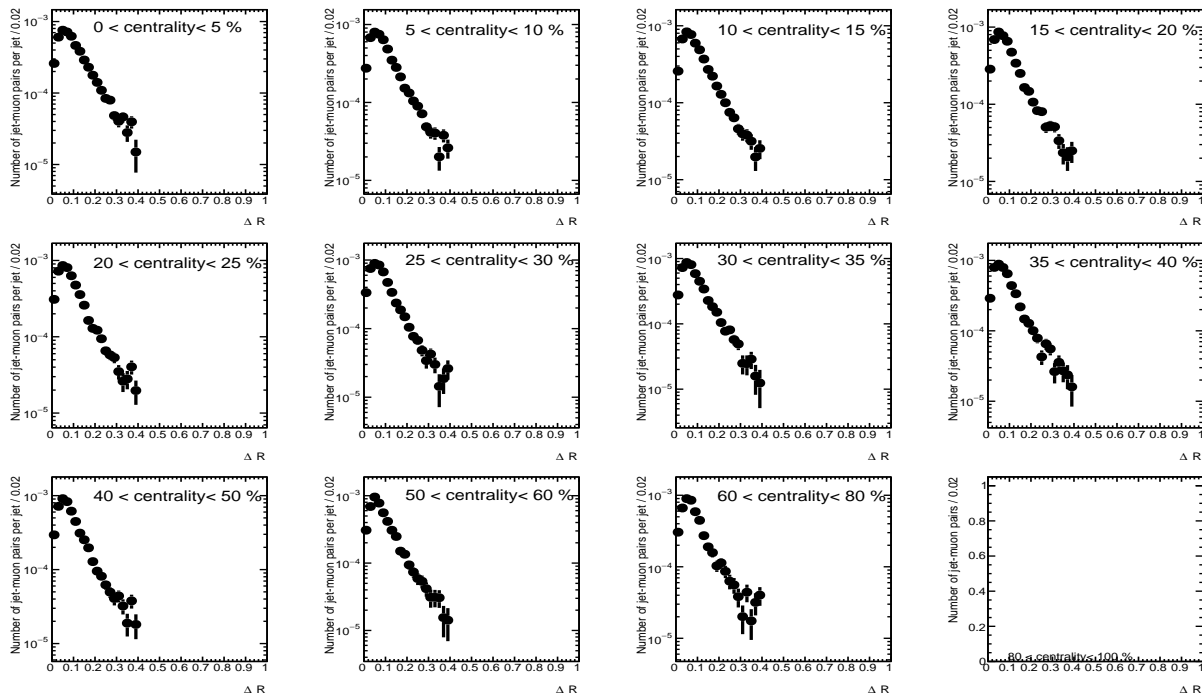


Figure 6.9: ΔR in different centrality bins after combinatoric subtraction for the full jet p_T range in 2011 Pb+Pb data.

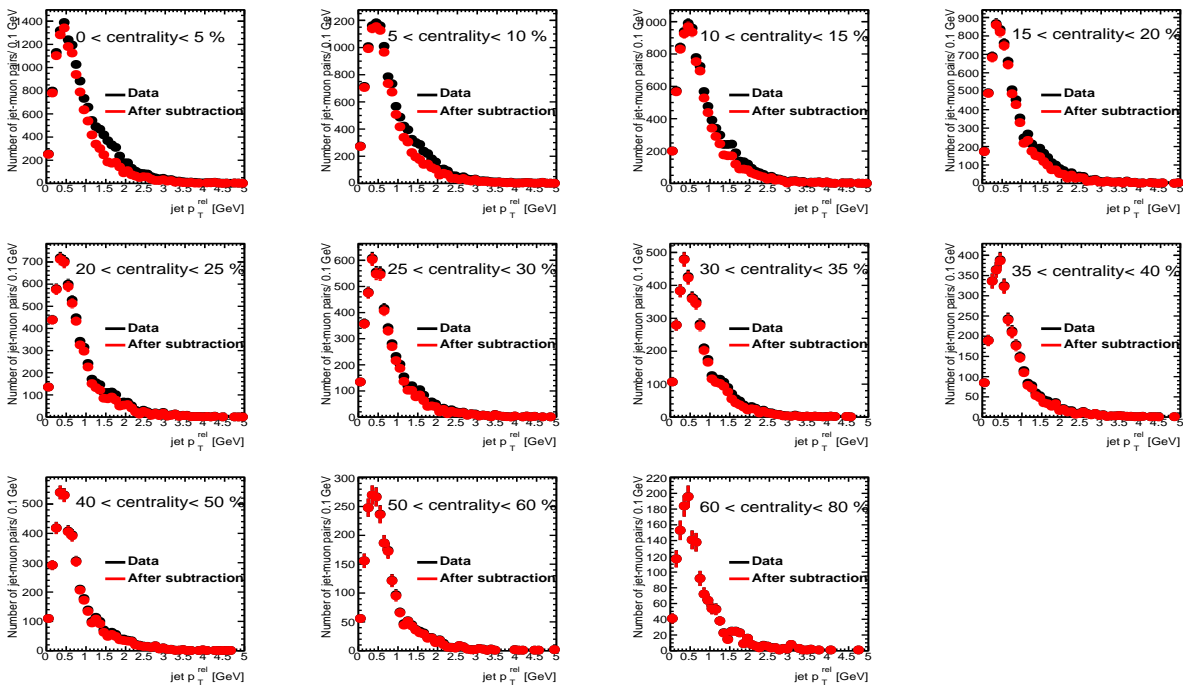


Figure 6.10: p_T^{rel} in different jet p_T bins for the full centrality range in 2011 Pb+Pb data, black is original distribution, red is after combinatoric background subtraction.

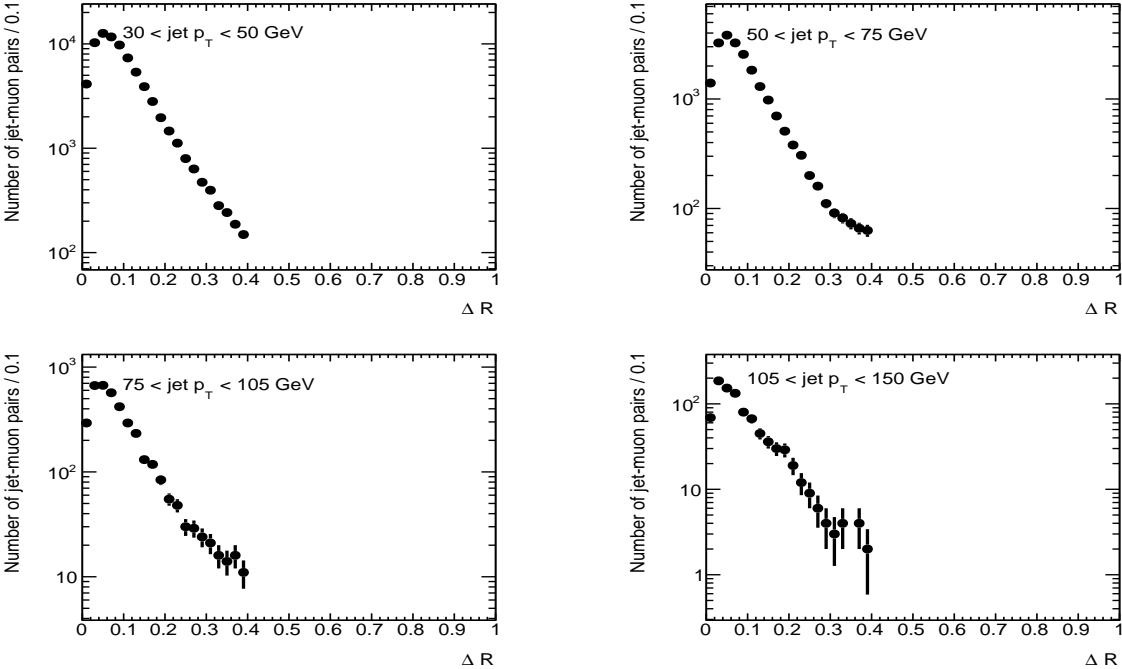


Figure 6.11: ΔR in different jet p_T bins in 2013 pp data.

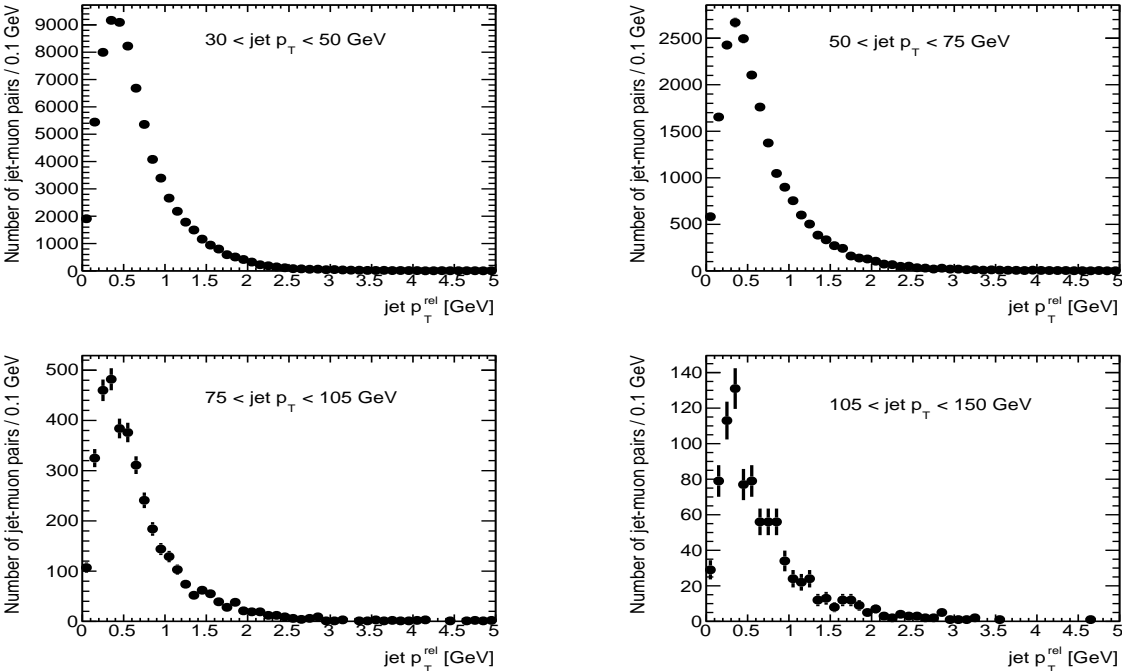


Figure 6.12: p_T^{rel} in different jet p_T bins in 2013 pp data.

6.4 Template Fitting Procedure

In order to get the b -jet fraction from the inclusive jets data samples, we have to build templates pdfs (probability density functions) for both background and signals from the MC samples. In our analysis we use RooFit for the template fitting procedure. The procedure uses data driven method to build light-jet template, and the muon filtered samples are used for the b,c -jet template building due to their better statistics. In addition, combinatoric background template is built from the Pb+Pb minimum bias data samples. RooFit uses non-parametric Kernel estimation to build the pdfs, and the binned log likelihood is used for fitting. Separate templates are constructed for each jet transverse momentum p_T and centrality bin.

6.4.1 Light Jet Template Construction

Fig. 6.17 shows the p_T^{rel} distribution in different centrality intervals for jets with $30 < p_T < 150$ GeV from three different flavors. They are all normalized to 1. The dependence of p_T^{rel} shape on centrality is stronger at low jet p_T than high jet p_T . This is because for lower jet p_T range it is more likely to be influenced by the underlying event background, which shows different behavior between central and peripheral events. The Fig. 6.18 shows the mean value of each individual p_T^{rel} distribution in that centrality bin. It indicates that the the p_T^{rel} shape of light-jet has stronger centrality dependence than other two kinds of jets.

Due to the centrality dependence of the light-jet template, centrality integrated templates can not be used for this analysis. Thus the statistics of true muons in light-jets from the MC samples is not sufficient to do a reliable fit. Additionally, it is not certain that the simulation models sources of muons in light-jets like decays-in-flight and hadrons which reach the muon system (“punch-through” particles) correctly. Therefore, a data-driven method has to be taken. We selected all the tracks in jets as an approximation for muon and the tracks are required to have

1. $p_T > 4$ GeV
2. $|\eta| < 2.5$
3. Number of pixel hits greater or equal to one
4. Number of B layer hits greater or equal to one
5. Number of SCT hits greater or equal to seven
6. The sum of pixel holes and SCT holes less than two
7. No SCT holes
8. $|d0_{PV}| < 5\text{mm}, |z0_{PV}| < 5\text{mm}$

A weight is applied to account for the difference between muon and track spectrum. Fig. 6.13 shows the weight, which defined as the muon spectrum divided by the track spectrum in different jet p_T bins. Studies on Monte Carlo show that the dominant source of muons in light-jets are decays-in-flight. The probability for such a decay-in-flight is anti-proportional to its transverse momentum. That explains why the weight goes down as muon momentum increases. A power law function is used to fit this distribution, and is applied as the weight to tracks transverse momentum in the following analysis.

Fig. 6.14 shows p_T^{rel} distribution between light-jet template defined in MC sample and template derived from data driven in data sample . Templates from data driven are subtracted from combinatoric background of random mix between tracks and jet using the same event mixing technique described in section 6.3.1. It presents reasonable agreement in different jet p_T bins which certifies data driven as a reliable template in this analysis.

On the top of Fig. 6.15, it shows p_T^{rel} distribution between light-jet template derived from the data driven method and the data sample for $30 < \text{jet } p_T < 50$ GeV region. Each event is applied with weight of $1/p_T^{\text{rel}}$ to account for the Jacobian effect. The p_T^{rel} will resemble

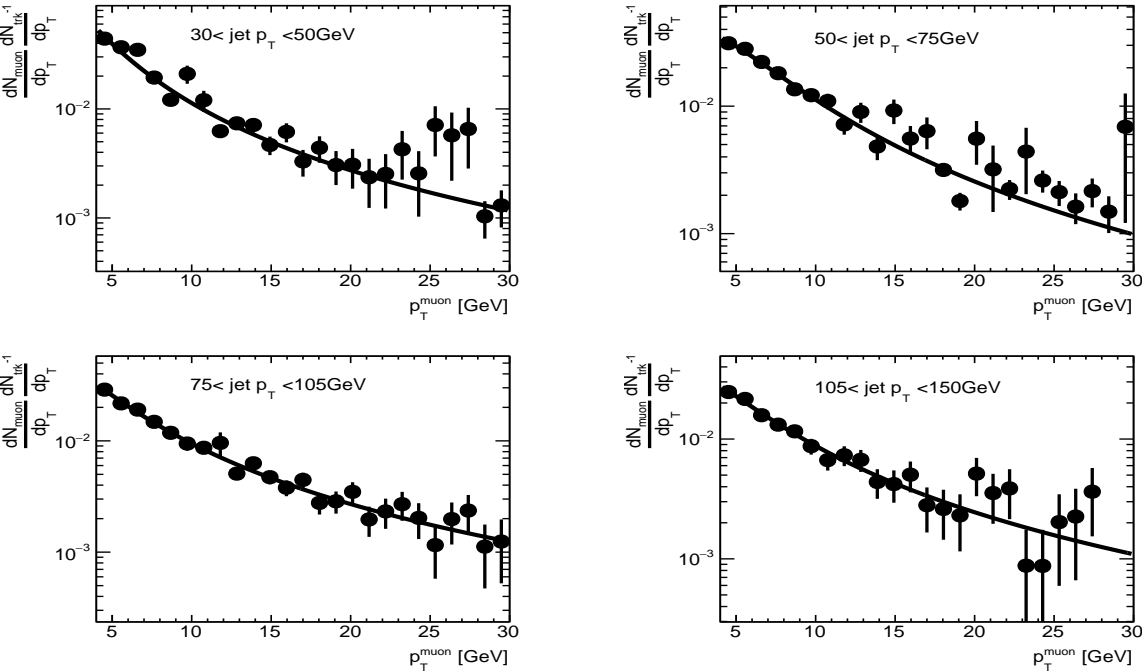


Figure 6.13: Weight distribution as a function of muon p_T in different jet p_T bin in 2011 Pb+Pb MC.

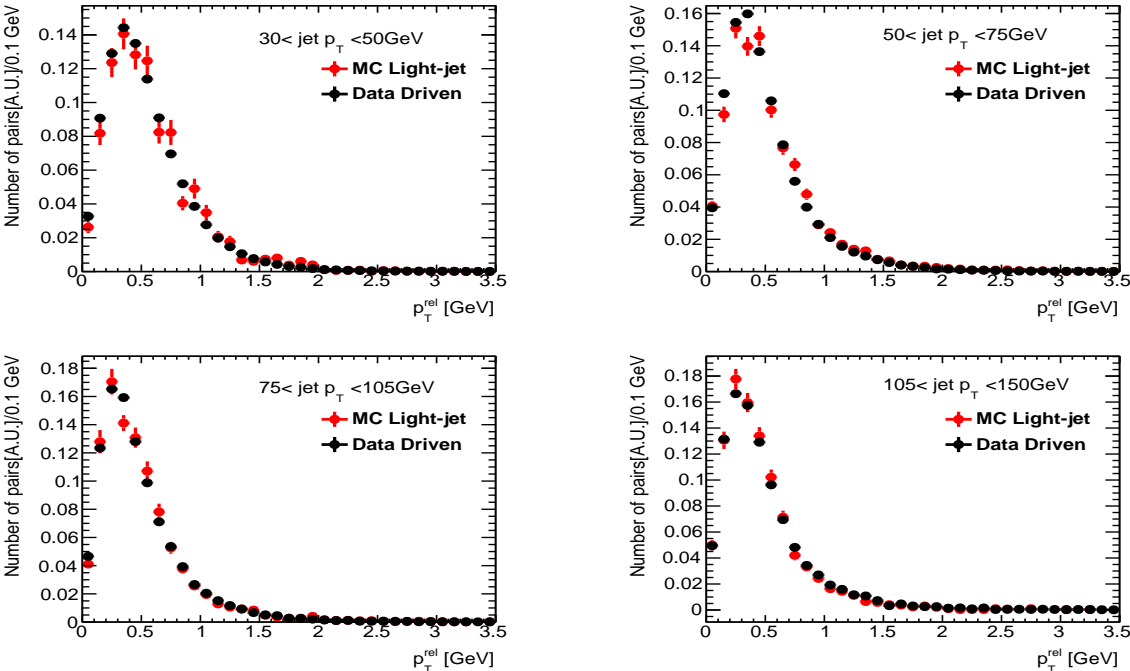


Figure 6.14: p_T^{rel} distribution between MC light-jet template and data driven template in different jet p_T bin .

gaussian distribution. The range is restricted between p_T^{rel} equals 0 and 1.5 GeV, where the light-jet dominates the data distribution. For p_T^{rel} below 0.2 GeV there is problematic behavior for the data sample. With accounting for the Jacobian effect, we can see this more clearly. In order to improve the template fitting, p_T^{rel} range below 0.2 GeV has to be excluded from our analysis. Since the distribution is not dominated by the b -jet template during that region, this cut should not have big impact on the final result. In addition, gaussian function with mean fixed at zero is used to fit to both distributions for $0.2 < p_T^{\text{rel}} < 0.9$ GeV. The σ is extracted after the fitting and is plotted on the bottom of Fig. 6.15 as a function of jet p_T . With this plot, we can clearly see whether the template and data distribution has better agreement in a quantitative way.

6.4.2 Extra Smearing on Light Jet

To do detail analysis for the mismatch between the distribution of the data sample and the data driven template, extra data smearing on the data driven template has to be taken account for this effect. The σ applied for extra smearing is calculated in the following way:

$$\sigma_{\text{extra}} = \sqrt{\sigma_{\text{data}}^2 - \sigma_{\text{data driven}}^2}, \quad (6.4)$$

where σ_{data} and $\sigma_{\text{data driven}}$ are gaussian width extracted from Fig. 6.15 in different centrality bin. Comparison between the data sample and the data driven template after extra smearing is shown in Fig. 6.16. The disagreement becomes less, and due to the fact that each σ is extracted on a average basis of each centrality bin, it still has a little mismatch between these two templates. In the following analysis, the data driven template with extra smearing is used for template fitting procedure in this analysis due to the better agreement with the data.

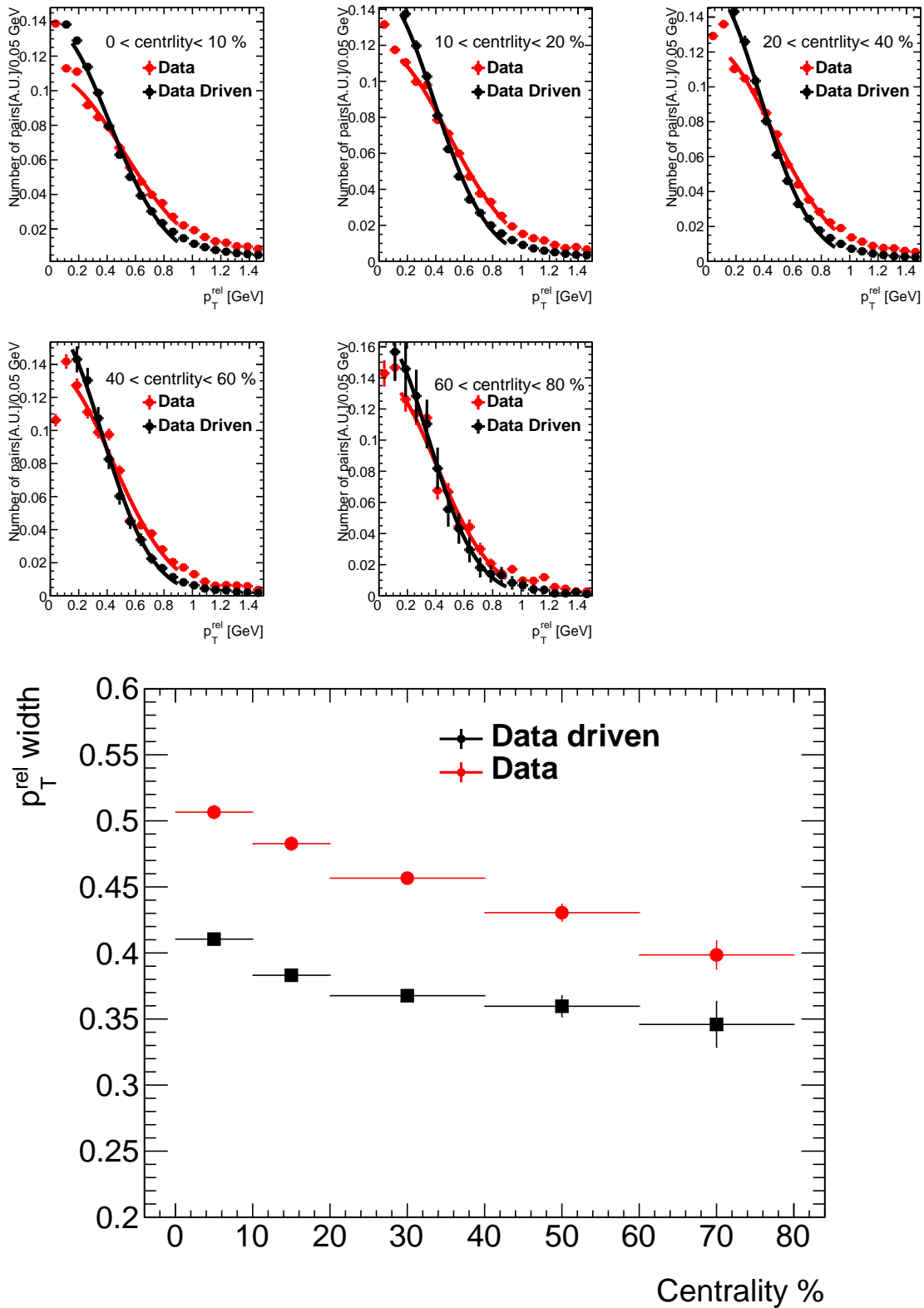


Figure 6.15: Top: p_T^{rel} distribution accounting for Jacobean between light-jet template and data, Bottom: p_T^{rel} width distribution for $30 < \text{jet } p_T < 50$ GeV in 2011 Pb+Pb data.

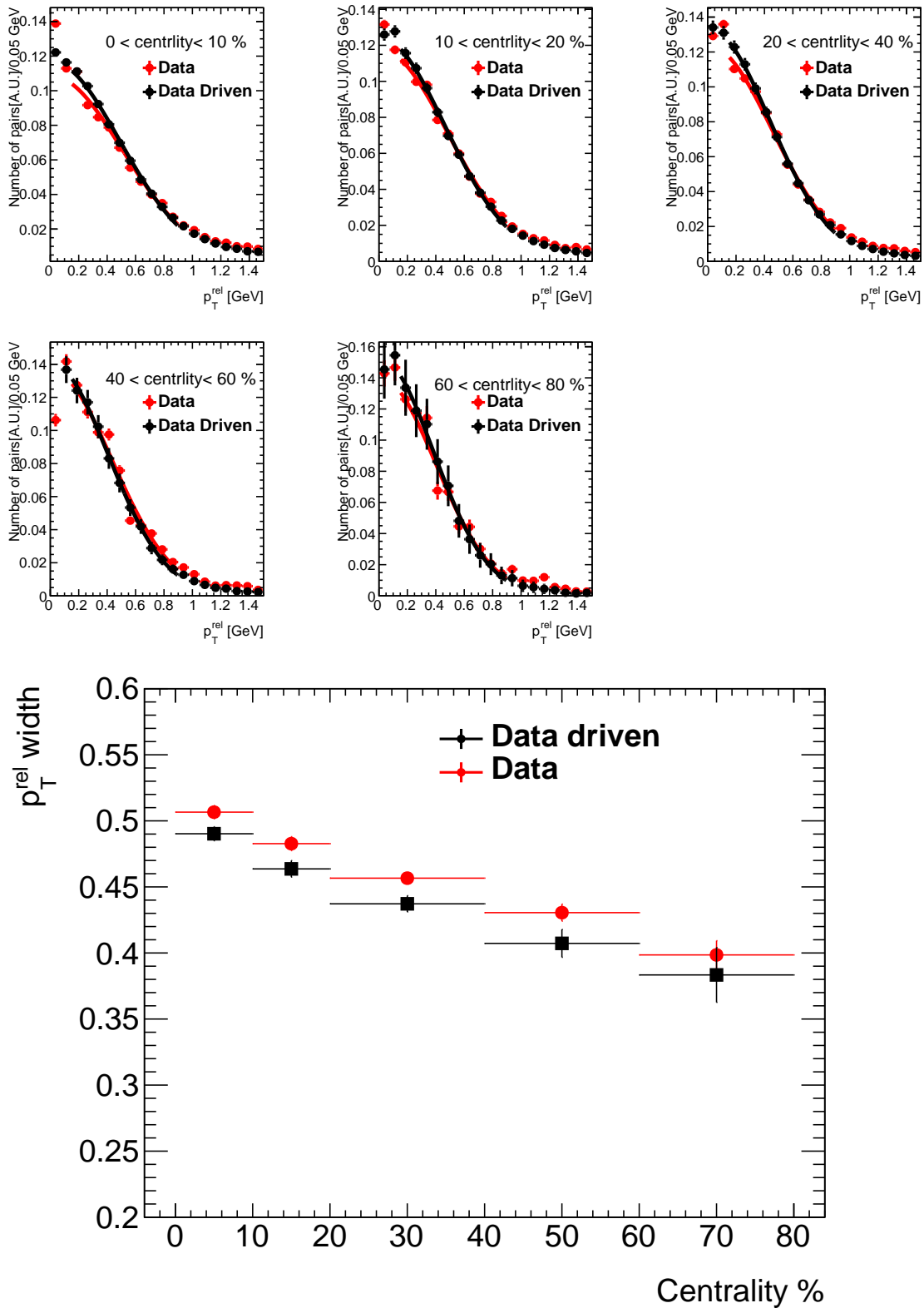


Figure 6.16: Top: p_T^{rel} distribution accounting for Jacobean between light-jet template after extra smearing and data, Bottom: p_T^{rel} width distribution for $30 < \text{jet } p_T < 50$ GeV in 2011 Pb+Pb data.

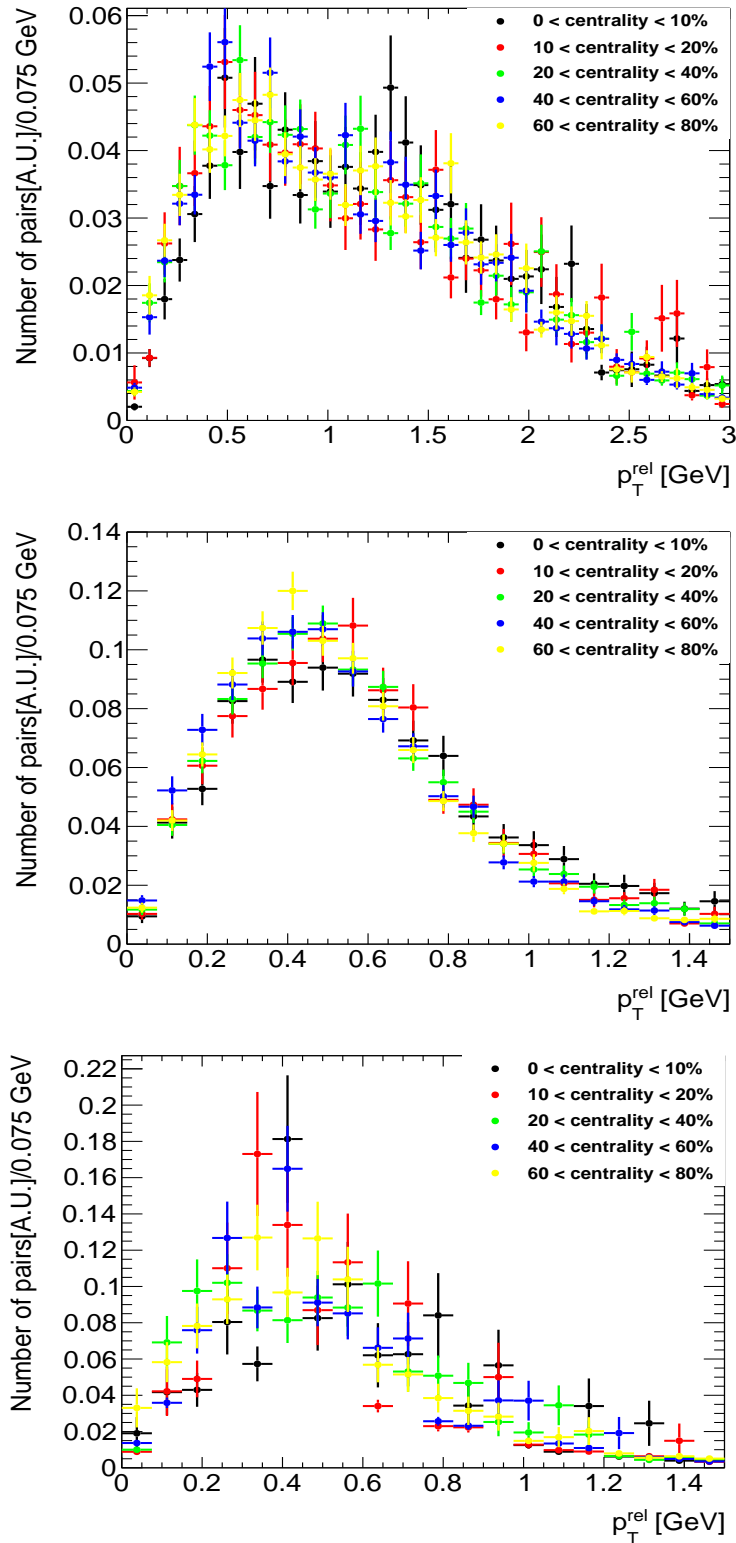


Figure 6.17: From top to bottom : *b*-jet, *c*-jet and light-jet's p_T^{rel} distribution in different centrality bins for the full jet p_T range in 2011 Pb+Pb MC.

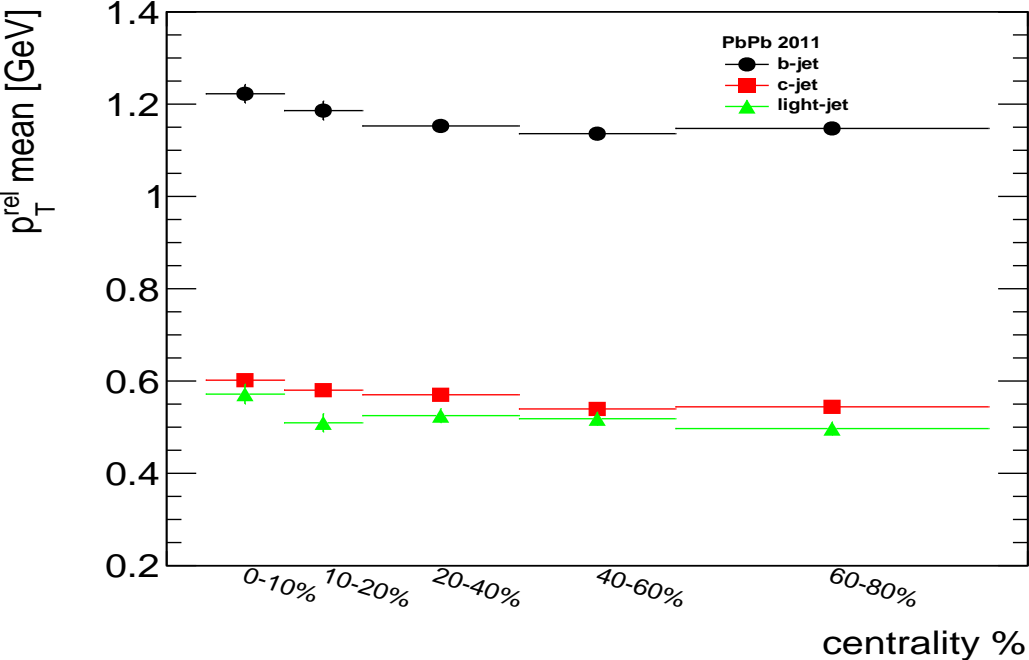


Figure 6.18: p_T^{rel} mean distribution as a function of centrality for the full jet p_T range in 2011 Pb+Pb MC.

6.4.3 Template Fitting Result

The template fitting procedure uses the idea that the data is a combination of different templates. The fitting method is to extract the fraction of each component. With the templates in different jet transverse momentum p_T ranges, the data is split into different subsets of each individual centrality and p_T bins, and the subsets are fitted to the corresponding templates. The templates constructed from the MC sample discussed in section 6.1 are used to construct a model of the expected probability density function (pdf) distribution in the data. B_{pdf} denotes the pdf for the signal b -jet component. C_{pdf} for the background c -jet component and L_{pdf} for the light-jet component. At the same time we use $Comb_{pdf}$ to describe the performance of the combinatoric distribution from the underlying event background. Each component has its own fraction denoted as f_B, f_C, f_L and f_{Comb} , and the combinatoric background distribution is estimated using the analysis in section 6.1. Thus the combinatoric ratio f_{Comb} can be fixed due to the study. As seen in Fig. 6.7, c -jet and light-jet have very similar p_T^{rel} distributions in most of the jet p_T bins. This results in poor separation between the c - and the light-jet contribution, but is not expected to affect the f_B . We finally decide to fix the relative ratio between the c -jet and light-jet using the information from the MC samples. The f_C/f_L ratio being fixed to this choice is studied as a systematic contribution.

The p_T^{rel} density distribution of data samples ($Data_{pdf}$) can be written as:

$$Data_{pdf} = f_B \times B_{pdf} + f_C \times C_{pdf} + f_L \times L_{pdf} + f_{Comb} \times Comb_{pdf}. \quad (6.5)$$

In order to get the signal fraction f_B , we have to maximize the likelihood function using “Roofit” [147].

The results of this procedure for each centrality and jet transverse momentum p_T bin are shown in Fig. 6.19- 6.22 for the Pb+Pb sample, and in Fig. 6.23 for the pp sample. From these plots we can see the p_T^{rel} distribution of template and data agree well using the light-jet template with extra smearing (Section 6.4.2). In Fig. 6.22 we can see the statistics is poor

for the two most peripheral bins: 40-60% and 60-80%. The template fitting procedure based on this statistics cannot provide reliable fitting results. Therefore these two centrality bins in the highest jet transverse momentum bin 105-150 GeV are excluded in this analysis.

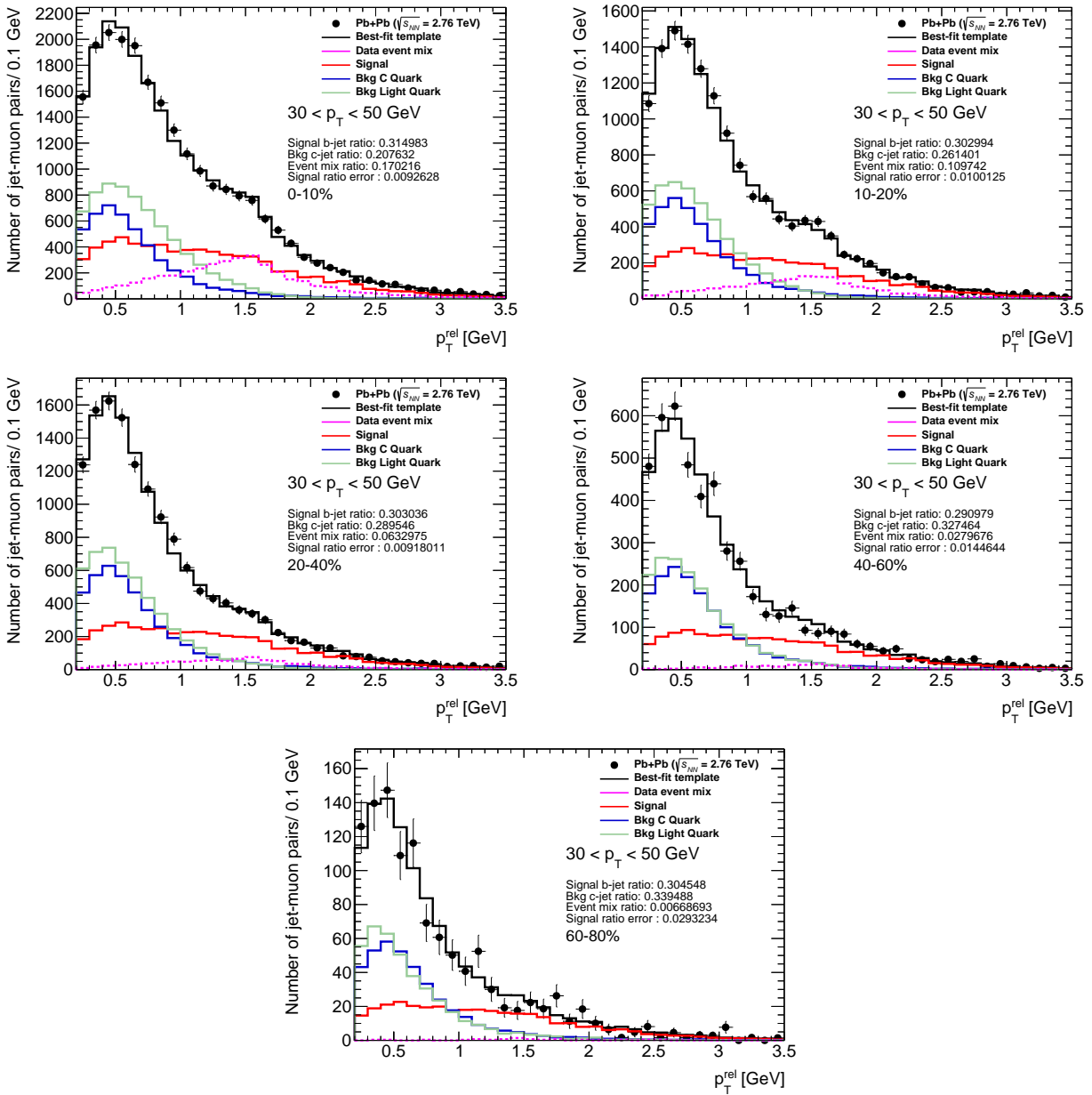


Figure 6.19: Template fitting result in different centrality intervals for $30 < \text{jet } p_T < 50 \text{ GeV}$.

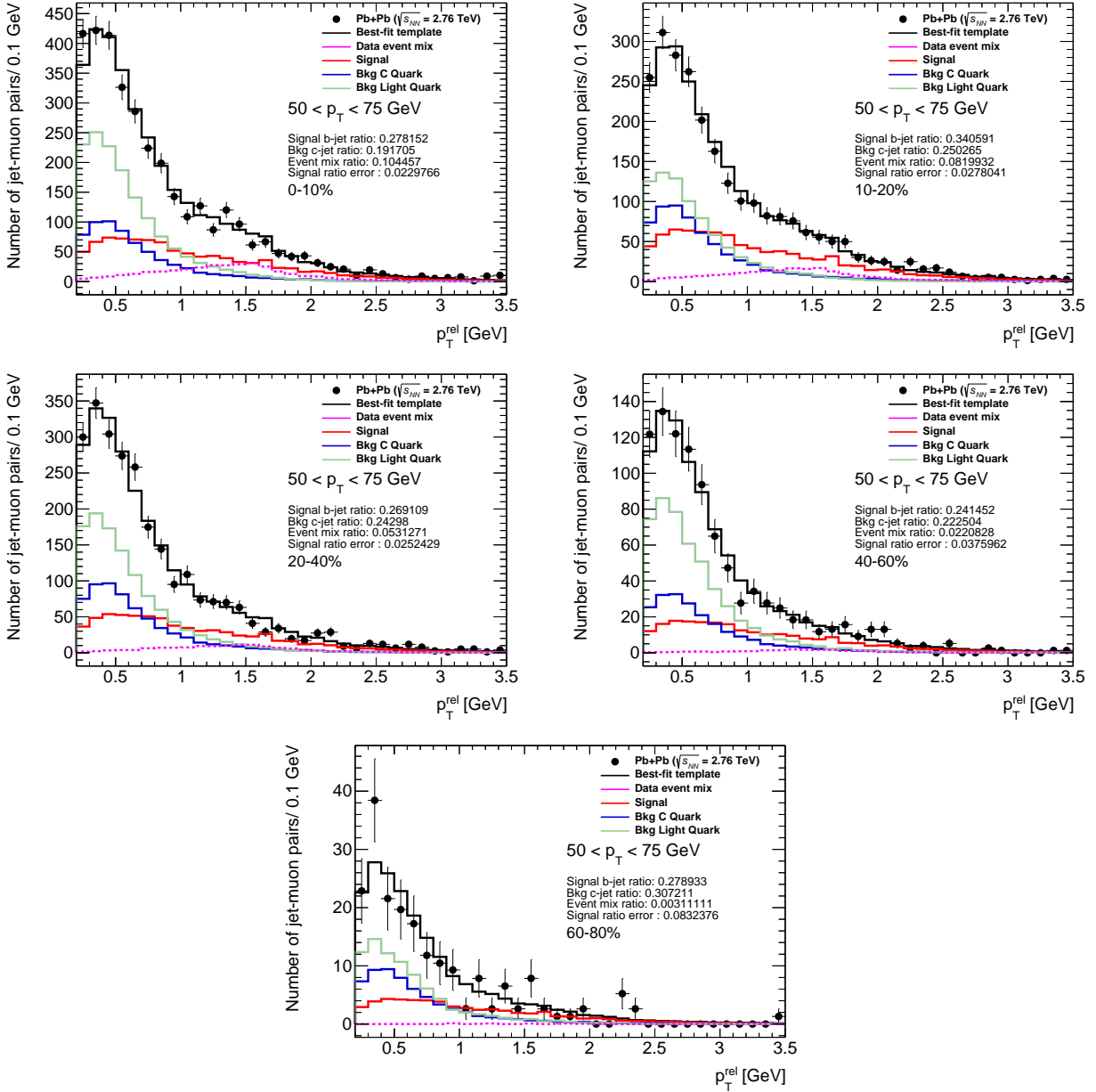


Figure 6.20: Template fitting result in different centrality intervals for $50 < \text{jet } p_T < 75$ GeV.

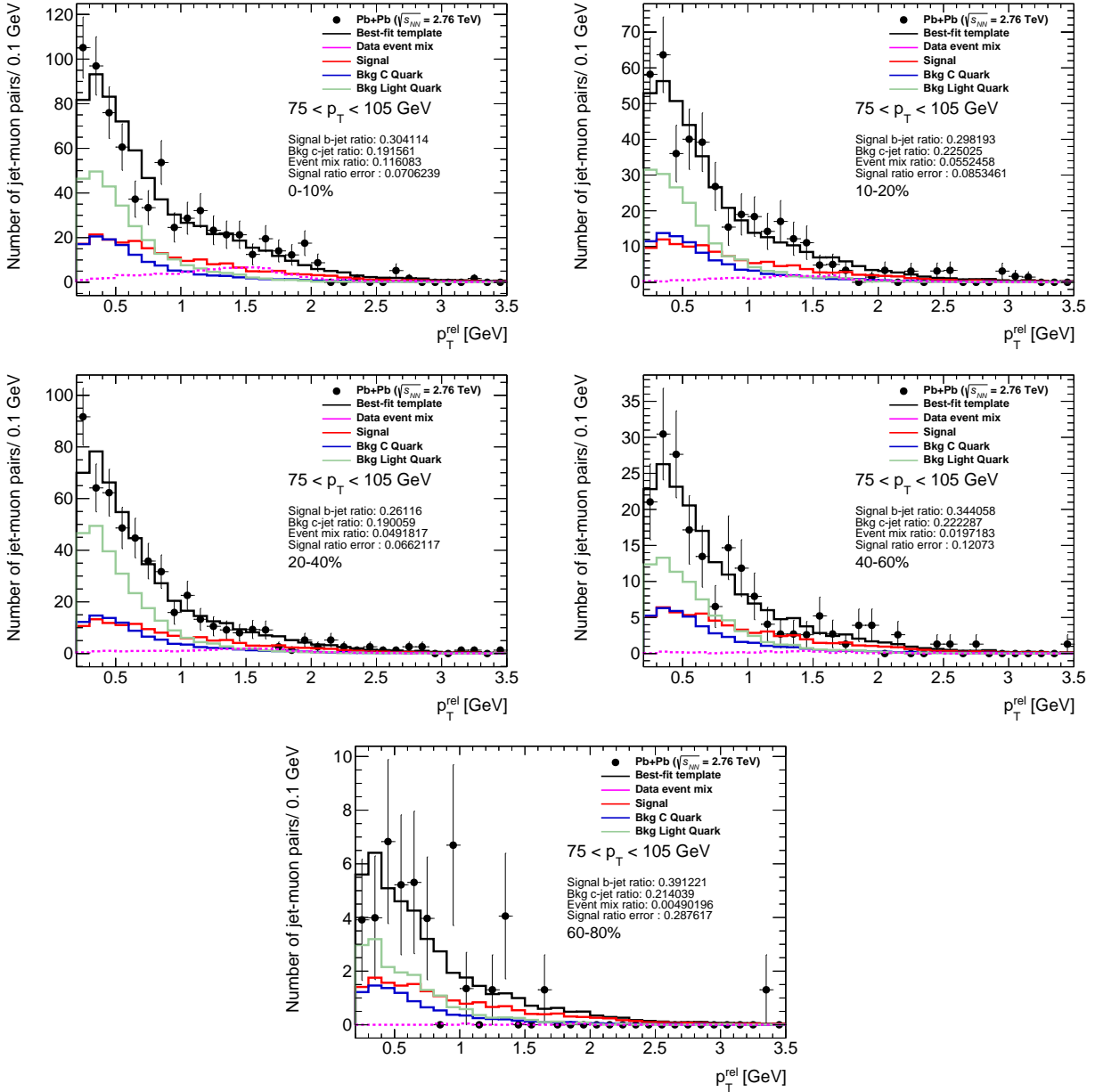


Figure 6.21: Template fitting result in different centrality intervals for $75 < \text{jet } p_T < 105$ GeV.

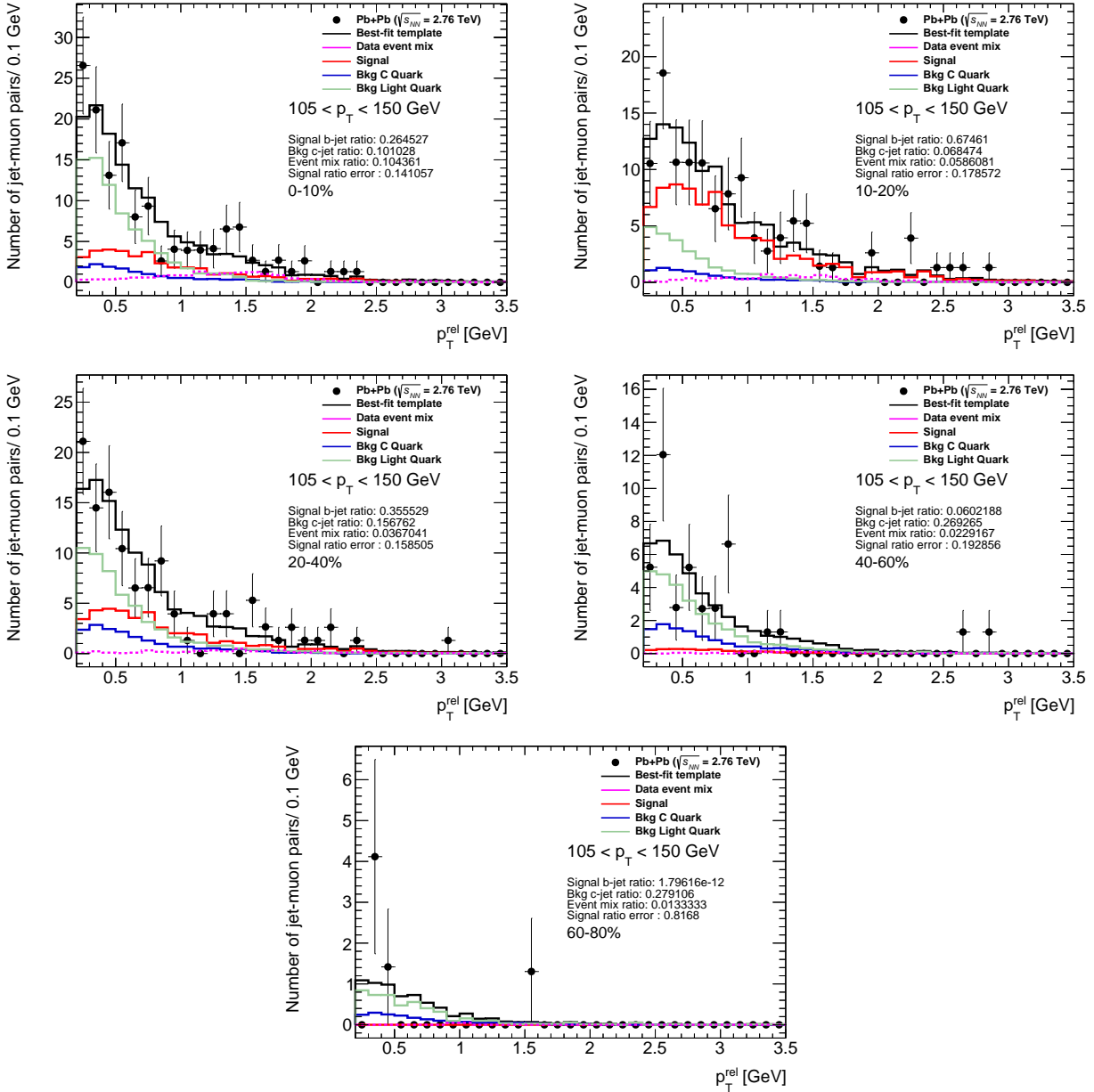


Figure 6.22: Template fitting result in different centrality intervals for $105 < \text{jet } p_T < 150$ GeV.

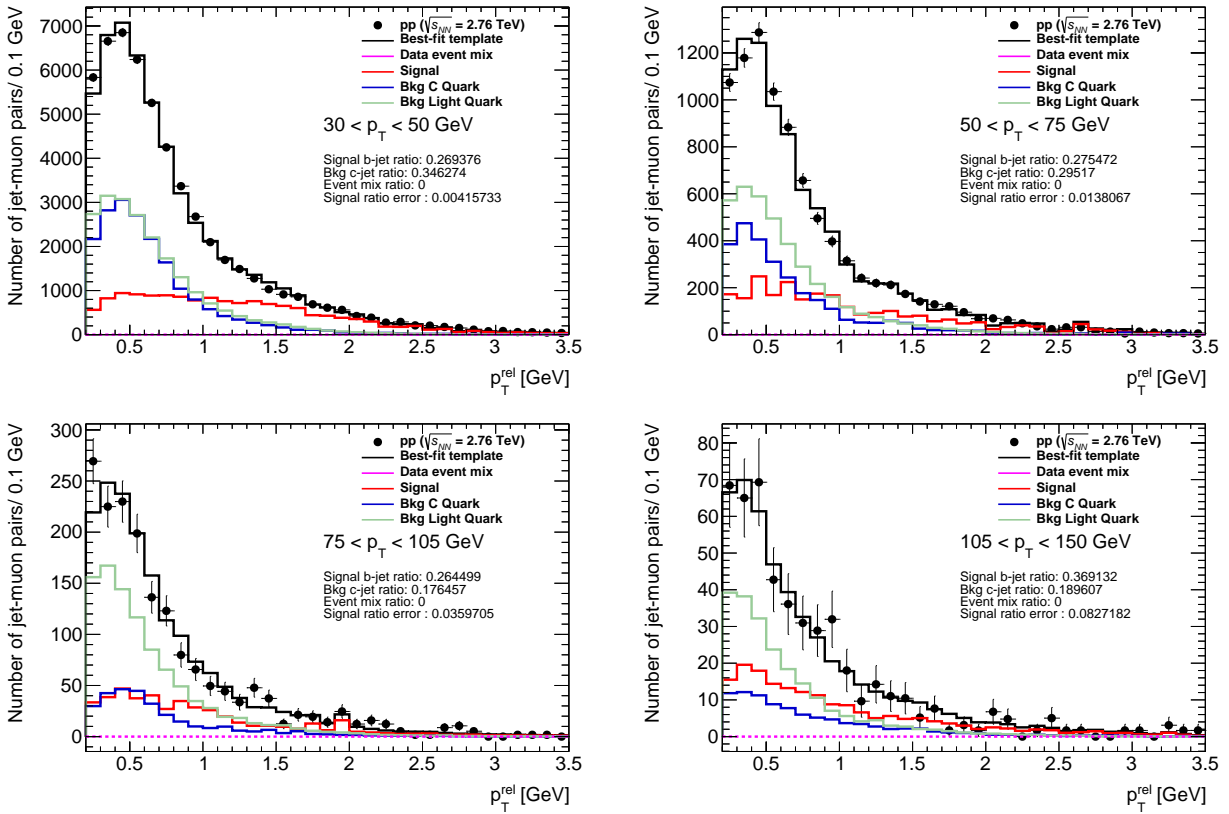


Figure 6.23: Template fitting result in different jet p_T intervals in pp sample.

6.5 Validation

6.5.1 Jet Energy Scale and Resolution

MC studies show higher response of energy (defined as $\mathfrak{R} = p_{T,\text{jet}}^{\text{EM+JES}}/p_{T,\text{jet}}^{\text{truth}}$) to quark initiated jets by up a few percent relative to the inclusive jets sample, which is used to determine the calibration. One of the reason is the part of the calorimeter measuring the jet may be hit by additional particles not belonging to the jet originated from the quark, and affecting our measurement. More details are documented in Ref [139, 142, 148]. Although such effects are in the MC sample and would be accounted for in the unfolding, they reduce the stability of the unfolding. Thus a correction reducing the jet transverse momentum p_T 's by 2% is applied to mitigate this. In order to study the energy resolution, we take each slice of the truth jet p_T bin and use gaussian function to fit to the distribution, and then plot its mean and sigma on top of the 2D plots. The following Fig. 6.25 shows the b -jet energy resolution and closure distribution as a function of truth jet p_T .

In addition, MC studies also show lower response to the light-jets that associated with muons relative to normal light-jets. The dominate source of muons in the light-jets (muon and jet within $\Delta R < 0.4$) are decays-in-flight, and most of them come from the π/K s decays. When muons are produced, instead of carrying the muons, the energy from the hadron in jets was not all deposited in the calorimeter, Thus light-jets will have lower energy compared to the real muon. Fig. 6.26 shows the energy scale distribution as a function of jet truth transverse momentum p_T for the light-jets with muons associated. On top of this 2D distribution, the mean value of energy scale for each truth jet p_T bin is plotted. Therefore another correction enhancing the jet transverse momentum p_T 's by 7% are applied for the light-jet template.

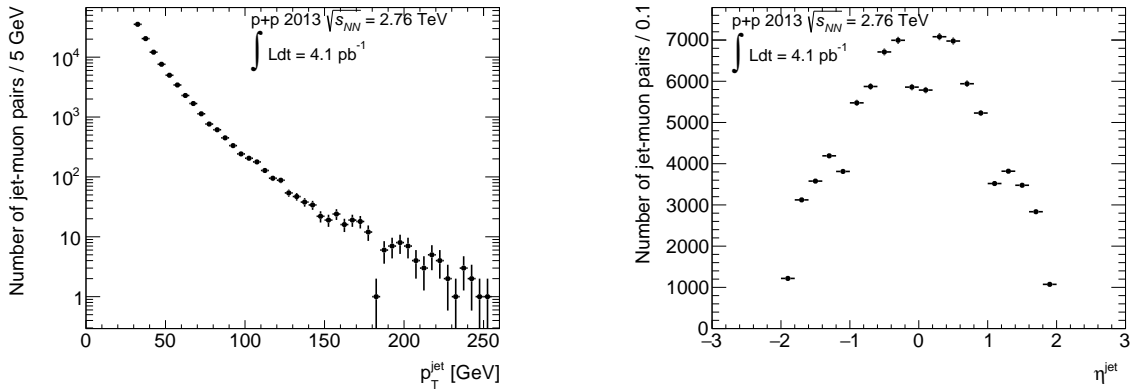


Figure 6.24: The jet p_T and η distributions from selected jet muon pairs are shown on the left and right, respectively, in 2013 pp collisions.

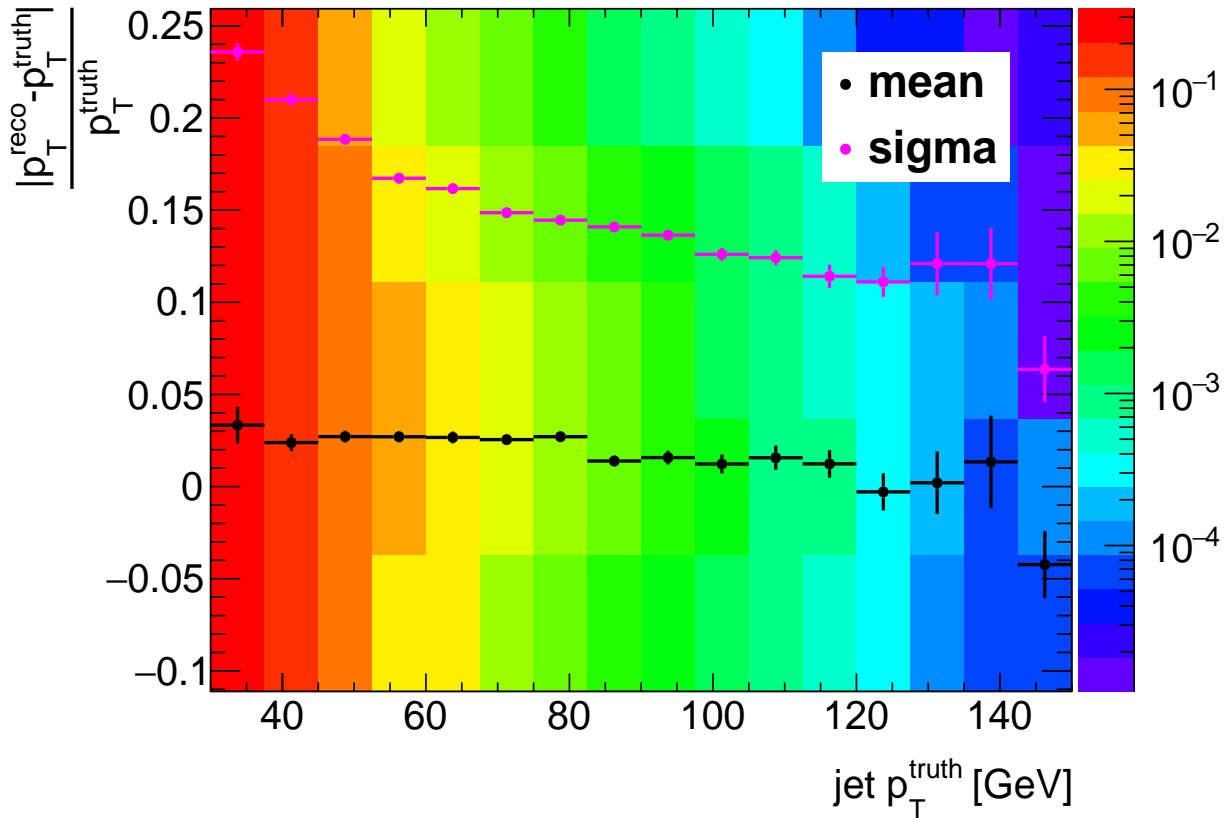


Figure 6.25: b -jet energy scale closure for the full centrality range in Pb+Pb sample.

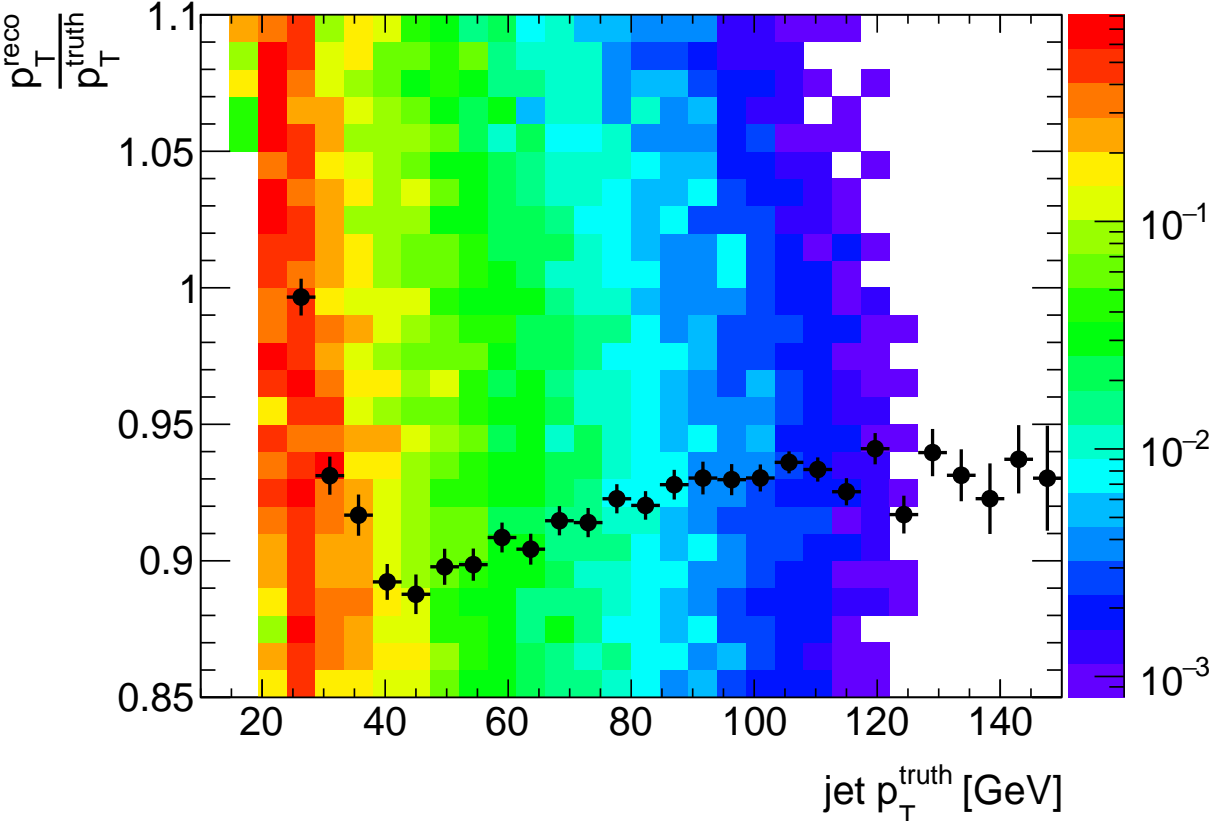


Figure 6.26: light-jet energy scale for the full centrality range in Pb+Pb sample.

6.6 Unfolding

The unfolding procedure accounts for the bin migration effects on the measured jets spectrum that are induced by the jet energy resolution, as well as any remaining inefficiencies or detector effects that have not been explicitly corrected for in the analysis. A bin by bin unfolding procedure is used with the corrections obtained from the PYTHIA dijet $JX\mu$ samples.

The following equation illustrates how the correction factor C_i is calculated:

$$C_i = \frac{T_i}{R_i}. \quad (6.6)$$

$$U_i = C_i \times D_i \quad (6.7)$$

Here T_i denotes the true simulated number of b -jets from $b \rightarrow \mu$ decays, which requires a true muon matched within $\Delta R < 0.4$. R_i denotes the number of reconstructed jets fulfilling the selection criteria for this analysis. The distribution for the correction factors in each jet transverse momentum p_T bin and centrality interval can be found in Fig. 6.27. The unfolded data spectrum U_i is obtained by multiplying the number of jets in data D_i with the correction factor. Fig. 6.28 shows the correction factors distribution from the pp sample. At the same time, efficiency and purity are defined as follows and are also shown on Fig. 6.27 and Fig. 6.28 to establish confidence in the applicability of the method.

1. purity: Defined as the ratio between the number of calorimeter jets with a spatially matched MC truth jet (within $\Delta R < 0.4$) and the total number of calorimeter jets.
2. efficiency: Defined as the ratio between the number of MC truth jets with a spatially matched calorimeter jet (within $\Delta R < 0.4$) and the total number of MC truth jets.

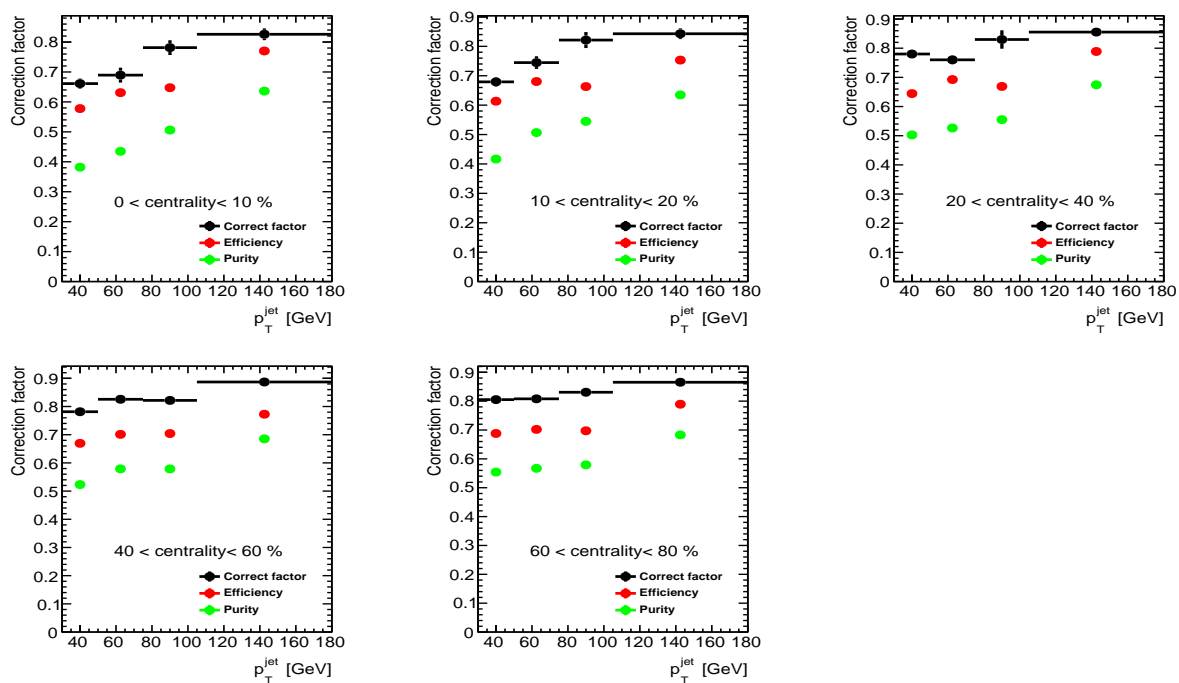


Figure 6.27: Unfolding correction factor distribution in different centrality intervals after energy scale in 2011 Pb+Pb samples.

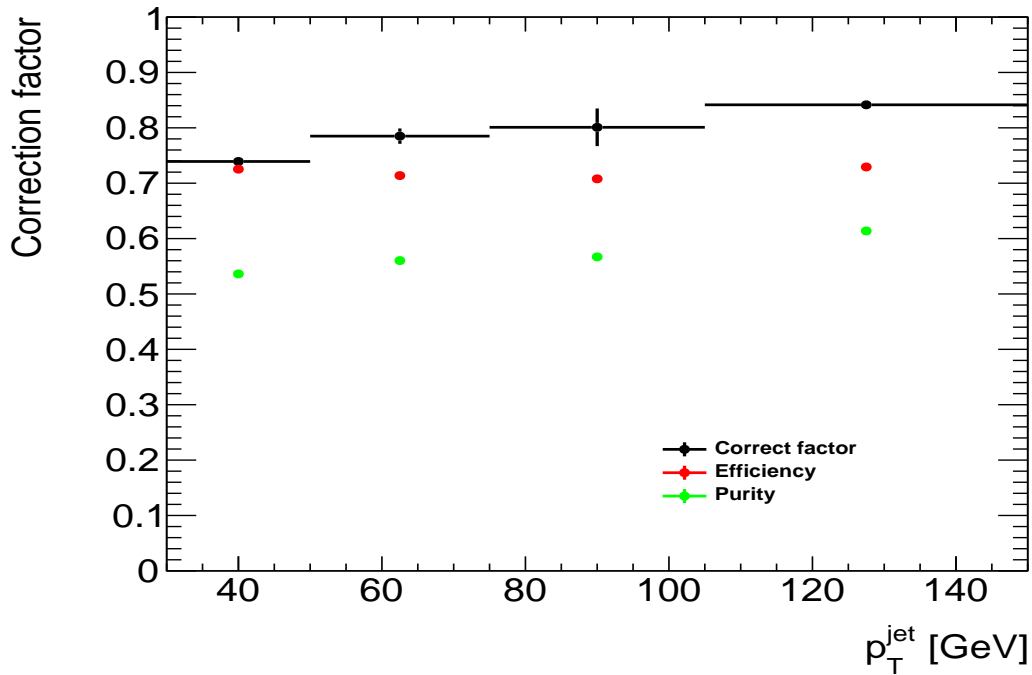


Figure 6.28: Unfolding correction factor distribution in 2012 pp samples.

6.6.1 Acceptance Correction

In this analysis we have measured the b -jet spectrum with jet muon pairs with the $\frac{\Delta p}{p_{ID}}$ cut on the muons. When we consider the muon tagged b -jet yield distribution, the acceptance for muons fail this cut has to be corrected for the final muon tagged b -jet cross section for both the Pb+Pb and the pp data samples using information from Fig. 5.5.

6.7 Systematic Uncertainties

The systematics uncertainties on jet yields in this analysis can be categorized into two classes: those that arise due to uncertainties on either multiplicative correction factors or the various scaling factors appearing in the R_{AA} and those that arise due to uncertainties on the unfolding procedure itself from the MC sample.

For uncertainties common to both the numerator and denominator of the R_{AA} , the uncertainties were taken as correlated. Thus for such uncertainties corresponding uncertainty on the ratio, $r = A/B$ was taken as:

$$\pm \delta r \Big|_C \equiv \frac{A \pm \delta A}{B \pm \delta B} - \frac{A}{B}. \quad (6.8)$$

For uncorrelated uncertainties, the uncertainty was propagated using the usual method:

$$\delta r \Big|_U \equiv \frac{A}{B} \sqrt{\left(\frac{\delta A}{A}\right)^2 + \left(\frac{\delta B}{B}\right)^2}. \quad (6.9)$$

6.7.1 Jet Energy Scale

The JES for HI jets and its uncertainties are discussed extensively in [143] and are summarized briefly in the following. The JES calibration for HI jets is derived using the existing calibration for TopoEM jets in 2012 8 TeV data, using a cross calibration procedure. Thus the HI JES inherits all of the TopoEM JES uncertainties, plus an additional contributions arising from the cross calibration procedure itself as well as adapting the energy scale from the 2012 conditions. These additional contributions are termed statistical (due to the statistical uncertainties in the derivation of the cross calibration), isolation (due to the selection of jets used to determine the cross calibration constants) and ‘‘OFC’’ (due to the difference in detector settings optimized for out of time pile up), and are generally small compared to the uncertainties inherited from the TopoEM jets. These latter uncertainties are composed of a ‘‘baseline’’ component (due to the statistics and modeling of the *insitu* calibration and uncertainty on the reference object energy scale) and flavor-dependent uncertainties.

An additional, centrality-dependent JES uncertainty was applied to the Pb+Pb data accounting for uncertainties in the calorimetric response to jets modified by quenching. The numerical inversion procedure is derived using the MC-simulated response to PYTHIA jets and the cross calibration accounts for additional aspects of the response not present in the

MC. However, changes in the distribution of particles within the jet caused by jet quenching may result in different response. More details are documented in Ref. [133].

Also the “DATA” component uncertainties arise from the variations on JES coming from simply varying the jet transverse momentum p_T by a factor of 1.5%. The “JET_SPECTRUM” component uncertainties comes from the variations on JES due to not applying the weight between the jet spectrum of the MC and the data sample discussed in section 6.2.

6.7.2 Jet Energy Resolution

In the initial evaluation of the ATLAS jet reconstruction performance in the Pb+Pb collisions [149], fits were performed to the JER using the functional form defined in the following equation:

$$\frac{\sigma[E_T]}{E_T} = \frac{a}{\sqrt{E_T}} \oplus \frac{b}{E_T} \oplus c, \quad (6.10)$$

where terms a and c represent the stochastic and constant contributions and are determined by the calorimeter response to shower development. The constant contribution controlled by b is directly influenced by the magnitude of the underlying event fluctuations. It was found by fixing b from an independent study of UE fluctuations, the JER can be described with a and c terms that were independent of centrality. Thus the variance in Δp_T is given by

$$\text{Var}[\Delta p_T] = \sigma_{\text{UE}} \oplus \sigma_0, \quad (6.11)$$

where the latter term is centrality independent and is the same as the JER for the pp collisions. In the MC sample used in the current analysis, the UE contribution to the calorimeter is fully determined by the data and thus contains no uncertainty. Therefore the uncertainty on the JER enters only through any potential inability of the MC sample to

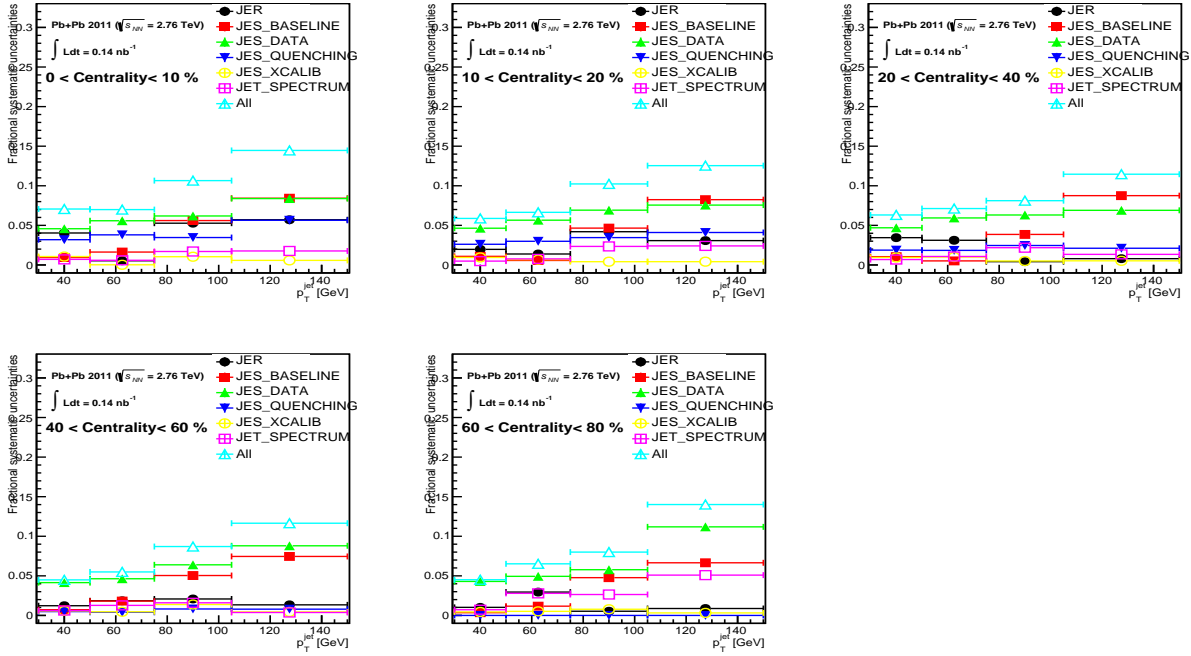


Figure 6.29: Systematics uncertainties on R_{AA} from JES and JER as a function of jet transverse momentum p_T in different centrality intervals.

describe the shower development in the calorimeter independent of the UE:

$$\delta\text{Var}[\Delta p_T] = \delta\sigma_0. \quad (6.12)$$

This uncertainty has been quantified in studies in the pp collisions. Systematic variations of the response matrices were generated by adding an additional Gaussian smearing to the reconstructed jet energies where the Gaussian σ is specified by the standard JetEnergyResolutionProvider tool [150]. Fig. 6.29 shows the systematics from different sources regarding the JES and the JER mentioned above.

6.7.3 Flavor Dependence of JES

The additional uncertainties are introduced to account for the impact of fragmentation differences in quark and gluon initiated jets in the jet response. These uncertainties are estimated by the systematic variations of Monte Carlo simulations. MC simulation samples based on the PYTHIA 6 event generator [138] with the AUET2B tune [151], and HERWIG++ [152] with the UE-EE-3 tune [153] were used to evaluate the impact of the jet fragmentation and other soft physics effects.

The JES uncertainty due to flavor effects is accounted as an additional physics analysis-dependent uncertainty. This uncertainty covers the possible shifts in the JES caused by uncertainties in the flavor composition of the sample (caused by a different flavor composition in data and in MC) and by the uncertainty on the flavor response itself (caused by a different calorimeter response depending on the jet flavor). The JES uncertainty due to flavor effects for a given event can be expressed as follows [154]:

$$\delta_{\text{flav}} = \delta f_g \times |\mathfrak{R}_q - \mathfrak{R}_g| \oplus f_g \times \delta \mathfrak{R}_g, \quad (6.13)$$

where the first and second terms are referred to as composition and response uncertainties, respectively. Here f_g is the gluon jet fraction, δf_g is the uncertainty on the gluon jet fraction. The transverse momentum response is defined as $\mathfrak{R} = p_{\text{T,jet}}^{\text{EM+JES}} / p_{\text{T,jet}}^{\text{truth}}$, while \mathfrak{R}_q and \mathfrak{R}_g are the jet responses for quark and gluon initiated jets respectively. The uncertainty on the difference between the response of quarks jets and gluon jets, denoted as $\delta \mathfrak{R}_g$, as well as the δf_g are estimated using the PYTHIA 6 and HERWIG++ MC simulations. Thus the expression may be written as:

$$\delta_{\text{flav}} = |f_g^{\text{Pythia}} - f_g^{\text{Herwig++}}| \times |\mathfrak{R}_q - \mathfrak{R}_g|^{\text{Pythia}} \oplus f_g^{\text{Pythia}} \times |\mathfrak{R}_g^{\text{Pythia}} - \mathfrak{R}_g^{\text{Herwig++}}|, \quad (6.14)$$

Fig. 6.30 shows the comparison of quark jets and gluon jets fraction of b -jet between the

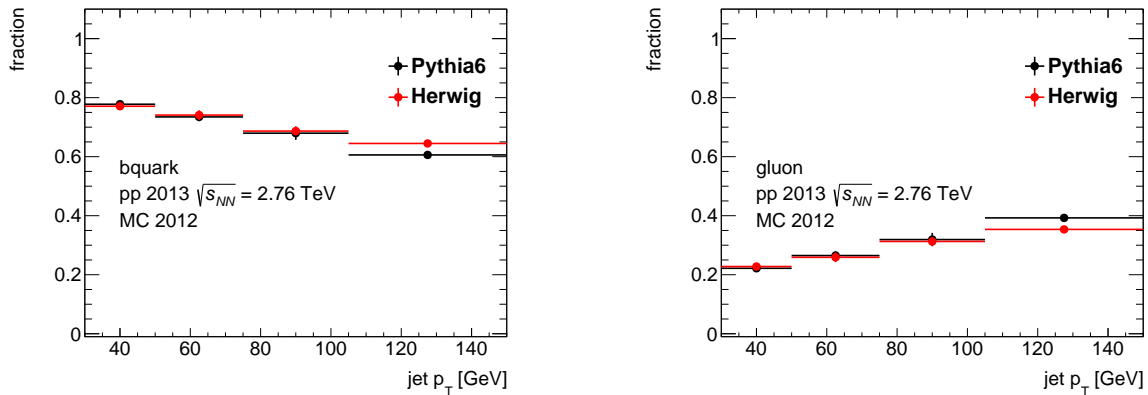


Figure 6.30: Left: Comparison of quark jet fraction of b -jet between the PYTHIA 6 and the HERWIG++ samples as a function of jet transverse momentum p_T . Right: Comparison of gluon jet fraction of b -jet between the PYTHIA 6 and the HERWIG++ samples as a function of jet transverse momentum p_T .

PYTHIA 6 and the HERWIG++ samples, respectively. The distribution agrees well except for the highest p_T bin. The reason is the fraction of b -jet comes from the gluon splitting differs in that p_T bin between these samples. Fig. 6.31 shows the response distribution of quark and gluon jets in the PYTHIA 6, respectively. The quark jets response \mathfrak{R}_q generally has value above one, and the gluon jets response \mathfrak{R}_g has value below one, which is expected.

Based on the information we got from Fig. 6.30 and Fig. 6.31, and also we know $|\mathfrak{R}_g^{Pythia} - \mathfrak{R}_g^{Herwig++}|$ is about 2.5% from Ref. [143]. The final JES uncertainties due to flavor effects are listed in Table 6.2:

Table 6.2: JES systematics uncertainties on R_{AA} due to flavor effects in each p_T bin in %

Jet p_T	Response	Composition	Total
30-50	0.55	0.016	0.55
50-75	0.66	0.015	0.66
75-105	0.80	0.027	0.80
105-150	0.98	0.14	0.99

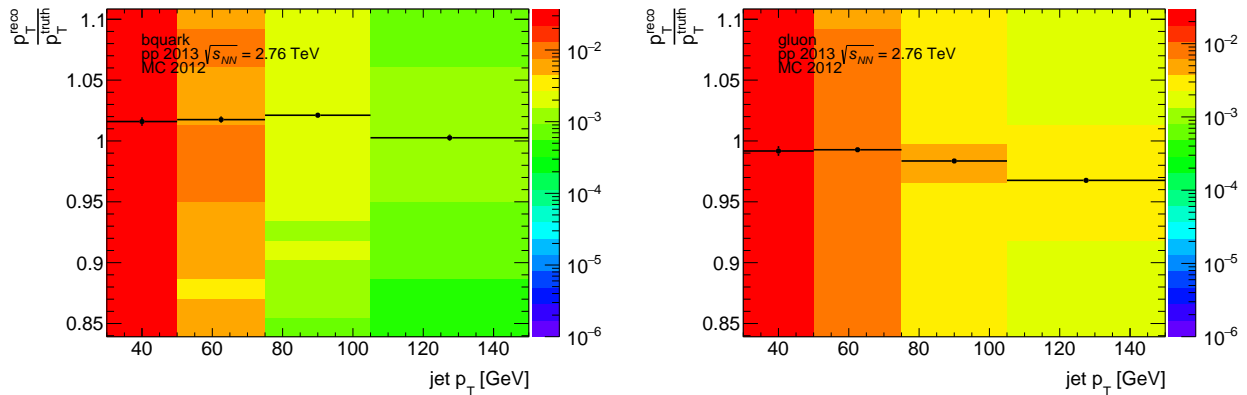


Figure 6.31: Left: Response distribution of quark jets as a function of jet transverse momentum p_T in the PYTHIA 6 sample. Right: Response distribution of quark jets as a function of jet transverse momentum p_T in the PYTHIA 6 sample.

6.7.4 JES between the Pb+Pb and the pp collisions

The differences between 2011 and 2012/2013 calorimeter response is not described in the MC sample, and this can be evaluated to study the jet energy scale (JES) for the Pb+Pb data sample. The tracks reconstructed in the inner detector (ID) and associated with the muon tagged jets are selected. With the same track selection cuts in section 6.4 and a requirement of ΔR cut of 0.4, where the ΔR stands for the separation between tracks and jets. The r_{trk} is defined as the ratio of the tracks scalar summed p_T and jet transverse momentum p_T for each jet:

$$r_{\text{trk}} = \frac{\sum p_T^{\text{trk}}}{p_T^{\text{jet}}}. \quad (6.15)$$

Both the data and the MC sample are used for r_{trk} evaluation. To account for the different templates ratio between the data and the MC sample, especially for the combinatoric background template, the fraction of each template in data is extracted from the template fitting procedure (section 6.4) and is applied to the MC sample for the r_{trk} estimation. In this part, the first two centrality bins 0-10% and 10-20% are combined as 0-20% for better statistics when evaluating the $\langle r_{\text{trk}} \rangle$ distribution. The mean r_{trk} distribution as a function of jet p_T is shown in Fig. 6.32 for both the 2011 Pb+Pb data sample and the MC sample

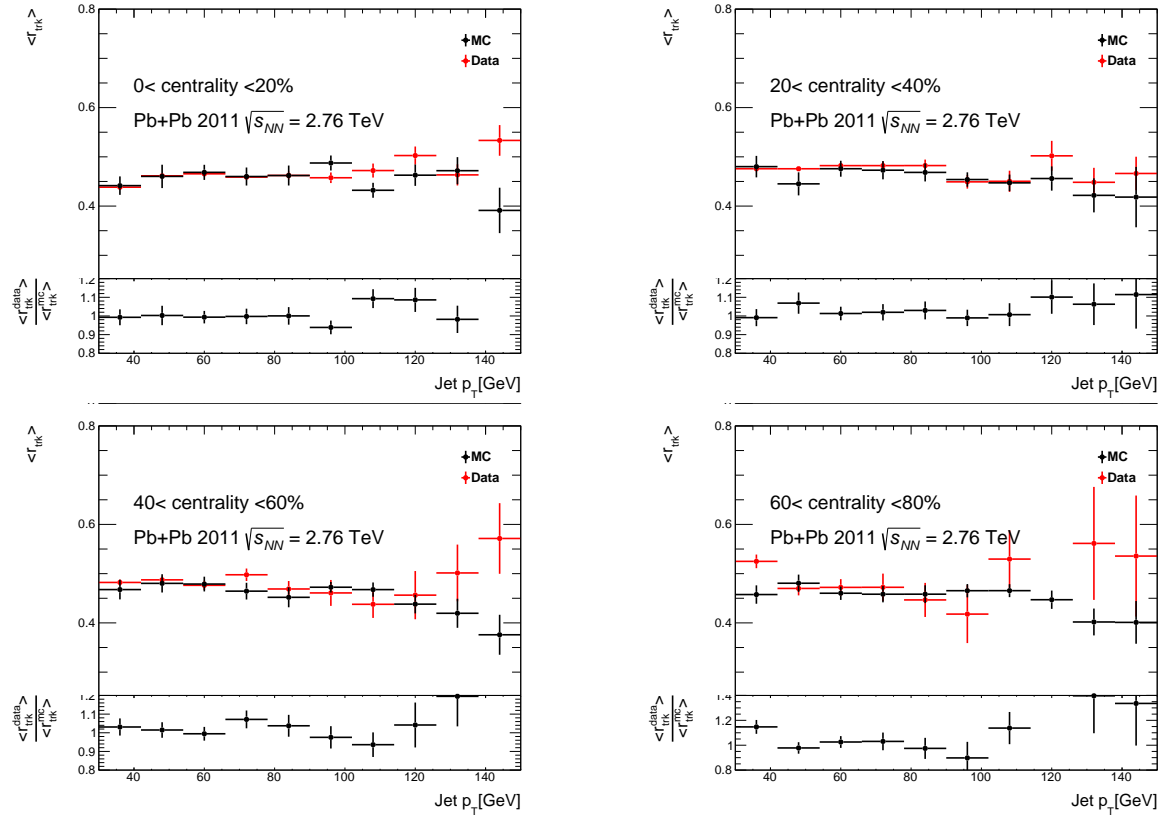


Figure 6.32: r_{trk} distributions between MC and data and their ratio as a function of jet p_{T} in centrality intervals in Pb+Pb sample.

in different centrality bins. The r_{trk} distribution for the 2013 pp data sample and the MC sample is shown in Fig. 6.33. Their ratio $R = \frac{\langle r_{\text{trk}}^{\text{data}} \rangle}{\langle r_{\text{trk}}^{\text{MC}} \rangle}$ is shown on the bottom. At the same time, the ratio of R calculated above in the Pb+Pb sample over the pp sample is evaluated as a systematic study on the JES in the Pb+Pb collisions. Fig. 6.34 shows the “double” ratio distribution as a function of jet p_{T} in different centrality intervals, and it is fitted to a constant in order to study this quantitatively. The uncertainties on the fitting are considered as the systematics uncertainties.

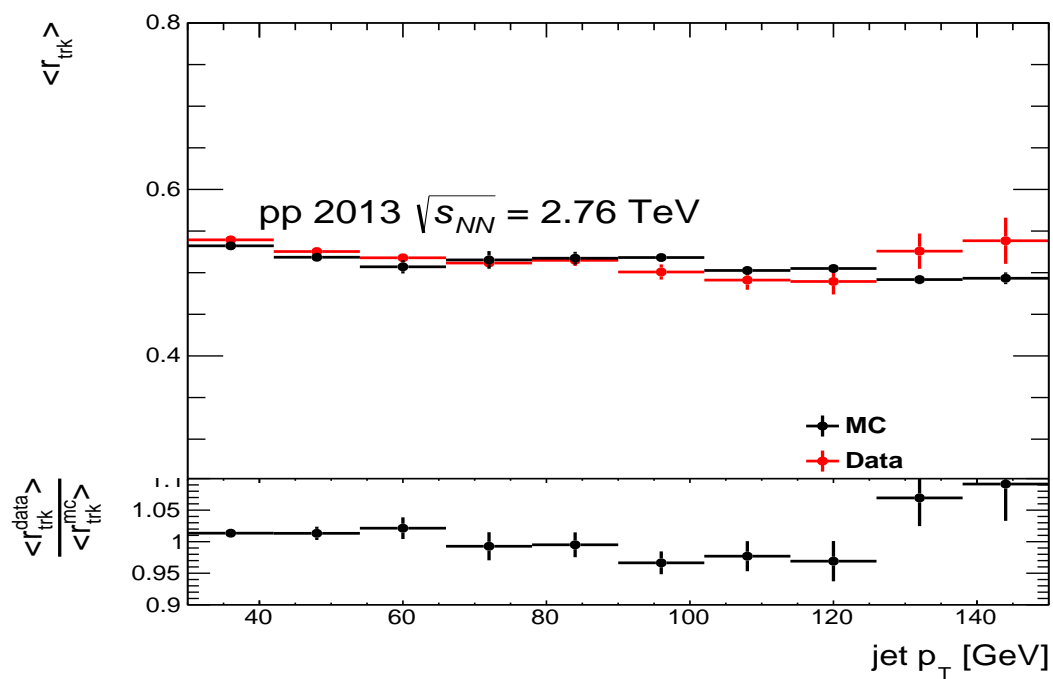


Figure 6.33: r_{trk} distributions between MC and data and their ratio as a function of jet p_T in pp sample.

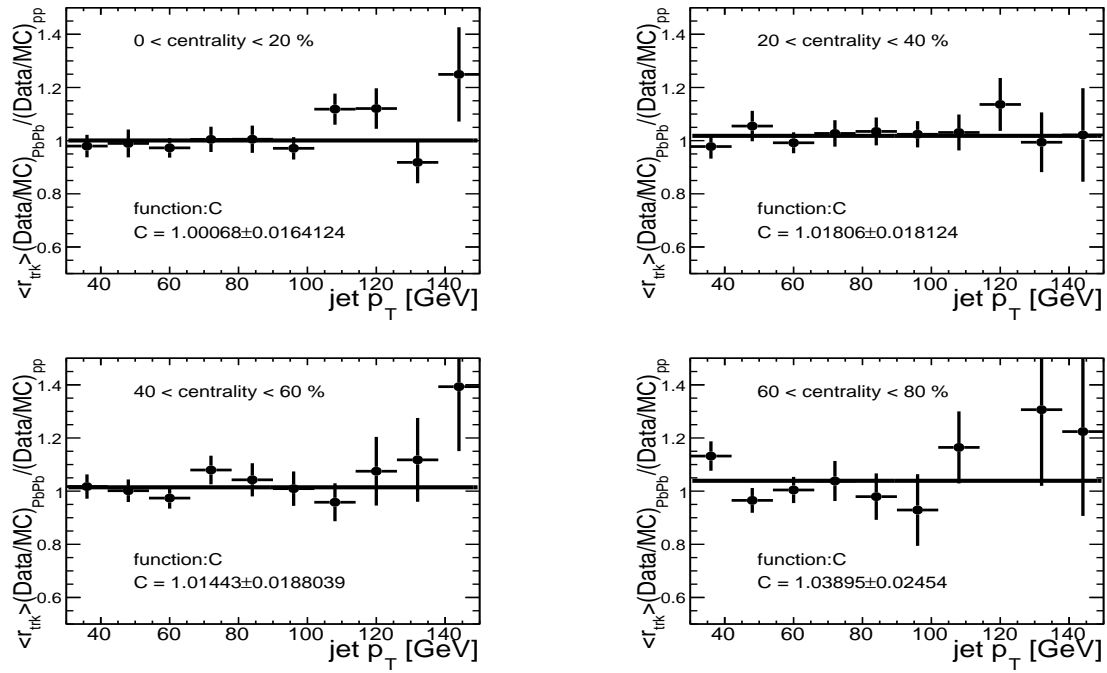


Figure 6.34: Systematics uncertainties on R_{AA} from JES between Pb+Pb and pp as a function of jet transverse momentum p_T are shown in different centrality intervals.

6.7.5 Uncertainties on b -jet Fraction

Different b -jet component

The influence of the different b -hadrons on the shape of the b -template has been studied by varying their contribution by a factor of 2, like $B^{+/-}$, B_0 and B_s components.

Relative c -jet to light-jet ratio

In the template fitting procedure we fix the relative ratio between c -jet and light-jet according to the information in the MC sample. In this section the relative ratio is varied up and down by a factor of 2 to see what effect it can have on the signal fraction. Fig. 6.35 shows the systematics uncertainties on R_{AA} distribution from b -jet fraction variations from template fitting procedure in different centrality bins. The “doubleBstar”, “doubleBsubs”, and “doubleBaryon” represent the uncertainties coming from doubling the B^* , the B_s and the B baryon, respectively. The “upCL2” and “downCL2” represent the uncertainties coming from varying the relative charm to light ratio by a factor of 2 and 0.5, respectively.

6.7.6 Uncertainties on efficiency

The influence of varying the muon reconstruction efficiency (Fig. 5.16, 5.17) and the muon trigger efficiency (Fig. 5.1, 5.8) in both the Pb+Pb and the pp sample is studied in this section. The one σ confidence interval is applied when evaluating the uncertainties of efficiencies. Fig. 6.36 shows the uncertainties on final b -jet suppression R_{AA} in different centrality intervals based on the variations of efficiencies.

6.7.7 Uncertainties on $\langle T_{AA} \rangle$ and luminosity

The uncertainties on $\langle T_{AA} \rangle$ were evaluated by varying the following inputs into the Glauber Model analysis: parameters a and R in the Woods-Saxon parameterization of the spacial nu-

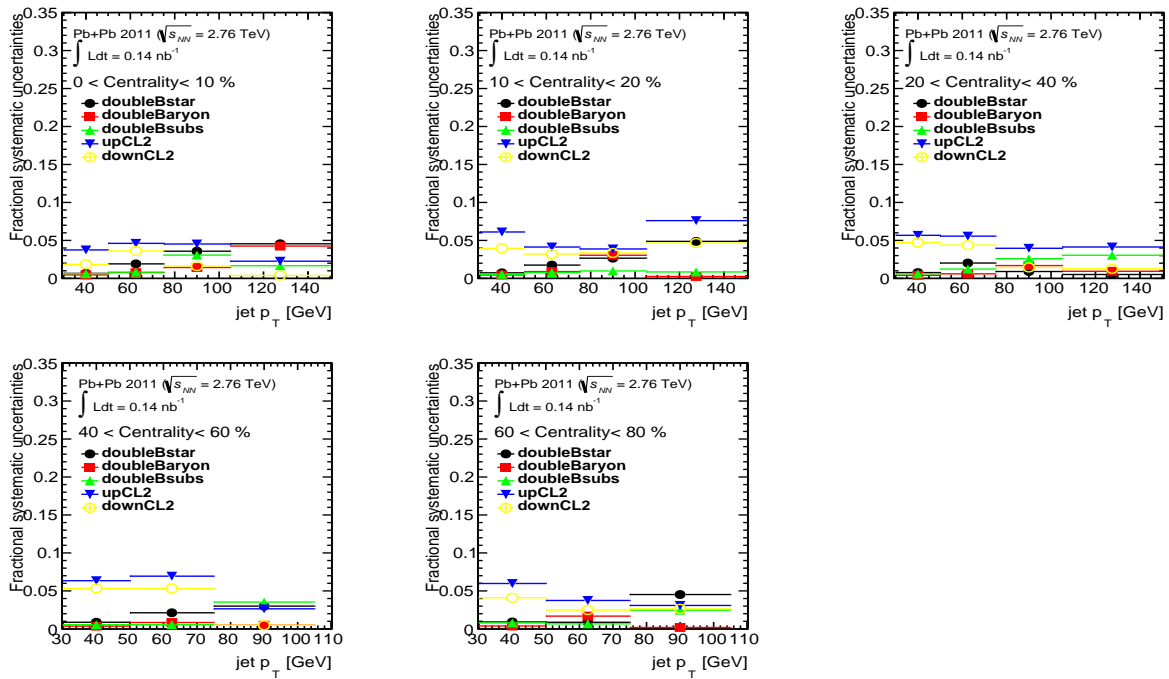


Figure 6.35: Systematics uncertainties on R_{AA} from b -jet fraction variations from template fitting procedure as a function of jet transverse momentum p_T in different centrality intervals.

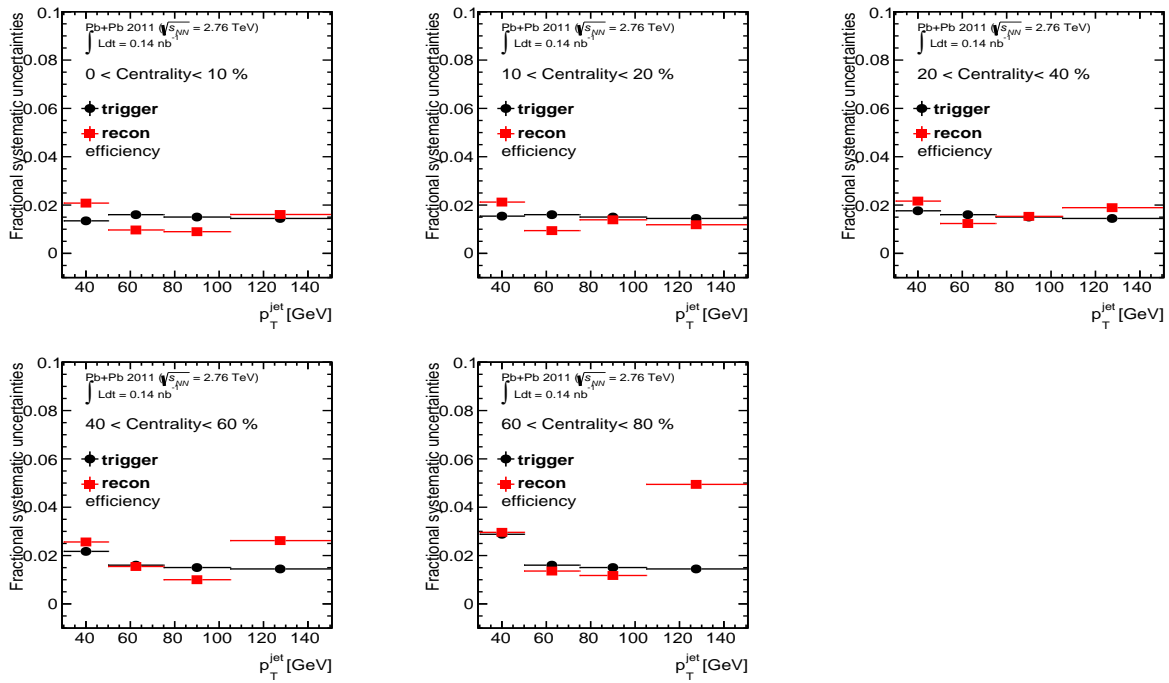


Figure 6.36: Systematics on R_{AA} from muon trigger efficiency and muon reconstruction efficiency as a function of jet transverse momentum p_T in different centrality intervals.

clear density distribution, the total inelastic nucleon-nucleon cross section and the minimum bias event selection events efficiency. The uncertainty analysis is described in Ref. [135]. The T_{AA} values and their uncertainties were obtained from the GlauberCalculator analysis software tool and are shown in Table 5.1.

Chapter 7

Results

7.1 Heavy Flavor Fractions

The extracted f_B with its statistical and systematics uncertainties is shown in Fig. 7.1 in the Pb+Pb and the pp samples. Table 7.1 shows the b -jet fraction in each jet transverse momentum p_T and centrality bin in the Pb+Pb and the pp samples.

Table 7.1: Signal b -jet ratio in each centrality and p_T bin from Pb+Pb and pp sample

Jet p_T	Centrality(%)	0-10	10-20	20-40	40-60	60-80	pp
	30-50	0.315	0.303	0.303	0.291	0.305	0.269
	50-75	0.278	0.341	0.269	0.241	0.279	0.275
	75-105	0.304	0.298	0.261	0.344	0.391	0.264
	105-150	0.265	0.675	0.356			0.369

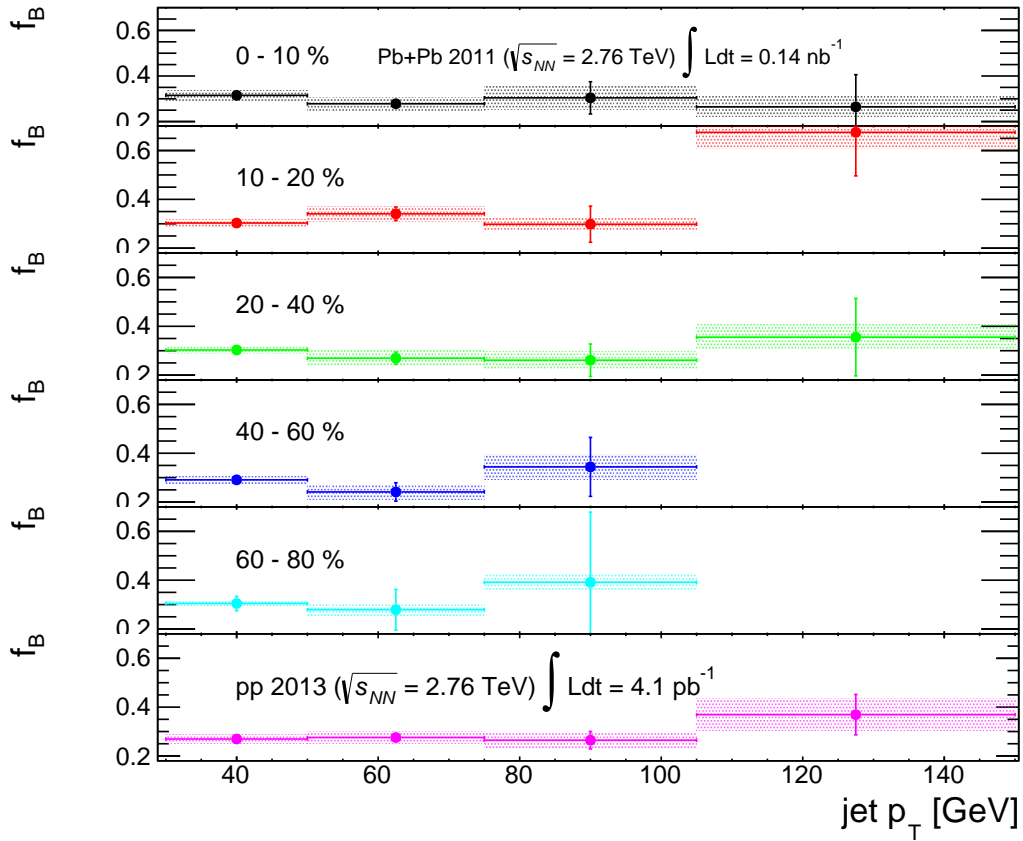


Figure 7.1: b -jet fraction distribution in different centrality intervals in Pb+Pb and pp sample.

7.2 b-jet Spectra

The per event normalized b -jet yield is defined as:

$$Yield(p_T) = \frac{1}{N_{\text{evt}} < T_{AA} >} N_{\text{jet}}(p_T) f_B(p_T) C(p_T) \Big|_{\text{cent}} \quad (7.1)$$

In this equation, N_{jet} is incorporated with the muon reconstruction efficiency ϵ_{reco} and the muon trigger efficiency ϵ_{trig} , which are functions of muon transverse momentum p_T . $\frac{1}{\epsilon_{\text{reco}}\epsilon_{\text{trig}}}$ is multiplied to reweight each jet muon pair in order to calculate the b -jet yield. f_B is the b -jet fraction from template fitting, and C is the b -jet correction factor from the unfolding procedure which is evaluated separately for each centrality and jet transverse momentum p_T bin. N_{jet} denotes the number of jet-muon pairs we have been studied. N_{evt} is the number of events and by construction it is proportional to the centrality interval used. The yields are shown in Fig. 7.2 for the Pb+Pb and the pp sample.

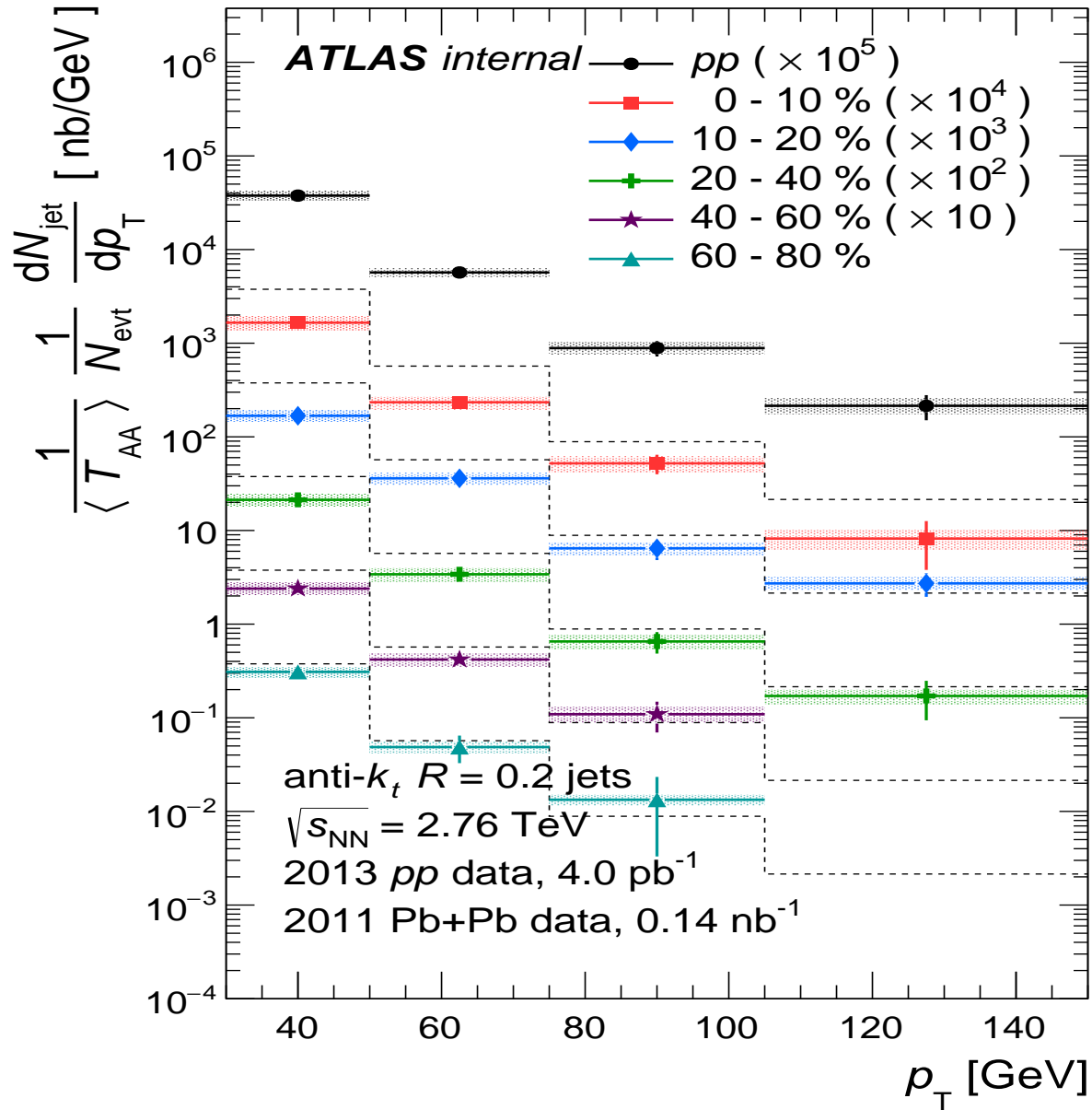


Figure 7.2: The b -jet yield as a function of jet transverse momentum p_T is shown for various centrality classes of Pb+Pb collisions as indicated in the legend. The yields are scaled by the equivalent number of minimum bias events sampled and by T_{AA} . The spectra are also scaled by powers of 10 for visibility. The b -jet cross section in pp collisions is also shown. The systematic uncertainties are shown as shaded boxes with transparent color filled. The statistical uncertainties are represented as error bars.

7.3 b -jet Suppression

Measurements of the modification of jet observables as a function of collision centrality can provide insight into the quenching mechanism and quantitative constraints on the medium transport coefficients. Energy loss will result in a systematic reduction in the jet yield at fixed jet transverse momentum p_T . Thus it is expected that hard scattering rates will be suppressed in central collisions relative to peripheral or the pp collisions. Central collisions receive an enhancement in hard scattering rate due to the larger geometric overlap between the colliding nuclei, resulting in a larger per-collision nucleon-nucleon luminosity. The centrality dependence of hard scattering rates must then be normalized by a factor, T_{AA} accounting for this geometric enhancement to allow for a proper assessment of the quenching effects. The suppression of b -jet can be quantified by the nuclear modification factor R_{AA} :

$$R_{AA} = \frac{\frac{1}{N_{\text{evt}}^{\text{tot}} \langle T_{AA} \rangle} \left. \frac{d^2 N_{b\text{-jet}}}{dp_T dy} \right|_{\text{cent}}}{\left. \frac{d^2 \sigma_{b\text{-jet}}}{dp_T dy} \right|_{pp}}, \quad (7.2)$$

Fig. 7.3 and Fig. 7.4 show the b -jet R_{AA} distribution as a function of jet transverse momentum p_T and N_{part} as a preliminary result.

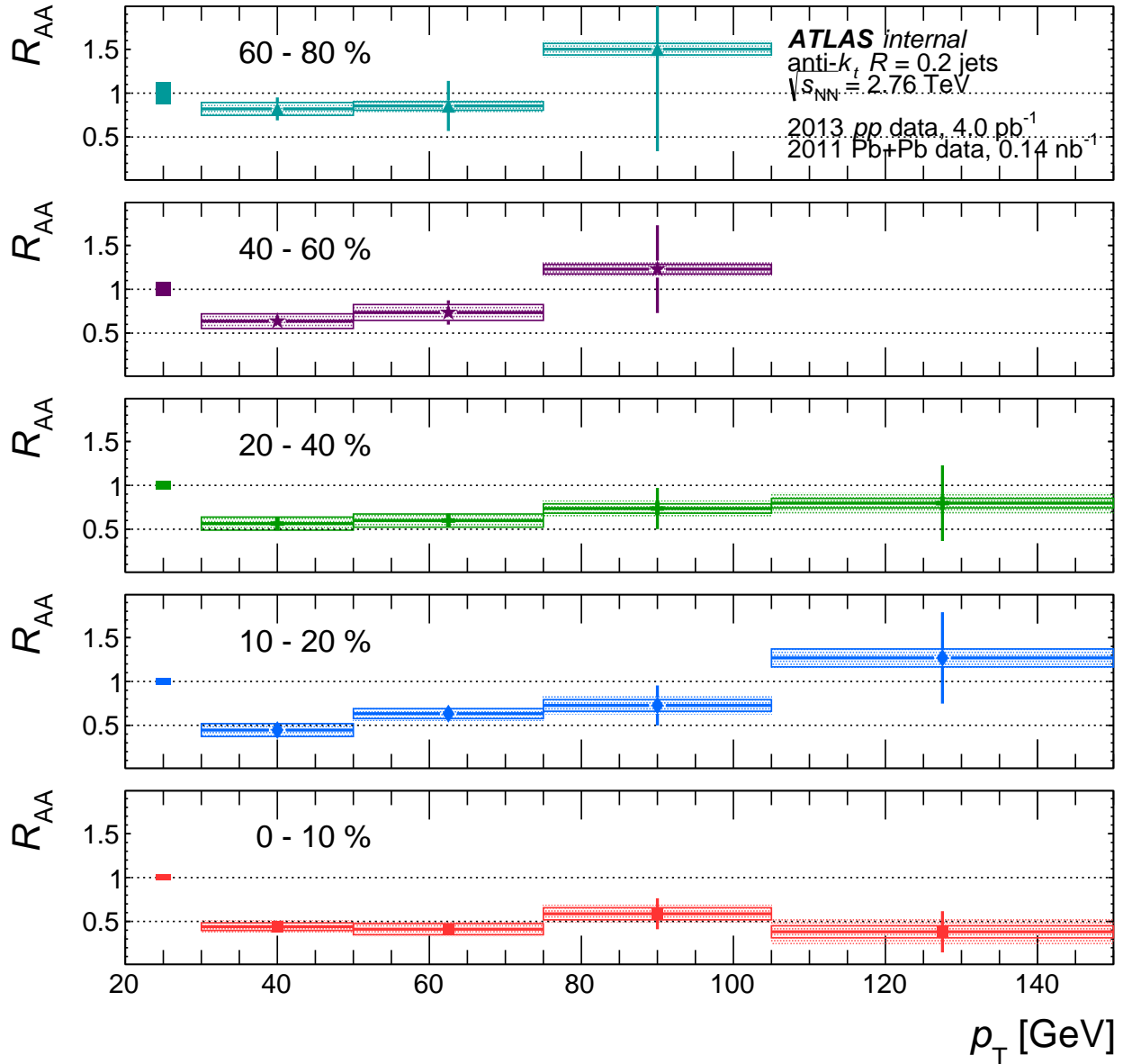


Figure 7.3: b -jet R_{AA} distribution as a function of jet transverse momentum p_T . Each panel indicates a different centrality interval. The fractional normalization uncertainties coming from the luminosity and the $\langle T_{AA} \rangle$ factors are indicated separately as shaded boxes centered at one with solid color filled. The systematics uncertainties due to the template fitting are shown as open boxes and they are uncorrelated in p_T . The remaining systematics uncertainties are fully correlated in p_T and are indicated by shaded boxes with transparent color filled. The statistical uncertainties are represented as error bars.

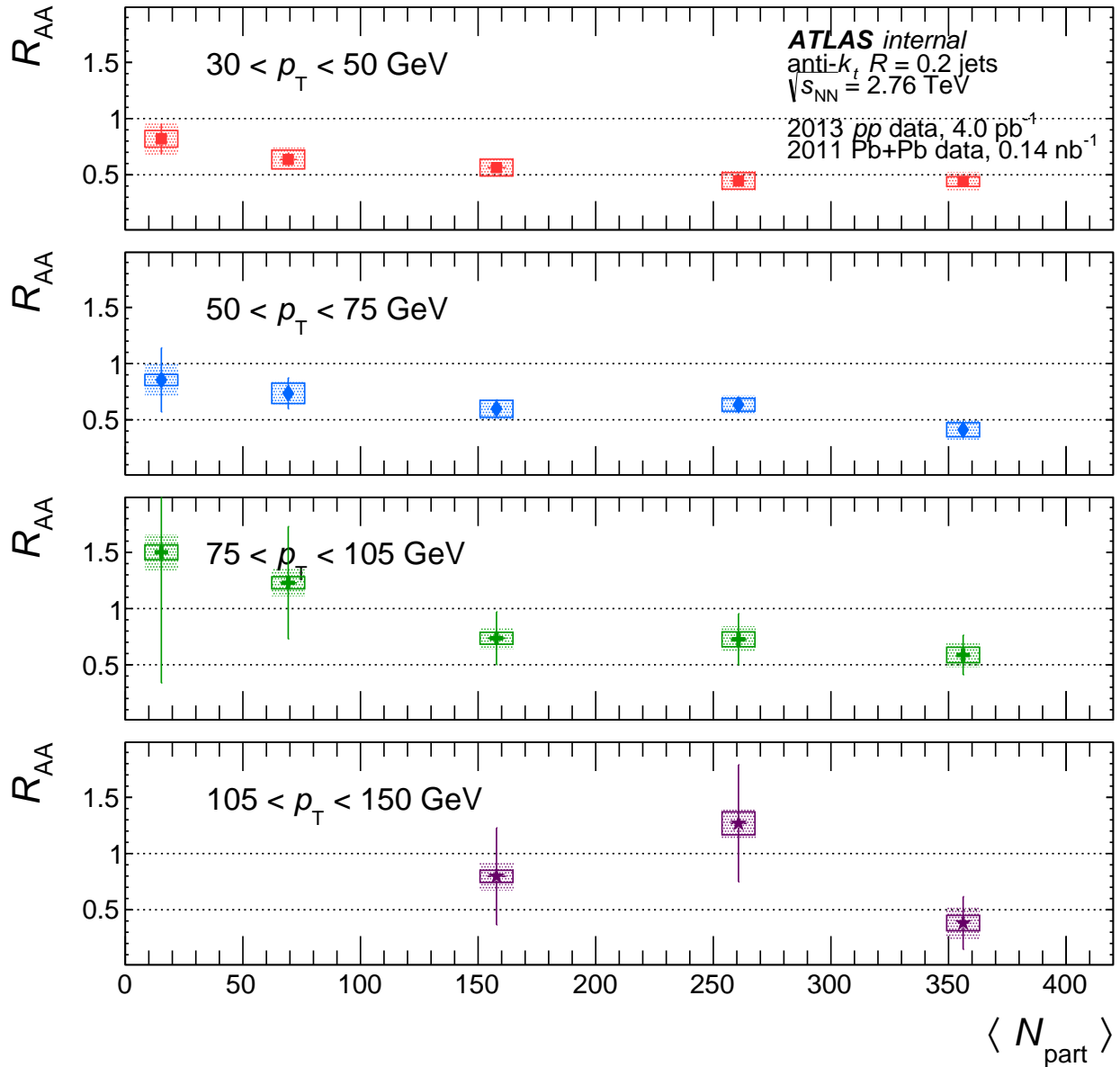


Figure 7.4: b -jet R_{AA} distribution as a function of N_{part} . Each panel indicates a different range in jet transverse momentum p_T . The systematics uncertainties due to the template fitting are shown as open boxes and they are uncorrelated in N_{part} . The remaining systematic uncertainties are partially correlated in N_{part} and are shown as shaded boxes with transparent color filled, including the fractional normalization uncertainties coming from the luminosity and the $\langle T_{AA} \rangle$ factors. The statistical uncertainties are represented as error bars.

Chapter 8

Conclusions

The inclusive b -jet suppression R_{AA} has been measured using muons in jets with the $\sqrt{s_{NN}} = 2.76$ TeV 2011 Pb+Pb collisions recorded by the ATLAS detector, where a b -jet corresponds to a jet with at least one muon clustered with the anti- k_t algorithm with parameter $R = 0.2$. The b -jets of $p_T^{b\text{-jet}}$ between 30 GeV - 150 GeV and $|\eta| < 2.1$ are identified by the semileptonic decay of beauty hadrons. Muons originating from background sources, primarily Charm hadrons, pion and kaon decays, have been removed from the analysis using template fits to the distribution of a quantity (p_T^{rel}) capable of statistically distinguishing between signal and background. The measured nuclear modification factor R_{AA} has been presented in different centrality bins as a function of the b -jet transverse momentum p_T . The results of R_{AA} indicate that the yield of the most central event (0-10%) experiences more suppression compared to the most peripheral event (60-80%) by a factor of approximate 2.

In Fig. 7.3, the R_{AA} is almost independent of transverse momentum p_T . It increases slightly from low p_T to high p_T for most of the centrality intervals without significant variation observed. The most central bin (0-10%) has a little variation on p_T , and the values are consistent with the increasing trend within uncertainties. Fig. 8.1 shows the distribution of b -jet R_{AA} as a function of jet transverse momentum p_T in Pb+Pb collisions between the ATLAS experiment and theory calculation. The values are consistent within uncertainties,

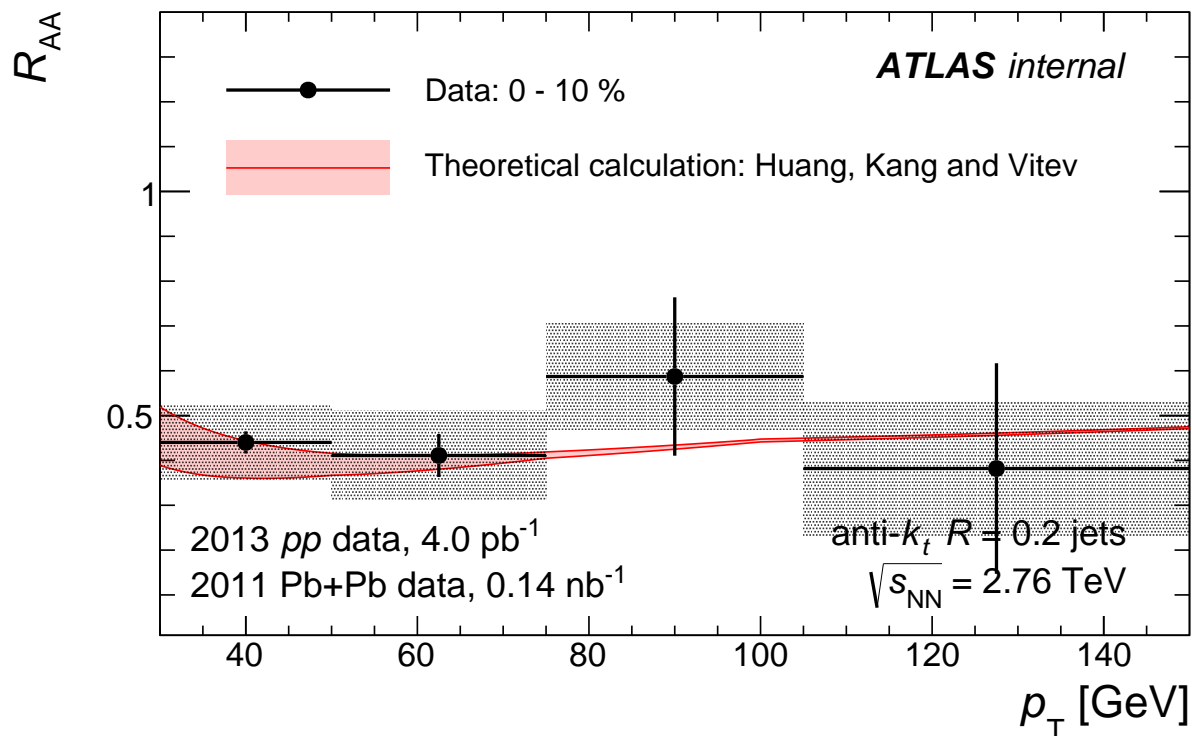


Figure 8.1: b -jet R_{AA} distribution as a function of jet transverse momentum p_T in Pb+Pb collisions between the ATLAS experiment and theory calculation [155]. The systematics uncertainties are shown as shaded boxes with transparent color filled. The statistical uncertainties are represented as error bars.

and slightly increasing trend with p_T is predicted by the theoretical calculation of the parton energy loss [155].

Fig. 7.4 shows the centrality dependence of the b -jet R_{AA} . It decreases smoothly from peripheral to central collisions for most of the jet p_T intervals, which is expected in experiment because heavy quarks are more suppressed in more central collisions. The highest jet p_T bin (105-150 GeV) has a little variation on $\langle N_{\text{part}} \rangle$, and the values are consistent with the decreasing trend within uncertainties. As mentioned in section 3.4, the CMS experiment has measured the b -jet suppression for the first time in the Pb+Pb collisions with $\sqrt{s_{NN}} = 2.76$ TeV at the LHC. The b -jet suppression measurement in this thesis is in different transverse

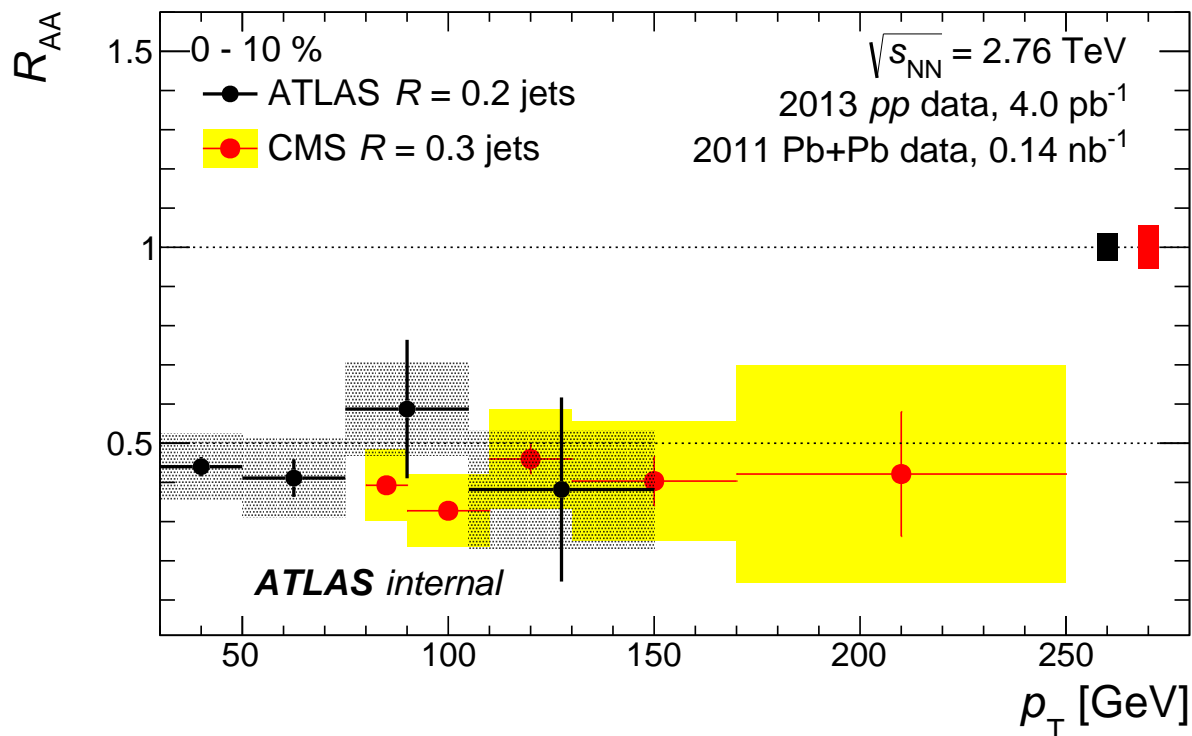


Figure 8.2: b -jet R_{AA} distribution as a function of jet transverse momentum p_T in Pb+Pb collisions between the ATLAS experiment and the CMS experiment [119]. The fractional normalization uncertainties coming from the luminosity and the $\langle T_{AA} \rangle$ factors are indicated separately as shaded boxes centered at one. The systematics uncertainties are shown as shaded boxes. The statistical uncertainties are represented as error bars.

momentum range. The comparison between these two experiments in the most central bin (0-10%) is shown in Fig. 8.2. In Fig. 8.2, the R_{AA} in p_T bins of 110-130 GeV and 130-170 GeV agree with the R_{AA} in p_T bin of 105-150 GeV presented in this analysis. However, the R_{AA} of the CMS measurement in the p_T bins of 80-90 GeV and 90-110 GeV are below the R_{AA} values measured in p_T bin of 75-105 GeV in this analysis. Fig. 8.2 also shows the measurement presented in this thesis provides ability to study the b -jet suppression in the lower p_T range of 30-75 GeV, which brings more insights to the QGP medium studies in that range.

The suppression of the electrons from heavy flavor decays measured in the PHENIX

experiment and the STAR experiment at the RHIC can also provide meaningful comparison with the b -jet suppression results presented here. As mentioned in section 3.4, Fig. 3.7 - 3.8 show the non-photonic electrons has a suppression level of around 0.3 for electron p_T above 4 GeV in the most central collisions (0-10%). The electrons from heavy flavor hadron decays contain the decays from both the bottoms quarks and the charm quarks. Due to the fact that the bottom quarks experience weaker suppression compared to the charm quarks, the results of b -jet suppression are expected to have higher values than the results of non-photonic electrons. At the same time, the suppression factors are not required to be related between jet and single particle.

As higher energy is achieved at the LHC, more data will be available to separate the $b\bar{b}$ produced in the parton shower from other b -jet. The separation of $b\bar{b}$ production can lead to insightful measurements such as double b -jets tagging, asymmetry of double b -jets and etc. Also the higher statistics will improve the precision of the measurements of b -jet. It provides more direct interpretation of the heavy flavor jet suppression and more thorough understanding of their interaction with the QGP medium.

Bibliography

- [1] A. Majumder and M. Van Leeuwen, *The Theory and Phenomenology of Perturbative QCD Based Jet Quenching*, Prog.Part.Nucl.Phys. **A66** (2011) 41–92, arXiv:1002.2206 [hep-ph].
- [2] Y. L. Dokshitzer and D. Kharzeev, *Heavy quark colorimetry of QCD matter*, Phys.Lett. **B519** (2001) 199–206, arXiv:hep-ph/0106202 [hep-ph].
- [3] M. Gell-Mann and Y. Ne’eman, *The Eightfold Way*. Westview Press, 2000.
- [4] V. Barnes, P. Connolly, D. Crennell, B. Culwick, W. Delaney, et al., *Observation of a Hyperon with Strangeness -3*, Phys. Rev. Lett. **12** (1964) 204–206.
- [5] M. Gell-Mann, *Symmetries of Baryons and Mesons*, Phys. Rev. **125** (1962) 1067–1084, <http://link.aps.org/doi/10.1103/PhysRev.125.1067>.
- [6] J. D. Bjorken, *Asymptotic Sum Rules at Infinite Momentum*, Phys. Rev. **179** (1969) 1547–1553, <http://link.aps.org/doi/10.1103/PhysRev.179.1547>.
- [7] M. Breidenbach, J. I. Friedman, H. W. Kendall, E. D. Bloom, D. Coward, et al., *Observed Behavior of Highly Inelastic electron-Proton Scattering*, Phys. Rev. Lett. **23** (1969) 935–939.
- [8] E. D. Bloom, D. Coward, H. DeStaebler, J. Drees, G. Miller, et al., *High-Energy*

- Inelastic $e p$ Scattering at 6-Degrees and 10-Degrees*, Phys. Rev. Lett. **23** (1969) 930–934.
- [9] J. D. Bjorken and E. A. Paschos, *Inelastic Electron-Proton and γ -Proton Scattering and the Structure of the Nucleon*, Phys. Rev. **185** (1969) 1975–1982,
<http://link.aps.org/doi/10.1103/PhysRev.185.1975>.
- [10] R. P. Feynman, *Very High-Energy Collisions of Hadrons*, Phys. Rev. Lett. **23** (1969) 1415–1417, <http://link.aps.org/doi/10.1103/PhysRevLett.23.1415>.
- [11] M. Gell-Mann and F. E. Low, *Quantum Electrodynamics at Small Distances*, Phys. Rev. **95** (1954) 1300–1312, <http://link.aps.org/doi/10.1103/PhysRev.95.1300>.
- [12] K. G. Wilson, *Non-Lagrangian Models of Current Algebra*, Phys. Rev. **179** (1969) 1499–1512, <http://link.aps.org/doi/10.1103/PhysRev.179.1499>.
- [13] C. G. Callan, *Broken Scale Invariance in Scalar Field Theory*, Phys. Rev. D **2** (1970) 1541–1547, <http://link.aps.org/doi/10.1103/PhysRevD.2.1541>.
- [14] K. Symanzik, *Small distance behaviour in field theory and power counting*, Communications in Mathematical Physics **18** no. 3, (1970) 227–246,
<http://dx.doi.org/10.1007/BF01649434>.
- [15] H. D. Politzer, *Reliable Perturbative Results for Strong Interactions?*, Phys. Rev. Lett. **30** (1973) 1346–1349, <http://link.aps.org/doi/10.1103/PhysRevLett.30.1346>.
- [16] D. J. Gross and F. Wilczek, *Ultraviolet Behavior of Non-Abelian Gauge Theories*, Phys. Rev. Lett. **30** (1973) 1343–1346,
<http://link.aps.org/doi/10.1103/PhysRevLett.30.1343>.
- [17] D. J. Gross and F. Wilczek, *Asymptotically Free Gauge Theories. I*, Phys. Rev. D **8** (1973) 3633–3652, <http://link.aps.org/doi/10.1103/PhysRevD.8.3633>.

- [18] D. J. Gross and F. Wilczek, *Asymptotically free gauge theories. II*, Phys. Rev. D **9** (1974) 980–993, <http://link.aps.org/doi/10.1103/PhysRevD.9.980>.
- [19] H. D. Politzer, *Asymptotic freedom: An approach to strong interactions*, Physics Reports **14** no. 4, (1974) 129 – 180, <http://www.sciencedirect.com/science/article/pii/0370157374900143>.
- [20] H. Georgi and H. D. Politzer, *Electroproduction scaling in an asymptotically free theory of strong interactions*, Phys. Rev. D **9** (1974) 416–420, <http://link.aps.org/doi/10.1103/PhysRevD.9.416>.
- [21] J. Xu, *Perturbative and Nonperturbative Aspects of Jet Quenching in Near-Critical Quark-Gluon Plasmas*. PhD thesis, Columbia U., 2016. <http://doi.org/10.7916/D84Q7TSD>.
- [22] Particle Data Group Collaboration, J. Beringer et al., *Review of Particle Physics (RPP)*, Phys. Rev. **D86** (2012) 010001.
- [23] E. Fermi, *High Energy Nuclear Events*, Progress of Theoretical Physics **5** no. 4, (1950) 570–583, <http://ptp.oxfordjournals.org/content/5/4/570.full.pdf+html>, <http://ptp.oxfordjournals.org/content/5/4/570.abstract>.
- [24] R. Hagedorn and J. Ranft, *Statistical thermodynamics of strong interactions at high energies*, Nuovo Cimento, Suppl. **6** no. CERN-TH-851, (1967) 169–354. 186 p, <https://cds.cern.ch/record/938671>.
- [25] J. C. Collins and M. J. Perry, *Superdense Matter: Neutrons or Asymptotically Free Quarks?*, Phys. Rev. Lett. **34** (1975) 1353–1356, <http://link.aps.org/doi/10.1103/PhysRevLett.34.1353>.

- [26] E. V. Shuryak, *Quantum chromodynamics and the theory of superdense matter*, Physics Reports **61** no. 2, (1980) 71 – 158,
<http://www.sciencedirect.com/science/article/pii/0370157380901052>.
- [27] A. Bazavov, T. Bhattacharya, M. Cheng, N. H. Christ, C. DeTar, S. Ejiri, S. Gottlieb, R. Gupta, U. M. Heller, K. Huebner, C. Jung, F. Karsch, E. Laermann, L. Levkova, C. Miao, R. D. Mawhinney, P. Petreczky, C. Schmidt, R. A. Soltz, W. Soeldner, R. Sugar, D. Toussaint, and P. Vranas, *Equation of state and QCD transition at finite temperature*, Phys. Rev. D **80** (2009) 014504,
<http://link.aps.org/doi/10.1103/PhysRevD.80.014504>.
- [28] S. Borsanyi, G. Endrodi, Z. Fodor, A. Jakovac, S. D. Katz, S. Krieg, C. Ratti, and K. K. Szabo, *The QCD equation of state with dynamical quarks*, JHEP **11** (2010) 077, arXiv:1007.2580 [hep-lat].
- [29] F. Karsch, *Lattice QCD at high temperature and density*, Lect. Notes Phys. **583** (2002) 209–249, arXiv:hep-lat/0106019 [hep-lat].
- [30] T. C. on the Assessment of, O. for Nuclear Physics; Board on Physics, A. D. on Engineering, and P. S. N. R. Council, *Nuclear Physics: Exploring the Heart of Matter*. <https://www.nap.edu/read/13438/chapter/4#91>.
- [31] A. Collaboration, *ATLAS One of the first Heavy ions collisions with stable beams-Event Display - November 2015*, General Photo, Nov, 2015.
- [32] J. D. Bjorken, *Highly relativistic nucleus-nucleus collisions: The central rapidity region*, Phys. Rev. D **27** (1983) 140–151,
<http://link.aps.org/doi/10.1103/PhysRevD.27.140>.
- [33] E. Iancu, *QCD in heavy ion collisions*, pp. , 197–266. 2014. arXiv:1205.0579

- [hep-ph].
<https://inspirehep.net/record/1113441/files/arXiv:1205.0579.pdf>.
- [34] M. L. Miller, K. Reygers, S. J. Sanders, and P. Steinberg, *Glauber modeling in high energy nuclear collisions*, *Ann.Rev.Nucl.Part.Sci.* **57** (2007) 205–243, arXiv:nucl-ex/0701025 [nucl-ex].
- [35] C. D. Jager, H. D. Vries, and C. D. Vries, *Nuclear charge- and magnetization-density-distribution parameters from elastic electron scattering*, *Atomic Data and Nuclear Data Tables* **14** no. 5, (1974) 479 – 508, <http://www.sciencedirect.com/science/article/pii/S0092640X74800021>.
- [36] C.-Y. Wong, *Introduction to High-Energy Heavy-Ion Collisions*. 1994.
- [37] H1 Collaboration, C. Adloff et al., *Deep inelastic inclusive e p scattering at low x and a determination of α_s* , *Eur. Phys. J.* **C21** (2001) 33–61, arXiv:hep-ex/0012053 [hep-ex].
- [38] E. Iancu and R. Venugopalan, *The Color glass condensate and high-energy scattering in QCD*, in *In *Hwa, R.C. (ed.) et al.: Quark gluon plasma* 249-3363*. 2003. arXiv:hep-ph/0303204 [hep-ph].
- [39] L. McLerran, *RHIC physics: The Quark gluon plasma and the color glass condensate: Four lectures*, 2003. arXiv:hep-ph/0311028 [hep-ph].
- [40] Y. Chen, *Charged Particle Multiplicity and Open Heavy Flavor Physics in Relativistic Heavy Ion Collisions at the LHC*. PhD thesis, Columbia U., 2013. <http://hdl.handle.net/10022/AC:P:19740>.
- [41] J. J. Torsti, *Cosmic-ray spectra and Hagedorn's thermodynamic model*, *Il Nuovo Cimento B (1971-1996)* **25** no. 2, (1975) 829–841, <http://dx.doi.org/10.1007/BF02724755>.

- [42] B. Müller, *Investigation of Hot QCD Matter: Theoretical Aspects*, Phys. Scripta **T158** (2013) 014004, arXiv:1309.7616 [nucl-th].
- [43] P. F. Kolb and U. W. Heinz, *Hydrodynamic description of ultrarelativistic heavy ion collisions*, arXiv:nucl-th/0305084 [nucl-th].
- [44] H. Stoecker and W. Greiner, *High-Energy Heavy Ion Collisions: Probing the Equation of State of Highly Excited Hadronic Matter*, Phys. Rept. **137** (1986) 277–392.
- [45] K. Geiger, *VNI 3.1 MC-simulation program to study high-energy particle collisions in QCD by space-time evolution of parton-cascades and parton-hadron conversion*, Computer Physics Communications **104** no. 1, (1997) 70 – 160,
<http://www.sciencedirect.com/science/article/pii/S0010465597000489>.
- [46] S. A. Bass, B. Muller, and D. K. Srivastava, *Parton rescattering and screening in Au+Au collisions at RHIC*, Phys. Lett. **B551** (2003) 277–283,
arXiv:nucl-th/0207042 [nucl-th].
- [47] B. Zhang, C. M. Ko, B.-A. Li, and Z. Lin, *Multiphase transport model for relativistic nuclear collisions*, Phys. Rev. C **61** (2000) 067901,
<http://link.aps.org/doi/10.1103/PhysRevC.61.067901>.
- [48] B. Muller, *The 'Perfect' Fluid Quenches Jets Almost Perfectly*, arXiv:0811.2979 [nucl-th], [Prog. Part. Nucl. Phys.62,551(2009)].
- [49] U. W. Heinz and P. F. Kolb, *Two RHIC puzzles: Early thermalization and the HBT problem*, pp. , 205–216. 2002. arXiv:hep-ph/0204061 [hep-ph].
<http://alice.cern.ch/format/showfull?sysnb=2303513>.
- [50] P. Huovinen, P. Kolb, and U. Heinz, *Is there elliptic flow without transverse flow?*, Nuclear Physics A **698** no. 1, (2002) 475 – 478,
<http://www.sciencedirect.com/science/article/pii/S0375947401014075>.

- [51] D. Teaney, J. Lauret, and E. V. Shuryak, *Flow at the SPS and RHIC as a Quark-Gluon Plasma Signature*, Phys. Rev. Lett. **86** (2001) 4783–4786, <http://link.aps.org/doi/10.1103/PhysRevLett.86.4783>.
- [52] D. Teaney, J. Lauret, and E. Shuryak, *Hydro + Cascade, flow, the equation of state, predictions and data*, Nuclear Physics A **698** no. 1, (2002) 479 – 482, <http://www.sciencedirect.com/science/article/pii/S0375947401014087>.
- [53] O. W. Greenberg, *The Parton model*, in *Compendium of Quantum Physics*, ed. D. Greenberger, K. Hentschel and F. Weinert, (Springer-Verlag, Berlin Heidelberg, 2009), 255–258. 2008. arXiv:0805.2588 [hep-ph]. <https://inspirehep.net/record/785968/files/arXiv:0805.2588.pdf>.
- [54] A. Angerami, *Jet Quenching in Relativistic Heavy Ion Collisions at the LHC*. PhD thesis, Columbia U., 2012. <https://doi.org/10.7916/D8DZ0GC4>.
- [55] P. Z. Skands, *QCD for Collider Physics*, in *Proceedings, High-energy Physics. Proceedings, 18th European School (ESHEP 2010): Raseborg, Finland, June 20 - July 3, 2010*. 2011. arXiv:1104.2863 [hep-ph]. <https://inspirehep.net/record/896215/files/arXiv:1104.2863.pdf>.
- [56] J. C. Collins, D. E. Soper, and G. Sterman, *Factorization for short distance hadron-hadron scattering*, Nuclear Physics B **261** (1985) 104 – 142, <http://www.sciencedirect.com/science/article/pii/0550321385905656>.
- [57] J. C. Collins, D. E. Soper, and G. Sterman, *Soft gluons and factorization*, Nuclear Physics B **308** no. 4, (1988) 833 – 856, <http://www.sciencedirect.com/science/article/pii/0550321388901307>.
- [58] J. C. Collins, D. E. Soper, and G. F. Sterman, *Factorization of Hard Processes in*

- QCD*, Adv. Ser. Direct. High Energy Phys. **5** (1989) 1–91, arXiv:hep-ph/0409313 [hep-ph].
- [59] R. Kogler, *Measurement of jet production in deep-inelastic $e p$ scattering at HERA*. PhD thesis, Hamburg U., 2011.
<http://www-library.desy.de/cgi-bin/showprep.pl?thesis11-003>.
- [60] G. Hanson, G. S. Abrams, A. M. Boyarski, et al., *Evidence for Jet Structure in Hadron Production by e^+e^- Annihilation*, Phys. Rev. Lett. **35** (1975) 1609–1612, <http://link.aps.org/doi/10.1103/PhysRevLett.35.1609>.
- [61] J. Alitti, R. Ansari, D. Autiero, P. Bareyre, et al., *Inclusive jet cross-section and a search for quark compositeness at the CERN pp Collider*, Physics Letters B **257** no. 1, (1991) 232 – 240,
<http://www.sciencedirect.com/science/article/pii/037026939190887V>.
- [62] ZEUS Collaboration, S. Chekanov et al., *Inclusive jet cross-sections in the Breit frame in neutral current deep inelastic scattering at HERA and determination of α_s* , Phys. Lett. **B547** (2002) 164–180, arXiv:hep-ex/0208037 [hep-ex].
- [63] DELPHI Collaboration, J. Abdallah et al., *Measurement of the energy dependence of hadronic jet rates and the strong coupling α_s from the four-jet rate with the DELPHI detector at LEP*, Eur. Phys. J. **C38** (2005) 413–426, arXiv:hep-ex/0410071 [hep-ex].
- [64] ZEUS Collaboration, S. Chekanov et al., *An NLO QCD analysis of inclusive cross-section and jet-production data from the zeus experiment*, Eur. Phys. J. **C42** (2005) 1–16, arXiv:hep-ph/0503274 [hep-ph].
- [65] CDF Collaboration, A. Abulencia et al., *Measurement of the Inclusive Jet Cross Section using the k_T algorithm in $p\bar{p}$ Collisions at $\sqrt{s} = 1.96$ TeV with the CDF II*

- Detector*, Phys. Rev. **D75** (2007) 092006, arXiv:hep-ex/0701051 [hep-ex],
[Erratum: Phys. Rev.D75,119901(2007)].
- [66] OPAL Collaboration, G. Abbiendi et al., *Inclusive Jet Production in Photon-Photon Collisions at $\sqrt{s_{ee}}$ from 189 to 209-GeV*, Phys. Lett. **B658** (2008) 185–192, arXiv:0706.4382 [hep-ex].
- [67] D0 Collaboration, V. M. Abazov et al., *Measurement of the inclusive jet cross-section in $p\bar{p}$ collisions at $\sqrt{s} = 1.96$ -TeV*, Phys. Rev. Lett. **101** (2008) 062001, arXiv:0802.2400 [hep-ex].
- [68] CDF Collaboration, T. Aaltonen et al., *Measurement of the Inclusive Jet Cross Section at the Fermilab Tevatron p anti- p Collider Using a Cone-Based Jet Algorithm*, Phys. Rev. **D78** (2008) 052006, arXiv:0807.2204 [hep-ex], [Erratum: Phys. Rev.D79,119902(2009)].
- [69] D0 Collaboration, V. M. Abazov et al., *Determination of the strong coupling constant from the inclusive jet cross section in $p\bar{p}$ collisions at $\sqrt{s}=1.96$ TeV*, Phys. Rev. **D80** (2009) 111107, arXiv:0911.2710 [hep-ex].
- [70] H1 Collaboration, F. D. Aaron et al., *Jet Production in ep Collisions at Low Q^2 and Determination of α_s* , Eur. Phys. J. **C67** (2010) 1–24, arXiv:0911.5678 [hep-ex].
- [71] ZEUS Collaboration, H. Abramowicz et al., *Inclusive-jet cross sections in NC DIS at HERA and a comparison of the kT , anti- kT and SIScone jet algorithms*, Phys. Lett. **B691** (2010) 127–137, arXiv:1003.2923 [hep-ex].
- [72] D0 Collaboration, V. M. Abazov et al., *Measurement of the dijet invariant mass cross section in $p\bar{p}$ collisions at $\sqrt{s} = 1.96$ TeV*, Phys. Lett. **B693** (2010) 531–538, arXiv:1002.4594 [hep-ex].

- [73] G. Sterman and S. Weinberg, *Jets from Quantum Chromodynamics*, Phys. Rev. Lett. **39** (1977) 1436–1439, <http://link.aps.org/doi/10.1103/PhysRevLett.39.1436>.
- [74] T. Kluge, K. Rabbertz, and M. Wobisch, *FastNLO: Fast pQCD calculations for PDF fits*, pp. , 483–486. 2006. arXiv:hep-ph/0609285 [hep-ph].
http://lss.fnal.gov/cgi-bin/find_paper.pl?conf-06-352.
- [75] K. Nakamura and P. D. Group, *Review of Particle Physics*, Journal of Physics G: Nuclear and Particle Physics **37** no. 7A, (2010) 075021,
<http://stacks.iop.org/0954-3899/37/i=7A/a=075021>.
- [76] T. E. Balestri and J. Jia, *W boson production in ultrarelativistic heavy-ion collisions at the CERN LHC*. PhD thesis, Stony Brook U., 2015.
<https://cds.cern.ch/record/2117070>. Presented 2016.
- [77] D. Kharzeev and M. Nardi, *Hadron production in nuclear collisions at RHIC and high density QCD*, Phys. Lett. **B507** (2001) 121–128, arXiv:nucl-th/0012025 [nucl-th].
- [78] X.-N. Wang and M. Gyulassy, *Energy and Centrality Dependence of Rapidity Densities at RHIC Energies*, Phys. Rev. Lett. **86** (2001) 3496–3499,
<http://link.aps.org/doi/10.1103/PhysRevLett.86.3496>.
- [79] B. Alver, M. Baker, C. Loizides, and P. Steinberg, *The PHOBOS Glauber Monte Carlo*, arXiv:0805.4411 [nucl-ex].
- [80] J. Aubert, G. Bassompierre, et al., *The ratio of the nucleon structure functions F_2^N for iron and deuterium*, Physics Letters B **123** no. 3, (1983) 275 – 278,
<http://www.sciencedirect.com/science/article/pii/0370269383904379>.

- [81] K. J. Eskola, H. Paukkunen, and C. A. Salgado, *EPS09: A New Generation of NLO and LO Nuclear Parton Distribution Functions*, JHEP **04** (2009) 065, arXiv:0902.4154 [hep-ph].
- [82] I. Schienbein, J. Y. Yu, K. Kovarik, C. Keppel, J. G. Morfin, F. Olness, and J. F. Owens, *PDF Nuclear Corrections for Charged and Neutral Current Processes*, Phys. Rev. **D80** (2009) 094004, arXiv:0907.2357 [hep-ph].
- [83] M. Hirai, S. Kumano, and T. H. Nagai, *Determination of nuclear parton distribution functions and their uncertainties in next-to-leading order*, Phys. Rev. **C76** (2007) 065207, arXiv:0709.3038 [hep-ph].
- [84] D. de Florian and R. Sassot, *Nuclear parton distributions at next-to-leading order*, Phys. Rev. **D69** (2004) 074028, arXiv:hep-ph/0311227 [hep-ph].
- [85] G. Altarelli and G. Parisi, *Asymptotic freedom in parton language*, Nuclear Physics B **126** no. 2, (1977) 298 – 318, <http://www.sciencedirect.com/science/article/pii/0550321377903844>.
- [86] V. N. Gribov and L. N. Lipatov, *Deep inelastic e p scattering in perturbation theory*, Sov. J. Nucl. Phys. **15** (1972) 438–450, [Yad. Fiz.15,781(1972)].
- [87] Y. L. Dokshitzer, *Calculation of the Structure Functions for Deep Inelastic Scattering and e+ e- Annihilation by Perturbation Theory in Quantum Chromodynamics.*, Sov. Phys. JETP **46** (1977) 641–653, [Zh. Eksp. Teor. Fiz.73,1216(1977)].
- [88] N. Armesto, *Nuclear shadowing*, J. Phys. **G32** (2006) R367–R394, arXiv:hep-ph/0604108 [hep-ph].
- [89] S. J. Brodsky, *Novel nuclear and heavy quark phenomena in QCD*, Nuclear Physics B-Proceedings Supplements **23** no. 2, (1991) 157–172.

- [90] S. J. Brodsky, *Novel QCD Phenomena at JLab*, PoS **QCDEV2015** (2015) 003, arXiv:1511.04142 [hep-ph].
- [91] M. Arneodo, *Nuclear effects in structure functions*, Physics Reports **240** no. 5, (1994) 301 – 393, <http://www.sciencedirect.com/science/article/pii/0370157394900485>.
- [92] S. Malace, D. Gaskell, D. W. Higinbotham, and I. Cloet, *The Challenge of the EMC Effect: existing data and future directions*, Int. J. Mod. Phys. **E23** no. 08, (2014) 1430013, arXiv:1405.1270 [nucl-ex].
- [93] M. G. Mustafa, *Energy loss of charm quarks in the quark-gluon plasma: Collisional vs radiative losses*, Phys. Rev. C **72** (2005) 014905, <http://link.aps.org/doi/10.1103/PhysRevC.72.014905>.
- [94] A. Ayala, J. Magnin, L. M. Montano, and E. Rojas, *Collisional parton energy loss in a finite size QCD medium revisited: Off mass-shell effects*, Phys. Rev. **C77** (2008) 044904, arXiv:0706.2377 [hep-ph].
- [95] D. d’Enterria, *Jet quenching*, Landolt-Bornstein **23** (2010) 471, arXiv:0902.2011 [nucl-ex].
- [96] J. D. Bjorken, *Energy Loss of Energetic Partons in Quark - Gluon Plasma: Possible Extinction of High $p(t)$ Jets in Hadron - Hadron Collisions*,.
- [97] E. Braaten and M. H. Thoma, *Energy loss of a heavy quark in the quark-gluon plasma*, Phys. Rev. D **44** (1991) R2625–R2630, <http://link.aps.org/doi/10.1103/PhysRevD.44.R2625>.
- [98] A. Peshier, *QCD Collisional Energy Loss Reexamined*, Phys. Rev. Lett. **97** (2006) 212301, <http://link.aps.org/doi/10.1103/PhysRevLett.97.212301>.

- [99] S. Peigné and A. Peshier, *Collisional energy loss of a fast heavy quark in a quark-gluon plasma*, Phys. Rev. D **77** (2008) 114017,
<http://link.aps.org/doi/10.1103/PhysRevD.77.114017>.
- [100] B. G. Zakharov, *Parton energy loss in an expanding quark-gluon plasma: Radiative vs. collisional*, JETP Letters **86** no. 7, (2007) 444–450,
<http://dx.doi.org/10.1134/S0021364007190034>.
- [101] X.-N. Wang and M. Gyulassy, *Gluon shadowing and jet quenching in $A + A$ collisions at $\sqrt{s} = 200$ A GeV*, Phys. Rev. Lett. **68** (1992) 1480–1483,
<http://link.aps.org/doi/10.1103/PhysRevLett.68.1480>.
- [102] P. Arnold, *Gluon Bremsstrahlung in Weakly-Coupled Plasmas*, Nuclear Physics A **830** no. 1, (2009) 211c – 214c,
<http://www.sciencedirect.com/science/article/pii/S0375947409006149>.
- [103] M. Gyulassy, P. Levai, and I. Vitev, *Jet quenching in thin plasmas*, Nucl. Phys. **A661** (1999) 637–640, arXiv:hep-ph/9907343 [hep-ph].
- [104] U. A. Wiedemann, *Gluon radiation off hard quarks in a nuclear environment: opacity expansion*, Nuclear Physics B **588** no. 1, (2000) 303 – 344,
<http://www.sciencedirect.com/science/article/pii/S0550321300004570>.
- [105] W. H. H. Bethe, *On the Stopping of Fast Particles and on the Creation of Positive Electrons*, Proceedings of the Royal Society of London. Series A, Containing Papers of a Mathematical and Physical Character **146** no. 856, (1934) 83–112,
<http://www.jstor.org/stable/2935479>.
- [106] A. B. Migdal, *Bremsstrahlung and Pair Production in Condensed Media at High Energies*, Phys. Rev. **103** (1956) 1811–1820,
<http://link.aps.org/doi/10.1103/PhysRev.103.1811>.

- [107] PHENIX Collaboration, K. Adcox et al., *Suppression of hadrons with large transverse momentum in central Au+Au collisions at $\sqrt{s_{NN}} = 130$ -GeV*, Phys. Rev. Lett. **88** (2002) 022301, arXiv:nucl-ex/0109003 [nucl-ex].
- [108] PHENIX Collaboration Collaboration, S. S. Adler, S. Afanasiev, et al., *Suppressed π^0 Production at Large Transverse Momentum in Central Au + Au Collisions at $\sqrt{s_{NN}} = 200$ GeV*, Phys. Rev. Lett. **91** (2003) 072301, <http://link.aps.org/doi/10.1103/PhysRevLett.91.072301>.
- [109] STAR Collaboration Collaboration, C. Adler, Z. Ahammed, et al., *Centrality Dependence of High- p_T Hadron Suppression in Au + Au Collisions at $\sqrt{s_{NN}} = 130$ GeV*, Phys. Rev. Lett. **89** (2002) 202301, <http://link.aps.org/doi/10.1103/PhysRevLett.89.202301>.
- [110] STAR Collaboration, J. Adams et al., *Transverse momentum and collision energy dependence of high $p(T)$ hadron suppression in Au+Au collisions at ultrarelativistic energies*, Phys. Rev. Lett. **91** (2003) 172302, arXiv:nucl-ex/0305015 [nucl-ex].
- [111] D. G. d'Enterria, *Hard scattering cross-sections at LHC in the Glauber approach: From pp to pA and AA collisions*, arXiv:nucl-ex/0302016 [nucl-ex].
- [112] I. Vitev, J. T. Goldman, M. B. Johnson, and J. W. Qiu, *Open charm tomography of cold nuclear matter*, Phys. Rev. **D74** (2006) 054010, arXiv:hep-ph/0605200 [hep-ph].
- [113] T. S. E. Norrbin, *Production and hadronization of heavy quarks*, Eur. Phys. J. C **17** (2000) 137–161.
- [114] J. D. Richman and P. R. Burchat, *Leptonic and semileptonic decays of charm and bottom hadrons*, Rev. Mod. Phys. **67** (1995) 893–976, <http://link.aps.org/doi/10.1103/RevModPhys.67.893>.

- [115] N. Cabibbo, *Unitary Symmetry and Leptonic Decays*, Phys. Rev. Lett. **10** (1963) 531–533, <http://link.aps.org/doi/10.1103/PhysRevLett.10.531>.
- [116] N. Armesto, C. A. Salgado, and U. A. Wiedemann, *Medium induced gluon radiation off massive quarks fills the dead cone*, Phys. Rev. **D69** (2004) 114003, [arXiv:hep-ph/0312106](http://arxiv.org/abs/hep-ph/0312106) [hep-ph].
- [117] PHENIX Collaboration Collaboration, A. Adare et al., *Heavy-quark production in $p + p$ and energy loss and flow of heavy quarks in $Au + Au$ collisions at $\sqrt{s_{NN}} = 200$ GeV*, Phys. Rev. C **84** (2011) 044905, <http://link.aps.org/doi/10.1103/PhysRevC.84.044905>.
- [118] Z. Ye, *Measurements of open heavy flavor in STAR experiment*, Nuclear Physics A **932** (2014) 45 – 50, <http://www.sciencedirect.com/science/article/pii/S0375947414004795>, Hard Probes 20136th International Conference on Hard and Electromagnetic Probes of High-Energy Nuclear Collisions.
- [119] CMS Collaboration Collaboration, S. Chatrchyan, V. Khachatryan, et al., *Evidence of b -Jet Quenching in $PbPb$ Collisions at $\sqrt{s_{NN}} = 2.76$ TeV*, Phys. Rev. Lett. **113** (2014) 132301, <http://link.aps.org/doi/10.1103/PhysRevLett.113.132301>.
- [120] J. Huang, Z.-B. Kang, and I. Vitev, *Inclusive b -jet production in heavy ion collisions at the LHC*, Physics Letters B **726** no. 1–3, (2013) 251 – 256, <http://www.sciencedirect.com/science/article/pii/S0370269313006357>.
- [121] ATLAS Collaboration, *The ATLAS Experiment at the CERN Large Hadron Collider*, tech. rep., 2008.
- [122] <http://sites.uci.edu/energyobserver/2012/11/26/introduction-to-the-atlas-detector-at-the-lhc/>.

- [123] ATLAS Collaboration, J. Schieck, *Track-based alignment for the ATLAS Inner Detector Tracking System*, JINST **7** (2012) C01012, arXiv:1110.4508 [hep-ex].
- [124] <http://atlasexperiment.org/photos/calorimeters-combined-barrel.html>.
- [125] ATLAS Collaboration, G. Aad et al., *Commissioning of the ATLAS Muon Spectrometer with Cosmic Rays*, Eur. Phys. J. **C70** (2010) 875–916, arXiv:1006.4384 [physics.ins-det].
- [126] ATLAS Collaboration, G. Aad et al., *The performance of the jet trigger for the ATLAS detector during 2011 data taking*, Eur. Phys. J. **C76** no. 10, (2016) 526, arXiv:1606.07759 [hep-ex].
- [127] M. Cacciari, G. P. Salam, and G. Soyez, *The Anti- $k(t)$ jet clustering algorithm*, JHEP **04** (2008) 063, arXiv:0802.1189 [hep-ph].
- [128] M. Cacciari, G. P. Salam, and G. Soyez, *FastJet User Manual*, Eur. Phys. J. **C72** (2012) 1896, arXiv:1111.6097 [hep-ph].
- [129] R. Achenbach, P. Adragna, V. Andrei, et al., *The ATLAS Level-1 Calorimeter Trigger*, Tech. Rep. ATL-DAQ-PUB-2008-001. ATL-COM-DAQ-2008-002, CERN, Geneva, Jan, 2008. <http://cds.cern.ch/record/1080560>.
- [130] ATLAS Collaboration, G. Aad et al., *Expected Performance of the ATLAS Experiment - Detector, Trigger and Physics*, arXiv:0901.0512 [hep-ex].
- [131] ATLAS Collaboration Collaboration, *Performance of the ATLAS muon trigger in 2011*, Tech. Rep. ATLAS-CONF-2012-099, CERN, Geneva, Jul, 2012. <http://cds.cern.ch/record/1462601>.
- [132] ATLAS Collaboration, G. Aad et al., *Performance of the ATLAS Trigger System in 2010*, Eur. Phys. J. **C72** (2012) 1849, arXiv:1110.1530 [hep-ex].

- [133] A. Angerami, B. Cole, and D. Perepelitsa, *Measurement of the inclusive jet spectrum and jet suppression using 2011 Pb+Pb data: Jet R_{AA} measurement*, Tech. Rep. ATL-COM-PHYS-2013-1370, CERN, Geneva, Sep, 2013.
<https://cds.cern.ch/record/1604232>.
- [134] <https://twiki.cern.ch/twiki/bin/viewauth/Atlas/HeavyIonRunList>.
- [135] A. Angerami, B. Cole, et al., *Centrality Determination in the 2010 Pb+Pb physics data*, Tech. Rep. ATL-COM-PHYS-2011-1733, CERN, Geneva, 2011.
- [136] ATLAS Collaboration, G. Aad et al., *Measurement of the pseudorapidity and transverse momentum dependence of the elliptic flow of charged particles in lead-lead collisions at $\sqrt{s_{NN}} = 2.76$ TeV with the ATLAS detector*, Phys.Lett. **B707** (2012) 330–348, arXiv:1108.6018 [hep-ex].
- [137] Y. Tian, S. Mohapatra, and B. Cole, *R_{AA} and V_2 of muons from heavy-quark decay in lead-lead collisions at $\sqrt{s} = 2.76$ TeV within the ATLAS detector*, Tech. Rep. ATL-COM-PHYS-2015-235, CERN, Geneva, Apr, 2015.
<https://cds.cern.ch/record/2007282>.
- [138] T. Sjostrand, S. Mrenna, and P. Skands, *PYTHIA 6.4 Physics and Manual*, JHEP **0605** (2006) 026, arXiv:hep-ph/0603175 [hep-ph].
- [139] *Jet energy scale and its uncertainty for jets reconstructed using the ATLAS heavy ion jet algorithm*, Tech. Rep. ATLAS-CONF-2015-016, CERN, Geneva, Apr, 2015.
<https://cds.cern.ch/record/2008677>.
- [140] ATLAS Collaboration, S. Mohapatra, *Measurement correlations between elliptic and higher-order flow harmonics in 2.76 TeV Pb+Pb collisions using the ATLAS detector*, Nucl. Phys. **A931** (2014) 959–964.

- [141] A. Angerami, B. Cole, et al., *Performance of Jet Reconstruction in Heavy Ion Collisions*, Tech. Rep. ATL-COM-PHYS-2011-427, CERN, Geneva, Dec, 2011.
- [142] ATLAS Collaboration, G. Aad et al., *Jet energy measurement with the ATLAS detector in proton-proton collisions at $\sqrt{s} = 7$ TeV*, Eur. Phys. J. **C73** no. 3, (2013) 2304, arXiv:1112.6426 [hep-ex].
- [143] A. Angerami, B. Cole, T. Kosek, D. Perepelitsa, M. Rybar, H. Santos, and M. Spousta, *Jet energy scale determination for heavy ion jet reconstruction: JES for HI jets*, Tech. Rep. ATL-COM-PHYS-2014-329, CERN, Geneva, Apr, 2014. <https://cds.cern.ch/record/1696485>.
- [144] ATLAS Collaboration Collaboration, G. Aad, E. Abat, B. Abbott, J. Abdallah, et al., *Expected performance of the ATLAS experiment: detector, trigger and physics*. CERN, Geneva, 2009. <https://cds.cern.ch/record/1125884>.
- [145] ATLAS Collaboration, *Measurement of the centrality dependence of open heavy flavour production in lead-lead collisions at $\sqrt{s} = 2.76$ TeV with the ATLAS detector*, Tech. Rep. ATLAS-CONF-2012-050, CERN, Geneva, May, 2012. <https://cds.cern.ch/record/1451883>.
- [146] ATLAS Collaboration, *Measurement of the b -jet production cross section using muons in jets with ATLAS in pp Collisions at $\sqrt{s} = 7$ TeV*, Tech. Rep. ATLAS-CONF-2011-057, CERN, Geneva, Apr, 2011. <https://cds.cern.ch/record/1343733>.
- [147] W. Verkerke and D. Kirkby. <https://roofit.sourceforge.net/>.
- [148] ATLAS Collaboration, G. Aad et al., *Jet energy measurement and its systematic uncertainty in proton-proton collisions at $\sqrt{s} = 7$ TeV with the ATLAS detector*, Eur. Phys. J. **C75** (2015) 17, arXiv:1406.0076 [hep-ex].

- [149] A. Angerami, B. Cole, D. Perepelitsa, P. Balek, T. Kosek, M. Rybar, M. Spousta, A. Galan, and H. Santos, *Performance of Jet Reconstruction in Heavy Ion Collisions*, Tech. Rep. ATL-COM-PHYS-2011-1733, CERN, Geneva, Dec, 2011.
<https://cds.cern.ch/record/1409453>. Supporting document for jet rcp paper which is in final pub com review.
- [150] <https://twiki.cern.ch/twiki/bin/viewauth/AtlasProtected/JetEnergyResolutionProvider>.
- [151] *ATLAS tunes of PYTHIA 6 and Pythia 8 for MC11*, Tech. Rep. ATL-PHYS-PUB-2011-009, CERN, Geneva, Jul, 2011.
<http://cds.cern.ch/record/1363300>.
- [152] M. Bahr et al., *Herwig++ Physics and Manual*, Eur. Phys. J. **C58** (2008) 639–707, arXiv:0803.0883 [hep-ph].
- [153] S. Gieseke, C. Rohr, and A. Siodmok, *Colour reconnections in Herwig++*, Eur. Phys. J. **C72** (2012) 2225, arXiv:1206.0041 [hep-ph].
- [154] ATLAS Collaboration Collaboration,, *Jet energy scale and its systematic uncertainty in proton-proton collisions at $\sqrt{s}=7$ TeV with ATLAS 2011 data*, Tech. Rep. ATLAS-CONF-2013-004, CERN, Geneva, Jan, 2013.
<https://cds.cern.ch/record/1509552>.
- [155] J. Huang, Z.-B. Kang, and I. Vitev, *Inclusive b-jet production in heavy ion collisions at the LHC*, Phys. Lett. **B726** (2013) 251–256, arXiv:1306.0909 [hep-ph].